Fluctuations of conserved charges in heavy-ion collisions from a transport perspective

Dissertation
zur Erlangung des Doktorgrades
der Naturwissenschaften

vorgelegt beim Fachbereich Physik
der Johann Wolfgang Goethe-Universität
in Frankfurt am Main

von
Jan Hammelmann
aus Frankfurt am Main

Frankfurt am Main 2023
D30

vom Fachbereich Physik der
Johann Wolfgang Goethe-Universität als Dissertation angenommen.

Dekan: Prof. Dr. Roger Erb

Gutachter: Prof. Dr. Hannah Elfner und
           Priv. Doz. Hendrik van Hees

Datum der Disputation:

Zusammenfassung

Die Untersuchung der Grundlegenden Kräfte, welche die Zusammensetzung und Entwicklung unseres Universums bestimmen, ist grundlegender Bestandteil von vielen experimentellen und theoretischen Studien. Die Kraft, welche in dieser Arbeit studiert wird, ist die starke Wechselwirkung oder auch Quantenchromodynamik (QCD) genannt. Die QCD beschreibt die Interaktionen zwischen Quarks und Gluonen, welche Bestandteile des Standard Models der Teilchenphysik sind, das die elementarsten Bausteine und deren Wechselwirkung zusammenfasst. Studien zu dem Zustand der QCD Marterie bei extrem hohen Temperaturen und Dichten, ähnlich wie sie vermutlich am Anfang des Universums existiert haben, sind experimentell sehr aufwendig. Die einzige Möglichkeit, um Materie bei diesen extremen Bedingungen zu erzeugen, ist Schwerionen mit beinahe Lichtgeschwindigkeit aufeinander zu schießen. Eine grundlegende Frage bezüglich den Zuständen der stark wechselwirkenden Materie bezieht sich auf die Phasen. Ähnlich wie bei Wasser, welches in drei verschiedenen Phasen auftritt (fest, flüssig und gasförmig), je nachdem welche Temperatur und Druck vorherrschen, wird vermutet, dass bei der QCD ebenfalls unterschiedliche Phasen existieren. Grundlage dieser Phasen ist die energieabhängige Kopplungskonstante der zugrundeliegenden Theorie, welche bei kleinen Energieüberträgen sehr groß und bei großen Energieüberträgen sehr klein ist. Hohe Kopplungswerte führen zum Einschluss (Confinement) der Quarks und Gluonen zu Hadronen, zu denen beispielsweise Protonen und Neutronen gehören aus denen unsere Welt aufgebaut ist. Umgekehrt wird die Kopplungskonstante bei sehr hohen Temperaturen klein, wodurch sich Quarks und Gluonen frei bewegen können. Dieser Zustand wird auch Quark Gluon Plasma (QGP) genannt. Der Verlauf einer Schwerionenkollision beginnt mit den beschleunigten Atomkernen. Nachdem diese miteinander kollidieren, erzeugen sie, je nach Energie, vermutlich das QGP. Nach einer gewissen Zeit kühlt die Materie wieder ab und es entstehen wieder Hadronen. Diese interagieren weiter miteinander, bis sie schließlich so weit voneinander entfernt sind, dass keine Wechselwirkungen mehr geschehen und sie in den Detektoren gemessen werden können. Bei vergleichsweise niedrigeren Energien wird kein QGP erzeugt und die Kollision der Schwerionen wird ausschließlich durch Interaktionen der Hadronen beschrieben. Die Schwerionenkollisionen werden bei unterschiedlichen Energien durchgeführt, wodurch die erzeugte Materie sich in Temperatur und baryonischer Dichte unterscheidet und wodurch das Phasen-Diagram der QCD Materie untersucht werden kann. Beispiele solcher Experimente sind der Large Hadron Collider (LHC) am Cern, dem Relativistic Heavy-Ion Collider (RHIC) am Brookhaven National Laboratory (BNL) oder dem HADES Experiment bei der Gesellschaft für Schwerionenforschung (GSI). Bei den höchsten Kollisionsenergien am LHC, hat die erzeugte Marterie nahezu keine baryonische Dichte und gleichzeitig

eine extrem hohe Temperatur, sodass angenommen wird, dass das QGP dort erzeugt wird. Je niedriger die Energie mit der die Schwerionen kollidiert werden, desto höher ist die baryonische Dichte in der Kollision, da mehr der ursprünglichen Protonen und Neutronen im zentralen Kollisionsbereich gestoppt werden. Eine der grundlegenden Fragen bezieht sich auf die Eigenschaft des Phasenübergangs zwischen der hadronischen Phase und dem QGP. Von Gittereichrechnungen ist bekannt, dass der Übergang bei verschwindender baryonischer Dichte von kontinuierlicher Natur ist. Eine Vorhersage von effektiven Rechnungen besagt, dass der Übergang bei höheren Dichten ein Phasenübergang erster Ordnung ist. Diese Erkenntnis setzt die Existenz eines kritischen Punktes in dem Übergang zwischen diesen beiden Bereichen voraus. Die experimentelle Suche nach der Natur des Phasenübergangs ist Bestandteil vieler Untersuchungen, beispielsweise durch das Beam Energy Scan (BES) Programm am BNL oder auch in Zukunft bei der Facility for Antiproton and Ion Research (FAIR) bei der GSI.

Für die Beschreibung solcher Kollisionen von theoretischer Seite werden dynamische Modelle genutzt. Da die zugrundeliegende Theorie nur in bestimmten Grenzfällen mit Gittereichtheorien exakt gelöst werden kann, müssen effektive Theorien der QCD Materie herangezogen werden. Die dynamische Beschreibung der Kollision in der hadronischen Phase wird üblicherweise mithilfe sogenannter Transport Modelle vorgenommen. Das in der Kollision entstehende Nichtgleichgewichtssystem wird dann mithilfe von kinetischer Theorie charakterisiert. Die Dynamik der extrem heißen und dichten Phase wird oft mithilfe hydrodynamischer Modelle beschrieben. Durch den Vergleich der Modelrechnungen mit bestimmten experimentellen Observablen lässt sich viel über die zugrundeliegenden Interaktionen und Eigenschaften der Marterie lernen. Ein Beispiel einer solchen Observable sind Fluktuationen erhaltener Ladungen. Erhaltene Ladungen, zu denen unter anderem die baryonische oder elektrische Ladung gehört, resultieren aus der Invarianz der zugrundeliegenden Theorie unter Eichtransformationen der $U(1)$ Symmetriegruppe. Fluktuationen beschreiben die Änderung einer bestimmten Observablen, wenn mehrere Messungen durchgeführt werden. Dies kann zum Beispiel die Anzahl an Teilchen aus mehreren Ereignissen oder aber die zeitliche Änderung sein. Beispielsweise sind in der Nähe eines kritischen Punktes die Fluktuationen der baryonischen Ladung von Kollision zu Kollision stark verändert, wodurch man sich erhofft, einen solchen durch Fluktuationen der Netto-Proton Zahl zu messen. Des Weiteren lassen sich aber auch andere Eigenschaften der Marterie durch die Untersuchung von Fluktuationen erhaltener Ladungen untersuchen. So kann zum Beispiel aus Fluktuationen der Ladungsströme über die Zeit die Eigenschaft der Marterie untersucht werden, wie gut eine erhaltene Ladung durch das Medium transportiert werden kann. Diese werden üblicherweise durch sogenannte Diffusionskoeffizienten charakterisiert.

Ziel dieser Arbeit ist es, durch die Untersuchung von Fluktuationen erhaltener Ladungen die Eigenschaften hadronischer Marterie zu untersuchen. Hierzu wird ein Transport Modell (SMASH) als Grundlage dieser Studien herangezogen. Im ersten Teil dieser Arbeit werden Transportkoeffizienten untersucht, speziell die Diffusionskoeffizienten erhaltener Ladungen und neben den diagonalen Termen wie zum Beispiel dem baryonische Diffusionskoeffizient κ_{BB} dessen Kreuztermen, beispiels-

weise der baryonisch-seltsamen Diffusionskoeffizient κ_{BS}. Zusammenfassend lassen sich diese durch die Diffusionskoeffizienten Matrix $\kappa_{qq'}$ beschreiben. Zusätzlich wird ein weiterer Transportkoeffizient untersucht, die Scherviskosität η, welche sich aus Fluktuationen des Energie-Impuls Tensors bestimmen lässt. Allgemein gesprochen charakterisieren Transportkoeffizienten die Entwicklung der Marterie aus Nichtgleichgewichtszuständen zurück ins Gleichgewicht. Die Scherviskosität spielt eine wichtige Rolle, um die Anisotropie der entstandenen Teilchen im Impulsraum, auch Flow genannt, zu beschreiben. Durch den Vergleich mit hydrodynamischen Rechnungen wurde gefunden, dass die Scherviskosität des erzeugten Mediums einen der geringsten Werte überhaupt besitzt und sich das Medium fast wie eine perfekte Flüssigkeit verhält.

Gegenstand des ersten Teils dieser Arbeit ist es, das hadronische Medium und die Interaktionen der einzelnen Teilchen einzuführen. Durch die systematische Erweiterung der Interaktionen und der Freiheitsgraden und die daraus resultierenden Transportkoeffizienten lassen sich deren Einfluss auf $\kappa_{qq'}$ und η genau bestimmen. Zu Beginn wird allerdings erst die Methodik verifiziert, um die Transportkoeffizienten aus dem Transport Modell zu bestimmen. Durch einen Vergleich mit Rechnungen in der Chapman-Enskog (CE) Annäherung wird gezeigt, dass die numerische Integration der Korrelationsfunktionen perfekt mit den CE Rechnungen übereinstimmt. Im nächsten Schritt wird der Einfluss von $3 \leftrightarrow 1$ Mehrteilchenreaktionen auf die Transportkoeffizienten in einem vereinfachten System bestimmt. Solche Mehrteilchenreaktionen werden in einem heißen und dichten hadronischen Medium in der Nähe des Phasenübergangs wichtig, allerdings auch kompliziert in einem Modell wie SMASH zu behandeln. Es wird gezeigt, dass die Scherviskosität in einem Gas aus π, ρ und ω Mesonen mit Mehrteilchenreaktionen bei hohen Temperaturen geringer ist als durch binäre Reaktionsketten. Der elektrische Diffusionskoeffizient des Mediums ist nicht verändert. Im nächsten Schritt wird das volle Hadrongas, welches in SMASH zur Verfügung steht, untersucht. Es werden der Einfluss von winkelabhängigen Wirkungsquerschnitten und zusätzlichen elastischen Wirkungsquerschnitten, beschrieben durch das Additive Quark Model (AQM), untersucht. Sowohl die Scherviskosität als auch die Diffusionkoeffizienten sind stark durch die AQM Wikungssquerschnitte beeinflusst, indem deren Werte verringert sind. Die winkelabhängigen Wirkungsquerschnitte, welche für mesonische und baryonische Prozesse angenommen werden, haben keinen Einfluss auf $\kappa_{qq'}$, während η erhöht wird. Als nächstes wird die Abhängigkeit der Transportkoeffizienten von der Anzahl an Freiheitsgraden bestimmt. Hierzu werden drei verschiedene Systeme ausgesucht, welche in ihrer Komplexität zunehmen. In einer vorherigen Studie zu dem elektrischen Diffusionskoeffizienten wurde eine Skalierung von $\kappa_{Qq'}$ mit der Anzahl an Freiheitsgraden gefunden. Dieser wird allerdings nicht für die volle Diffusionskoeffizienten Matrix verifiziert. Trotzdem ist eine starke Abhängigkeit gegeben. Die Scherviskosität hingegen ist weniger stark beeinflusst, vor allem bei den Gasen, welche durch die Erzeugung von Resonanzen interagieren. Im letzten Schritt werden die Transportkoeffizienten bei nicht verschwindender baryonisch-chemischen Potenzial μ_B untersucht. Die gefundene Abhängigkeit von $\kappa_{qq'}$ von μ_B ist vergleichbar mit derjenigen aus CE Rechnungen. Die genauen Werte allerdings sind unterschiedlich. Im Vergleich zu vorherigen Rechnungen ist die Scherviskosität nicht von μ_B

abhängig. Modifikationen von η/s stammen ausschließlich von eine Änderung der Entropiedichte s. Abschließend lässt sich zusammenfassen, dass η stark von einzelnen Wirkungsquerschnitten und der Modelierung einzelner Interaktionen bestimmt ist. Die Diffusionskoeffizienten Matrix hingegen ist sowohl durch die Ladungsdichte als auch durch den totalen Wirkungsquerschnitt der Konstituenten des Hadron Gases bestimmt. Der Vergleich mit Rechnungen der Transportkoeffizienten aus anderen Modellen zeigt, das die in SMASH implementierten Interaktionen sowie die Anzahl an Freiheitsgraden vergleichbar und realistisch sind.

Als nächstes werden Fluktuationen erhaltener Ladungen in Form von Kumulanten von Teilchenzahlen untersucht. Wie bereits beschrieben, ist dies wichtig zur Untersuchung von Phasenübergängen. Speziell soll der Einfluss der hadronischen Phase einer Schwerionenkollision auf die Kumulanten bestimmt werden. Hierzu wird wieder SMASH verwendet, dessen Interaktionen und Gleichgewichtseigenschaften in Form von Transportkoeffizienten im ersten Teil bestimmt wurden. Zunächst wird der Einfluss von globaler Ladungserhaltung auf die Kumulanten erhaltener Ladungen in einer Box mit periodischen Randbedingungen berechnet. Hierzu wird das System in kleinere Volumen unterteilt und die Fluktuationen werden in Abhängigkeit der Größe dieser Volumina angegeben. Dazu wird zu Beginn ein Vergleich mit einer vorherigen Rechnung in einem einfachen System, welches aus π und ρ Mesonen besteht, durchgeführt. Vor allem wird gezeigt, wie der Einfluss der vierten Kumulante der Netto-Ladung durch Fluktuationen der totalen Ladungszahl beeinflusst ist. Im nächsten Schritt wird ein vereinfachtes baryonisches System und vor allem baryonische Vernichtungsprozesse untersucht. Ähnlich wie bei der elektrischen Ladung wird bewiesen, dass solche Prozesse eine Fluktuation der totalen Ladung induzieren, und dabei primär die vierte Kumulante beeinflussen. Bei endlichem μ_B existieren nicht genug solcher Prozesse, sodass der μ_B-abhängige Übergang zwischen der Poisson und Binomial Verteilung beobachtet werden kann. Bei den beiden Systemen wird eine gute Übereinstimmung zwischen den Ergebnissen aus SMASH und analytischen Rechnungen gefunden. Zusätzlich verändern Einschränkungen des Impulsraumes die Kumulanten, indem Korrelationen durch die exakte Ladungserhaltung reduziert werden. Als nächstes wird das Verhältnis zwischen den Fluktuationen der gesamten baryonischen Ladung des Systems und der Netto-Proton Zahl bestimmt. Dieses ist besonders wichtig, da die letztere in experimentellen Messungen stellvertretend für die Fluktuationen der erhaltenen gesamten baryonischen Ladung genommen wird. Ähnlich wie bei Einschränkungen des Impulsraumes, folgen die Netto-Proton Fluktuationen nicht den analytischen Erwartungen von exakter Ladungserhaltung, sondern sind in größeren Volumen erhöht. Eine Binomiale Abbildung ist aufgrund von dynamischen Korrelationen nicht in der Lage, die baryonischen Kumulanten aus den Proton Fluktuationen zu bestimmen. Schließlich wird noch gezeigt, dass die Korrelationen der Netto-Proton bei verschwindendem μ_B vergleichbar mit Messungen von ALICE sind. Eine abschließende Studie zur Bestimmung des Einflusses von Formation von Deuteron zeigt, dass die Netto-Proton Fluktuationen nicht durch diese beeinflusst sind.

Im nächsten Schritt wird die Entwicklung kritischer Fluktuationen im hadronischen Medium untersucht. Hierzu wird zunächst ein System mit kritischen Gleich-

gewichtsfluktuationen präpariert, welche aus der Kopplung des Hadron Resonanz Gases (HRG) mit dem drei dimensionalen (3d) Ising Modell bestimmt werden. Die Wahrscheinlichkeitsverteilung der Teilchenzahlen, welche benötigt werden, um die Entwicklung in SMASH zu untersuchen, wird aus dem Prinzip der maximalen Entropie bestimmt. Hierzu wird im ersten Schritt gezeigt, dass diese Verteilungen, bzw. die generierten Anzahlen an Teilchen und Antiteilchen, die gewünschten kritischen Fluktuationen wiedergeben. Als nächstes soll die Entwicklung dieser Verteilungen in einer expandierenden Kugel untersucht werden, dessen Anfangszustand zunächst im Impuls und Koordinatenraum beschrieben wird. Die Impulsverteilung und das Volumen der Sphäre wird an experimentelle Messungen angepasst. Als Anfangsbedingungen werden die Temperatur T und die chemischen Potenziale μ_B, μ_Q und μ_S von einer Bestimmung des chemischen Endzustandes im Gleichgewicht von Schwerionenkollisionen als Funktion der Strahlenenergie $\sqrt{s}$ benutzt. Die Entwicklung des Systems wird dementsprechend entlang $\sqrt{s}$ initiiert. Die Berechnungen der thermodynamischen Eigenschaften und der Anzahl der Kollisionen zeigen, wie sich das System im Phasenraum verhält. Während der Expansion sinken die Temperaturen und das baryon chemische Potenzial steigt. Eine Analyse der Anzahl spezifischer Kollisionskanäle zeigt, dass vor allem Resonanz Zerfälle und Erzeugungen die Dynamik des hadronischen Mediums bestimmen. Die Berechnung der Netto-Proton Kumulanten als Funktion der Zeit zeigt, dass die Fluktuationen stark durch das hadronische Medium beeinflusst sind. Die kritischen Fluktuationen ändern sich besonders stark in den ersten Zeitschritten der Evolution. Diese Entwicklung kann hauptsächlich den Resonanz Zerfällen und Erzeugungen zugeordnet werden. Die Betrachtung der Fluktuationen im Endzustand der Expansion liefert Informationen darüber, inwieweit die kritischen Fluktuationen die Entwicklung überleben. Es wird gezeigt, dass ein Großteil der Korrelationen durch Isospin Randomisierungsprozesse verringert wird. Betrachtet man beispielsweise die Netto-Nukleon Anzahl zeigt sich, dass die kritischen Fluktuationen besser erhalten sind. Schließlich wird im letzten Abschnitt noch die Abhängigkeit der Kumulanten vom Rapiditätsfenster betrachtet, bei der eine nicht monotone Abhängigkeit sichtbar ist.

Im letzten Teil werden Kollisionen der Isobare Ru and Zr bei $\sqrt{s_{NN}} = 200\,\mathrm{GeV}$ studiert. Bei diesen Energien kann die gesamte Schwerionenkollision nicht durch Transport Modelle beschrieben werden. Die QGP Phase wird durch eine hydrodynamische Rechnung beschrieben. Zunächst werden allerdings die Anfangsbedingungen mittels SMASH untersucht. Hier wird vor allem der Fokus auf die nukleare Struktur der Isobare gelegt. Es wird gezeigt, dass die Deformationsparameter β einen starken Einfluss auf die geometrische Struktur des Anfangszustandes haben. Die Triaxialität γ hingegen hat keinen sichtbaren Einfluss. Des Weiteren wird der Einfluss von Korrelationen zwischen Nukleon-Nukleon Paaren auf Fluktuationen der Exzentrizitäten studiert. Es wird allerdings kein Einfluss festgestellt. Im nächsten Schritt werden die bereits untersuchten Anfangsbedingungen mit dem hydrodynamischen Modell vHLLE entwickelt. Der Wechsel zwischen der hydrodynamischen Beschreibung und der kinetischen, geschieht mittels der Cooper-Frye Formel. Des Weiteren werden die Hadronen auf der Hyperfläche mit dem kanonischen Ensemble generiert, wodurch die erhaltenen Ladungen B, Q und S nicht nur im Ereignis Mittel, sondern exakt erhalten

sind. Zusätzlich wird der sogenannte "Neutron Skin" Effekt betrachtet, welcher die elektrische Ladungsverteilung der Anfangszustände ändert, indem mehr Protonen im Inneren der Kerne vorhanden sind. Nachdem die Hadronen auf den Hyperflächen generiert sind, wird die späte Phase der Kollision durch SMASH bis zum kinetischen Ausfrieren der Teilchen simuliert. Hier werden dann Bulk Observablen und Fluktuationen berechnet, um den Einfluss des kanonischen Ensembles und Neutron Skins zu bestimmen. Zunächst wird gezeigt, dass der Neutron Skin die mittlere Anzahl geladener Teilchen in peripheren Kollisionen beeinflusst. Da hier die Neutronen reiche Bereiche der Kerne sich treffen, werden dementsprechend weniger geladene Teilchen produziert. Allerdings ist kein Einfluss auf die Fluktuationen zu erkennen. Durch das kanonische Ensemble allerdings werden die Fluktuationen verändert. Wird die skalierte Varianz als Funktion des Rapiditätsfensters $\Delta\eta$ betrachtet, sieht man, dass die Fluktuationen in großen $\Delta\eta$ unterdrückt ist, da die Ladungen im vollen Phasenraum konstant ist. Die hadronische Phase ändert die Fluktuationen der Netto-Pion, Netto-Kaon und Netto-Protonen, indem Annihilationsprozesse die Varianz ändern. Diese Dissertation basiert auf folgenden Publikationen:

- Impact of hadronic interactions and conservation laws on cumulants of conserved charges in a dynamical model. J. Hammelmann & H. Elfner, Phys.Rev.C 107 (2023) 4, 044910 [1]

- Impact of hadronic interactions and conservation laws on cumulants of conserved charges in a dynamical model. J. Hammelmann & H. Elfner, PoS FAIRness2022 (2023) 019 [2]

- Collision term dependence of the hadronic shear viscosity and diffusion co-efficients. J. Hammelmann, J. Staudenmaier & H. Elfner, arXiv:2307.15606 [nucl-th] (2023). Submitted to Phys. Rev. C (2023) [3]

- Fate of critical fluctuations in an interacting hadronic medium using maximum entropy distributions. J. Hammelmann, M. Bluhm, M. Nahrang & H. Elfner, arXiv:2310.06636 [nucl-th] (2023) [4]

Weitere Publikationen, die im Laufe dieser Arbeit erschienen sind:

- Particle production in a hybrid approach for a beam energy scan of Au+Au/Pb+Pb collisions between $\sqrt{s_{\mathrm{NN}}} = 4.3$ GeV and $\sqrt{s_{\mathrm{NN}}} = 200.0$ GeV. A. Schäfer, I. Karpenko, X. Wu, J. Hammelmann & H. Elfner, Eur.Phys.J.A 58 (2022) 11, 230 [5].

- Theoretical and Experimental Constraints for the Equation of State of Dense and Hot Matter. MUSES collaboration, arXiv:2303.17021 [nucl-th] [6].

- Thermodynamics of an updated hadronic resonance list and influence on hadronic transport, J. M. San Martin, R. Hirayama, J. Hammelmann, J. M. Kartheim, P. Parotto, J. Noronha-Hostler, C. Ratti and H. Elfner, arXiv:2309.01737 [nucl-th] [7]

Contents

1
Introduction

One of the goals in the very broad field of physics is to grasp the complex, most fundamental interactions of our universe. Our understanding so far is collected in the standard model of particle physics, which contains all the elementary particles with their respective interactions. This thesis mainly focuses on one of the fundamental forces, the strong interaction, and in this chapter some of the phenomenological aspects of it will be discussed and experimental ways to study the strong interaction will be described. In the first part of this chapter, a historical introduction will be given which is mainly inspired by [8].

1.1 A brief historical introduction to quantum chromodynamics

The starting point for the development of the theory of quantum chromodynamics (QCD) was given by Gell-Mann and Zweig in 1963. With their proposal of the fundamental strongly interacting particles called quarks, the starting point of the theory was laid. Their goal was to understand the underlying concept of the so-called particle zoo, a collection of measured particles whose underlying concept could not be understood. In order to describe the variety of founded particles, Gell-Mann and Zweig proposed the existence of three quarks which are elementary Fermions, particles with half-odd-integer spin, which were then called up, down and strange quarks. Two different kinds of hadrons, particles made of quarks, bound by the strong interaction, could be formed with these three quarks. The first kind are mesons, formed by a quark and anti-quark pair, which have spin 0 or 1 and generally fall into the class of Bosons (particles with integer value spin). The second type are baryons, formed by three quarks, and are Fermions as well. It was additionally proposed that the electric charge Q of the quarks has to be $+2/3$ for the up and strange quark and $-1/3$ for the down quark, in order to explain the electric charge

states of the observed hadronic spectrum. Later, the existence of three more quarks was discovered. The top quark has an electric charge of $+2/3$ and the charm and bottom quark have $Q = -1/3$. The six quarks define the so-called flavor of QCD. In addition to the fractional electric charge that the quarks carry, it was proposed that they have an additional charge, named color, to fix the symmetry of the wave function of the hadrons. The idea was then to assign three colors to the quarks which are invariant under a global $SU(3)$ symmetry. As a result, the hadronic states must be formed by quarks such that their wave function is invariant under the $SU(3)$ symmetry group. Possible solutions are hadrons formed by a quark anti-quark pair (mesons) and hadrons formed by three quarks or anti-quarks (baryons). At this point, it was not clear what the exact underlying theoretical description of the interaction between the quarks looked like, mainly because single quarks were not measured. The clue that QCD is an asymptotic free theory came from two experimental results which will be briefly discussed in the following.

In one of the experiments, proton-proton collisions were performed at an energy of $\sqrt{s} \gtrsim 10\,\mathrm{GeV}$ [8]. During the collision of the two protons many pions, a meson with quark content up and down, are produced. The momenta of the pions, however, when compared to the initial momenta of the protons, aligned mainly along the collision axis. This means that the momentum transfer of the initial quarks into the transverse plane is very small and therefore the quarks have to be weakly bound in the proton. Otherwise, the measured transverse momentum distribution of the pion spectra would be much larger. The second experiment that additionally tested this hypothesis was scatterings of electrons on a hydrogen target measuring deep inelastic scattering at the Standford Linear Accelerator Center (SLAC) [9]. Similar to the results of proton-proton collisions, it was thought that the angular distribution of the scattered electrons have a similar momentum distribution collinear to the collision axis. The reason is that the quarks in the proton are loosely bound in addition to a low scattering rate. However, the opposite behavior was found, that a large scattering rate of deep inelastic processes with a large number of produced hadrons appears. This meant that the electrons interacted electromagnetically with a particle inside the proton. To explain this phenomenon, Bjorken and Feynman built the so-called parton model, which describes the proton as a collection of weakly bound electrically charged partons. If an electron hits the proton, it interacts electromagnetically with one of the partons and kicks it out of the proton. Even though the other quarks don't obtain a large momentum transfer, the hit quark scatters softly with the other partons, producing other hadronic species. This hadronic jet is again collinear to the collision axis, due to the weak coupling.

With the realization that QCD should be an asymptotically free theory and that non-Abelian gauge theories incorporate asymptotic freedom, it was natural to take QCD as a non-Abelian gauge theory with the gauge group $SU(3)$. This result was found by Gross, Wilczek and Politzer in 1973 [10, 11], which was awarded the Nobel Prize in 2005. The resulting Lagrangian of QCD can be written as

$$\mathcal{L} = \sum_f \bar{\psi}_f \left(i\gamma^\mu D_\mu - m \right) \psi - \frac{1}{4} F_a^{\mu\nu} F_{\mu\nu}^a \,, \tag{1.1}$$

$$F_a^{\mu\nu} = \partial^\mu A_a^\nu - \partial^\nu A_a^\mu + f^{abc} A_b^\mu A_c^\nu \, . \tag{1.2}$$

It describes the vector bosons that mediate the force, the gluons, coupled to the fermions, the quarks. The first part Eq. 1.1 describes the dynamics of the fermions using the Dirac equation. The sum runs over all flavors and the coupling of the quarks to the gauge sector originates from the covariant derivative D^μ. The dynamics of the gauge bosons is described by the second term of Eq. 1.1 with the field strength tensor $F_a^{\mu\nu}$. The invariance of the Lagrangian under the $SU(3)$ gauge symmetry physically means, that the interaction does not change under rotation in color space. Because of asymptotic freedom, it then became evident why no free quark state was measured, since it is a colored object and only color-neutral ones are gauge invariant objects of QCD.

So far, asymptotic freedom has been mentioned a couple of times even though the concept has not been explained in detail yet. If a theory is asymptotically free, it means that the coupling strength α between its constituents is energy dependent such that α becomes small if the energy becomes large. This is in contrast to the theory of quantum electrodynamics (QED), in which the coupling strength shows the opposite energy dependence. The analytic expression of the coupling at leading order as a function of the energy scale Q is

$$\alpha_s(Q) = \frac{2\pi}{b_0 \log(Q/\Lambda_{\mathrm{QCD}})} \, , \tag{1.3}$$

where $b_0 = 11 - \frac{2}{3} n_f$ with n_f the number of flavors and Λ_{QCD} is the energy scale at which α_s becomes strong with decreasing Q. It can be measured experimentally and it is approximately $\Lambda_{\mathrm{QCD}} \approx 200\,\mathrm{MeV}$ [8].

The asymptotic freedom of QCD also leads to the previously described observation that no single particle that carries a color charge was ever measured. This effect is also known as color confinement. If one tries to separate the quarks in a quark anti-quark bound state, the energy in the color flux tube between the quarks will at some point be large enough to create new quark anti-quark pairs from the vacuum. As a result, one is left with two color-neutral bound states. It is also because of the increasing coupling strength at small energy scales that the usual techniques of perturbation theory do not work. In the region of $\alpha_s \gg 1$, higher order QCD processes get more important and it is not clear how to deal with this issue. Wilson suggested a solution on a discrete space and time [12] and is the only first principle method for QCD in the strong coupling regime, also known as lattice QCD calculations. As the methodology includes a Wick rotation to imaginary time, no dynamical effects can be computed within this formulation. The computation of thermodynamical quantities such as the equation of state or susceptibilities, on the other hand, can be performed. Lattice methods only work around zero baryon chemical potential due to the infamous sign problem [13], however there exist methods for extending lattice calculations towards larger baryon chemical potentials, see e.g. [14]. In the weakly coupled regime of QCD, perturbative methods (pQCD) work again. There exist other effective model calculations in the strongly coupled regime, but a more detailed description will be given later in the next section.

The final paragraph in this section is about the definition of a conserved charge. A conserved charge originates from an underlying local symmetry transformation of the theory. According to Noether's theorem, a conserved quantity exists for each continuous symmetry that leaves the theory invariant. In the case of the electric charge, if the solution of the theory is invariant under a rotation of the phase $\alpha(x)$, that is additionally dependent on space and time, also known as the $U(1)$ gauge-group, the net electric charge number, defined as the number of charges minus the number of anti-charge states, is a conserved quantity of that theory. Mathematically, the $U(1)$ transformation can be written as

$$\psi \to \psi' = e^{i\alpha(x)}\psi \,. \tag{1.4}$$

The charges of interest in this thesis are the baryonic charge defined as $B = \frac{1}{3}(n_q - n_{\bar{q}})$, the electric charge Q which is simply the sum of the electric charges of the constituent quarks. And finally, the strange charge $S = -(n_s - n_{\bar{s}})$, which are conserved quantities in the strong interaction. The following sections will discuss some of their properties and the question, of why fluctuations are interesting observables.

1.2 The QCD phase diagram

In the previous section where the theory of QCD was introduced, it was explained, that one of the fundamental properties of QCD is asymptotic freedom and the confinement of color. Further, it was illustrated that at a large energy scale Q, the coupling strength of the strong interaction decreases, starting around the value of Λ_{QCD}. So one can naturally expect that there exist two phases of QCD matter, one in the color-confined phase, where quarks and gluons only appear in a color singlet bound state at small values of the energy scale. The second phase would be the color deconfined phase, in which quarks and gluons move relatively freely at large energy scales. This phase is also known as the quark-gluon plasma (QGP).

The following will discuss the current state of knowledge about the different phases of QCD matter. It is therefore instructive to describe the different regions of the phase diagram in a sketch including the different experiments that are able to detect them. Fig. 1.1 shows a sketch of the QCD-phase diagram as a function of temperature T and baryon chemical potential μ_B. The baryon chemical potential can be approximately seen as the net baryon density n_B. It is known from lattice QCD calculations, that the order of the phase transition along the temperature axis at zero baryon chemical potential is of a cross-over type [15]. The temperature of the transition region is calculated as $T_{c,0} \approx 155\,\mathrm{MeV}$ [16]. The order parameter of the transition is the chiral condensate that is defined as

$$\langle\bar{\psi}\psi\rangle_q = \frac{T}{V}\frac{\partial\ln Z}{\partial m_q}\,, \ q = u, d, s \,. \tag{1.5}$$

The transition temperature is calculated by finding the inflection point of the chiral condensate as a function of the temperature and is often referred to as the pseudo-critical temperature T_c. A cross-over type of phase transition means, that no
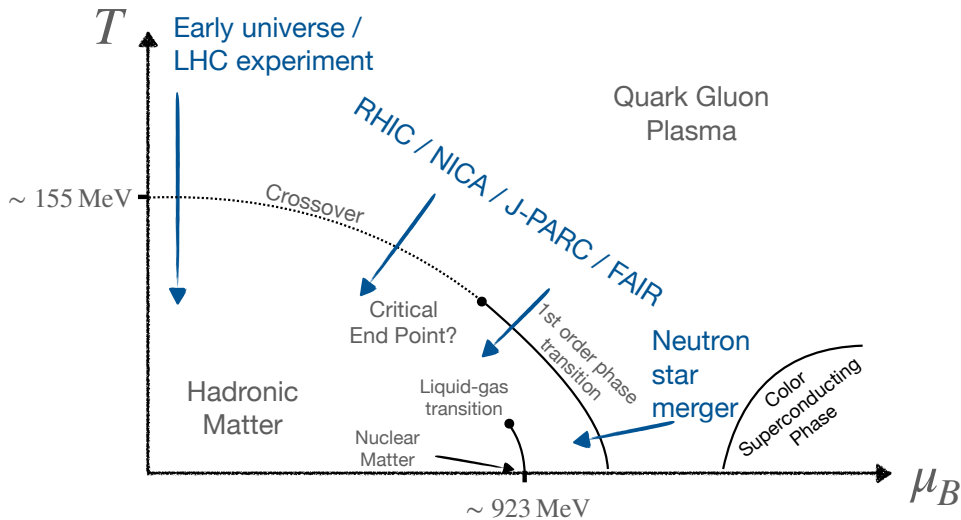
Figure 1.1: Sketch of the QCD phase diagram and experiments available.

discontinuities in thermodynamic quantities exist when going from one phase to another. The "breaking" of the hadrons into quarks and gluons is continuous. Below the cross-over transition, hadrons are the relevant degrees of freedom. A simple model for describing the thermodynamic properties of the hadron gas is the so-called hadron resonance gas model (HRG). This particular model will be introduced later in this thesis. A description of nuclear matter including attractive and repulsive interactions can be done with the van der Waals equation of state which includes a first-order phase transition including a critical point at the liquid-gas phase transition [17]. At large temperatures and equivalently at large μ_B, the state of QCD matter is in the QGP phase.

It is also known from effective field theoretical calculations that a first-order phase transition exists at high baryon chemical potential μ_B [18]. As a consequence, there has to exist a critical point between those two regions, but the exact location is not known at this point. Recent computations within the functional renormalization group (fRG) [19, 20, 21] or Dyson Schwinger framework [22, 23], which are effective calculations of QCD suggests that the location of the critical point is located at rather $\mu_B/T \gtrsim 4$. Other effective models of QCD are based on the holographic argument [24] or chiral effective field theories [25]. At very large baryon chemical potential, a hypothetical color superconducting phase has been proposed [26] in which quarks form Cooper pairs resulting in an effective color screening.

The experimental method that will be the most important one for this work are heavy-ion collisions (HIC). By accelerating heavy nuclei close to the speed of light, the QCD medium created in the collision is extremely hot and dense and it yields the only possibility to study such conditions on Earth. For comparison, the approximate pseudocritical temperature, converted from MeV to Kelvin yields

$T = 160\,\mathrm{MeV} \approx 1.9 \cdot 10^{12}\,\mathrm{K}$, whereas the temperature in the core of our sun is $T = 1.57 \cdot 10^7\,\mathrm{K}$[1].

Another promising observation to probe the QCD phase diagram that became more relevant in the last years is the observation of neutron star mergers with gravitational waves in combination with gamma-ray burst measurements, see e.g. [28]. During the merging process of two neutron stars, the created matter has similar thermodynamic properties to the ones created in a heavy-ion collision, yielding new opportunities to study the phase transitions of QCD [29]. With additional measurements of neutron star masses [30] or tidal deformability [31], the QCD equation of state can be constrained [6].

Striking evidence that the deconfined phase of QGP has been reached in experiments does not exist yet. It is found, that the formed medium rather behaves as a strongly-coupled medium [32]. On the other hand, experimental measurements such as jet quenching observables [33] or the general applicability of hydrodynamics with very small shear viscosity (see e.g. [34, 35]) support the hypothesis that the QGP stage has been reached. A measurement that confirms the crossover-type transition between the hadron gas and the QGP at the LHC or RHIC has also not been made yet. A systematic study aiming to scan the phase diagram of QCD at various different collisional energies is performed in the RHIC BES program and the current status will be briefly discussed in the next section.

1.3   Heavy-ion collisions

Accelerator experiments have a long-standing history. By accelerating particles and colliding them with a target, the nuclear substructures can be resolved. The facility that can reach the highest beam energies is the Large Hadron Collider (LHC) at CERN [36], reaching a collisional energy for PbPb collisions at a center-of-mass energy per nucleon pair of $\sqrt{s_{NN}} = 5.02\,\mathrm{TeV}$ and even $\sqrt{s} = 13.6\,\mathrm{TeV}$ for pp collisions. Along the beam pipe, there exist many different experiments such as ALICE, ATLAS, LHCb and CMS. The one of them that is the most relevant to the topic of this thesis is the ALICE experiment with a focus on the study of the formation of the QGP. Continuing with the Relativistic Heavy Ion Collider (RHIC) at the Brookhaven National Lab (BNL) reaching $\sqrt{s_{NN}} = 200\,\mathrm{GeV}$ for AuAu collisions, their experimental facilities are STAR, PHENIX, PHOBOS and BRAHMS. Within the beam energy scan (BES) program at STAR the energy range goes down to $\sqrt{s_{NN}} = 7.7\,\mathrm{GeV}$ [37]. Another experimental facility at CERN is the Super Proton Synchrotron (SPS) and, in addition to STAR, another experiment dedicated to the search of the critical point at NA61 SHINE experiment in the energy range of $\sqrt{s_{NN}} = 5.1 - 27.4\,\mathrm{GeV}$. Continuing with collider experiments at the lower end of the beam energies important in this study is the HADES experiment at the Gesellschaft für Schwerionenforschung (GSI), a fixed target experiment operating at $\sqrt{s_{NN}} \leq 4.5\,\mathrm{GeV}$. An extension at the GSI facility with FAIR (CBM) is currently built [38]. Other facilities are e.g. NICA [39] or

---

[1]The current record for the highest achieved temperature made it to the Guinness World Records [27] with $T \sim 5 \cdot 10^{12}\,\mathrm{K}$.

J-PARC [40]. The several, previously introduced experimental facilities that perform collider experiments at various different beam energies yield the opportunities to reach different phases of QCD matter. In the so-called intermediate energy regime in $\sqrt{s_{NN}} = 7.7 - 64\,\text{GeV}$ larger values of the baryon chemical potential are reached due to the baryon-stopping mechanism and more baryons are placed around mid-rapidity. At $\sqrt{s_{NN}} \sim 3\,\text{GeV}$ which is achieved e.g. at the HADES experiment, the medium has approximately $\mu_B \sim 900\,\text{MeV}$ and it is unclear whether the QGP phase is reached in these experiments.

Many different experimental observables exist, dedicated to studying the properties of QCD matter at high energies and large densitites, see e.g. [41] for a review. Listing all of these would go beyond the scope of this work. One of them, dedicated to the search of the critical end point however will be discussed in the next section.

Experimental search for the critical point with cumulants of conserved charges

The thermodynamic properties of any medium close to a critical point drastically change and their behavior is dependent on the type of phase transition. At the critical point at the end of the first-order phase transition, the net baryon density fluctuations diverge due to the strong increase in the correlation length of the medium [42]. It was suggested by several authors that a sensitive probe to a possible critical point of QCD are cumulants of conserved charges [43, 44, 45] and the quest, both experimentally and theoretically is still ongoing [46].

Cumulants are useful objects from probability theory for quantifying properties of a distribution function. The first cumulant is the mean and the second cumulant the variance, quantifying the width of the distribution is. Higher order cumulants are sensitive to e.g. asymmetries or the shape of the tails of the distribution. Cumulants are powerful tools because, on the one hand side, they can be obtained from an experiment. Given that e.g. particle numbers are measured on an event-by-event basis, the n-th order cumulant κ_n can be calculated from the particle distribution in the statistical sense. On the other hand, cumulants of conserved charges can also be calculated by taking higher order derivates of the partition function $\mathcal{Z}$ with respect to the corresponding chemical potential μ_q. This direct comparison yields a promising way of comparing theory with experiments.

During the RHIC BES I phase, experiments at different beam energies have been conducted and one of the many observables are net proton number cumulants [47]. Cumulants of the net proton number are thought to serve as a proxy of the fluctuations of the conserved net baryon number [45], since unfortunately, it is not possible to measure all created baryons in the collision. Due to the different thermodynamic properties that are reached in heavy-ion collisions, performed at different beam energies, any observable presented as a function of $\sqrt{s_{NN}}$, their dependency across the phase diagram can be studied. Fig. 1.2 shows measurements of the proton kurtosis $\kappa\sigma^2 = \kappa_4/\kappa_2$ as a function of the beam energy $\sqrt{s_{NN}}$. The fluctuations are measured within a small rapidity window in midrapidity and only the most central collisions were taken into account. If a critical point at $\mu_B > 0$
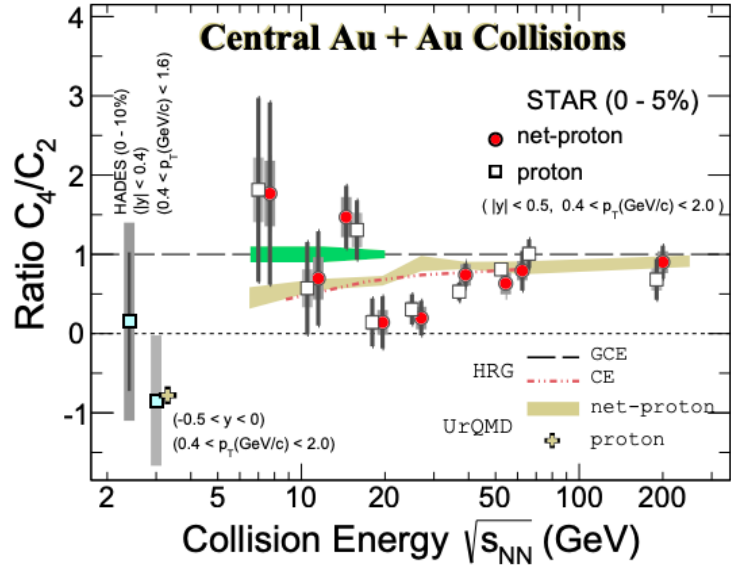
7

Figure 1.2: Ratio of net proton fourth to second cumulant as a function of the beam energy measured by the STAR experiment. Figure is taken from [47].

exists, a non-monotonic behavior of $\kappa\sigma^2$ is expected to appear in the net proton fluctuation, compared to the baseline model which yields unity along the beam energy axis. Starting at $\sqrt{s_{NN}} = 200\,\mathrm{GeV}$, the proton kurtosis is close to unity. When the beam energy is decreased, a trend of $\kappa\sigma^2 < 1$ is observed. This behavior can be associated with the effects of global charge conservation in the heavy-ion collision and the behavior is approximately reproduced with transport calculations (yellow band). Around an energy of $\sqrt{s_{NN}} = 5 - 20\,\mathrm{GeV}$, the data seems to show a non-monotonic behavior, however, the errors of the experimental measurements are too large such that no clear statement can be made. At the lowest collision energy measure by HADES [48] at $\sqrt{s_{NN}} = 2.4\,\mathrm{GeV}$ and STAR at $\sqrt{s_{NN}} = 3\,\mathrm{GeV}$ the value of the fluctuations is below unity which, again, is associated to global charge conservation. A calculation within the UrQMD model at $\sqrt{s_{NN}} = 3\,\mathrm{GeV}$ appears to match with the experimental measurements [49]. It is the hope, that with the improved statistics of the RHIC BES II phase, the errors of the fluctuations can be reduced.

Another observable that is thought to be sensitive to a possible critical point is the intermittency analysis [50]. In the scaling region of the critical point, correlation functions $F_q(M)$ in momentum space form self-similar patterns which can be observed from scaled factorial cumulants in momentum bins M. Close to the critical point, the self-similar property leads the following scaling behavior of the correlation function $F_q(M) \sim (M^D)^{\phi_q}$ for large enough M [50, 51]. Where ϕ_q is the intermittency index. So far, no sign of the proposed scaling behavior of $F_q(M)$ has been observed in a systematic study at the NA49 and NA61/SHINE collaboration at CERN SPS [52].

There exist many issues when it comes to the comparison of experimental results with the theoretical models and an overview can be found in [53]. In this work, the goal is to address the effects of the hadronic stage of the heavy-ion collision. It has

been shown that the produced correlations in the hadronic phase are substantial [54]. The question of how the hadronic stage modifies fluctuations in a system with global charge conservation will be studied. In addition, the fate of critical equilibrium fluctuations in an expanding hadronic system with pure hadronic interactions will be investigated.

1.4   Theoretical description of heavy-ion collisions

The full description of the dynamics of a heavy-ion collision cannot be directly performed from the Lagrangian of QCD. Instead one has to rely on dynamical models to describe the collision and open input parameters have to be taken from theoretical calculations or experimental measurements. In addition, depending on the beam energy, different regions of the QCD phase diagram are probed and therefore different physical aspects have to be considered. At the top LHC energies, where the QGP phase is reached, different stages govern the evolution of the ultra-relativistic heavy-ion collision that have to be modeled using different tools, which will be explained in this section. Their application towards lower beam energies will be described as well.

1.4.1   Initial conditions

It was found that the behavior of the QGP phase of an ultra-relativistic heavy-ion collision can be explained using a hydrodynamical description in which a prerequisite is the appearance of local equilibrium [55]. The very first stage of such a collision however starts in a system far from equilibrium. It is therefore necessary to understand the dynamics of the medium, starting with the nuclei at rest, towards the stage at which the system can be described by hydrodynamics. Depending on the energy scale, different models exist to describe the first part of the collision. The starting point is usually the density distribution of the nuclei at rest and usually, here, the Woods-Saxon distribution is used for large nuclei.

At the highest beam energy at the LHC or at RHIC, the Color Glass Condensate (CGC) provides an effective description of QCD. CGC-based models use the saturation scale in which the accelerated nuclei are fully dominated by gluonic radiation and the evolution directly after the first collision is modeled using the Yang-Mills equation for classical fields [56]. Models that incorporate these ideas are e.g. IP-Glasma or KLN approaches [57, 58, 59]. Other effective models of QCD are based on kinetic theory in which the non-equilibrium dynamics are described using the Boltzmann equation [60, 61, 62]. A more simplistic model which is purely based on geometric arguments is the Glauber model. Here, the nucleons are distributed according to the Woods-Saxon distribution, and the initial energy density profile is obtained from the first collisions of the nucleons when they overlap [63].

With decreasing collision energy, models based on the picture of gluon saturations break down and other effective models of QCD must be referred to. Here, a wide class of transport approaches can be used which evolve the medium until sufficient thermalization is expected. Examples of such approaches are SMASH [5], UrQMD [64], EPOS [65] or AMPT [66]. The switching criterion from transport to fluid

dynamics is performed on hypersurfaces of constant proper time. Another option is a dynamical approach, in which a certain local energy density has to be reached [67]. In the case of SMASH or UrQMD the initial processes are described by an external model called PYTHIA [68, 69].

Recently, large developments have been made studying the effects of the nuclear structure of the nuclei on final state observables in heavy-ion collisions, see e.g. [70, 71, 72]. It is known that the nuclei used to perform the collider experiments are not perfectly spherical or have uniform (electric) charge distributions. Deviations of the surface of the nucleus from a sphere are referred to as nuclear deformations. Such deformations can be experimentally determined by measuring hyperfine splitting of the atomic levels. In the modeling of heavy-ion collisions, the geometric interpretation of these deformations is used, even though the experimentally measured values are strictly speaking not the same [71]. The effects of various different deformation parameters are studied later in this thesis, in the context of the isobar experiments conducted at RHIC [49]. Another effect known from nuclear structure that has gained more attention in recent years is the so-called neutron skin effect, which leads to differences between the proton and neutron distribution inside the nucleus. It can be measured in different ways, for a review of two different measurement techniques the reader is referred to [73]. Again, this effect will be further studied later in this work and the effects of fluctuations of conserved charge numbers will be investigated with an improved description of the model introduced in [5].

1.4.2 Hydrodynamical Models

One of the big successes in the field of heavy-ion collision was the discovery that the formed medium behaves as an almost perfect liquid with a very small shear viscosity over entropy density η/s [55]. This result was obtained with relativistic hydrodynamic models that incorporate viscous corrections. The theory of hydrodynamics is essentially described by the local conservation of the energy-momentum tensor $T^{\mu\nu}$ and the conservation of conserved currents J_i^μ. The equations can then be written in the following form

$$\partial_\mu T^{\mu\nu} = 0\,, \tag{1.6}$$

$$\partial_\mu J_i^\mu = \partial_\mu(n_i u^\mu) = 0\,. \tag{1.7}$$

Here, n_i is the charge density and u^μ the velocity of the fluid. The conserved charge currents are e.g. the baryonic, strange or electric charge B, Q, S. The energy-momentum tensor, depending on the order of expansion, incorporates an ideal part and, when first-order corrections are used, a viscous part. A more detailed description will be given later in this thesis. The applicability of hydrodynamics is given if the size of the system is much larger compared to the size of the interaction scale. An often-used quantity is the Knudsen number $\mathrm{Kn} = \lambda_{\mathrm{mfp}}/L$, defined as the ratio of the mean free path λ_{mfp} over the size of the considered system L. The regime of applicability is $\mathrm{Kn} \ll 1$. In addition to the microscopic scale of the system, it is necessary for the medium to be in local equilibrium. Besides the theoretical basis of the hydrodynamic theory, it has been found that even though the theory is

derived assuming local equilibrium it can describe systems out of equilibrium and their solution converge towards so-called attractor solutions, see [74] for a review. It is thus interesting that hydrodynamic behavior was found in pp or pPb collisions [75, 76].

The system of equations Eq. 1.6-1.7 cannot be solved directly because it is not closed. What is missing is usually referred to as an equation of state (EoS), which relates the energy density with the pressure and charge density $\epsilon = \epsilon(P, n_i)$. The EoS plays an essential role because it can be taken from first principle lattice QCD calculations [77]. At finite baryon densities, one has to rely on effective models e.g. chiral effective field theory [78].

Fluid dynamical models have successfully described bulk observables such as multiplicities, momentum distributions, or flow [79]. Another important aspect is the natural incorporation of phase transitions via the EoS and therefore, such phenomena can be captured. Fluctuations on the other hand cannot be obtained because thermal fluctuations are not included in the description of the fluid in local equilibrium. When it comes to the search for the critical point, it is the fluctuations of thermal modes that grow rapidly close to the critical region, and in addition, the correlation length diverges, breaking the assumption that Kn $\ll$ 1. To investigate these phenomena a theory called fluctuating hydrodynamics has to be derived which in the case of critical phenomena is still ongoing research, see e.g. [80].

Another set of parameters besides the EoS which governs the evolution of the fluid are transport coefficients. The most prominent one is the shear viscosity η, describing the reaction of the fluid to shear stresses and it is important to describe flow in heavy-ion collisions. Its value is found to be the smallest in comparison to other liquids [55]. A more detailed introduction to transport coefficients will be given in the following section. Current hydrodynamical models that are widely used in the community are MUSIC [81], CLVisc [82] and vHLLE [83]. The latter one will also be used in this work.

Hydrodynamical models are not capable of providing quantities that can be measured in experiments such as particle yields. It is therefore necessary to switch the perspectives from hydrodynamical fields to discrete sets of particles. The standard procedure is provided by the Cooper-Frye formula [84], where the distribution function is assumed to be in local equilibrium and small viscous corrections are taken into account. Usually, it is used in the grand-canonical ensemble (GCE), where the particle number fluctuates around its mean value determined by the temperature of the fluid. This procedure leads to the fact that conserved charges are only conserved on average and it is known, that some observables can only be described if the charges are globally conserved on the hypersurfaces. This leads to another motivation for the work in this thesis to extend the hybrid model described in [5] such that observables related to global charge conservation can be studied.

1.4.3 Transport Approaches

Hadronic transport models for heavy-ion collisions, generally speaking, describe the QCD medium in the confined regime using kinetic theory. They provide an effective

solution to the relativistic Boltzmann equation which reads

$$k^\mu \partial_\mu f_{i,k}(x) + m_i F^\alpha \partial_\alpha f_{i,k}(x) = \mathcal{C}^{i,j}_{\text{coll}}[f_{i,k}] \,. \tag{1.8}$$

Here, the individual quantities are:

- Single-particle distribution function $f_{i,k}(x) = \frac{d^6 N_i}{d^3 x d^3 k}$ of particle species i.

- Mass of the particle m_i.

- External force F^α.

- Collision term $\mathcal{C}^{i,j}_{\text{coll}}[f_{i,k}]$ between particle species i and j, depending on $f_{i,k}$.

The single particle distribution function describes the phase space density and is the main objective that is propagated by transport models. The propagation of f itself in space is performed by the left-hand side of Eq. 1.8. The first term describes the linear propagation of f according to its momenta and the second term describes changes of f under external forces such as, e.g. nuclear potential or magnetic fields. Collisions between the constituents are modeled via the collision integral on the right-hand side, which describes the loss and gain of the individual distribution functions. The Boltzmann equation is a coupled 6+1 dimensional integro-differential equation which, in practice is very hard to solve for a multi-component gas that includes many hadronic species. Transport approaches provide an effective solution of Eq. 1.8 such that the equations are not solved directly, but effectively describe the dynamics of point-like particles on a Monte-Carlo basis. In Section 2, a study is described in which the effective solution of a transport code is directly compared to a semi-analytic solution of the Boltzmann equation. Contrary to hydrodynamics, kinetic theory is able to evolve systems from out-of-equilibrium states, back to equilibrium.

Heavy-ion collisions at $\sqrt{s_{NN}} \lesssim 10\,\text{GeV}$ can be approximately described using purely a hadronic transport approach. The other use case of such models is the evolution of the particle spectra in the late stages of an ultra-relativistic heavy-ion collision in a so-called afterburner calculation. Here, the hadronic medium is dilute and the fluid dynamical picture breaks down. The hadron gas in afterburner calculations is evolved until the appearance of the kinetic freeze-out condition. At this stage, no hadronic interactions appear anymore and hadrons are described by free-streaming and resonance decays.

In the baryon dense regime, e.g. at HADES energies of $\sqrt{s_{NN}} \lesssim 3\,\text{GeV}$, the nuclear potential has to be included. There are two types of transport codes employing different formulations. The first one is the Boltzmann-Uehling-Uhlenbeck (BUU) approach, in which the density is computed from the test particles method. The other widely used method is the Quantum Molecular Dynamics (QMD) approach, where the density is computed from Gaussian wave packages. The model that is going to be used in this work is SMASH [85] which uses the BUU ansatz. Examples of other transport models are GiBUU [86], UrQMD [87], (P)HSD [88, 89], JAM [90], BAMPS [62], AMPT [91]. A large study comparing the results of different transport models has been conducted in [92]. There also exists transport models that aim to

describe the partonic stage of the heavy-ion collision like BAMPS [62] or AMPT which is developed as multi-stage transport.

Like hydrodynamic models, transport approaches are not parameter-free but rely on the input of experimental and theoretical calculations. One of the relevant quantities are the cross-sections between the constituents of the model. The cross-section σ is the probability, that a certain outcome appears of a scattering. In a quantum field theory, the scattering amplitude can be calculated from the scattering matrix S, from which the transition amplitude is obtained from the square matrix element $|\mathcal{M}|^2$. Importantly, the cross-section can also be measured in experiments.

The model which is used to obtain the most parts of the results in this work is called SMASH (Simulating Many Accelerated Strongly-interacting Hadrons) and it is developed as an open-source code [93, 94, 93]. SMASH has been successfully conducted in studies for various different applications in heavy-ion collisions [95, 96, 97, 98, 99, 100]. An extension of the model to describe the hot and dense stage of the heavy-ion collision using hydrodynamics has been performed in [5]. Further studies in which SMASH has been used as an afterburner can be found in [101, 102]. More relevant for the purpose of this thesis, SMASH has been successfully used to extract equilibrium properties like transport coefficients of the hadronic phase [103, 104, 105, 106, 107]. Transport coefficients play an important role in understanding the properties of a medium. The ones that are of interest in this work will be introduced in the next section.

1.4.4 Transport Coefficients

Transport coefficients are very interesting quantities describing the behavior of a medium from an out-of-equilibrium state back to equilibrium. If one goes beyond ideal hydrodynamics, the system is expanded in terms of gradients of the charge currents or in the case of viscous hydrodynamics, expanded in terms of gradients of the hydrodynamical fields. The response of these gradients is determined by the corresponding transport coefficient. In this thesis, the two transport coefficients of interest are the diffusion coefficients of conserved charges $\kappa_{qq'}$ with $q, q' \in \{B, Q, S\}$ and the shear viscosity η.

If a first-order correction of the charge currents is taken into account, the response of the medium to local deviations of the charge chemical potential μ_q is determined by the diffusion coefficient of the respective charge κ_q. The response of the charge current J_q^μ in a system of one conserved is determined from Fick's law

$$J_q^\mu = -\kappa_q \nabla^\mu \left(\frac{\mu_q}{T} \right) . \tag{1.9}$$

In the case of the baryonic charge, at top RHIC or LHC energies where the medium in the central region of the collision has almost zero net baryon density [108], the effects of charge diffusion processes are small [109]. However, when decreasing the beam energy, the baryon deposition during the collision becomes important and the description of charge diffusion processes as well. In a multi-component system, the diffusion coefficient of one charge κ_q is extended by the diffusion coefficient matrix $\kappa_{qq'}$, effectively coupling the charge currents with each other. The goal of this thesis

is to determine the full diffusion coefficient matrix from the hadronic transport model that incorporates not only the diagonal components (κ_{BB}, κ_{QQ}, κ_{SS}) but also the cross terms (κ_{BQ}, κ_{BS}, κ_{QS}). A first calculation of the hadronic $\kappa_{qq'}$ within the Chapman-Enskog (CE) approximation has been performed in [110]. In [111], these coefficients have been introduced in a hydrodynamic model and the effects of the full diffusion coefficient matrix are studied. It has been found that regions of non-zero strangeness density appear due to the coupling of the conserved charge currents. A similar calculation within the CE approximation and the relaxation time approximation (RTA) for the transition region between the hadronic and the partonic sector of QCD was performed in [112]. The electric charged diffusion coefficient, which is directly related to the electric conductivity $\kappa_{QQ}/T = \sigma_{el}$, has different applications in heavy-ion collisions. One of which is the evolution of the generated magnetic fields, that is determined by the strength of the electrical conductivity [113] and can be calculated within the framework of magneto-hydrodynamics [114, 115]. It is also possible to relate the emission of dileptons to σ_{el}, which yields an interesting opportunity for comparison with measurements [116, 117]. Previous calculations of the diffusion coefficients (conductivities) have been performed in SMASH [105, 107]. Other calculations in the hadronic sector can be done using chiral perturbation theory [118] or kinetic theory [119].

The other transport coefficient that will be computed is the shear viscosity, describing the reaction of medium to shear forces. Viscous corrections appear when the first-order corrections of the gradients of the hydrodynamical field u^μ are considered and another transport coefficient that appears in the same expansion is the bulk viscosity ζ. The shear viscosity gained much attention when the QGP phase was first studied using relativistic hydrodynamics. With ideal fluid dynamics, the strength of the flow anisotropy could not be described, whereas other bulk observables matched with the calculations [120]. With the extension towards viscous hydrodynamics, it was then possible to describe the observation of anisotropic flow with the usage of a very small shear viscosity over entropy density [121, 122, 123, 55]. The specific value of η/s is one of the smallest shear viscosity of any material known so far [124]. It is also close to the lowest bound of $\eta/s \gtrsim 1/4\pi$ conjectured from the AdS/CFT correspondence [125], which is also referred to as the KSS bound. There are multiple studies calculating the value of the shear viscosity in the hadronic regime of QCD using transport models [126, 127, 128, 129, 130, 131], chiral perturbation theory [132] or other methods like HRG with excluded volume effects [133]. In [103], the effect of lifetimes of resonances on the shear viscosity was investigated in SMASH. This result shows that the treatment of microscopic interactions plays an important role when calculating the shear viscosity. There is a large effort to use Bayesian analysis techniques to extract the shear viscosity over entropy density from experimental data [134, 135, 136, 137, 138, 139]. The value of η/s from the dynamical models has been found to be close to the KSS bound and other methods to extract the shear viscosity from dynamical models show a similar picture [140, 141]. When comparing the specific value of η/s between SMASH and UrQMD (see Fig. 13 in [103]), it was found that the value of the transport coefficient of SMASH is much larger compared to the one from UrQMD.

It was already pointed out that the values of the transport coefficients are sensitive to the microscopic interactions of the model. So if the description of the microscopic interactions within the model improves, it is natural to expect that its transport coefficients change. For future studies, it is therefore helpful to establish a good understanding of the behavior of $\kappa_{qq'}$ and η, when it comes to modifications of microscopic interactions. As an example, in [142], a new feature has been implemented in SMASH to account for multi-particle reactions which enhances the applicability of the model in very dense systems. Another goal of this work is to compute the diffusion coefficients of the baryonic and strange sector from SMASH and compare them to other calculations. It is also hoped that the calculation of the transport coefficients becomes feasible from first principle calculations. Contrary to the shear viscosity η, the electric conductivity σ_{el} as well as the diffusion coefficient D have been calculated from first principle lattice QCD calculations [143, 116, 117]. These comparisons yield a very good opportunity to gauge the interactions and degrees of freedom of the model correctly.

1.5   Outline of this work

The outline of this thesis is as follows. First, in Chapter 2, the model is shortly introduced which is used to calculate most results presented in this thesis. In the following, in chapter 3, the diffusion coefficient matrix $\kappa_{qq'}$ of the three conserved charges B, Q and S is calculated as well as the shear viscosity η. These transport coefficients can be computed from correlation functions of equilibrium fluctuations of the conserved charge currents of the spatial component i, $\langle J_q^i(t) J_{q'}^i(0) \rangle$ using the Green-Kubo approach. Similarly, the shear viscosity η is calculated from correlation functions of the off-diagonal components of the energy-momentum tensor $\langle T^{ij}(t) T^{ij}(0) \rangle$. This chapter aims to investigate the behavior of the transport coefficients by gradually increasing the complexity of the collision kernel and the number of degrees of freedom. By doing so, the properties of the hadronic medium can be investigated and an understanding of its behavior for future studies can be established.

In Chapter 4, properties of the interacting medium are investigated by studying fluctuations in the form of cumulants $\kappa_n = \langle (\delta N_q)^n \rangle_c$ of particle species. The study of cumulants of conserved charges is strongly related to the search of the QCD phase diagram as already discussed in the introduction. In the first part of chapter 4, specifically in Section 4.3, the influence of hadronic interactions on cumulants under global charge conservation is studied in an infinite matter simulation. The behavior of $\langle (\delta N_q)^n \rangle_c$ is then investigated as a function of subvolume sizes. By doing so, the influence of the hadronic interactions on these fluctuations can be studied and a baseline can be established for measurements in heavy-ion collisions. In Section 4.4, the influence of the hadronic medium on critical equilibrium fluctuations is investigated. The starting point is the particle distribution function obtained from the principle of maximum entropy which generates cumulants of the three-dimensional (3d) Ising model coupled to the HRG. These distributions are then evolved in the transport model in an expanding system with the initial phase-space distribution fitted to measurements in heavy-ion collisions. Within this dynamical system, the

time dependency $\langle (\delta N_q(t))^n \rangle_c$ can be studied, as well as the final state fluctuations.

Finally, in the first part of Chapter 5, the influence of nuclear deformations on the initial state of hydrodynamical simulations, at a collisional energy of $\sqrt{s_{NN}} = 200\,\mathrm{GeV}$ is studied. After the subsequent hydrodynamic evolution, the switching between the hydrodynamical and the dilute stage of the heavy-ion collision is improved such that the B, Q and S charges are conserved globally on the hydrodynamical hypersurfaces, according to the canonical ensemble. These particle spectra are then fed into SMASH and differences in final state observables are studied. In addition, the effect of the neutron skin on final state observables is investigated.

2

Hadronic transport approach

In this section, the transport model is introduced. A more detailed description, especially when it comes to the interactions between the hadrons, will be given at the corresponding places in the text. The explanation and derivations in this chapter on the basics of the model are mainly taken from the original publication [85]. SMASH is a hadronic transport approach built to describe non-equilibrium dynamics of the confined phase of QCD, in which the interactions between the hadrons are dominated by resonance formation and decays, or the effects of nuclear potentials. Besides the regions of collider energies in which the heavy-ion collision can be purely described by transport models, another application of such models is to evolve the hadronic late stages of an ultra-relativistic heavy-ion collision. The key ingredients for a transport approach are the hadronic degrees of freedom and the interactions between them. So the goal of this section is to develop a basic understanding of these aspects.

Degrees of freedom

Starting with the degrees of freedom, the hadrons that are incorporated into SMASH are the most abundant baryons and mesons that are classified with a 3 to 4-star rating from the particle data group (PDG) [144]. The PDG collects experimental data about particles and their properties and assigns a rating depending on the uncertainty of the experimental measurement. The highest rating are 4 stars, meaning the state is confirmed with a very high probability. The information that is used for this model are the masses, decay width and parity information of the particle species. Note that each hadron is represented by a point-like particle. The stable hadrons have fixed masses according to the PDG values and the masses of the corresponding isospin partners are taken to be the same, assuming isospin symmetry. The mass distribution of unstable hadrons is represented by relativistic Breit-Wigner spectral functions with mass-dependent decay widths. Further details of this procedure will

follow later in this thesis.

Starting with the mesonic degrees of freedom, SMASH includes the pseudo scalar states like π, η and η', plus strange mesons such as K. Vector states like ρ, ω and ϕ or the strange $K^\star$ meson and pseudoscalar mesons like σ, f_0, a_0 are included as well. The baryonic degrees of freedom include the stable N, Λ, Σ, Ξ and Ω but also some of their respective excited states like Δ, $N^\star$, $\Delta^\star$.

So far, only hadronic states consistent with u, d and s quarks are incorporated. An extension to the heavier charm or bottom quarks has yet not been done. A full list of the hadrons can be seen in the file `particles.txt` in [93].

Interactions

Cross sections

The interactions between the constituents of SMASH are modeled using the respective cross-sections and are fundamental quantities of transport approaches. Since they can also be measured in experiments, they serve as an important input for these models. At the considered energies where the interactions are dominated by the formation of resonance states, one can raise the question, which portion of the total cross-section originates from a single state. SMASH uses a so-called bottom-up approach in which each resonance contributes to the total cross-section with its partial cross-section, such that the total cross-section σ_{tot} matches with experimental measurements. In the bottom-up approach, σ_{tot} can be expressed as

$$\sigma_{\text{tot}}(\sqrt{s}) = \sum_R \sigma_R^{2\to1}(\sqrt{s}) + \sum_{P_1,P_2} \sigma_{P_1P_2}^{2\leftrightarrow2}(\sqrt{s}) + \sigma^{\text{string}}(\sqrt{s})\,. \tag{2.1}$$

Here, $\sigma^{\text{string}}(\sqrt{s})$ is the cross section for a string interaction, which will be explained in Chapter 5. The bottom-up approach has the benefit that the total cross-section is based on the knowledge of the number of resonances and their properties. On the other hand, one faces the difficulty that the total cross-section overshoots experimental data, when new states are included in the model. In the top-down approach, the total cross-section is fixed and the partial ones are computed according to the number of resonance states. Fig. 2.1 shows an exemplary cross-section of a proton pion reaction. One can see that the total and elastic measured cross-section is well reproduced by SMASH. Since there exist many more such plots for all possible reactions between the constituents, the interested reader is referred to [146], where a collection of results calculated with SMASH is publicly available.

In addition, it is worth mentioning in the context of this thesis, that at each interaction, SMASH perfectly conserves the baryonic, strange and electric charge.

Detailed Balance

Detailed balance is a property of dynamical systems which means, that one cannot distinguish if the time runs in a forward or backward direction. It therefore has to be fulfilled for a physical system that is invariant under time reversal transformation,
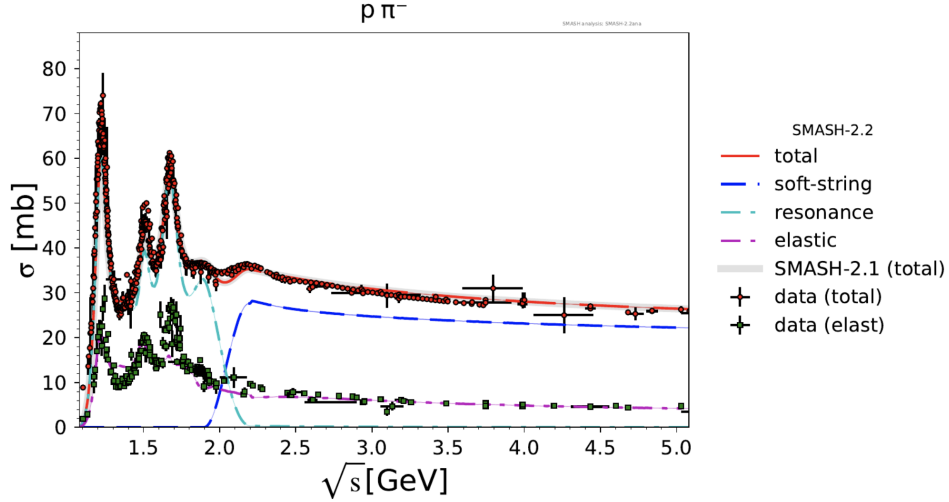
Figure 2.1: Total cross section of the reaction $p\pi^-$ as a function of the collision energy $\sqrt{s}$. The figure is taken from [145].

which is the case for QCD. The probability of a reaction from an initial phase space Γ_i to the final phase space distribution Γ_f therefore has to follow

$$p(\Gamma_i, \Gamma_f) = p(\Gamma_f, \Gamma_i).$$ (2.2)

Detailed balance preserves the principle of ergodicity, that each thermal equilibrium state of the system can be reached. Using this principle, one can directly relate cross-sections that are known in one direction, e.g. $\sigma_{ab\to cd}$, to the backward reaction $\sigma_{cd\to ab}$. In SMASH, this principle is fulfilled by calculating the cross-sections of a reverse process reaction directly from the matrix element of the forward direction $|M_\to| = |M_\leftarrow|$. Results that detailed balance is indeed fulfilled in a box with periodic boundary conditions can be found in [147].

Solving the Boltzmann Equation

It was written in the introduction that transport models provide an effective solution of the Boltzmann equation by describing the dynamics of point-like particles on a Monte-Carlo basis. In this section, a study is used to show that this is indeed true. As it is impossible at this point to solve the Boltzmann equation with all the degrees of freedom and cross sections from SMASH, a comparison to a simplified case, in which a solution to the Boltzmann equation is known has to be made. In [148], a calculation has been performed for massless particles initialized in a sphere with an expanding metric where a solution can be computed semi-analytically. The system contains only one particle species interacting via a constant elastic cross-section. Fig. 2.2 shows the evolution of the distribution function f as a function of the momenta of the particles. One can see that the result of the SMASH simulation matches perfectly with the analytic expectation. Even though this comparison is
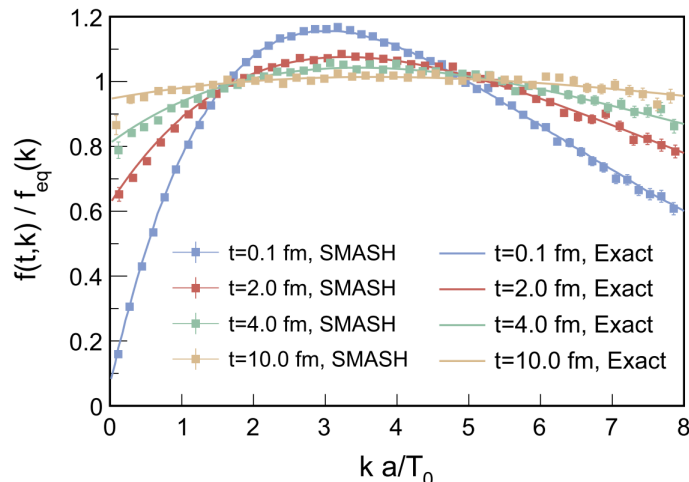
Figure 2.2: Distribution function normalized to the initial equilibrium distribution of SMASH (symbols) in comparison to analytic expectation (line) as a function of the scaled momentum ka/T_0 for different times. The figure is taken from [148].

only performed for a simple test case and the result cannot be directly transferred to the full dynamical simulation, it shows that the SMASH code reproduces exact results of the Boltzmann equation in the regime of the presented study.

The topic of studying fluctuations in the context of kinetic theory and especially in the context of the Boltzmann equation is, in principle, not straightforward. It is not possible to study fluctuations of a particle number on an event-by-event basis because the solution of the Boltzmann equation, the distribution function $f_{i,k}$, is only of probabilistic nature. However, within the realization of the solution in transport models, the full phase space information of each particle becomes accessible at each point in time. Therefore, such models yield the possibility to study fluctuations even though it is not possible from the underlying equation. However, it becomes problematic when nuclear potentials are taken into account, which will be discussed in the next section. SMASH follows the BUU approach meaning that the test particle method is applied in order to smoothen the nuclear density. These introduced test particles reduce the fluctuations and only bulk observables can be calculated. This limits the applicability to calculate e.g. event-by-event fluctuations with nuclear potentials.

Propagation of particles and incorporation of potentials

The propagation of the hadrons, if no interaction occurs, are on straight lines according to their momenta. In the beginning, when SMASH was introduced first, the model was based on a fixed timestep Δt. Particles were then propagated without any interaction until the next Δt. At the respective end of a timestep, interactions were searched between all particles and performed. This treatment has the disadvantage,

that results might be affected by the actual value of Δt. Since then, SMASH has been adapted to a more flexible way (similar to [87]). The main difference is that each particle is only propagated until the next interaction takes place. When such an interaction happens, SMASH searches for new ones and evolves the hadrons until the beginning of the next earliest process.

An important aspect of heavy-ion collisions, especially at low energies, is the incorporation of nuclear potentials which act as forces on the trajectories of the hadrons via the BUU approach. In SMASH, the repulsive and attractive interactions are modeled by the mean-field Skyrme potential

$$U(\rho, \rho_{I_3}) = a(\rho/\rho_0) + b(\rho/\rho_0)^\tau \pm 2S_{pot}(\rho_{I_3}/\rho_0) \,, \qquad (2.3)$$

where ρ is the baryon density, ρ_{I_3} is the isospin 3 density (I_3/I) and $\rho_0 = 0.168\,1/\text{fm}^3$, the nuclear ground state density. The density in Eq. 2.3 has to be evaluated in the Eckart rest frame density of the medium. The other parameters a, b, τ, S_{pot} determine the shape of the nuclear equation of state (EoS). The resulting force acting on the trajectories of the hadrons can then be written as

$$\begin{aligned}
\vec{F} = &\frac{\partial U_{sk}}{\partial \rho_B} \left[-(\vec{\nabla}\rho_b + \partial_t \vec{j}_B) + \dot{\vec{x}} \times (\vec{\nabla} \times \vec{j}_B) \right] \\
&+ \frac{\partial U_{sk}}{\partial \rho_{I_3}} \left[-(\vec{\nabla}\rho_{I_3} + \partial_t \vec{j}_{I_3}) + \dot{\vec{x}} \times (\vec{\nabla} \times \vec{j}_{I_3}) \right]
\end{aligned} \qquad (2.4)$$

In this work, no nuclear mean field potentials have been used and all results are obtained using the so-called "cascade" mode in which the hadrons are propagated only on straight lines.

3

Equilibrium properties of a hadronic medium

In this chapter, transport coefficients will be calculated from SMASH and the results are based on [3]. Their behavior is determined from the microscopical interactions of the constituents of the medium and the goal is therefore to subsequently establish the collision kernel of the interacting hadronic medium of SMASH and calculate the transport coefficients depending on these processes. The derivation of the presented formulas are taken from [85]. So far, the following hadronic transport coefficients were calculated from SMASH:

- Shear viscosity η [103].

- Electric cross conductivities σ_{QQ}, σ_{QB}, σ_{QS} [105, 107].

- Bulk viscosity ζ [106].

- Jet quenching coefficient [104].

As it will be shown later in this chapter, the electric conductivity $\sigma_{qq'}$ is related to the diffusion coefficients by a factor of temperature $\sigma_{qq'} = \kappa_{qq'}/T$. It seems that besides the extension of $\kappa_{qq'}$ to the baryonic and strange sector (κ_{BB}, κ_{SS}, κ_{BS}), a repetition of the previous calculations are performed. However, the reasons for these specific calculations are two-fold. First, since the time of the previous publications of the results of η and σ_{ij}, new interactions have been implemented into SMASH, so the results are outdated. In addition, a detailed study of the dependency on the collision kernel helps for a better understanding of the behavior if, again, new interactions are implemented. Second, in the case of the diffusion coefficient matrix, one of the main results of [107] was that the coefficients scale with the degrees of freedom of the system. Therefore it is of great interest to investigate if this behavior holds in the baryonic and strange sector. As an example, one of the newly implemented interactions is the so-called stochastic collision criterion [142] with which it is possible

to study the effects of multi-particle reactions on transport coefficients in the hadronic regime of QCD in SMASH.

Before the methodology, the model and the results are presented, some derivations of the underlying theory of transport coefficients are shown in the next sections.

3.1 The Green-Kubo formalism

Similar to the previously conducted studies to extract transport coefficients from microscopic models, this study makes use of the Green-Kubo approach. The simplest derivation of the Green-Kubo relation is using the example of Brownian motion in the Langevin equation. The following derivation of the fluctuation-dissipation, which is an equally important theorem, originates from the paper by Kubo [149][1]. The fluctuation-dissipation theorem is a tool that is used in many different applications in physics. It provides a relation between the correlations of equilibrium fluctuations to response quantities of the medium. A fundamental prerequisite is that the system is in detailed balance. One way of deriving the main equation is using the classical example of Brownian motion which describes e.g. the movement of a heavy particle in a surrounding medium in equilibrium. Usually, the Langevin equation is used as a phenomenological approach to this problem

$$m\dot{u}(t) = -\gamma u(t) + R(t) \,. \tag{3.1}$$

Here m is the mass of the molecule, γ is a friction constant and R describes a random force that acts on the movement of the velocity $u(t)$ of the particle, by collisions with its surroundings. There are several constraints one can make on the properties of the random force R. The first one is that the process $R(t)$ is normal distributed and uncorrelated in time such that $\langle R(t)R(t')\rangle = 2\pi G_R \delta(t - t')$ where G_R is a constant and the second assumption is, that the force averages to zero over time $\langle R(t)\rangle = 0$. The solution of the Langevin equation is then

$$u(t) = u(0)e^{-\gamma t/m} + \frac{1}{m}\int_0^t dt' e^{-\gamma/m(t-t')} R(t') \,. \tag{3.2}$$

In an equilibrium state, the averaged squared velocity is related to the temperature of the medium. Therefore, the squared velocity is

$$\langle u(t_1)u(t_2)\rangle = u(0)^2 e^{-\frac{\gamma}{m}(t_1+t_2)} + \frac{1}{m^2}\int_0^{t_1} du\, e^{-\frac{\gamma}{m}(t_1+u)} \int_0^{t_2} ds\, e^{-\frac{\gamma}{m}(t_2+s)} \langle R(u)R(s)\rangle \,. \tag{3.3}$$

Setting the times to be equal and using $\langle u(t)^2\rangle = T/m$ in the limit of $t \to \infty$, one can integrate one part of the solution in addition to the fact that only differences in the time are of interest

$$\lim_{t\to\infty} \langle u(t)^2\rangle = \frac{T}{m} = \frac{1}{2m\gamma}\int_{-\infty}^{\infty} ds\, e^{-\frac{\gamma}{m}s} \langle R(0)R(s)\rangle \,. \tag{3.4}$$

---

[1] This example was also used in [150].

Under the assumption, that the timescale of the perturbation is much smaller in comparison to the timescale that the friction has on the medium, one can assume $\gamma/m \ll 1$ and finally one obtains

$$\gamma = \frac{1}{2T} \int_{-\infty}^{\infty} ds \langle R(0)R(s) \rangle \,. \tag{3.5}$$

The derived equation shows the main concept behind the Green-Kubo relation. The integration over the correlation function of the random force over time yields the friction coefficient γ, that governs the evolution of the particle. This concept will be used to determine the diffusion coefficient matrix $\kappa_{qq'}$ and the shear viscosity from equilibrium fluctuations of the charge currents $\mathbf{J}_q$ and the energy-momentum tensor T^{ij}. Before continuing with the results, the basic properties of the two transport coefficients will be explained.

3.2 Diffusion coefficients

As already introduced, a $U(1)$ conserved charge necessarily generates a charge current $\mathbf{J}_q$, since the medium has to transport the charges, if some imbalances appear. This phenomenon directly leads to the property of the charge transport and its strength is characterized by the corresponding transport coefficient.

In this section, the diffusion coefficients $\kappa_{qq'}$ are introduced. They describe the ability of the medium to evolve an inhomogeneous charge distribution towards a homogenous state in a medium. In an external field, the current corresponding to the $U(1)$ conserved charge q can be written as

$$j_q^i(X) = \sigma_q E_q'^{,i}(X) \,. \tag{3.6}$$

Where j_q^i is the i-th component of the charge current and $q \in \{B, Q, S\}$. $\sigma_q = \frac{\kappa_q}{T}$ is the conductivity and κ_q the corresponding diffusion coefficient and the four-vector $X = (t, \vec{x})$. The electric field responsible for the generation of the force acting on the charge can be expanded in

$$E_q'^{,i} = E^i \delta_{qQ} - T \nabla^i (\mu_q/T) \,. \tag{3.7}$$

Here, the first term on the right-hand side corresponds to an external field only in the case of the electric charge and the second term describes density imbalances in the medium, generated by deviations of the charge chemical potential. In the following, only the effects of the second term, the thermodynamic force will be investigated. The resulting expression is also known as Fick's law. In a microscopic theory, the fluctuations are described by $\delta j_q^i(X)$ of the charge q which alter the current with

$$j_q^i(X) = -\frac{\kappa_q}{T} T \nabla^i (\mu_q/T) + \delta j_q^i(X) \,. \tag{3.8}$$

Since Ohm's law Eq. 3.6 has to be true when the system is averaged over many events, the fluctuations have to obey

$$\langle \delta j_q^i(X) \rangle = 0 \,. \tag{3.9}$$

The 2-point correlation function of the fluctuations however is not zero because of the fluctuations-dissipation theorem [151], it reads

$$\langle \delta j_q^i(X) \delta j_q^j(X') \rangle = 2T \frac{\kappa_q}{T} \delta^{ij} \delta^{(4)}(X - X') = 2\kappa_q \delta^{ij} \delta^{(4)}(X - X') \,. \qquad (3.10)$$

where the transport coefficient appears in the 2-point correlation function of the fluctuation. The type of noise in Eq. 3.10 is also called white noise because it is uncorrelated, meaning that the correlation only exists when the spatial and temporal conditions of the delta function match. The 2-point function of the charge current can be written similarly. Introducing the space-average current $\mathbf{J}_q(t) = \frac{1}{V} \int d^3x \, \mathbf{j}_q(X)$ first, and because of Eq. 3.9 one gets

$$\langle J_q^i(t) J_q^j(t') \rangle = \frac{2\kappa_q}{V} \delta^{ij} \delta(t - t') \,. \qquad (3.11)$$

Finally, after integrating the equation above, the Green-Kubo relation for the diffusion coefficient κ_q is obtained for the white noise case

$$\kappa_q = \frac{V}{3} \int_0^\infty dt \langle \mathbf{J}_q(t) \cdot \mathbf{J}_q(0) \rangle \,. \qquad (3.12)$$

Here, the factor 3 originates from the δ^{ij} and the factor 2 cancels from setting $t > t'$ and $t' = 0$. This expression already yields the Green-Kubo relation for the diffusion coefficient κ_q.

In the hadronic medium, there exist cases where a hadron carries more than one conserved charge. Due to the specific quark content, e.g. the Sigma baryon Σ^+ carries the valence quarks (u, u, s) and therefore has a baryonic, electric and strangeness charge simultaneously. In the presence of a medium with a non-zero local charge chemical potential μ_Q the associated charge current J_Q^μ automatically generates a strangeness and a baryon current as well. It is therefore straightforward to extend Eq. 3.8 to incorporate the described effect and write the diffusion coefficient matrix as [110]

$$\begin{pmatrix} J_B^i \\ J_Q^i \\ J_S^i \end{pmatrix} = - \begin{pmatrix} \kappa_{BB} & \kappa_{BQ} & \kappa_{BS} \\ \kappa_{QB} & \kappa_{QQ} & \kappa_{QS} \\ \kappa_{SB} & \kappa_{SQ} & \kappa_{SS} \end{pmatrix} \begin{pmatrix} \nabla^i(\mu_B/T) \\ \nabla^i(\mu_Q/T) \\ \nabla^i(\mu_S/T) \end{pmatrix} \,. \qquad (3.13)$$

So far, the Green-Kubo relation has been motivated by employing the fluctuation-dissipation theorem in the case of white noise. However, it will be shown, that the charge currents $\mathbf{J}_q$ are not completely uncorrelated over time (see Fig. 3.1). Also, it is known that Fick's law is inconsistent with causality since an instantaneous thermodynamic force creates an instantaneous charge current. This problem can be fixed using the so-called colored noise which preserves causality of Fick's law by introducing a memory kernel for the corresponding conserved charge(s) $G_{qq'}^{ij}(X - X')$. The charge current for the multiple conserved charges is modified to

$$j_q^i(X) = - \int d^4X' G_{qq'}^{ij}(X - X')(T \nabla_j(\mu_{q'}/T))(X') + \delta j_q^i(X) \,, \qquad (3.14)$$

25

where δj_q^i describes the colored fluctuations. Here, one can see that the thermodynamic force generated from the chemical potential of q' also generates a current of charge q. The fluctuation-dissipation theorem is equivalently modified to [152]

$$\langle \delta j_q^i(X) \delta j_{q'}^j(X') \rangle = T G_{qq'}^{ij}(X - X') \tag{3.15}$$

Up to now, the shape of $G_{qq'}^{ij}$ is not fixed however, it could in principle be calculated from first principle calculations. By employing the relaxation time approximation (RTA) which describes small perturbations of the distribution function by an exponential decay in time, one can write the memory kernel $G_{qq'}$ as

$$G_{qq'}^{ij}(X - X') = \frac{\kappa_{qq'}}{\tau_{qq'}} \delta^{ij} \delta^{(3)}(\vec{x} - \vec{x}') \exp\left\{ -\frac{(t - t')}{\tau_{qq'}} \right\} . \tag{3.16}$$

Here, the relaxation time of the conserved charge τ_q has been introduced and the diffusion coefficient has now multiple conserved charges. According to the fluctuation-dissipation theorem, the 2-point function of the averaged charge currents is

$$\langle J_q^i(t) J_{q'}^j(t') \rangle = \frac{\kappa_{qq'}}{\tau_{qq'}} \delta^{ij} \exp\left\{ -\frac{(t - t')}{\tau_{qq'}} \right\} . \tag{3.17}$$

Integrating the 2-point correlation function in order to obtain the diffusion coefficients then yields the Green-Kubo relation for the diffusion coefficient matrix

$$\frac{\kappa_{qq'}}{T} = \frac{V}{3T} \int dt \langle \mathbf{J}_q^i(t) \cdot \mathbf{J}_{q'}^j(0) \rangle = \frac{\tau_{qq'} V \langle \mathbf{J}_q(0) \cdot \mathbf{J}_{q'}(0) \rangle}{T} . \tag{3.18}$$

The motivation for the derivation above is that the introduction of the colored noise makes Ohm's law consistent with causality and second-order hydrodynamics. Additionally, the time τ_q can be interpreted as a relaxation time of the conserved charge q. It can be further shown that Eq. 3.14 is equivalent to the stochastic diffusion equation [152, 153] for only one charge q

$$\tau_q \frac{\partial J_q^i}{\partial_t} + J_q^i = -\frac{\kappa_q}{T} T \nabla^\mu(\mu_q/T) + \xi_q^i , \tag{3.19}$$

with ξ_q being white noise. For example, in [154] the stochastic diffusion equation for the net baryon density was studied including the full diffusion coefficient matrix to investigate the competition between expansion and diffusion in a heavy-ion collision.

The relation between the diffusion coefficient, the conductivity and the often used diffusion coefficient D_q are additional thermal relations [111]

$$J_q^\mu = D_q \nabla^\mu n_q(T, (\mu_q/T)) = D_q \left(\frac{\partial n_q}{\partial T} \nabla^\mu T + \frac{\partial n_q}{\partial(\mu_q/T)} \nabla^\mu(\mu_q/T) \right) . \tag{3.20}$$

In an isotropic medium with constant temperature, the term $\nabla^\mu T = 0$ and one can therefore relate κ_q and D_q via

$$\kappa_q = \frac{\partial n_q}{\partial(\mu_q/T)} D_q . \tag{3.21}$$

26

3.3 Shear viscosity

The other transport coefficient of interest is shear viscosity η. It is not directly related to fluctuations of conserved charges, but to the fluctuations of off-diagonal spatial terms of the energy-momentum tensor. The derivation using the theory of second-order hydrodynamic fluctuations is similar to the derivation presented for the diffusion coefficients. The shear viscosity is a property of a fluid that determines its macroscopic property, in terms of its reaction to shear forces. For example, honey behaves differently in comparison to water, when placed on an inclined surface, due to different values of the shear viscosity.

As a starting point, one can write the energy-momentum tensor in terms of the four-velocity u^μ

$$T^{\mu\nu}(t,x) = \varepsilon u^\mu u^\nu - p\Delta^{\mu\nu} + P^\mu u^\nu + P^\nu u^\mu + \pi^{\mu\nu}. \tag{3.22}$$

The energy density is defined as $\varepsilon = u_\alpha u_\beta T^{\alpha\beta}$, $p = -\frac{1}{3}\Delta_{\alpha\beta}T^{\alpha\beta}$, $P_\mu = \Delta_{\mu\alpha}u_\beta T^{\alpha\beta}$ and $\pi_{\mu\nu} = (\Delta_{\mu\alpha}\Delta_{\nu\beta} - \frac{1}{3}\Delta_{\mu\nu}\Delta_{\alpha\beta})T^{\alpha\beta}$. The projection operator orthogonal to u_μ is defined as $\Delta_{\alpha\beta} = g_{\mu\nu} - u_\mu u_\nu$ and $g_{\mu\nu}$ is the metric.

Similar to the previously defined diffusion current J_q^i, the corresponding thermodynamic property that responds to shear forces is the shear stress-tensor $\pi^{\mu\nu}$ and the thermodynamic force is

$$\partial_{\langle\alpha}u_{\beta\rangle} = \Delta_{\alpha\beta\gamma\delta}\partial^\gamma u^\delta, \tag{3.23}$$

where $\Delta^{\alpha\beta\gamma\delta} = \frac{1}{2}(\Delta^{\mu\alpha}\Delta^{\nu\beta} + \Delta^{\mu\beta}\Delta^{\nu\alpha}) - \frac{1}{3}(\Delta^{\mu\nu}\Delta^{\alpha\beta})$. The resulting dissipative current generated by the thermodynamic force Eq. 3.23

$$\pi^{\mu\nu} = \int d^4 X' G_\pi(X - X')^{\mu\nu\alpha\beta}(\partial_{\langle\alpha}u_{\beta\rangle}|_{X'}) + \delta\pi^{\mu\nu}. \tag{3.24}$$

Here, the memory kernel of the shear-stress tensor has been introduced and $\delta\pi^{\mu\nu}$ are fluctuations of $\pi^{\mu\nu}$. According to the fluctuation-dissipation theorem, the 2-point function is

$$\langle\delta\pi^{\mu\nu}(X)\delta\pi^{\alpha\beta}(X')\rangle = TG_\pi(X - X')^{\mu\nu\alpha\beta}. \tag{3.25}$$

Again, one can assume a specific shape of the memory kernel in the RTA that follows an exponential decay with the relaxation time, similar to Eq. 3.16. Replacing the fluctuations with the averaged shear-stress tensor yields then yields

$$\langle\pi^{\mu\nu}(t)\pi^{\alpha\beta}(t')\rangle = 4T\eta\exp\left\{-\frac{(t-t')}{\tau_\eta}\right\}\Delta^{\mu\nu\alpha\beta}. \tag{3.26}$$

Similar to the previous section, the goal is now to integrate Eq. 3.26 to obtain the Green-Kubo relation for the shear viscosity. After setting the indices appropriately and fixing additional factors, the resulting relation reads in the local rest-frame $u^\mu = (1, 0, 0, 0)$

$$\eta = \frac{V}{T}\int_0^\infty \langle\pi^{ij}(0)\pi^{ij}(t)\rangle dt, \tag{3.27}$$

Here, the off-diagonal components of the shear-stress tensor are employed with fixed indices i and j. When results of Eq. 3.26 will be presented the off-diagonal components of the energy-momentum instead of the shear-stress tensor will be used, since the two are equivalent in the local rest frame of an isotropic medium.

3.4   The Chapman-Enskog expansion

In the previous section, the Green-Kubo relations have been derived using the fluctuation-dissipation theorem. This is particularly useful for a model from which the equilibrium currents $\mathbf{J}_q(t)$ or $T^{ij}(t)$ are known because one can directly compute the correlation function and integrate it to obtain the transport coefficient. There also exists the possibility to compute transport coefficients from an approximate solution of the Boltzmann equation, which is known as the Chapman-Enskog (CE) approximation. For a microscopic model such as SMASH, which effectively solves the Boltzmann equation (see Section 2), this yields a good opportunity to compare the results between the Green-Kubo formalism from SMASH and the CE calculation, which will be shown later in this chapter. It is therefore instructive to roughly explain the derivation of the diffusion coefficient in the CE approximation. The calculation of the CE results has been performed by the author of [111] and this section is mainly inspired by [132, 111, 150].

The starting point for the computation of the transport coefficients in the CE approximation is to expand the collision term of the Boltzmann equation in a series of non-equilibrium corrections δf and identify the transport coefficients as the respective prefactors. This method yields an elegant way to compute e.g. the diffusion coefficients or viscosities. There are certain limits of the microscopic system that have to be fulfilled, in order for the approximation to be valid. Similarly to the introduction, the Knudsen number is defined as the ratio of the microscopic length scale (or the range of interaction) or the mean free path to the total size of the system L, $\mathrm{Kn} = l_{micro}/L$. If the Knudsen number is small $\mathrm{Kn} \ll 1$, the microscopic collisions are important and the Boltzmann equation is valid to describe the evolution of the distribution function. In order for the CE approximation to be valid, the following relation has to be fulfilled

$$L \gg \lambda_{mfp} \gg l_{micro}\,. \tag{3.28}$$

If the above separation of scales is fulfilled, the solution of the Boltzmann-equation only depends on the local hydrodynamic fields T, μ, u^μ, resulting in a local equilibrium distribution function

$$f_k(x) = f_k[T(x), \mu(x), u^\mu(x)]\,. \tag{3.29}$$

f_k can then be expressed as a series in terms of an expansion parameter ε, which is a measure of the relative strength of gradients in the system

$$f_k = f_k^{(0)} + \varepsilon f_k^{(1)} + \varepsilon^2 f_k^{(2)} + \dots\,. \tag{3.30}$$

The expansion parameter ε can also be identified as the Knudsen number $\varepsilon \sim \mathrm{Kn}$. The diffusion coefficients can be extracted already from the inclusion of $f_k^{(1)}$ and

orders of $\mathcal{O}(\text{Kn}^2)$ will be dropped under the premise that $\text{Kn} \ll 1$. The Boltzmann equation that includes corrections in $\mathcal{O}(\text{Kn})$ of some particle species i is then

$$k_i^\mu \partial_\mu f_{k,i}^{(0)} = \sum_{j=0}^{N_{species}} \mathcal{C}_{ij}[f_{j,k}(x)] \,. \tag{3.31}$$

Here, $\mathcal{C}_{ij}[f_{j,k}]$ is the collision term between the considered particle species i and j. The solution to the zeroth order is the well-known Juettner distribution.

$$f_k^{(0)}(x) = \frac{g}{(2\pi)^3} \left(\exp\left(\frac{k^\mu u_\mu(x) - \mu(x)}{T(x)} \right) \pm \delta \right)^{-1} \,. \tag{3.32}$$

With $\delta = 0, +1, -1$ for the Boltzmann, Fermi, and Bose distribution respectively and g the degeneracy factor. The collision term on the right-hand side of Eq. 3.32 is

$$\mathcal{C}_{ij}[f_{j,k}(x)] = \sum_{j=1}^{N_{species}} \sum_{a=1}^{N_{species}} \sum_{b=1}^{N_{species}} \int \frac{dk_j}{(2\pi)^3 k_j^0} \int \frac{dp_a}{(2\pi)^3 p_a^0} \int \frac{dp_b}{(2\pi)^3 p_b^0} \delta^{(4)}(k_i + k_j - p_a - p_b)$$
$$\times \mathbf{L}[f(x)](k_i, k_j, p_a, p_b) s\sigma_{ij \to ab}(s, \Omega) \,. \tag{3.33}$$

Here, the sums run over all possible particle species that can scatter with the incoming particle species i and j. The cross-section of the interaction $\sigma_{ij \to ab}(s, \Omega)$ is generally energy-dependent and might have a dependency on the scattering angle Ω. The collision term describes the amplitude of the scattering process $ij \to ab$. The functional $\mathbf{L}[f(x)]$ is linear in the perturbation $f^{(1)}$ and its exact form is not important here but can be found in [111].

The transport coefficients arise when the left-hand side of Eq. 3.31 is further studied. One can see that only the equilibrium distribution function $f^{(0)}$ appears on the left-hand side, whereas the perturbed distribution function is in the collision term on the right-hand side. The source term on the left-hand side can be calculated by decomposing the derivative in terms of derivatives of the hydrodynamical fields, together with the conservation laws of energy and momentum. It has a lengthy expression and one then has to identify the corresponding thermodynamic force and its transport coefficient

$$k^\mu \partial_\mu f^{(0)} = -\mathcal{S}(x, k_i) \,. \tag{3.34}$$

For more details on the exact expressions for the shear and bulk viscosity, the interested reader is referred to e.g. [111, 132]. In this work, only a comparison between the diffusion coefficient matrix calculated from the CE approximation and the Green-Kubo formalism from SMASH is performed. Therefore, the calculation of shear viscosity within the CE formalism is not described here. A derivation including exact comparisons has already been performed in [150].

When only the corresponding source term for the diffusion coefficients is taken into account, one is left with

$$-\sum_{q \in \{B,Q,S\}} f_{i,k}^{(0)} \Delta_\alpha^\mu k^\alpha \nabla_\mu \frac{\mu_q}{T} \left(\frac{E_{i,k} n_q}{\epsilon + P_0} - q_i \right) = \sum_{j=1}^{N_{species}} \mathcal{C}_{ij}[f_{j,k}] \tag{3.35}$$

Here, $E_{i,k} = \sqrt{m_i^2 + k^2}$ is the energy of a particle with mass m_i, ϵ and P_0 the thermodynamic energy density and pressure of the system and n_q the charge density of the specific type of charge q. To obtain the diffusion coefficient matrix $\kappa_{qq'}$, one has to approximate the perturbed distribution function $f^{(1)}$ in terms of a power series in the energy

$$f_{i,k}^{(1)} = \sum_{q \in \{B,Q,S\}} f_{i,k}^{(0)} \Delta_\alpha^\mu k^\alpha \nabla_\mu \frac{\mu_q}{T} \sum_{m=0}^{M} \lambda_{m,q}^{(i)} E_{i,k}^m \,. \tag{3.36}$$

The final expression of the $\kappa_{qq'}$-matrix can then be derived by comparing the diffusion currents j_q^μ from Eq. 3.13 and the one generated by the distribution function $f^{(1)}$ Eq. 3.36. The diffusion coefficient matrix is then expressed in terms of the expansion coefficients $\lambda_{m,q}^{(i)}$

$$\kappa_{qq'} = \frac{1}{3} \sum_{i=1}^{N_{species}} q_i \sum_{m=0}^{M} \lambda_{m,q}^{(i)} \int \frac{dk_i}{(2\pi)^3 k_i^0} E_{i,k}^m (m_i^2 - E_{i,k}^2) f_{i,k}^{(0)} \,. \tag{3.37}$$

These expansion coefficients have to be evaluated numerically by solving sets of linear equations of particle species and their interactions for each conserved charge q. This calculation was performed by the author of [111] and calculations that are not in the original publication are from private communication. It becomes evident that the comparison between the CE version of $\kappa_{qq'}$ and the GK results are very good in order to verify the correctness of both results.

Diffusion coefficient in the RTA

It is useful for the interpretation of the results of the diffusion coefficient matrix to derive the analytic result of $\kappa_{qq'}$ within the RTA. The final expression of $\kappa_{qq'}$ is rather simple and one can identify important quantities that govern the behavior of the diffusion coefficients. The derivation of the following equations is, again, taken from [111].

The starting point for calculations in the RTA is the approximation of the collision kernel of the Boltzmann equation

$$k_i^\mu \partial_\mu f_{i,k} = \sum_{j}^{N_{species}} \mathcal{C}_{ij}^{(1)}[f_{j,k}] = -\frac{E_{i,k}}{\tau} f_{i,k}^{(1)} \,. \tag{3.38}$$

Here, $\mathcal{C}$ is the linearized collision term and τ is the relaxation time of the specific process, which in this case is the mean free time on a global scale. In this approximation, one can analytically calculate the transport coefficients and the relaxation time τ serves as an input. It would in principle be possible to extract the relaxation time τ from SMASH and compare the RTA to the Green-Kubo method. After some steps of derivation, the diffusion coefficient matrix in the RTA has the following form

$$\kappa_{qq'} = \frac{\tau}{3} \sum_{i=1}^{N_{species}} q_i q_i' \int d^4 K' \frac{1}{E_{i,k}} (E_{i,k}^2 - m_i^2) f_{i,k}^{(0)} - \tau \frac{T n_q n_{q'}}{\epsilon + P_0} \,. \tag{3.39}$$

In the equation above, there exist two counteracting terms. Both terms are proportional to the relaxation time of the system. If the scattering rate of the system increases, the relaxation time will decrease, since they are inversely proportional to $\tau \sim 1/\Gamma_{scat}$. As a result, the charges of the medium can, in a shorter period of time, be distributed throughout the medium and therefore the diffusion coefficient decreases as well. The first term on the left-hand side is proportional to the total charge density n_{tot} due to the symmetry of the qq' factor. The second term is proportional to the net charge density and it becomes important when the net charge density is in the same order of magnitude as n_{tot}. The second term becomes important in a medium with a finite chemical potential μ_q.

3.5   Methodology

Infinite matter calculations

Before the details are explained on how the Green-Kubo relations are applied to extract the transport coefficients, the setup will presented. For computing transport coefficients from SMASH, a box of length L with periodic boundary conditions is used, which simulates an infinite matter system. This is realized such that if a particle crosses a wall of the box, it will be placed on the other side of the box without any loss of energy. The initial phase-space distribution is obtained from the Boltzmann distribution $f_k^{(0)}$, see Eq. 3.32. The density n_i of particle species i given temperature T and chemical potential μ_i is then calculated by integrating $f_k^{(0)}$ over the three momenta which yields

$$n_i(T, \mu_i) = \frac{e^{\mu_i/T}}{2\pi^2} m^2 T \, K_2(m_i/T) \,. \tag{3.40}$$

The mean number of particles is obtained from $N_i = n_i L^3$ and the sets of particles are computed from sampling a Poisson distribution according to the grand-canonical ensemble (GCE). The probability distribution of the particles in momentum space and in spherical coordinates with angles θ and ϕ are

$$w(\mathbf{k}) \sim \exp\left(-\frac{E_{i,k}}{T}\right) k^2 dk \sin\theta d\theta d\phi \,, \tag{3.41}$$

When a finite set of particles is sampled from the equation above, the resulting total momentum $\vec{k}_{tot} = \sum_i \vec{k}_i$ will have a finite value, due to fluctuations. This effectively leads the system to move in one direction even though this should not be the case. In order for $\mathbf{k}_{\text{tot}} = 0$, the momenta of each individual particles is shifted by $\mathbf{k}_i \rightarrow \mathbf{k}_i - \vec{k}_{\text{tot}}/N_{\text{particles}}$.

During the simulation, it is necessary to compute the temperature of the hadron gas in order to see, if thermal equilibrium has been reached. The temperature is calculated from the mean energy density of a particle species at a given point in time. Assuming that the momenta follow the Boltzmann distribution, the mean energy

density of a particle species i in the local rest frame can be computed from

$$\langle e \rangle_i = u_\mu T^{\mu\nu} u_\nu = \int \frac{d^3 k}{k^0} (k^\mu u_\mu)^2 f_{i,k}^{(0)} = \frac{e^{\mu_i/T} g_i T^4}{2\pi^2} \frac{m}{T} \left(3 K_2 \left(\frac{m}{T} \right) + \frac{m}{T} K_1 \left(\frac{m}{T} \right) \right).$$
(3.42)

By inverting the equation above, one can directly obtain the temperature from the inverse function, because Eq. 3.42 is a monotonically increasing function in temperature. Technically, the inverse is computed by numerically interpolating the temperature as a function of the energy density. Using this trick, one can then use the energy density of a given species from SMASH and directly calculate the temperature. The total temperature of the medium is computed by averaging the individual ones of the lightest stable hadrons that have electric, baryonic and strangeness quantum numbers, which are the pion nucleon and kaon

$$T = \frac{T_\pi N_\pi + T_N N_N + T_K N_K}{N_\pi + N_N + N_K}.$$
(3.43)

Here, N_X is the number of particles of species X at each timestep with their respective temperature T_X. The obtained value of T should in principle be a proxy of the temperature of the medium in thermal equilibrium since T is an intensive quantity. An extension towards unstable particles is more complicated because one has to incorporate the spectral function $\mathcal{A}(m)$ in Eq. 3.42.

In the next step, the methodology to compute $\kappa_{qq'}$ and η from the infinite matter simulation is explained.

The Green-Kubo method

In this section, the methodology to calculate the transport coefficients from the Green-Kubo relations and to compute thermodynamic properties like the entropy density from a microscopic transport approach is introduced. The Green-Kubo relations for the shear viscosity η and the diffusion coefficient matrix $\kappa_{qq'}$ are

$$\eta = \frac{V}{T} \int_0^\infty \langle T^{ij}(0) T^{ij}(t) \rangle dt,$$
(3.44)

$$\frac{\kappa_{qq'}}{T} = \frac{V}{3} \int_0^\infty \langle \mathbf{J}_q(0) \cdot \mathbf{J}_{q'}(t) \rangle dt.$$
(3.45)

Here, V is the volume and T is the temperature of the system. The correlation functions are calculated using the off-diagonal components of the energy-momentum tensor T^{ij} and the charge currents $\mathbf{J}_q$. In equilibrium and in the local rest frame of the medium, the off-diagonal components of the energy-momentum tensor are equivalent to the viscous shear-stress tensor π^{ij} for an isotropic medium. The correlation functions are calculated using the following equation

$$\langle \mathcal{I}(0) \mathcal{I}(t) \rangle = \left\langle \lim_{t_{\max} \to \infty} \frac{1}{t_{\max}} \int_0^{t_{\max}} \mathcal{I}(t + t') \mathcal{I}(t') dt' \right\rangle$$
(3.46)

$$= \left\langle \frac{1}{N_{t_{\max}}} \sum_{j=1}^{N_{t_{\max}}} \mathcal{I}(j\Delta t) \mathcal{I}(j\Delta t + i\Delta t) dt' \right\rangle.$$
(3.47)

Here, Δt is the timestep, $t_{\max}$ the end-time, $N_{t_{\max}} = t_{\max}/\Delta t$ the maximum amount of timesteps in the simulation and $i\Delta t = t$. $\mathcal{I}(t)$ stands representative for one of the equilibrium currents T^{ij} or $\mathbf{J}_q$. In addition, $\langle ... \rangle$ denotes the average over many events. The error of $\langle \mathcal{I}(0)\mathcal{I}(t) \rangle$ is computed using the standard deviation $\sigma/\sqrt{N_{\text{events}}}$.

The time evolution of the equilibrium currents is governed by the implemented interactions of the transport model. As the transport code evolves each single particle distribution function, the distribution function f is calculated with

$$f_k(x) = \sum_{i=1}^{N} \delta^{(3)}(x - x_i)\delta^{(3)}(k - k_i)\,, \tag{3.48}$$

where the sum runs over all particles in the system. Using the above expression, the spatially averaged energy-momentum tensor can be written as

$$T^{ij} = \frac{1}{V}\int d^3x \int \frac{d^3k}{k^0} k^i k^j f_k(x) = \frac{1}{V}\sum_{l=1}^{N} \frac{k_l^i k_l^j}{k_l^0}\,. \tag{3.49}$$

and simultaneously, the charge current is

$$J_q^i = \frac{1}{V}\int d^3x \int \frac{d^3k}{k^0} q k^i f_k(x) = \frac{1}{V}\sum_{l=1}^{N} q_l \frac{k_l^i}{k_l^0}\,. \tag{3.50}$$

As the full phase space information of each particle is available, the equilibrium currents, Eq. 3.49 and 3.50 are evaluated at each timestep of the simulation.

Since the shear viscosity is usually normalized to another thermodynamic quantity like the entropy density, they also have to be computed from the simulation. In this work, the definition of the Gibbs-free energy is used. Starting from the infinitesimal change of entropy dS, one can write

$$TdS = dU + pdV - \sum_k \mu_l dN_l\,. \tag{3.51}$$

Here, the sum runs over the conserved charges $\{B, Q, S\}$ in the medium. As the volume is fixed during the simulation and $dw = dU + pdV$, the entropy density s can be calculated as

$$s = \frac{w - \sum_k \mu_k n_k}{T}\,, \tag{3.52}$$

where $w = \epsilon + P$ the enthalpy. Since the computational frame of the simulation is equivalent to the local rest frame, the individual quantities from Eq. 3.52 can be calculated as

$$\epsilon = \langle T^{00} \rangle \tag{3.53}$$

$$P = \frac{1}{3}\sum_{i=1}^{3} \langle T^{ii} \rangle\,. \tag{3.54}$$

The computation of Eq. 3.44 and 3.45 where previously performed by fitting the correlation function Eq. 3.47, assuming that it follows an exponential decay

$$\langle \mathcal{I}(t)\mathcal{I}(0) \rangle = \langle \mathcal{I}(0)\mathcal{I}(0) \rangle \exp\left(-\frac{t}{\tau}\right) . \qquad (3.55)$$

Here, $\langle \mathcal{I}(t)\mathcal{I}(0) \rangle$ is the value of the correlation function at the initial time and τ is the relaxation time of the system. The above expression can then be fitted to the actual correlation function to obtain the relaxation time of the medium. The exponential ansatz was motivated in the previous section when it was shown that the memory kernel in the RTA had an exponential shape. This also shows that τ which appears in Eq. 3.55 can be interpreted as the associated time corresponding to the relaxation of $\mathcal{I}(t)$. By plugging Eq. 3.55 into Eq. 3.44, one can easily get the expression of the transport coefficient. For example, the shear viscosity is

$$\eta = \frac{V}{T} \int_0^\infty \langle T^{ij}(0)T^{ij}(t) \rangle dt = \frac{V\tau \langle T^{ij}(0)T^{ij}(t) \rangle}{T} . \qquad (3.56)$$

However, the ansatz that the correlation function has an exponential shape has its limitations and there exist cases in which the above description is not valid. By directly integrating Eq. 3.46, one is not limited to any assumptions of the shape of the correlation function and can additionally capture any information in their tails that might not be included by the fitting procedure.

In the following section, the procedure will be explained to obtain the transport coefficients by directly integrating Eq. 3.47 numerically and the result will be compared to a CE calculation of the same system. Cases, in which the assumption breaks down are for example, the bulk viscosity, where the correlation function follows a multi-exponential function (see e.g. Fig. 5 in [106]). It was also shown in the case of a very dense system, that the correlation function slightly varies from an exponential (see e.g. Fig. 12 in [103]).

The integration of correlation function is performed using the trapezoidal rule which is sufficient with a timestep size of $dt = 0.05$ fm, since the end times of the simulations are usually in the order of $\sim 10^3$ fm. The error of the transport coefficients is calculated by integrating the correlation function both within the lower/upper error. Since the correlation functions suffer from large noise in their tails it is important to evaluate the convergence of the numerical integration, which will be checked at the beginning of the next section. For all following calculations, the timestep is chosen to be $dt = 0.05$ fm.

Fig. 3.1 shows the fluctuations of the conserved charge current j^x_{BQS} and the off-diagonal components of the energy-momentum tensor T^{ij}. Comparing Fig. 3.1 to the discussion in the previous section (Section 3.2 and Section 3.3), one can see that the fluctuations are not white noise fluctuations. There exist correlations in the noise over time which results in some timescale that a small perturbation needs, in order to relax. Over time, the equilibrium currents fluctuate around zero.

The goal is now to apply the above-described methodology in a simple test case and compare it to CE calculations.
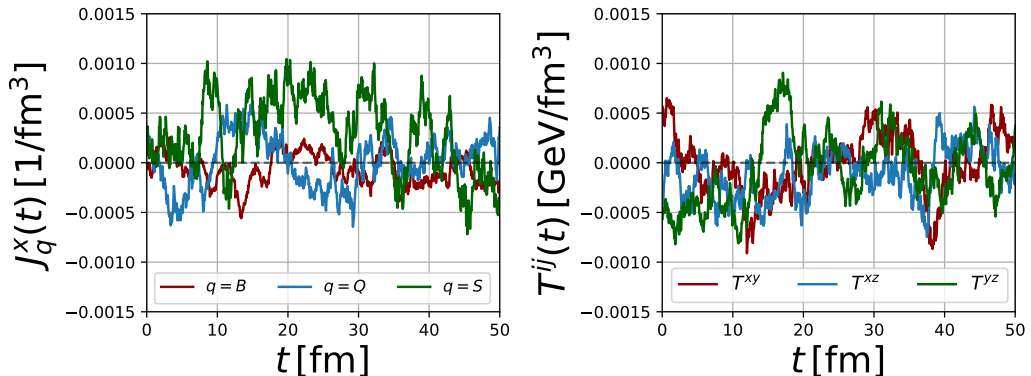
34

Figure 3.1: Example of the fluctuations of the x-component of the conserved charge current j_{BQS} (left) and the off-diagonal components of the energy momentum tensor T^{ij} (right) as a function of the temperature. The system is a multi-component hadron gas that will be introduced in Section 3.6.7 interacting via a constant elastic cross section at a temperature of $T = 150\,\mathrm{MeV}$ in a box of $V = (30\,\mathrm{fm})^3$.

3.6 Results from the hadron gas with interactions

The structure of the following sections is as follows. Since the goal is to sequentially study the influence of the collision kernel and the number of degrees of freedom on the transport coefficients, the details of the interactions will be explained as well. So first, the interactions will be introduced and then, the impact on the transport coefficients will be studied. In the first step, a simple system of pions interacting with a constant isotropic cross-section is investigated, to test the numerical integration of the correlation function and compare it to CE calculations.

3.6.1 Introducing the collision term

An effective solution of the Boltzmann equation can be found by evolving the single-particle distribution function on a Monte-Carlo basis. To do so, a criterion is needed for the collision between two particles and one of the possible criteria is the geometric collision criterion, that has been used in many different transport approaches (see e.g. [86, 87]). It defines that a collision takes place if the relative transverse distance between two particles $d_\perp$ is smaller than the following quantity

$$d_\perp < \sqrt{\frac{\sigma_{\mathrm{tot}}(\sqrt{s})}{\pi}}\,, \tag{3.57}$$

where $\sigma_{\mathrm{tot}}(\sqrt{s})$ is the total energy-dependent cross section of the reaction. The geometric collision criterion uses the geometric interpretation of the cross-section, in which σ_{tot} acts as the total surface area of the disc. The distance between the particles is evaluated from

$$d_\perp^2 = (\mathbf{r}_a - \mathbf{r}_b)^2 - \frac{((\mathbf{r}_a - \mathbf{r}_b) \cdot (\mathbf{k}_a - \mathbf{k}_b))^2}{(\mathbf{k}_a - \mathbf{k}_b)^2}\,. \tag{3.58}$$

35

In the equation above, $\mathbf{r}$ and $\mathbf{k}$ are the spatial and momentum three vectors of particle a and b in the center-of-mass frame of the collision. A covariant formulation of the collision criterion by Hirano et al. is used [155]. One problem with the geometric collision criterion is that it is not possible to describe interactions with more than 2 incoming particles. A solution to this will be presented later in this chapter.

In the following section, the transport coefficients are calculated for a single species gas with three electric charges ($\pi^{\pm,0}$), interacting via a constant isotropic cross-section of $\sigma = 30$ mb.

3.6.2 Simple test case

We are now ready to test the methodology for a hadron gas consisting of three pions interacting via a constant isotropic cross-section of $\sigma_{\text{tot}} = 30$ mb. This specific comparison between the Green-Kubo result from SMASH and CE calculations has been done before, see e.g. [156] and it is known that both calculations should return the same result. However, what has been newly introduced in this work is the direct numerical integration of the correlation function. It is therefore the goal of this section to gauge the calculations and study its limitations.

As a starting point, it can also be helpful to verify the computation with the value of the correlation function at time $t = 0$. At the initial time, the value is fully determined by thermal fluctuations and e.g. for the electric charge current, $\langle \mathbf{J}_q(0)\mathbf{J}_q(0) \rangle$ can be evaluated semi-analytically by calculating moments of the equilibrium Boltzmann-distribution $f_k^{(0)}$. Starting with one component of the charge current, one can write the correlation between the two charges q and q' as

$$\langle J_q^x(0)J_{q'}^x(0) \rangle = \left\langle \sum_{m=1}^{N_{\text{species}}} q_m \frac{k_m^x}{k_m^0} \sum_{n=1}^{N_{\text{species}}} q'_n \frac{k_n^x}{k_n^0} \right\rangle = \left\langle \left(\sum_{n=1}^{N_{\text{species}}} \sqrt{q_n q'_n} \frac{k_n^x}{k_n^0} \right)^2 \right\rangle \quad (3.59)$$

$$= \sum_{n=1}^{N_{\text{species}}} \frac{q_n q'_n g_n}{6\pi^2 V} \int_0^\infty dk \frac{k^4}{E_{n,k}} f_{n,k}^{(0)} . \quad (3.60)$$

In the last step, a sum over the number of particle species was introduced with the respective degeneracy g_n. Even though the computation is not relevant in this section, for the sake of completeness the equation for the correlation function of the energy-momentum tensor at the initial time is calculated from

$$\langle T^{ij}(0)T^{ij}(0) \rangle = \sum_{a=0}^{N_{\text{species}}} \frac{g_a}{30\pi^2 V} \int_0^\infty dk \frac{k^6}{E_{a,k}} f_{a,k}^{(0)} . \quad (3.61)$$

Fig. 3.2 shows the comparison of the correlation function at time $t = 0$ obtained from SMASH and the results of Eq. 3.60. One can see that the comparison matches perfectly between the simulation and the derived formula. With the confidence that at least the initial value of the correlation function is computed correctly, the next step is to integrate the correlation function in order to obtain the transport coefficient.
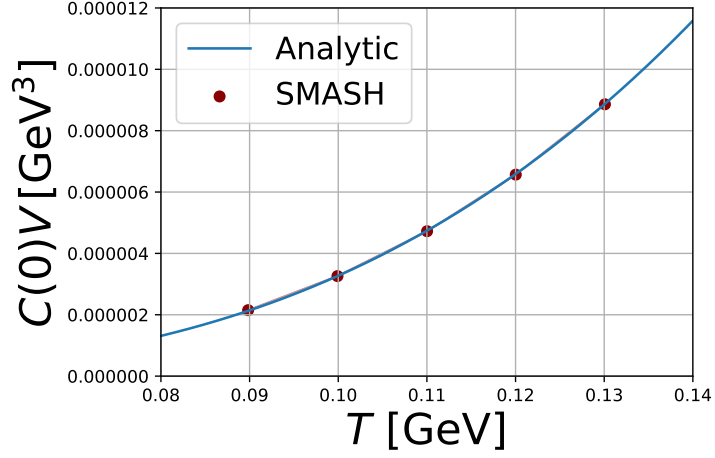
Figure 3.2: Comparison of the value of the correlation function at time $t = 0$ as a function of the temperature between SMASH and semi-analytical calculation.

The time-dependent correlation function and the dependency of the electric charge diffusion coefficient on the upper time of the integration are shown in Fig. 3.3. The quantity on the right-hand side is defined as

$$\frac{\kappa_{QQ}(t)}{T^2} = \frac{V}{3T} \int_0^t \langle \mathbf{J}_q(0)\mathbf{J}_q(t') \rangle dt' \,. \tag{3.62}$$

The upper and lower error of Eq. 3.62 is calculated by integrating the respective upper/lower error of the correlation function. Fig. 3.3 shows an important result because of two things. First, the integration of the correlation function converges within the time scale of the simulations and second, the values of the integration converge perfectly towards the CE calculation. In addition, this simple test case can be used to define a criterion when to stop the integration of the Green-Kubo relation because, for obvious reasons, it is not possible to integrate until infinity. At some point, only the error increases, whereas the mean value stays relatively constant. It is found that a good result within the errors is achieved when the integration is performed until a relative error of 5% is reached. The same criterion is applied for the rest of the results presented in this chapter for the shear viscosity η and the diffusion coefficient matrix $\kappa_{qq'}$. The final temperature dependence of κ_{QQ} is presented in Fig. 3.4, obtained from the procedure explained above. A perfect agreement between the methodology from this work and CE calculations is found, ensuring that the numerical integration works perfectly and can be used for further studies.

In the next step, the goal is to study more complex systems going beyond two-body interactions. However, before the results are presented, the treatment in SMASH of unstable particles is shown.
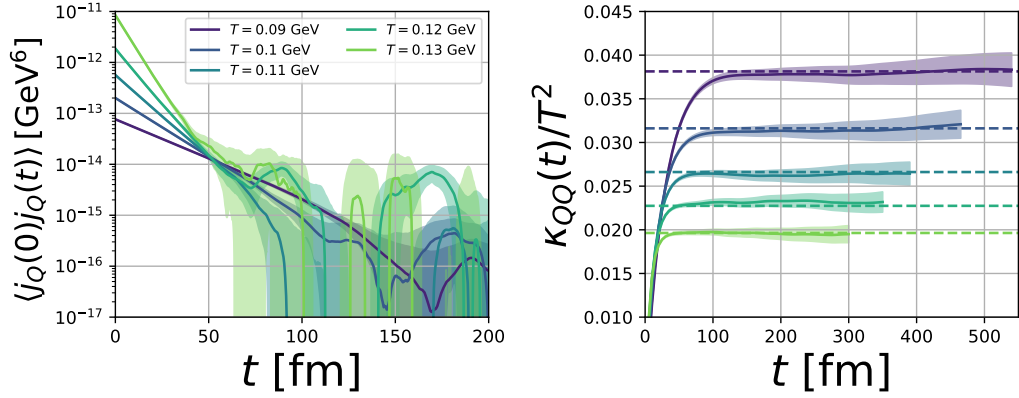
Figure 3.3: Left: Correlation function of the electric charge current as a function of time for different temperatures. Right: Dependency of the diffusion coefficient of the electric charge as a function of the upper limit of integration for multiple temperatures. The dashed lines show the value of the CE calculation for each individual temperature.
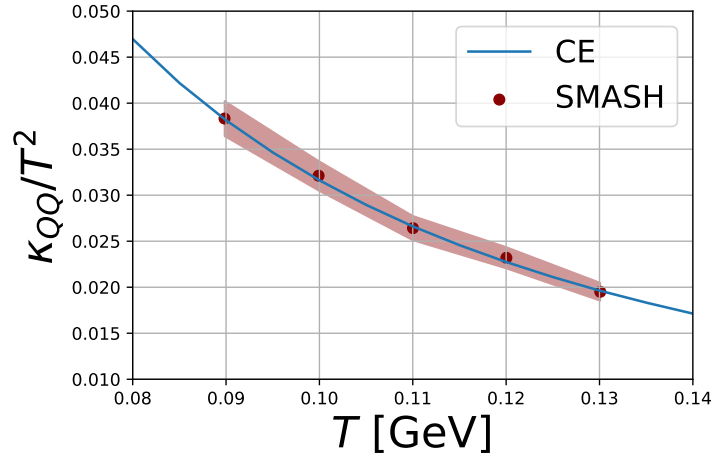

Figure 3.4: Electric charge diffusion coefficient as a function of temperature. Comparison of the results from SMASH (red points) to CE calculations (blue line).

3.6.3 Extension of the collision term towards multi-particle interactions

In this section, the details of the implementation of unstable particles in SMASH are presented. This includes resonance formation processes $2 \to 1$ as well as decays $1 \to 2$. In addition, the treatment of multi-particle reactions is shown.

$2 \to 1$ processes

To treat $2 \leftrightarrow 1$ processes, the notion of an unstable particle has to be known and its behavior has to be treated in the calculation. The starting point is the spectral function of unstable particles, which describes the probability distribution around its pole mass M_0. In vacuum, they can be represented by relativistic Breit-Wigner distributions

$$\mathcal{A}(m) = \frac{2\mathcal{N}}{\pi} \frac{m^2 \Gamma(m)}{(m^2 - M_0^2)^2 + m^2 \Gamma(m)^2} . \tag{3.63}$$

Here, m is the off-shell mass of the resonance and $\mathcal{N}$ a constant such that the spectral function is normalized to unity $\int_0^\infty \mathcal{A}(m)dm = 1$. $\Gamma(m)$ is the mass-dependent decay width and is defined as

$$\Gamma(m) = \sum_R \Gamma_R(m) , \tag{3.64}$$

where the sum runs over all possible resonance states and $\Gamma_R(m)$ is the decay width of an individual decay process. The decay width can in principle be treated as a constant however, it is more physical to treat it as mass-dependent. Below a certain threshold $m_{\min}$, defined by the lightest resonance, the spectral function has to vanish as there exist no decay channels. The treatment in SMASH of mass-dependent decay width of the individual decay channel of a resonance R decaying into particle a and b follows the description of Manley et al. [157]

$$\Gamma_{R \to ab} = \Gamma_{R \to ab}^0 \frac{\rho_{ab}(m)}{\rho_{ab}(M_0)} . \tag{3.65}$$

In the equation above the function $\rho_{ab}(m)$ is defined as
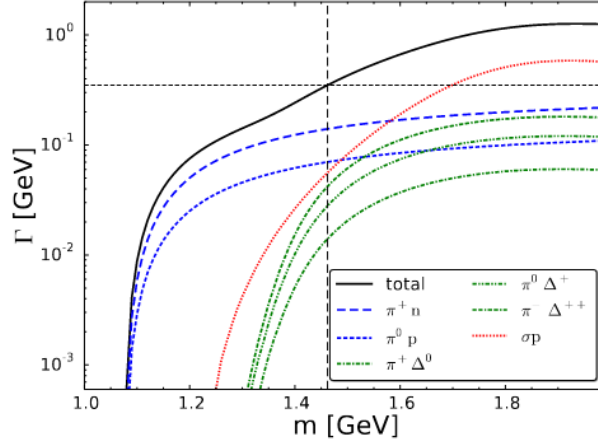

Figure 3.5: Mass dependent decay width of the $N^\star(1440)^+$ resonance. The total decay width is shown as the full black line whereas the partial channels are depicted as colored lines. The figure is taken from [85].

$$\rho_{ab}(m) = \int dm_a dm_b \mathcal{A}_a(m_a) \mathcal{A}_b(m_b) \frac{|\mathbf{k}_f|}{m} B_L^2(|\vec{p}_f|R) \mathcal{F}_{ab}^2(m) , \tag{3.66}$$

where the integration is performed over the off-shell masses of the decay products. In the case of a decay into a stable hadron, the spectral function simply becomes $\mathcal{A}(m) = \delta(m - M_0)$ and the integral collapses. If one of the decay products is a resonance itself, the integration has to be performed and the form factor $\mathcal{F}$ becomes important. They are defined as

$$\mathcal{F}_{ab} = \frac{\lambda^4 + 1/4(s_0 - M_0^2)^2}{\lambda^4 + (m^2 - 1/2(s_0 + M_0^2))^2}\,, \tag{3.67}$$

where λ is a cut-off parameter that is implemented for different decay products (for further details see [85]). $|\mathbf{k}_f|$ is the absolute final state momentum in the center-of-mass frame which can be written as

$$\mathbf{k}_f^2 = \frac{(m^2 - (m_a + m_b)^2)(m^2 - (m_a - m_b)^2)}{4m^2}\,. \tag{3.68}$$

In Eq. 3.66, $B_L(p)$ are the so-called Blatt-Weisskopf functions [158] which depend on the angular momentum of the decay products a and b. The first Blatt-Weisskopf functions are

$$B_0(p) = 1\,, \tag{3.69}$$

$$B_1(p) = \frac{p}{\sqrt{1 + p^2}}\,, \tag{3.70}$$

$$B_2(p) = \frac{p^2}{\sqrt{9 + 3p^2 + p^4}}\,. \tag{3.71}$$

An example of $\Gamma(m)$ is shown in Fig. 3.5 of the unstable baryon $N^\star(1440)^+$ with all its decay channels. One can see that the decay width vanishes at some minimal mass $m_{\min}$ where no decay channels exist.

It is worth noting that the presented expressions describe the vacuum properties of the resonance, whereas it is known that at non-zero temperature, the spectral function changes, however, in-medium modifications are not implemented in SMASH. A study of an effective modification due to the hadronic scatterings can be found in [159].

Finally, the resonance formation cross-section is calculated using [86]

$$\sigma_{ab \to R}(s) = \frac{2J_R + 1}{(2J_a + 1)(2J_b + 1)} \mathcal{S}_{ab} \frac{2\pi^2}{\mathbf{k}_i^2} \Gamma_{ab \to R}(s) \mathcal{A}_R(\sqrt{s})\,. \tag{3.72}$$

With J the spin of the particle, $\mathcal{S}_{ab}$ a symmetry factor, which is 2 if a and b are the same and 1 if not and $\mathbf{k}_i$ the center of mass momentum (see Eq. 3.68).

In the expression above, the in-width $\Gamma_{ab \to R}(m)$ is the width of the inverse reaction of $R \to ab$ and it is generally not the same as in the case of the forward reaction $R \to ab$, except if the particles in the initial state are the same. If the incoming particles are not the same, the in-width is computed from

$$\Gamma_{ab \to R}(m) = \Gamma_{R \to ab}^0 \frac{|\vec{p}_{ab}|B_L(|\vec{p}_{ab}|R)\mathcal{F}_{ab}(m)}{m\rho_{ab}(M_0)}\,. \tag{3.73}$$

In the next step, the details of performing the decay of an unstable particle will be explained.

$1 \rightarrow 2$ **processes**

In the previous section, the description of resonance formation processes was explained. For the modeling of the decay within the simulation the lifetime of the resonance which is simply $\tau = \Gamma(m)^{-1}$ is needed. Then, the probability of decay within a timestep in the limit of $\Delta t \to 0$ is

$$P_{\text{decay}}(t) = \exp(-\Gamma(m)t)\,. \tag{3.74}$$

In the case where there exist multiple possible decay channels, one of them is randomly chosen from the probability

$$p_i = \frac{\Gamma_i(m)}{\Gamma(m)}\,. \tag{3.75}$$

Finally, the treatment of multi-particle reactions will be presented next, before the dependency of the transport coefficients of these processes will be studied.

Multi-particle reactions in transport approaches

In order to treat multi-particle reactions directly, it is necessary to use a different collision criterion that is easily generalized to interactions with more than two incoming particles, the stochastic collision criterion [160, 161, 62]. It was recently introduced in SMASH [142] to study multi-particle reactions in a hadronic medium.

For the stochastic collision criterion, a collision probability is defined for each possible reaction within a phase space cell $\Delta^3 x \Delta^3 k$ within a given timestep Δt. This probability can be directly introduced for a $n \to m$ reaction as

$$P_{n \to m} = \frac{\Delta N_{\text{reactions}}^{n \to m}}{\prod_{j=1}^{n} \Delta N_j}\,. \tag{3.76}$$

Here, ΔN_j is the number of particles within the cell and $\Delta N_{\text{reactions}}^{n \to m}$ the number of reactions for the timestep within the cell. With the scattering rate given by the collision term of the Boltzmann equation, the probability for 2- and 3-body reactions can be expressed in terms of the cross-section or decay width of the reverse process. More details of this derivation and the numerical treatment are found in [142].

The probability of an arbitrary 2-to-m scattering is given by

$$P_{2 \to m} = \frac{\Delta t}{\Delta^3 x} v_{\text{rel}} \sigma_{2 \to m}(\sqrt{s}) \tag{3.77}$$

with the timestep size Δt, the cell volume $\Delta^3 x$, the cross-section of the process and the relative velocity

$$v_{\text{rel}} = \frac{\lambda^{1/2}(s; m_1^2, m_2^2)}{2E_1 E_2}\,, \tag{3.78}$$

which uses the abbreviation $\lambda(s; m_1^2, m_2^2) = (s - m_1^2 - m_2^2)^2 - 4m_1^2 m_2^2$.

The probability for a 3-to-1 reaction is given by

$$P_{3 \to 1} = \left(\frac{g_{1'}}{g_1 g_2 g_3}\right) \mathcal{S}! \frac{\Delta t}{(\Delta^3 x)^2} \frac{\pi}{4E_1 E_2 E_3} \frac{\Gamma_{1 \to 3}(\sqrt{s})}{\Phi_3(s)} \mathcal{A}(\sqrt{s})\,, \tag{3.79}$$

in terms of the decay width of the reverse process $\Gamma_{1\to3}(\sqrt{s})$, the spectral function of the formed resonance $\mathcal{A}(\sqrt{s})$, the 3-body phase space $\Phi_3(s)$, the spin degenercy factor $g_j = 2\mathfrak{s}_j + 1$ ($\mathfrak{s}_j$ being the spin of the state) and $\mathcal{S}$ the number of identical incoming particles. With this, the inverse reactions to mesonic Dalitz decays i.e. 3-to-1 reactions are accounted for in SMASH in order to obtain detailed balance. The 3-body phase space is then sampled isotropically for the outgoing particles.

The 3-to-1 reactions in SMASH are $\pi\pi\pi \to \omega$, $\pi\pi\pi \to \phi$ and $\pi\pi\eta \to \eta'$. Other multi-particle reactions realized in SMASH are the light nuclei generation with 3-to-2 interactions and the back-reaction of $N\bar{N}$ annihilations via 5-to-2 reactions. Results with them are discussed in [142] and [101] respectively. However, since their influence is not studied in this work the details are not included here.

3.6.4 Quantitative influence of multi-particle scatterings

In this section, the influence of multi-particle scatterings is studied in the hadronic regime. Multi-particle reactions become important in a very dense medium and processes with more than two interaction partners become more probable.

The calculation of the transport coefficients is performed in a hadron gas with only three constituents consistent of π, ρ and ω (plus their corresponding charge and anti-particle states). The reaction of interest is the mesonic $3 \leftrightarrow 1$ reaction $\omega \leftrightarrow 3\pi$ which, using only binary reactions is modeled via $\omega \leftrightarrow \pi\rho \leftrightarrow 3\pi$. Here, the ρ meson acts as an intermediate step to reach the 3π final state. The probability $P_{3\leftrightarrow1}$ is given by Eq. 3.79. To be able to draw a fair comparison between the two cases ($3 \leftrightarrow 1$ vs. binary reaction chain), the process $\rho \leftrightarrow \pi\pi$ is added to the case with multi-particle reactions. In order to reduce systematic uncertainties, both simulations are performed using the stochastic collision criterion. The probability of the $P_{2\leftrightarrow1}$ process is given by Eq. 3.77.

One of the findings of the newly implemented hadronic multi-particle reactions is, that the time of chemical and thermal equilibration is reduced [142]. It is therefore reasonable to assume that the transport coefficients are affected as well, due to their proportionality to the relaxation time of the medium. The question is still, which type of relaxation times are affected? In this section, the shear viscosity, as well as the electric charge diffusion coefficient κ_{QQ} is of interest.

Fig. 3.6 shows the correlation function at $t = 0$ of SMASH compared to Eq. 3.60 and 3.61. In both cases, the integration over momenta has to be extended with an integration over the spectral function, since both the ρ and ω are unstable particles. Here, the functional form of Eq. 3.66 is taken. The comparison between the semi-analytical calculation and the results from SMASH are consistent with each other which ensures that the computation of the correlation function was performed correctly. In addition, it shows that the variance of the energy-momentum tensor $T^{\mu\nu}$ and the charge current J_Q^i of the two systems have the same values. Any difference that appears in the final value of the transport coefficients therefore has to originate from the relaxation time of the medium.

Fig. 3.7 shows the shear viscosity η and the electric charge diffusion coefficient κ_{QQ} for the comparison between with and without multi-particle reactions. Starting
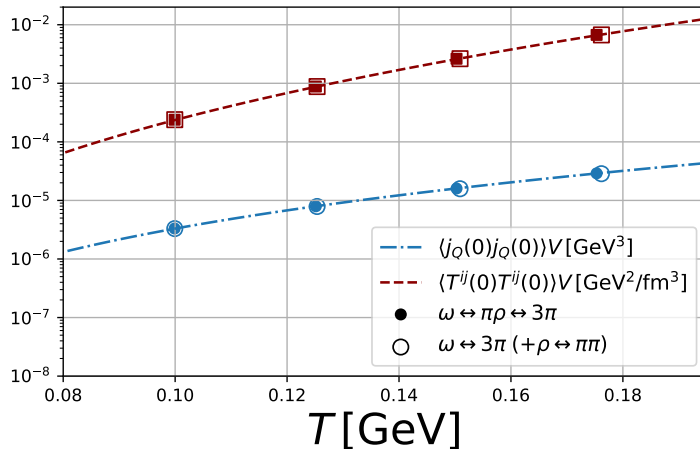
Figure 3.6: Comparison of the value of the correlation function at time $t = 0$ of the electric charge current j_Q and off-diagonal components of the energy momentum tensor T^{ij} as a function of the temperature between SMASH (symbols) and semi-analytical calculation (lines). The simulation using multi-particle reactions (open symbol) and using only the binary reaction chain (full symbols) are presented.

with the shear viscosity, the value of η has a strong temperature dependence and it grows with increasing temperature. Starting around $T \sim 150\,\mathrm{MeV}$, the influence of the multi-particle reaction becomes dominant and it effectively decreases the shear viscosity. The reason for the growing difference is that at lower temperatures, the energy is not sufficiently large to form a ρ or ω mesons, since both have masses $m_{\rho/\omega} \sim 780\,\mathrm{MeV}$. Around $T \sim 150\,\mathrm{MeV}$, the possible reaction channels open up and the multi-particle reactions become important. Even though η is obtained by integrating the correlation function, it is helpful to look at Eq. 3.56 for a better understanding of the different components relevant for the transport coefficient. Since V and T are fixed in the simulation $\eta \sim \langle T^{ij}(0)T^{ij}(0)\rangle\tau$ and since $\langle T^{ij}(0)T^{ij}(0)\rangle$ is equivalent for the two cases, the relaxation time relevant for η of the two systems has to be $\tau^{\eta}_{3\leftrightarrow1} < \tau^{\eta}_{3\leftrightarrow2\leftrightarrow1}$. This is in accordance with previous findings in which the equilibration time has been found to be reduced with direct $3 \leftrightarrow 1$ reactions. For the shear viscosity, the relevant quantity is the timescale of equilibration of T^{ij} from small perturbations. With multi-particle reactions, there exists the direct process $\omega \leftrightarrow 3\pi$ which is effectively faster in terms of relaxing T^{ij} from out of equilibrium, compared to $\omega \leftrightarrow \pi\rho \leftrightarrow 3\pi$.

In contrast, the electric charge diffusion coefficient κ_{QQ} or electric conductivity shows no influence on multi-particle processes. Since the value of the correlation function at time $t = 0$ is equivalent for the two cases, the relaxation time for the diffusion coefficient is the same as well $\tau^{\kappa_{QQ}}_{3\leftrightarrow1} \sim \tau^{\kappa_{QQ}}_{3\leftrightarrow2\leftrightarrow1}$. It is worth noting that the type of relaxation time is different between η and κ_{QQ}, as they describe different processes. For the electric charge diffusion coefficient, it is relevant how fast perturbations in the electric current j_Q can equilibrate. As the electric charge is
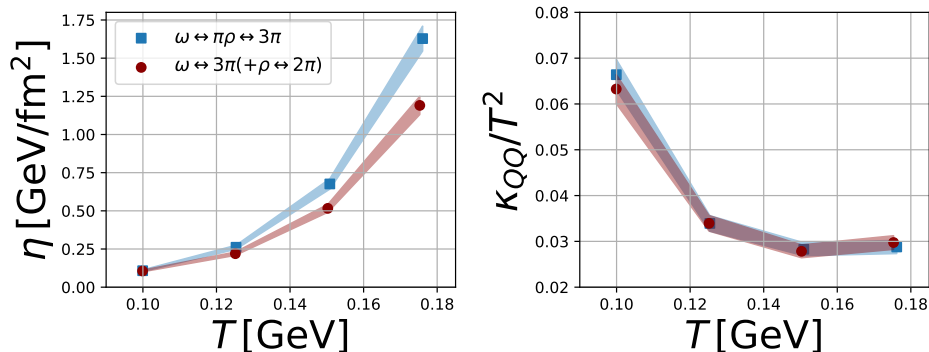
Figure 3.7: Shear viscosity (left) and electric charge diffusion coefficient (right) as a function of the temperature. Results obtained with multi-particle reactions (red circles) as well as with the binary reaction chain (blue squares) are presented.

conserved in the process $\omega \to 3\pi$, other interactions in between don't matter since the charges are propagated nevertheless.

A similar result has been found when comparing the electrical conductivity and the shear viscosity of an interacting hadron gas consistent of π and ρ mesons (Fig. 9 in [105] and Fig. 6 in [103]). After the resonance is formed, it propagates and eventually decays with a certain probability. When comparing the results from SMASH to CE calculations for the same gas but with a parametrized elastic cross section $\sigma_{2\leftrightarrow2}(\sqrt{s}) = \sigma_{\pi\pi\to\rho\to\pi\pi}(\sqrt{s})$, a large difference on the level of η was found, but not in σ_{el}. When the lifetime of the ρ-meson in SMASH was artificially set to (approximately) zero, the shear viscosity matches perfectly with the CE calculation whereas the electric conductivity is not largely affected. A similar phenomenon can be found in the case with $3 \leftrightarrow 1$ reactions versus $3 \leftrightarrow 2 \leftrightarrow 1$. The shear viscosity is largely affected by the intermediate reaction chain, which hinders relaxation of shear stress whereas κ_{QQ} mostly depends on the total cross section and charge density which is equivalent in the two cases.

Unfortunately, the calculation using multi-particle reactions cannot easily be extended towards the full SMASH hadron gas. First, the usage consumes much more computational time and the simulation of full SMASH hadron gas would simply take too long. In addition, there are only a limited amount of reactions implemented, so the changes caused by these few processes on the transport coefficients are assumed to be negligible. However, this test case shows that multi-particle reactions become important at temperatures around $T \gtrsim 130\,\mathrm{MeV}$ for the shear viscosity.

In the next step, the goal is to establish new interactions that have been implemented since the publication of the previous results of transport coefficients and then systematically study their influence on the full diffusion coefficient matrix and the shear viscosity.

3.6.5 Further extensions of the collision kernel

It was shown that the results from SMASH using the Green-Kubo method and CE calculations match perfectly in a simple hadronic system. The main benefit of the Green-Kubo approach is that one can relatively easily introduce new interactions in the microscopic model and extract the transport coefficients.

The goal of this section is to do a more thorough analysis of the dependency of the transport coefficient η and κ_{ij} on the collision kernel within the full SMASH hadron gas. Besides the interactions that have been used so far, (in-)elastic $2 \to 2$ reactions, as well as anisotropic cross-sections and the additive quark model will be introduced.

Elastic $2 \to 2$

Elastic binary collisions are collisions in which the incoming particles are equal to the outgoing particles. When viewed from the experimental side however it is not possible to distinguish between a reaction where the incoming particles only "bounce" from each other or where a reaction of the type $ab \to R \to ab$ took place. Therefore, the elastic cross sections in the case of meson-baryon or meson-meson collisions are calculated from the previously explained resonance formation plus their respective decay. In the case of nucleon-nucleon scatterings, parametrizations from [162] are used. If the energy of the reaction is below the threshold for the formation of the resonance, parametrization of the $2 \to 2$ reactions is taken.

Inelastic $2 \to 2$

In the case of inelastic binary collisions where the final state particles differ from the initial state, there are two cases that have to be treated differently. First, the case where there is one resonance in the final state $ab \to cR$. Here, one has to integrate the cross-section over the spectral function of the respective resonance. The energy-dependent cross-section is then computed as

$$\sigma_{ab \to cR}(s) = \frac{(2J_R + 1)(2J_c + 1)}{s|\vec{p_i}|} \sum_I (C_{ab}^I C_{cR}^I)^2 \frac{|\mathcal{M}|^2_{ab \leftrightarrow cR}(s, I)}{16\pi}$$
$$\times \int_0^{\sqrt{s} - m_c} dm \mathcal{A}_R(m) |\vec{p_f}|(\sqrt{s}, m, m_c). \tag{3.80}$$

The sum over I runs over isospin states and C_{ab}^I are Clebsch-Gordon coefficients of the isospin states of particle a and b. The matrix elements $|\mathcal{M}|$ are obtained by fitting parametrized expressions to model calculations. In the case of $NN \to N\Delta$, a fit to the One-Boson Exchange model is performed [163]. For other processes, an isospin-dependent expression of $|\mathcal{M}|$ is used.

For the second case, where two resonances are in the final state of the binary interaction $ab \to R_1 R_2$, Eq. 3.80 has to be extended by an additional integration over the spectral function of the second resonance R_2 and the integral has to be

exchanged with

$$\int_{m_1^{min}}^{\sqrt{s}-m_2^{min}} dm_1 \mathcal{A}_1(m_1) \int_{m_2^{min}}^{\sqrt{s}-m_1^{min}} dm_2 \mathcal{A}_2(m_2) |\vec{p}_f|(\sqrt{s}, m_1, m_2) \,. \qquad (3.81)$$

Generally, the following processes are included, which differ in the final state particle content

- Single resonance excitation,

- Double resonance excitation,

- (Double) Resonance absorption (inverse of single and double resonance excitation),

- Strangeness exchange $\bar{K}N \to \pi \Upsilon(\Lambda, \Sigma, \Xi)$,

- Inelastic charge exchange,

- Nucleon-nucleon to double mesonic interaction $N\bar{N} \to h_1 \pi$.

Angular distributions

It is known that the cross-sections of some scattering processes depend on the angle Ω of the outgoing particles. For the previous results, only isotropic cross-sections have been used which are independent of the scattering angle. In this section, the extension of the cross-section towards $\sigma(\sqrt{s}) \to \sigma(\sqrt{s}, \Omega)$ in SMASH is explained.

The incorporation of angular distributions on the final state of elastic and inelastic binary interactions of the form

$$d\sigma/dt \propto e^{-bt} \qquad (3.82)$$

is used [164]. Here, the baseline is the measurement of the angular distribution in elastic pp interactions. Starting with elastic NN processes, in which the distribution is measured, it is argued in [164] that the final state in $NN \to N\Delta$ scatterings has a similar shape as the elastic NN interaction, which is why the same distribution is applied for a scattering with a Δ in the final state. Due to the lack of experimental data on the measurements of the angular distributions, additionally, the same distributions for all baryonic and mesonic elastic scatterings are included in the calculation. This is the main extension with respect to the previous computations. Fig. 3.8 shows the angular distribution $d\sigma/dt$ as a function of the Mandelstam variable t. The red curve shows the contribution of the elastic NN scattering and one can see that it matches well with experimental data. The distribution of heavier resonance states is not symmetric anymore due to restrictions in the phase space distributions. As there are no measurements of the angular distributions of inelastic scatterings, SMASH cannot be tuned to data but overall the results are comparable to the measurements. The energy dependence of the parameter b in Eq. 3.82 is computed from the parametrization in [164].
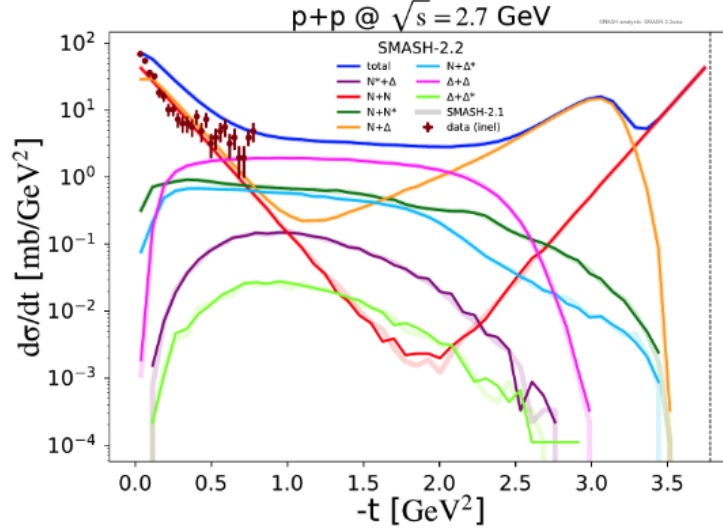
Figure 3.8: Angular distribution of inelastic pp scatterings. The figure is taken from [165] and the data points are from [166].

AQM cross sections

The next extension of interactions in SMASH are cross-sections calculated using the additive quark model (AQM). These are parametrizations for cross-sections between hadrons that are not known experimentally and they can be written as

$$\sigma_x^{AQM} = 40 \left(\frac{2}{3}\right)^{n_{\mathrm{meson}}} (1 - 0.4 x_1^s)(1 - 0.4 x_2^s), \qquad (3.83)$$

where n_{meson} is the number of mesons and $x_{1,2}^s$ is the fraction of strange over non-strange quarks of the two incoming hadrons. The cross-section of unknown processes is then scaled according to

$$\frac{\sigma_{\mathrm{process}}^{\mathrm{AQM}}}{\sigma_{\mathrm{ref-process}}^{\mathrm{AQM}}} \sigma_{\mathrm{ref-process}}^{\mathrm{AQM}}. \qquad (3.84)$$

Here, $\sigma_{\mathrm{ref-process}}^{\mathrm{AQM}}$ is a reference process where the actual cross section is experimentally well defined. The inclusion of AQM cross-sections will enhance the number of interactions as there are more cross-sections between hadrons.

The extension with the AQM cross-sections is the second extension of the collision kernel whose effects will be studied in the following section.

3.6.6 Influence from angular distributions and AQM cross-sections

In this section, the influence of the previously explained extensions of the collision kernel in SMASH on the shear viscosity and the diffusion coefficient matrix will be systematically studied. Since the full SMASH hadron gas is used, the full diffusion coefficient matrix $\kappa_{qq'}$ can be presented. In the following, the results from the SMASH

version used in this work (SMASH-2.2) in which the above-described interactions are included will be compared to the previously obtained results of the shear viscosity from [103], which was calculated using the version SMASH-1.6. Here, no AQM cross-sections were included and the angular distributions were only applied for $NN \to NN$ and $NN \to NN^\star$ reactions.
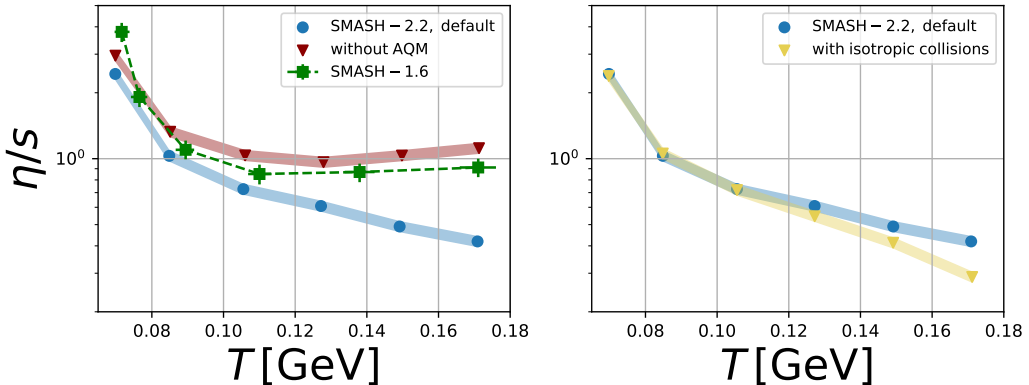

Figure 3.9: Shear viscosity over entropy density versus temperature. The results of the SMASH-2.2 version (blue) are compared to the results of SMASH-1.6 (green). On the left, the influence of additional elastic cross-sections via the AQM description is presented (red triangles). On the right, the influence of isotropic angular distributions (yellow triangles) is shown.

Starting with the shear viscosity, it is found that both angular distributions, as well as the AQM cross-sections, have a strong impact on the dimensionless quantity shear viscosity over entropy density η/s, as is depicted in Fig. 3.9. The impact of additional elastic cross-sections drastically reduces η. Whereas the temperature dependence of the SMASH-1.6 results shows a plateau from $T \sim 110$ MeV on, the shear viscosity of version SMASH-2.2 further decreases. When the hadron gas is evolved without the AQM cross-sections, the plateau behavior and the result of SMASH-1.6 are approximately recovered. η/s is a little bit larger in comparison to the results of SMASH-1.6 at larger temperatures and smaller at the lowest temperature point.

The description of the AQM cross-section provides an estimation of elastic cross-sections for interactions between particles that are not known. Especially at higher temperatures where the energy of the system is sufficiently large to produce more exotic particle species, the interactions via AQM cross-sections become more important. The additional elastic cross-sections reduce the relaxation time of the energy-momentum tensor and as a result, the shear viscosity decreases.

The influence of anisotropic scatterings is shown on the right-hand side of Fig. 3.9. In comparison to the SMASH-2.2 version, treating all interactions isotropically further reduces η at larger temperatures, even though this effect is not as dominant as the inclusion of the AQM cross-section. The decrease of η originates from the reduction of the phase space of the outgoing particles of an interaction. If a small perturbation

in T^{ij} occurs, the relaxation of this perturbation is faster if the full phase space is open. If anisotropic angular distributions are incorporated the relaxation time increases and the viscosity increases as well.

Interestingly, at the lowest temperature point $T \sim 70\,\mathrm{MeV}$ a difference in η/s is observed. In this temperature region, the system is dominated by pions, and the relevant quantity is their respective cross-section. As these were not modified within the changes from version SMASH-1.6 to SMASH-2.2 it is important to understand where this difference comes from. Fig. 3.10 shows the correlation function of the
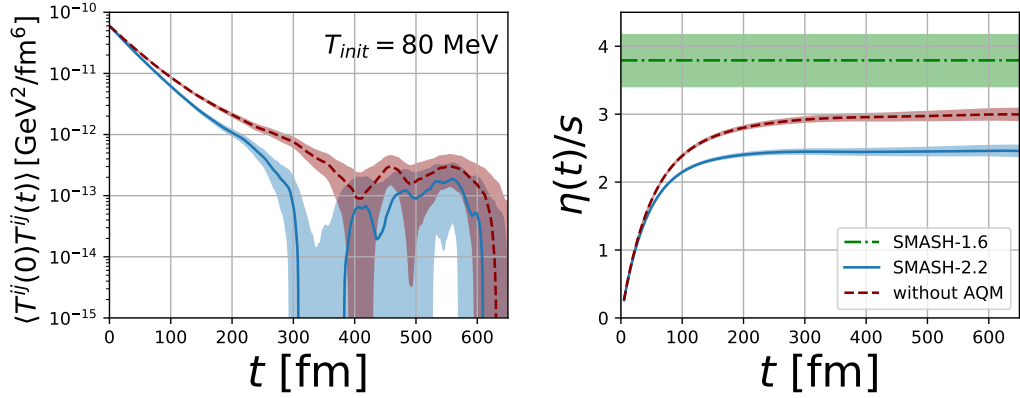
Figure 3.10: Left: Averaged correlation function of the energy-momentum tensor at a temperature of $T = 80\,\mathrm{MeV}$ for SMASH-2.2 (blue) and SMASH-2.2 without AQM cross-sections (red). Right: Dependence of η/s on the upper limit of integration. The green band shows the results of SMASH-1.6.

energy-momentum tensor of the two following systems. The default SMASH-2.2 result and the result of the medium without the AQM cross-sections. The shape of the correlation function differs clearly between the two presented cases. Starting from $t \sim 80\,\mathrm{fm}$ the two curves split and the one without AQM cross-sections is above the one from default SMASH-2.2. It is also worth noting that the two functions do not follow a clear exponential decay at least until $t \sim 300\,\mathrm{MeV}$. As a result, the methodology of integrating the correlation function yields a better result, since it captures the information in the correlation function at these late times. Similar to Eq. 3.62, the dependency on the upper value of the integration is presented on the right-hand side of Fig. 3.10

$$\frac{\eta(t)}{s} = \frac{V}{Ts} \int_0^t \langle T^{ij}(0) T^{ij}(t') \rangle dt' . \tag{3.85}$$

First of all, a convergence of the integral is found and the final value of η/s clearly differs between the two cases. The system that is simulated without the AQM cross-sections saturates at $\eta/s \sim 3$ whereas the SMASH-1.6 case is $\eta/s \sim 3.8$. Within the approximated error of the SMASH-1.6 computation, the difference is still significant. Another contributing factor could be the difference in the methodology used to extract

49

the shear viscosity. The SMASH-1.6 results were obtained using the fitting method which might not capture the full structure encoded in $\langle T^{ij}(0)T^{ij}(t)\rangle$. However, it is not clear at this point where the difference to the SMASH-1.6 result comes from and is left for future studies.
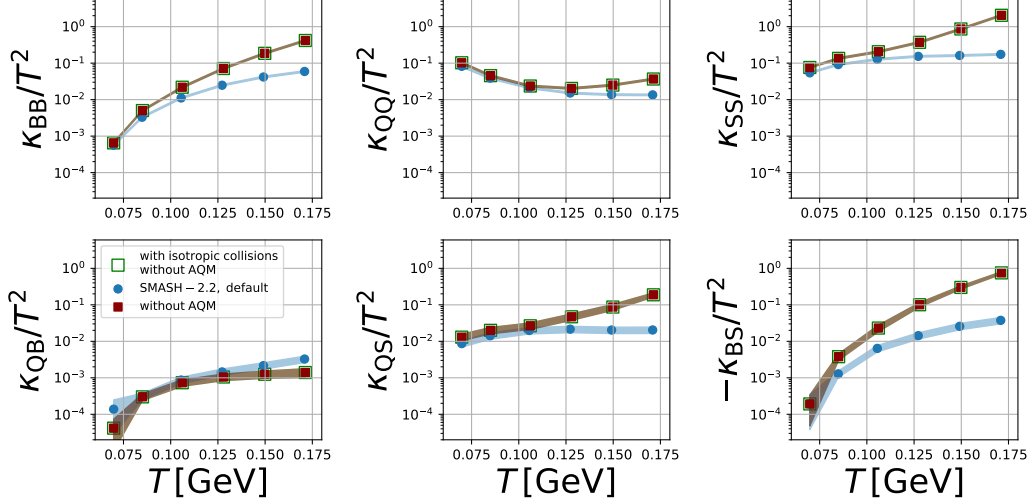

Figure 3.11: Full diffusion coefficient matrix of conserved charges as a function of temperature. The result of the full SMASH collision kernel (blue), the impact of additional elastic cross-sections via the AQM description (red squares) and the influence of isotropic collisions (open green squares) is shown.

Fig. 3.11 shows the full diffusion coefficient matrix of conserved charges from SMASH, which additionally shows the influence of angular distributions and AQM cross-sections. For all diffusion coefficients, except κ_{QQ}, a monotonically increasing behavior as a function of temperature is found. This is a result of an increase in the charge density as more charge carriers become available to the system. In the case of κ_{BB}, the lightest charge carrier is the nucleon, for κ_{SS} the kaon and in the case of κ_{BS} it is the Λ baryon, which carries both baryon and strangeness charge. However, with increasing hadron density the scattering rate increases as well which suppresses the diffusion coefficients.

The additional cross-sections from the AQM model have a strong impact on all diffusion coefficients. At low temperatures where the hadron gas is mostly dominated by the lightest mesons, the inclusion of the AQM cross-section plays no large role. With increasing temperature, however, where the baryonic degrees of freedom start to dominate, the additional elastic cross-section significantly decreases the diffusion coefficients. This originates from the fact that the diffusion coefficients are proportional to the scattering rate and the cross-section $\sim 1/\Gamma_{\text{scat}} \sim 1/(n_{\text{tot}}\sigma_{\text{tot}})$. Therefore with additional cross-sections the coefficients $\kappa_{qq'}$ decrease.

Interestingly and in contrast to the shear viscosity η, non-isotropic distributions have no visible influence on the diffusion coefficient. A possible explanation is that the strength of the anisotropy is simply not large enough.

50

3.6.7 Dependency on degrees of freedom

In the previous section, a detailed investigation of the collision kernel dependency on η and $\kappa_{qq'}$ was performed. In this section, the dependency on the number of degrees of freedom will be determined. To do this, the transport coefficients of three different systems are computed and their values are compared with each other. In Tab. A.1 in App. A.2, the detailed hadronic degrees of freedom and their properties are described as well as their notation in the presented figures.
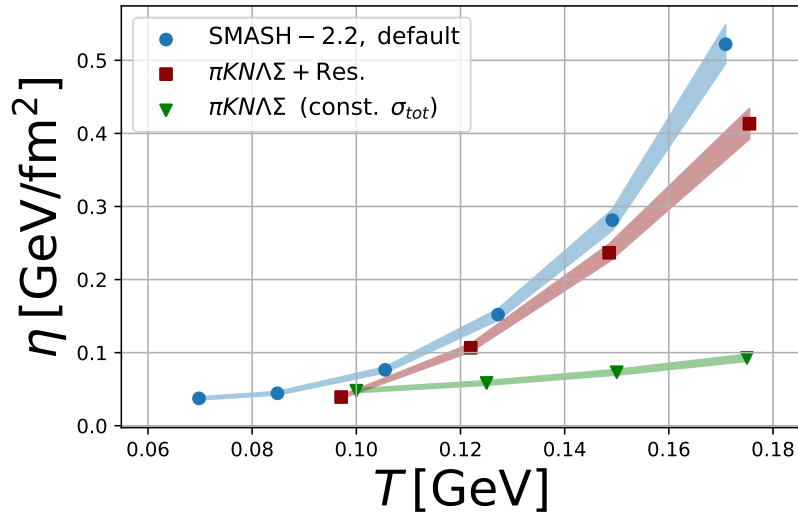
Figure 3.12: Shear viscosity versus temperature. Results of the full SMASH hadron gas (blue), $\pi K N \Lambda \Sigma +$ Res. gas (red) and the elastically interacting $\pi K N \Lambda \Sigma$ (green). For more details, the reader is referred to App. A.2.

Fig. 3.12 shows the dependency of the shear viscosity on the number of degrees of freedom in the system. Here, one can already see a clear difference between system $\pi K N \Lambda \Sigma$ (const.) where the shear viscosity is much smaller for $T > 100\,\text{MeV}$ in comparison to the other two systems. Around $T \sim 100\,\text{MeV}$, the value of η of the three systems approximately converge. The shear viscosity of the SMASH-2.2 hadron gas and the subset $\pi K N \Lambda \Sigma +$ Res. have similar values and a similar shape, even though η of the latter is a bit smaller. The small difference in shear viscosity between the systems can be understood as follows. As more heavy baryonic resonances are present in the SMASH-2.2 hadron gas in comparison to the $\pi K N \Lambda \Sigma +$ Res gas, their lifetimes become important effectively increasing η, as it was shown in [103]. In the temperature region $T < 100\,\text{MeV}$ where the medium is dominated by mesonic interactions, the purely elastically interacting hadron gas with $\sigma_{\text{elastic}} = 30\,\text{mb}$ seems to be a good approximation of the full SMASH hadron gas.

The influence of varying degrees of freedom on the diffusion coefficient matrix κ_{ij} is presented in Fig. 3.13. Similar to the shear viscosity, it is found that the κ_{ij} strongly differs between $\pi K N \Lambda \Sigma$ (const.) and the other two more complex hadron gases. The difference however between $\pi K N \Lambda \Sigma$ (+Res.) and the SMASH-2.2 gas
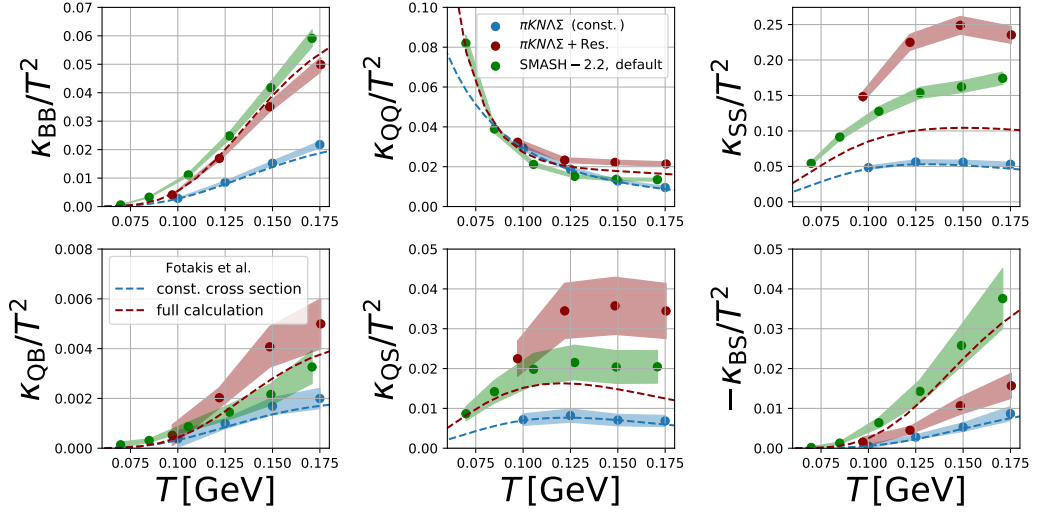
Figure 3.13: Diffusion coefficient matrix as a function of temperature. Results of the full SMASH hadron gas (blue), $\pi K N \Lambda \Sigma$ + Res. gas (red) and the elastically interacting $\pi K N \Lambda \Sigma$ (green). The dotted lines show results from [111]. For more details, see App. A.2.

needs closer inspection. Similar to the elastic pion gas, the comparison between the CE calculation of the $\pi K N \Lambda \Sigma$ (const.) gas and the Green-Kubo results are shown. Within the errors, excellent agreement between the two calculations is found, again verifying the methodology of this work.

As the $\pi K N \Lambda \Sigma$ + Res gas is similar in its degrees of freedom with respect to the one used in [111], a comparison between the two is interesting since the impact of resonance formation processes becomes visible. Whereas the comparison between the CE and the Green-Kubo calculation is consistent between κ_{BB} and κ_{QQ}, the other κ_{SS} and the cross-diffusion coefficients differ strongly. The results from SMASH of $\kappa_{QB,QS,SS}$ overshoot the CE results, hinting that either the relaxation time or the charge density is larger in SMASH. For $-\kappa_{BS}$, the opposite behavior is observed, meaning the relaxation time or the density in the CE calculation is over-predicted.

In [107], where the electric charged sector of the diffusion coefficient matrix was presented, the dependency on the degrees of freedom was much clearer. A clear hierarchy was observed where the diffusion coefficients decreased with increasing numbers of degrees of freedom. Here, the more baryons and mesons are in the medium the larger the cross-sections are in SMASH, the scattering rate increases and the diffusion coefficients decrease as they are proportional to $\sim 1/\Gamma_{\text{scat.}}$. This behavior is reproduced in the present calculations for the electrically charged sector and the strange diffusion coefficient. However, in the case of κ_{BB} and $-\kappa_{BS}$ the opposite behavior is observed, that the diffusion coefficients increase with more degrees of freedom. Here, the statement that more hadrons lead to larger cross-sections is also true, but $\kappa_{qq'}$ also depends on the total charge density n_{tot} (see the interpretation in the RTA of Eq. 3.39). For the two coefficients in the baryonic sector, the charge

density counteracts the reduction of the relaxation time and as a result, the diffusion coefficient increases.

Unfortunately, the statement made in [107] cannot directly be made for the full diffusion coefficient matrix since the dependencies are seemingly more complex in the baryonic sector.

3.6.8 Finite value of chemical potential

In the last section, the dependency of the transport coefficients on the value of the baryon chemical potential μ_B is investigated. This is of course of interest as heavy-ion collisions not only probe regions of $\mu_B = 0$ at the highest collision energies but also regions of finite $\mu_B > 0$ at smaller collisional energy. For example, at fixed target experiments at $E_{\text{kin}} = 1.58\,A\,\text{GeV}$ at HADES, a value of $\mu_B \sim 900\,\text{MeV}$ is reached [100]. In a heavy-ion collision, it is thought that the global strange chemical potential is zero throughout the collision as there are no strange particles in the colliding nuclei. Even though on the local scale this is not always true [111]. In addition, the isospin 3 chemical potential can also be approximated as $\mu_{I_3} = 0$.

To mimic these conditions, the medium is not only initialized with a finite μ_B but also such that the effective strange and isospin 3 chemical potentials are zero. The effective chemical potential is the resulting, e.g. strangeness imbalance in the case of a non-zero μ_B. It is calculated via

$$\mu_q^{\text{eff.}} = \frac{T}{2}\log\frac{\sum_{i=1}^{N_{\text{species}}^q} n_i(T,\mu_k)}{\sum_{i=1}^{N_{\text{species}}^{\bar{q}}} n_i(T,\mu_k)}\,. \tag{3.86}$$

Here, $n_k(T,\mu_k)$ is the density of particle k (see Eq. 3.40). The upper sum runs over all particles given charge q and the lower sum over all particles given the opposite charge $\bar{q}$. The values of $\mu_{B,Q,S}$ are then obtained by solving the following three equations

$$\mu_B^{\text{eff.}}(T,\mu_{B,Q,S}) = \mu_B\,, \tag{3.87}$$

$$\mu_S^{\text{eff.}}(T,\mu_{B,Q,S}) = 0\,, \tag{3.88}$$

$$\mu_{I_3}^{\text{eff.}}(T,\mu_{B,Q,S}) = 0\,. \tag{3.89}$$

Fig. 3.14 shows the dependence of the shear viscosity, the entropy density and enthalpy on the baryon chemical potential. In order to eliminate the effects of the chemical potential on the ratio η/s, often the ratio to the enthalpy $\eta T/w$ is presented. The shear viscosity η alone shows no influence on increasing μ_B contrary to the results of version SMASH-1.6. Here, again the AQM cross-sections are the relevant factor as they increase the scattering rate in the baryon-dense regions where previously cross-sections between exotic baryons were missing. As a result of the shear viscosity not affected by μ_B, all changes on the level of the ratio η/s or $\eta w/T$ originate from the thermodynamic potentials. As for $\mu_B = 0$, the value of η/s differs largely between the versions SMASH-1.6 and 2.2. Again starting at $T \gtrsim 110\,\text{MeV}$ the transport coefficient decreases by approximately a factor of 2 for $\mu_B = 0$ and
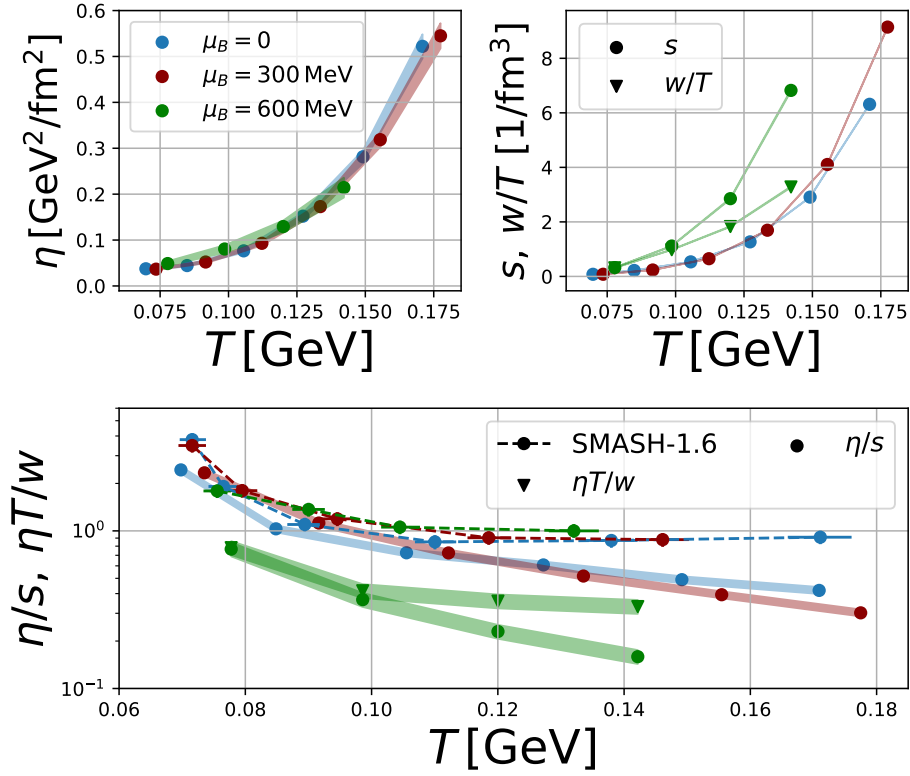
Figure 3.14: Shear viscosity η (upper left), entropy density (circles) and enthalpy (triangles) (upper right) and shear viscosity over entropy density (circles) or entropy density over enthalpy (triangles) (bottom) versus temperature. Results of $\mu_B = 0$ (blue) $\mu_B = 300\,\text{MeV}$ (red) and $\mu_B = 600\,\text{MeV}$ (green) are presented.

$\mu_B = 300\,\text{MeV}$. The largest difference, however, is the shear viscosity at a baryon chemical potential of $\mu_B = 600\,\text{MeV}$. Due to the increased entropy density and enthalpy of the system, both η/s and $\eta T/w$ are drastically reduced, also in contrast to SMASH-1.6. There, a counteracting effect is observed that both η and s increased and as a result the ratio η/s stays constant. The influence of the charge chemical potentials on the entropy density via $\sum_{x=\{B,Q,S\}} \mu_x n_x$ on the ratio η/s is contained in the triangles. At $T \sim 140\,\text{MeV}$ the ratio η/s is reduced by an additional factor.

Now coming to the baryon chemical potential dependence of the full diffusion matrix, which is depicted in Fig. 3.15. In contrast to shear viscosity η, a strong dependency of the whole $\kappa_{qq'}$ matrix on μ_B is found and additionally, the results from SMASH are compared to the CE from [111]. Note that a simplified version of the hadron gas is used there. First of all, the general shape and the orders of magnitude coincide between the two calculations which is a sign that they describe similar systems and are robust in terms of their general behavior. When it comes to the exact values of $\kappa_{qq'}$, it is found that the details of both calculations play a large role. As the degrees of freedom and the description of interactions like resonance
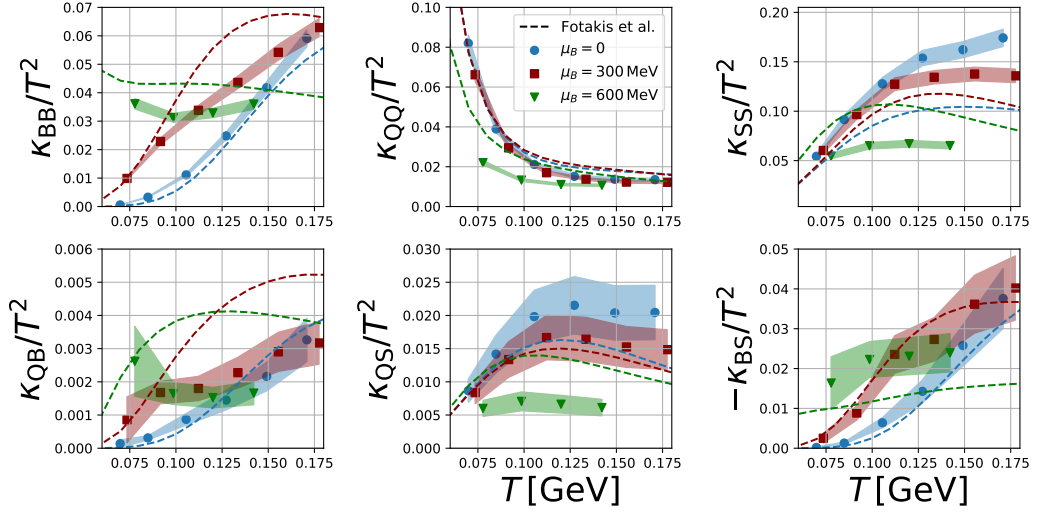
Figure 3.15: Diffusion coefficient matrix as a function of temperature. Results of GK (symbols) and CE (dashed line) are shown for $\mu_B = 0$ (blue) $\mu_B = 300\,\text{MeV}$ (red) and $\mu_B = 600\,\text{MeV}$.

formation etc. are very different, it is also expected that the curves don't coincide with each other exactly. This comparison shows that the diffusion coefficients are a good quantity when it comes to comparisons with first principle calculations, but it is also difficult as it depends on counteracting quantities like the relaxation time and (total and net) charge densities. No clear trend of $\kappa_{qq'}$ when going from 0 to $\mu_B = 300\,\text{MeV}$ is found. The diffusion coefficients of the baryonic sector κ_{BB}, κ_{QB} and $-\kappa_{BS}$ increase, which can also be seen in the CE calculations. The strangeness and electric charge coefficients in contrast show a decreasing behavior. It is found that for the highest value of $\mu_B = 600\,\text{MeV}$, the diffusion coefficients seem to behave approximately as $\kappa_{ij} \sim T^2$ and as a result, the ratio κ_{ij}/T^2 flattens as a function of temperature. A similar trend can be observed in the CE calculations. A possible explanation is the second term of the diffusion coefficients in the RTA Eq. 3.39, which is proportional to the total charge density and at a non-zero chemical potential, this term becomes important and decreases the diffusion coefficient.

This study now opens the possibility for more precise modeling of heavy-ion collisions, especially at low collisional energies using a hydrodynamical description. In the last step, the previously obtained transport coefficients will be compared to other calculations.

3.6.9 Comparison to other calculations

In this section, the previously obtained results of the shear viscosity will be discussed in the context of other calculations of η/s.

Fig. 3.16 compares various calculations of η/s in the cross-over region of QCD at zero μ_B. First, the difference between the two SMASH versions was already discussed
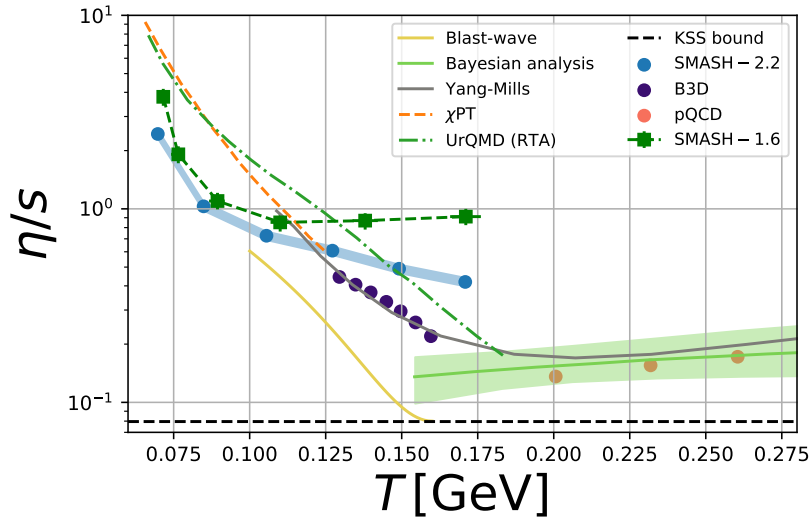
55

Figure 3.16: Comparison of the shear viscosity over entropy density of SMASH (blue) with various different calculations. Extraction from a blast-wave model (yellow line) [141], Bayesian analysis [138], Yang-Mills (grey line) [167], B3D (blue circles) [168], pQCD (orange circles) [169] and the KSS bound (black dashed line) [125]. Chiral perturbation theory (orange dashed) [132] and RTA using UrQMD cross sections (green dashed-dotted) [170].

in a previous section. The present result compares better with other computations since the value of η/s is smaller and does not show the plateau behavior at large temperatures. However, its value is still larger compared to the extraction from Bayesian analysis [138] or from a pure Yang-Mills calculation [167]. This is not surprising as different interactions start to matter in these temperature regions, which are not captured by the calculations presented here. It is expected that with the incorporation of multi-particle reactions the shear viscosity further decreases as was already shown in a quantitative way. In addition, hard QCD processes from the string model cannot be used in the infinite matter simulations as they break detailed balance. Their inclusion would further decrease η as the phase space opens up in these $2 \rightarrow n$ reactions. Chiral perturbation theory is an effective theory of low-energy QCD. Its applicability is in the temperature region where the dynamics are mainly dominated by pions. The resulting shear viscosity is in the same order of magnitude but generally larger than the SMASH results due to larger cross-sections in the region where resonances become important. Interestingly, the value of η/s from the Blast-wave model [141] reaches the lowest value in the hadronic regime.

A comparison between the diffusion coefficient matrix of conserved charges and the result of various other approaches is presented in Fig. 3.17. The results in the electric charged sector between this work and the calculation performed in [107] coincide with each other and the CE in the hadronic regime from [111] was already discussed in previous sections. The comparison to the CE calculation using the
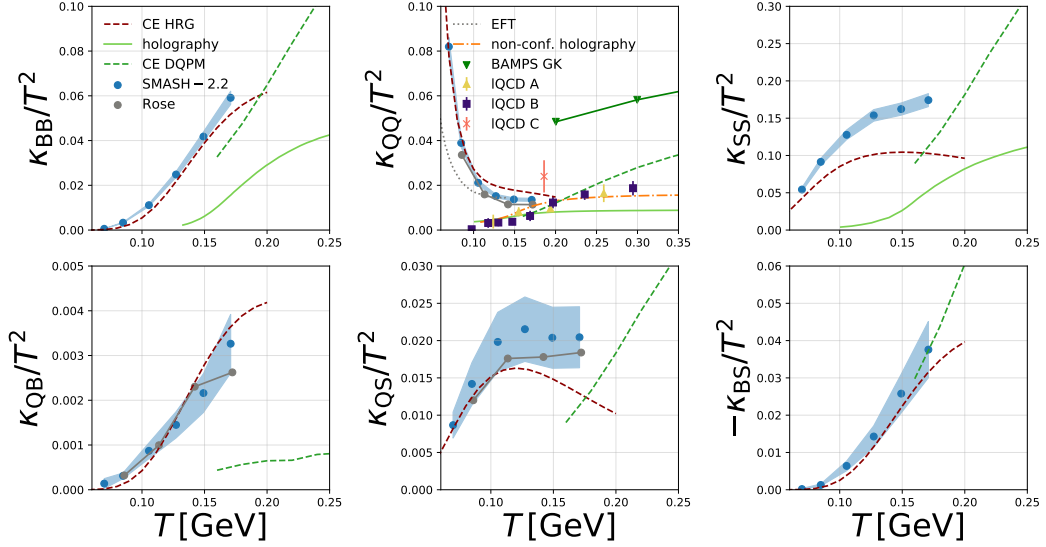
Figure 3.17: Diffusion coefficient matrix as a function of temperature at vanishing baryon chemical potential from different calculations. The results of SMASH (blue) and previous calculation from SMASH (grey circles) are shown [107]. The partonic cascade calculation BAMPS is shown as green triangles [171]. CE calculation in the hadronic phase [110, 111] (red line). CE computation in the partonic phase (DQPM) (green dashed line) [112]. Chiral effective field theory (grey dotted line) [132]. Lattice QCD in $N_f = 2$ (lQCD A: yellow triangle) [172], lattice QCD in $N_f = 2 + 1$ (lQCD B: blue squares) [173], quenched lattice (lQCD C: orange cross) [174]. Conformal holographic (green line) [175] and non-conformal holographic calculation (dashed dotted orange line) [176].

DQPM cross sections [112] yields a great opportunity to compare the full $\kappa_{qq'}$ matrix to results from the partonic sector. Close to the pseudo-critical temperature T_c the electric charge diffusion coefficient is consistent with lattice QCD calculations, holographic models, or the CE DQPM calculation. With decreasing temperature and below T_c the transport coefficient rapidly increases whereas the value of κ_{QQ}/T^2 from lQCD, holographic, or DQPM approximately goes to zero. The electric charge cross terms κ_{QB}/T^2 and κ_{QS}/T^2 from SMASH and HRG CE are larger than the CE calculation using the DQPM model. A possible explanation could be the different chemical compositions that have been pointed to be important in [107]. A similar discrepancy, yet not as strong can also be found for the diagonal baryonic and strange diffusion coefficient, whereas κ_{BS}/T^2 matches very well.

3.6.10 Summary

In this chapter, the interacting hadronic medium was established by studying the transport coefficients η and $\kappa_{qq'}$. By subsequently increasing the complexity of the hadron gas in terms of the number of degrees of freedom and their interactions, a

good understanding of the behavior of the transport coefficients could be established. The influence of multi-particle reactions, additional cross-sections, the number of degrees of freedom and the baryon chemical potential were computed. Using a new technique to extract the transport coefficients by integrating the corresponding correlation functions enables one to capture more information in their tails. It has been shown that multi-particle reactions reduce the shear viscosity in a simplified hadron gas at $T \gtrsim 130\,\mathrm{MeV}$ whereas the electric charge diffusion coefficient shows no modification. Continuing with the full SMASH hadron gas, it has been found that the AQM cross-sections strongly decrease both η and $\kappa_{qq'}$. Additionally, the inclusion of angular distributions enhances the shear viscosity but no influence on κ_{ij} is found. On the other hand, varying the number of degrees of freedom leaves the shear viscosity relatively unaffected until the cross-over region $T \approx 150\,\mathrm{MeV}$, in contrast to the diffusion coefficient matrix. Here it is found that the scaling behavior that has been observed for the electric charge sector does not hold in the baryonic sector and both the density and the cross sections become the relevant factors. Contrary to previous findings, there is no dependency of η on μ_B leaving the dependency of the ratio η/s and $\eta T/w$ fully on the thermodynamic properties of the medium. Finally, the $\kappa_{qq'}/T^2$ matrix has a strong μ_B dependence with the tendency of evolving a plateau behavior at $\mu_B \approx 600\,\mathrm{MeV}$. The comparison of the shear viscosity and diffusion coefficient matrix at vanishing baryon chemical potential with other calculations shows that the here-established hadronic medium and its interactions are consistent with other models.

After the hadron gas has been established using the fluctuation-dissipation theorem of the conserved charge currents $\mathbf{J}_q(t)$ the next chapter is dedicated to studying fluctuations of the conserved charges at equal times by calculating correlations in the form of cumulants of particle numbers.

4

Fluctuations of conserved charges from the hadron gas

So far the interacting hadronic medium of SMASH has been introduced and its equilibrium properties investigated by studying the diffusion coefficients of conserved charges and the shear viscosity. In this chapter, equal time correlations of particle numbers, namely cumulants are the main target of interest and the influence of hadronic interactions will be studied within two projects. The first project is a study regarding the influence of hadronic interactions on cumulants of conserved charges in a system with global charge conservation, which is based on [1]. The second project investigates the evolution of critical equilibrium fluctuations in SMASH and is based on [4]. In the first part of this chapter, some basic definitions of fluctuations are introduced, as well as the hadron-resonance gas (HRG) model. Then, the results are presented in the following sections.

4.1   The definition of fluctuations

The starting point for defining fluctuations or cumulants is the probability distribution $P(X)$ of some random variable X. It describes the probability of the outcome of the variable X when an experiment is performed multiple times. For example, in the case of a dice with 6 sides the probability distribution for one side X_i is $P(X_i) = 1/6$. A more formal definition of fluctuations can be given in terms of cumulants. Cumulants describe properties of the probability distribution function $P(X)$ and e.g. the first two cumulants are the mean and the variance. The third and fourth cumulants are called skewness and kurtosis and describe whether the distribution is asymmetric or the behavior of the tails. A useful starting point is the definition of the moment-generating function $M(t)$, which is the expectation value of e^{tx} given $P(x)$. For a

continuous random variable X, one can write

$$M(t) = E[e^{tx}] = \int_{-\infty}^{\infty} e^{tx} P(x) dx \,. \tag{4.1}$$

The cumulant-generating function $K(t)$ is related to the moment-generating function simply by taking the natural logarithm

$$K(t) = \ln M(t) \tag{4.2}$$

It is also useful to note that the cumulant-generating function can be written in terms of an infinite sum of the cumulants κ_n of P

$$K(t) = \sum_{n=1}^{\infty} \kappa_n \frac{t^n}{n!} \,. \tag{4.3}$$

Once the cumulant-generating function is known, the n-th cumulant can be calculated by taking the n-th derivative at $t = 0$ of $K(t)$

$$\kappa_n = \left. \frac{d^n K(t)}{dt^n} \right|_{t=0} \,. \tag{4.4}$$

The main reason why the cumulants are beneficial is their cumulative properties. From Eq. 4.2 one can see that for two independent random variables X_1 and X_2 one obtains

$$K_{X_1+X_2}(t) = \log E\left[e^{t(X_1+X_2)}\right] = \log E\left[e^{tX_1} e^{tX_2}\right] = K_{X_1}(t) + K_{X_2}(t) \,. \tag{4.5}$$

This is generally not the case for the moments of P. Another quantity that is related to the moments and cumulants are the central moments and they are defined as the expectation value around the mean μ of P

$$\mu_n = E[(X - E[X])^n] = \int_{-\infty}^{\infty} (x - \mu)^n P(x) dx \,. \tag{4.6}$$

With the expectation value $\mu = E[X]$. Later in this work, the expectation operator will be written as $E[X] = \langle X \rangle$[1]. It is also useful to relate the central moments to the cumulants via

$$\kappa_1 = \mu \,, \tag{4.7}$$
$$\kappa_2 = \mu_2 \,, \tag{4.8}$$
$$\kappa_3 = \mu_3 \,, \tag{4.9}$$
$$\kappa_4 = \mu_4 - 3\mu_2^2 \,, \tag{4.10}$$
$$\kappa_n(n > 3) = \mu_n - \sum_{m=2}^{n-2} \binom{n-1}{m-1} \kappa_m \mu_{n-m} \,. \tag{4.11}$$

---

[1]In the following sections often the notation $\langle (\delta N)^n \rangle$ with $\delta N = N - \langle N \rangle$ is used instead of μ_n.

So far, the cumulants have been derived from a probability distribution that is assumed to be known. However, the reverse is also possible, where an experiment has been conducted and the outcome of the experiment $\{X_1, ..., X_N\}$ is measured. The question then might be what are the properties of the probability distribution, that generated the outcome of the experiment? In reverse, one can measure the central moments of the sample $\{X_1, ..., X_N\}$ to obtain knowledge about the underlying distribution $P(X)$

$$\mu_n = \frac{1}{N} \sum_{i=1}^{N} (X_i - \langle X \rangle)^n \,, \text{ with } \langle X \rangle = \frac{1}{N} \sum_{i=1}^{N} X_i \,. \tag{4.12}$$

The cumulants can then be calculated from Eq. 4.7-4.11. Especially the higher-order cumulants take large statistics in the sense that they need large amounts of events, in order to be determined with a high precision. The errors of the cumulants are calculated from the formulas derived in [177].
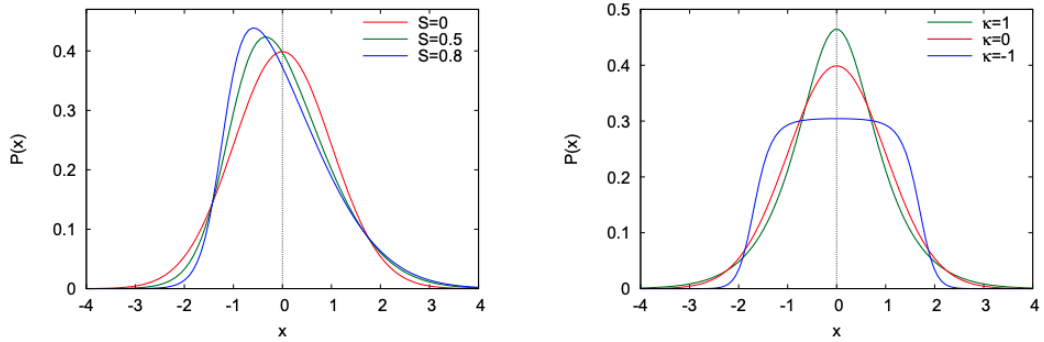

Figure 4.1: Effect of the skewness and kurtosis on an exemplary distribution. The figure is taken from [178].

A visual representation of the effects of a non-zero skewness S and kurtosis κ in comparison to a Gaussian distribution is presented in Fig. 4.1. The Gaussian distribution has a variance σ and $S = \kappa = 0$, meaning it can be seen as a baseline distribution when skewness and kurtosis are used. The influence of a non-zero skewness is shown on the left-hand side of Fig. 4.1. One can see that for an increasing value of S, the asymmetry of the distribution increases and it gets tilted towards one side. For $S < 0$ the distribution would be tilted towards the other side. The kurtosis describes the "sharpness" of the distribution which means that it either appears more flattened or more peaked compared to the Gaussian.

After the fluctuations in terms of cumulants have been introduced, the relation to theory describing the thermodynamics of conserved charges will be explained in the following. A thermal system with some given temperature T in a volume V can be described by its partition function $\mathcal{Z}$ and the thermodynamic pressure P is then related to $\mathcal{Z}$ via

$$\frac{P}{T^4} = \frac{1}{VT^3} \ln \mathcal{Z}(T, V, \mu_B, \mu_Q, \mu_S) \,. \tag{4.13}$$

Where $\mu_{B,Q,S}$ are the chemical potentials of the baryon, electric and strange charge respectively. The dynamics of the system is described within the partition function $\mathcal{Z}$ and can be e.g. calculated from first principle lattice QCD [179]. From here, one can define the susceptibility of a conserved charge χ_n^q as the n-th derivative of the adimensional pressure P/T^4 with respect to the chemical potential of charge q over the temperature $\hat{\mu}_q \equiv \mu_q/T$

$$\chi_n^q \equiv \frac{1}{VT^3} \frac{\partial^n \ln \mathcal{Z}}{\partial \hat{\mu}_q^n} \, . \tag{4.14}$$

One can show that the susceptibilities are related to the cumulants of the particle number associated with the charge q via $\kappa_q^n = VT^3 \chi_q^n$, which is presented in Appendix A.3. As a result, and similar to the expression above, one can write

$$\kappa_n^q = \frac{1}{VT^3} \frac{\partial^n \ln \mathcal{Z}(T, V, \mu_q)}{\partial (\mu_q/T)^n} \, . \tag{4.15}$$

When comparing the expression of Eq. 4.4 to the equation above, one can clearly see that the logarithm of the partition function acts as the cumulant generating function of the physical system described by the partition function $\mathcal{Z}$. This enables one to compare experimental measurements of cumulants of some particle distribution in the statistical sense via Eq. 4.12, to the cumulants of a physical theory via Eq. 4.15. In order to cancel possible dependencies of the volume and the temperature, usually ratios of cumulants are presented. The standard ones are the skewness and kurtosis

$$S_q = \frac{\kappa_3^q}{(\kappa_2^q)^{3/2}} \, , \quad \kappa_q = \frac{\kappa_4^q}{(\kappa_2^q)^2} \, . \tag{4.16}$$

Finally, the widely used observables that will be mostly used in this work are

$$\sigma/M = \frac{\kappa_2^q}{\kappa_1^q} \, , \quad S_q \sigma_q = \frac{\kappa_3^q}{\kappa_2^q} \, , \quad \kappa_q \sigma_q^2 = \frac{\kappa_4^q}{\kappa_2^q} \, . \tag{4.17}$$

4.2 The hadron resonance gas model

A simple model that has been successfully used to describe statistical observables in heavy-ion collisions is the (ideal) hadron resonance gas (HRG) model. It describes each hadron as an independent, non-interacting particle. In accordance with the previously described derivation of fluctuations in thermodynamic systems, the partition function of the HRG can be written in the following way

$$\begin{aligned} \frac{P}{T^4} &= \frac{V}{T^3} \ln \mathcal{Z}(T, V, \mu_B, \mu_Q, \mu_S) \\ &= \frac{1}{\pi^2} \sum_{i \in X} g_i \left(\frac{m_i}{T}\right)^2 K_2 \left(\frac{m_i}{T}\right) \cosh \left(\frac{\mu_B B_i + \mu_Q Q_i + \mu_S S_i}{T}\right) \end{aligned} \tag{4.18}$$

One can also start from the previously defined Juettner distribution Eq. 3.32 which describes the density of some state in a phase space cell. The density of this state

is an invariant scalar and one can derive it in the local rest frame of the fluid $u^\mu = (1, 0, 0, 0)$

$$n_i = N_i^\mu u_\mu = u_\mu \int \frac{d^3 k}{k^0} p^\mu f_{i,k}^{(0)} = \frac{e^{\mu_i/T}}{(2\pi)^3} \int d^3 k \frac{1}{e^{E_{i,k}/T} \mp 1} \,. \tag{4.19}$$

By omitting the $\mp$ sign, the Boltzmann statistic is approximated and the integral simply becomes

$$n_i(T, \mu_i) = \frac{e^{\mu_i/T}}{2\pi^2} m^2 T \, K_2(m_i/T) \,. \tag{4.20}$$

with K_2 being the modified Bessel function of the second kind.

The fluctuations κ_n of the particle number distribution originating from the thermal heat bath can also be calculated by taking higher order derivatives of n_i/T with respect to (μ_i/T) at a constant temperature and given a fixed volume V

$$\kappa_{n,i} = V T^3 \left. \frac{\partial^{n-1}(n_i/T^3)}{\partial(\mu_i/T)^{n-1}} \right|_T \,. \tag{4.21}$$

When plugging Eq. 4.20 into Eq. 4.21, the cumulants of all order are equivalent

$$\kappa_{n,i} = \kappa_{1,i} \quad \forall \, n > 1 \,. \tag{4.22}$$

The only probability distribution that satisfies Eq. 4.22 is the Poisson distribution defined as

$$P_\mu(N) = \frac{\mu^N}{N!} e^{-\mu} \tag{4.23}$$

with μ being the mean of the distribution.

Eq. 4.21 defines the cumulants in the grand canonical ensemble (GCE) where the particles are freely generated by a heat bath T. In contrast, the situation where the total number of particles is fixed is the canonical ensemble (CE).

Until now, the cumulants of only one particle species i were considered. The interesting quantity in the context of QCD are the conserved charge numbers. Within the HRG model, the fluctuations are easily obtained since the model itself describes a non-interacting and independent system of particles. In addition, because the sum of two independent Poisson distributed quantities is equal to a Poisson distribution, the total charge distribution is therefore also of Poisson nature. The difference between two independent Poisson distributed quantities is called Skellam distribution and it is defined as

$$P(k, \mu_1, \mu_2) = e^{-(\mu_1 + \mu_2)} \left(\frac{\mu_1}{\mu_2} \right)^{k/2} I_k(2\sqrt{\mu_1 \mu_2}) \,. \tag{4.24}$$

Here, I_k is the modified Bessel function of the first kind. The cumulants of the net and total particle numbers are

$$\kappa_{i,n}^{\text{net}} = \kappa_{i,n} + (-1)^n \kappa_{\bar{i},n} \tag{4.25}$$

$$\kappa_{i,n}^{\text{tot}} = \kappa_{i,n} + \kappa_{\bar{i},n} \,. \tag{4.26}$$

Where $\bar{i}$ is the respective anti-particle of i.

Besides fluctuations, it is also possible to calculate thermodynamic properties such as the energy density or the pressure from the HRG model and compare them to results from lattice QCD. The HRG EoS is computed in the grand-canonical ensemble from the following equations

$$n_{q=B,Q,S} = \frac{T^3}{2\pi^2} \sum_h g_h q_{X,h} \exp\left(\frac{\mu_h}{T}\right)\left(\frac{m_h}{T}\right) K_2\left(\frac{m_h}{T}\right), \tag{4.27}$$

$$e = \frac{T^4}{2\pi^2} \sum_h g_h \exp\left(\frac{\mu_h}{T}\right)\left(\frac{m_h}{T}\right)\left(3K_2\left(\frac{m_h}{T}\right) + \left(\frac{m_h}{T}\right) K_1\left(\frac{m_h}{T}\right)\right), \tag{4.28}$$

$$p = T \sum_h n_h. \tag{4.29}$$

Here, the sum runs over all hadrons in the system and $\mu_h = \sum_{i=B,Q,S} \mu_i Q_{i,h}$. The pressure is computed by summing over all hadron densities (Eq. 4.27 without $q_{X,h}$). Fig. 4.2 shows a comparison of the QCD EoS from first-principle lattice QCD
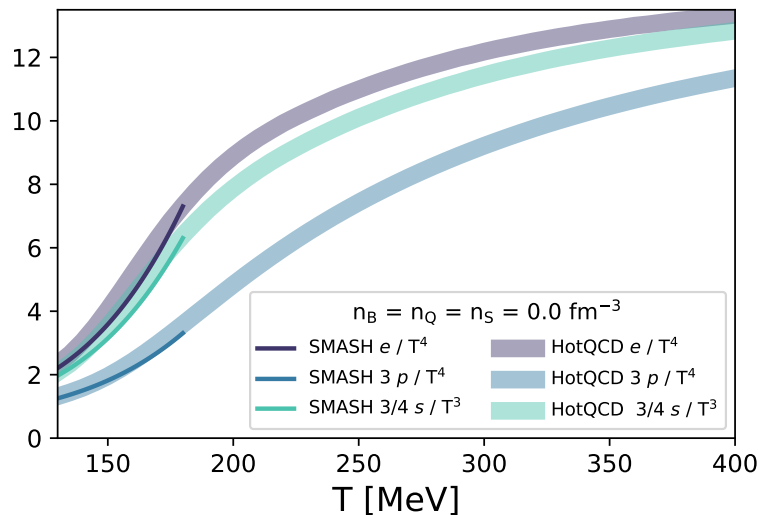

Figure 4.2: Comparison of the energy density (purple), the pressure (green) and the entropy density (blue) between the SMASH HRG EoS to Lattice QCD calculation from the HotQCD collaboration [180]. The figure is taken from [181].

calculations to the SMASH hadron gas EoS. One can see that the lattice results are well reproduced below $T \lesssim 170\,\mathrm{MeV}$. This is expected as the ideal HRG is known to known to be consistent with the lattice EoS roughly below the cross-over transition $T_{c,0} = 155\,\mathrm{MeV}$. In these temperature regimes, hadrons are the degrees of freedom. In [7], a calculation has been performed comparing the charged susceptibilities from the HRG to lattice QCD calculations. The calculation in the HRG model uses different particle lists, one of which is the current one of SMASH. It shows, how adding more confirmed states changes the susceptibilities. An overall agreement between the SMASH particle list and lattice calculations below T_c is found.

Because the Poisson distribution is found to be the basis and it approximately reproduces thermodynamic quantities from QCD it is also assumed that the Poisson distribution is the baseline of measurements of fluctuations in HIC.

4.3 Impact of conservation effects on cumulants

Motivation for the study of hadronic interactions on exact charge conservation

The first study in this section is about the effects of global charge conservation and the influence of hadronic interactions on cumulants of the net baryon number. The results are based on [1, 2]. The motivation for this study is the finding that in a heavy-ion collision, the created medium emits the particles not according to the grand-canonical ensemble, but according to the canonical ensemble since the initial number of charges are fixed by the colliding nuclei. The fluctuations from the created medium are then suppressed in the limit of the full phase space. To circumvent this problem in the experimental measurement, the fluctuations are measured in a small rapidity window $|y| < 0.5$. The hope is that by decreasing the rapidity window, the medium can exchange its charges with its surroundings and the fluctuations converge to the grand-canonical picture [182]. However, if the rapidity window is smaller than the size of the correlation length y_{corr} of the medium, the measurement does not capture the relevant physics which is also known as the "Poissonian limit".

The relevant question for this study is how the hadronic phase of the heavy-ion collision changes the fluctuations within a system with global charge conservation. There exist previous studies that have investigated the effects of global charge conservation on fluctuations of conserved charges which will be briefly summarized. In [183], analytic expressions of cumulants up to sixth order were derived as a function of the size of the subvolumes. In [184], a direct relation between the grand-canonical susceptibilities of any theory and the fluctuations of a conserved charge in subvolumes of that theory has been derived. However, in these calculations ([183, 184]), no dynamical effects are accessible. Within [185], a baseline calculation of fluctuations including conservation laws as a function of beam energy has been provided employing the hadronic transport approach UrQMD. Recently, a model including critical dynamics has been used to study the scaled variance [186]. Here, the study performed in [187] will be the starting point, in which the effect of global net charge conservation was studied in a simplified interacting hadronic gas. The goal will be to reproduce the results of [187] and extend this calculation towards the baryonic sector. With the knowledge of the previously defined model, various different effects like baryon-annihilation processes or deuteron formation can be studied. Another important aspect is the relation between the net baryon and the net proton number. The primary motivation is the study of fluctuations of a conserved charge, hence the net baryon number. However, not all produced baryons can be measured in the experiment, which is why the net proton number is used as a proxy of the net baryon fluctuation. In this study, this particular relation can be directly verified as the transport approach gives access to the full phase space information.

This study is performed within an infinite matter simulation, which was already introduced in Chapter 3. In this way, the effect of the hadronic interaction can be isolated and other dynamical effects do not contribute. By performing the calculation at different chemical potentials and temperatures, their dependency on the influence of exact charge conservation can be studied as well.

4.3.1 Study of charge conservation effects in SMASH

The goal of this section is to extract fluctuations from a system that conserves the charges $\{B, Q, S\}$ globally. To do this, a box with periodic boundary conditions is used, similar to Chapter 3. The fluctuations are studied depending on subvolumes of size $x = (V/V_0)$ within that system. It is worth noting that the subvolume in this calculation is taken in coordinate space whereas measurements of fluctuations are taken in momentum space. It has been argued in previous studies, see e.g. [184], that correlations between coordinate and momentum space exist, especially at the highest beam energies. This is due to the Bjorken-type expansion of the fluid which correlates the longitudinal momenta of the particles with the coordinate of the beam direction. One can also interpret the size of the subvolume as the number of accepted particles over the total amount of measured particles

$$x = \frac{V}{V_0} = \frac{\langle N_{\mathrm{acc}} \rangle}{\langle N_{\mathrm{full}} \rangle} \,. \tag{4.30}$$

A key premise for the study itself is that the hadronic density in the system is distributed isotropically. If this is not the case, the result of the fluctuations would depend on the definition of the subvolume. Fig. 4.3 shows the normalized density
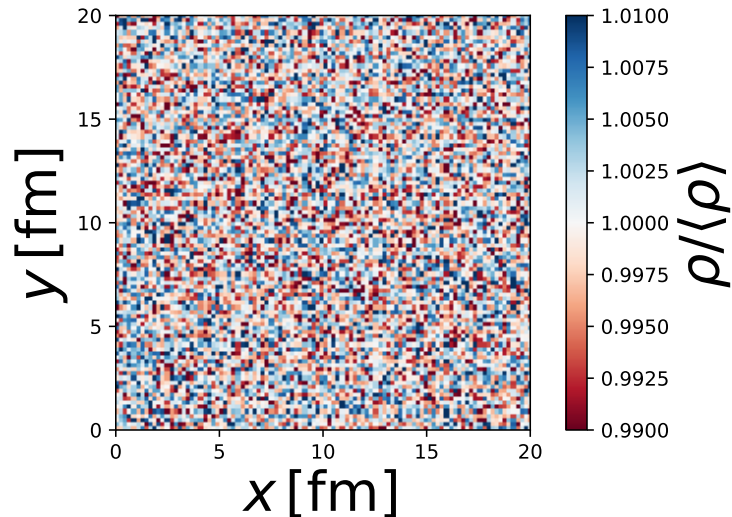

Figure 4.3: Normalized density of the SMASH hadron gas system in the xy-plane. The mean value of the density is $\langle \rho \rangle = 0.253\,1/\mathrm{fm}^3$.

$\rho/\langle \rho \rangle$. The density ρ is computed by averaging each cell in the system over many

events and $\langle\rho\rangle$ is the spatial averaged value of ρ. The system contains the full list of hadrons provided by SMASH. This result shows that the density is distributed homogeneously inside the box and fluctuations appear on the order of $\sim 1\%$ which are distributed equally as well.
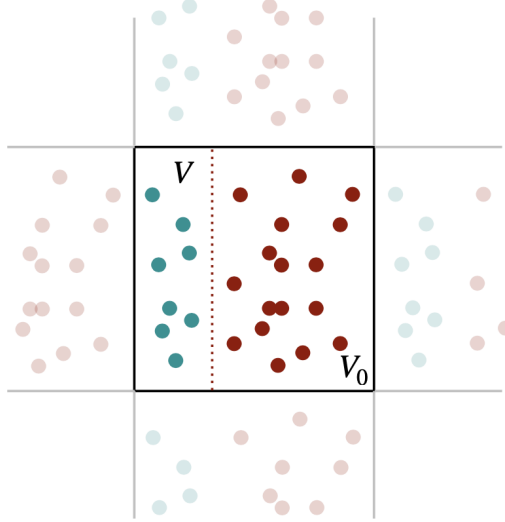

Figure 4.4: Sketch of the definition of subvolumes of the box.

The goal of this section is to determine the fluctuations of conserved charges as a function of the size of the subvolume. The starting point is the net charge density of the system $n_q(x, y, z)$. By integrating over parts of the system the x-dependent charge density is computed via

$$Q(\tilde{x}) = \int_0^{L_{\text{box}}} \int_0^{L_{\text{box}}} \int_0^{\tilde{x}=z/L_{\text{box}}} n_q(x, y, z) dx dy dz \,. \tag{4.31}$$

The cumulants are than calculated from $\langle(\delta Q(\tilde{x}))^n\rangle$. Fig. 4.4 shows a sketch of the subvolumes of the box. The condition if a particle is in a subvolume is determined from one coordinate (here the z-coordinate is used) with

$$z_i < x \cdot L_{\text{Box}} \,, \tag{4.32}$$

where z_i is the coordinate of the i-th particle, $x = (V/V_0)$ and L_{Box} is the length of the box. However, as it has been shown that the density of the medium is homogeneously distributed and therefore, the definition of the subvolume is not relevant. The system is simulated many times with the same initial condition over many events and the fluctuations of the net and total particle number distributions $N_Q^{\text{net/tot}} = N_{Q^+} \mp N_{Q^-}$ in the subvolumes are calculated and presented as a function of the probability x.

4.3.2 Expectations

Before the results from the SMASH simulations are presented, it is useful to think about the expectation of the results of such a system. In an ideal system with N

randomly distributed particles of one particle species, the probability of finding n particles is given by the Binomial distribution

$$B(n|N,\ x) = \binom{N}{n} x^n (1-x)^{N-n}\,.$$ (4.33)

The cumulant-generating function of Eq. 4.33 is

$$K(t) = N\log(1 - x + xe^t)\,.$$ (4.34)

The desired ratios of the cumulants can be calculated from Eq. 4.4 and are

$$\omega = \frac{\kappa_2}{\kappa_1} = \frac{Nx(1-x)}{Nx} = 1 - x\,,$$ (4.35)

$$S\sigma = \frac{\kappa_3}{\kappa_2} = \frac{Nx(1-x)(1-2x)}{Nx(1-x)} = 1 - 2x\,,$$ (4.36)

$$\kappa\sigma^2 = \frac{\kappa_4}{\kappa_2} = \frac{Nx(1-x)(1-6x+6x^2)}{Nx(1-x)} = 1 - 6x + 6x^2\,.$$ (4.37)

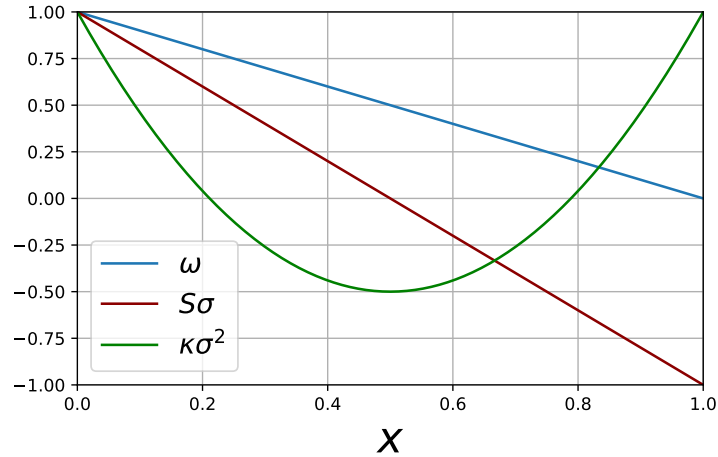Fig. 4.5 shows the result of Eq. 4.35 - 4.37. Since the number of particles or trials N is

Figure 4.5: Ratios of binomial cumulants as a function of probability x.

constant, this result shows the expectation of the effect of global charge conservation.

The quantity of interest is the fluctuations of the net and total particle number of some conserved charge q, one can extend the Binomial model with a second charge and in the following, the derivations from [188] are followed. The starting point is the probability distribution P, describing the number of measured charges $n_\pm$

$$P(n_+, n_-; x) = \sum_{N_+, N_- = 0}^{\infty} \mathcal{P}(N_+, N_-) B(N_+, n_+|x) B(N_-, n_-|x)\,.$$ (4.38)

Here, B is the Binomial distribution of the respective charge and

$$\mathcal{P}(N_+, N_-) = P(N^{\mathrm{tot}})\delta(N_+ - N_- - N^{\mathrm{net}})\,.$$ (4.39)

In the definition of $\mathcal{P}(N_+, N_-)$, the delta enforces the conservation of the net charge number N^{net} and $P(N^{\mathrm{tot}})$ describes the probability distribution of the total charge number, which is not a conserved quantity. Further, it has been assumed that the probability x is the same for each positive and negative charged particle. From Eq. 4.39, the cumulants of the net charge q distribution are

$$\kappa_1[q] = x(\langle N_+ \rangle - \langle N_- \rangle)\,, \tag{4.40}$$

$$\kappa_2[q] = \xi_2(\langle N_+ \rangle + \langle N_- \rangle)\,, \tag{4.41}$$

$$\kappa_3[q] = \xi_3(\langle N_+ \rangle - \langle N_- \rangle)\,, \tag{4.42}$$

$$\kappa_4[q] = \xi_4(\langle N_+ \rangle + \langle N_- \rangle) + 3\xi_2^2 \kappa_2[N^{\mathrm{tot}}]\,. \tag{4.43}$$

In the equations above, ξ_n are polynomials of x defined as

$$\xi_1 = x\,, \quad \xi_2 = x(1-x)\,, \quad \xi_3 = \xi_2(1-2x)\,, \quad \xi_4 = \xi_2(1-6\xi_2)\,. \tag{4.44}$$

Again, computing the ratios, one finds

$$\omega[q] = \frac{N_{ch}}{N_{\mathrm{net}}}(1-x)\,, \tag{4.45}$$

$$S\sigma[q] = \frac{N_{\mathrm{net}}}{N_{ch}}(1-2x)\,, \tag{4.46}$$

$$\kappa\sigma^2[q] = 1 + 3x(1-x)(\omega[N_{ch}] - 2)\,, \tag{4.47}$$

where $N_{ch} = \langle N_+ \rangle + \langle N_- \rangle$. When comparing Eq. 4.45 - 4.47 with Eq. 4.35 - 4.37, it is found that, besides the prefactors related to the charges, that the fourth cumulant $\kappa\sigma^2$ is modified by fluctuations of the total charge number.

4.3.3 Simple interacting system

As a start, the influence of exact charge conservation is studied in a simplified interacting hadronic system. A box containing π and ρ mesons that interact via an energy dependent cross section $\sigma_{\pi\pi\to\rho}(\sqrt{s})$. The system is initialized with a fixed number of pions and the electric charge number is the conserved quantity. Since only positive and negative charged particles are present in the initial state, the only interaction, by design is

$$\pi^\pm \pi^\mp \leftrightarrow \rho^0\,. \tag{4.48}$$

Fig. 4.6 shows the influence of electric charge conservation on the scaled variance and kurtosis. The system is initialized with, in total $N_{\mathrm{init}} = 200\pi^+ + 200\pi^-$ and zero ρ mesons in the initial state. The presented cumulants are calculated after simulating the system until it is in chemical and thermal equilibrium. Since the net charge number is exactly zero, only the scaled variance and the kurtosis are considered in this study. Starting with the results in full phase space, a difference between the cumulants obtained in the smaller volume is found. The cumulants obtained in the larger volume compare well between the binomial expectation and the numerical results from SMASH. For the smaller volume, the scaled variance is
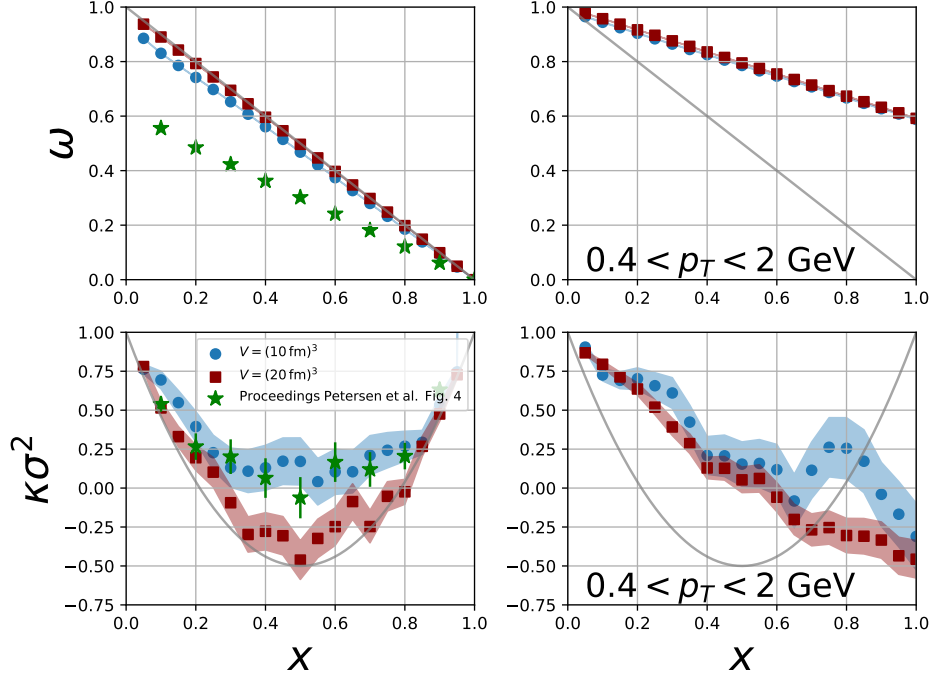
Figure 4.6: Scaled variance (top row) and kurtosis (bottom row) as a function of x. Full-phase space cumulants are presented on the left and on the right side with an imposed cut in p_T. The system is simulated in two different volumes $V = (10\,\text{fm})^3$ (blue) and $V = (20\,\text{fm})^3$ (red). The grey lines show the binomial expectation Eq. 4.35 and Eq. 4.37. Green data points show the results from [187].

slightly decreased at small values of x and the kurtosis increases around $x = 1/2$, deviating from the binomial baseline.

When imposing a cut in momentum space the scaled variance and the kurtosis go to the same value in $x \to 0$. For larger subvolumes, both ω and $\kappa\sigma^2$ increase in comparison to the binomial baseline. As the net charge number is no longer globally conserved within the subset of particles with this specific p_T cut, their cumulants don't follow the analytic expectations. However, there are still exist correlations, since the dependency on x is not erased.

The comparison between the results from this SMASH version and [187], in which the same system was studied reveals a difference in the scaled variance but not the kurtosis. The explanation of this difference of ω is of a technical nature. After the system reaches the final state, when the fluctuations are calculated, the question is how to deal with unstable particles. In nature, the detectors only observe the stable hadrons, therefore, unstable hadrons are usually forced to decay into the stable decay products. In [187] this is done whereas in the presented calculation the unstable mesons are left in the final state. Using "forced" decays, the mean of $\langle N^{\text{tot}} \rangle$ increases to the initial state value. This results in an effective decrease of the scaled variance. Since the two decay products are placed at the same position in space, the second net

charge cumulant is left unaffected. The fourth cumulant however should be affected since κ_2^{tot} vanishes when decays are performed. So, it is not clear why this result matches with [187] and the latter is not close to the binomial baseline.

In the next step, the goal is to understand the behavior of the individual cumulants and their deviations from the binomial baseline. Fig. 4.7 shows the individual
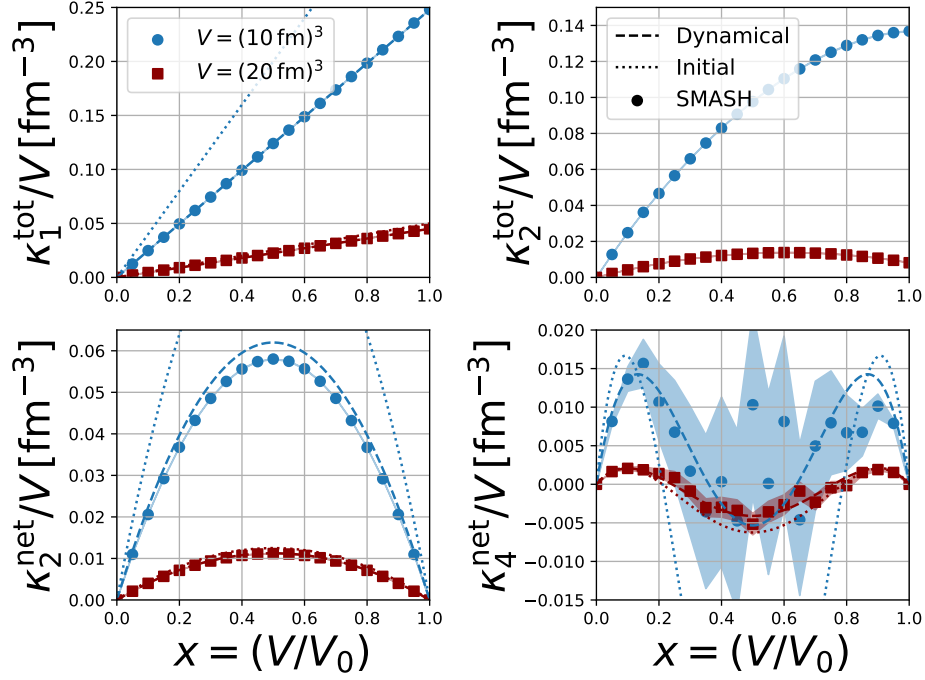

Figure 4.7: Net and total cumulants as a function of x normalized to the volume of the system. Results of $V = (10\,\text{fm})^3$ and $V = (20\,\text{fm})^3$ are shown in blue and red respectively. The upper left and upper right plots show the first and second cumulant of the total charge number. In the lower left and right, the second and fourth cumulant of the net charge number are presented. The dashed lines show the results of the analytic expectations after dynamical evolution and the dotted line the initial cumulants Eq. 4.40 - 4.43.

normalized cumulants of interacting π and ρ meson system. From the total charge density (upper left in Fig. 4.7), one can directly observe the main difference between the two systems. Since both boxes are initialized with the same number of positive and negative charged pions, the initial charge numbers are the same in the two systems. After the dynamical evolution, however, the difference between initial and final state numbers is different. The reason is that in the smaller box, more ρ^0 states are created, effectively decreasing the total charge number. As a result, the fluctuations $\kappa_2[N_{ch}]$ in full phase space increase. Note that, in the initial state, the total charge number is a conserved quantity and follows the same parabola shape as $\kappa_2[q]$. The net charge is strongly affected as well. Together with the fluctuations of the total charge number, the results from SMASH and the analytic formulas

Eq. 4.40 - 4.43 are in good agreement with each other. In the larger volume, the creation of the ρ^0 meson does not happen as frequently, the cumulants are close to the initial cumulants. In the dense medium, however, the fluctuations of the total charge number increase, which affects the fourth cumulant around $x = 1/2$.

Still, κ_2^{net} slightly deviates from the analytic expectation which is already observed in the scaled variance in Fig. 4.6. One reason might be that some minimal distance between the mesons is enforced by the geometric collision criterion. This would deviate the cumulants from the ideal picture [189].

4.3.4 Effect of baryon annihilation

In this section, the influence of a baryon baryon annihilation process on the cumulants up to fourth order is investigated. For this purpose, a hadron gas with the following species is simulated

$$\pi, \ \rho, \ N, \ \Delta, \ (+h_1(1170)) \tag{4.49}$$

Besides the resonance formation processes ($\pi\pi \leftrightarrow \rho$ and $\pi N \leftrightarrow \Delta$) the $h_1(1170)$ mesons yield the option to add the baryon annihilation process $NN \leftrightarrow 5\pi$ (on average) via the following reaction chain, that was originally proposed in [190]

$$N\bar{N} \leftrightarrow h_1(1170)\rho \quad h_1(1170) \leftrightarrow \rho\pi \quad \rho \leftrightarrow \pi\pi. \tag{4.50}$$

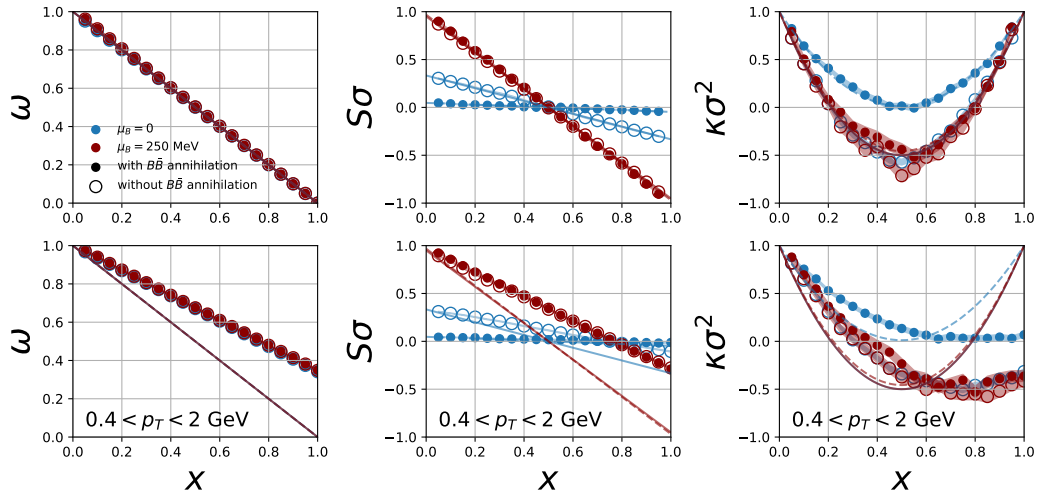For all these reactions detailed balance is present.

Figure 4.8: Scaled variance (left column) skewness (middle column) and kurtosis (right column) of the net baryon number as a function of x of a hadronic system with (closed symbols) and without (open symbols) a nucleon-nucleon annihilation process. The upper row shows the cumulants in full phase space whereas the results in the lower row contain a cut in momentum space. The ratios of cumulants are shown for $\mu_B = 0$ (blue) and $\mu_B = 250$ MeV (red).

Fig. 4.8 shows the ratios of cumulants for the system presented in Eq. 4.49. By including the $h_1(1170)$ meson, or leaving it out of the system, the influence of a

$N\bar{N}$-annihilation process can be studied. The main difference of such a process in the system studied here is, that the total charge number is no longer a conserved quantity. As a result, the fluctuations of the total charge influence the fourth cumulant via Eq. 4.43. First, on the level of the second cumulant without a cut on p_T, no difference due to the baryon annihilation process is observed as well as no dependency on the baryon chemical potential. The skewness on the other hand is affected. Here, the difference comes purely from the ratio $N_{\text{net}}/N_{\text{tot}}$, which is driven by the baryon chemical potential. With increasing μ_B, the ratio becomes $N_{\text{net}}/N_{\text{tot}} \approx 1$ whereas at $\mu_B = 0$ it becomes $N_{\text{net}}/N_{\text{tot}} \approx 0$. Finally, the kurtosis strongly depends on the baryon annihilation process. Similar to the process $\pi^{\pm}\pi^{\mp} \leftrightarrow \rho^0$, the $N\bar{N} \leftrightarrow 5\pi$ reduces the total baryon number and the fluctuations $\kappa_2[N_{ch}]$ become important around $x = 1/2$ for the case $\mu_B = 0$. In both limits, $x \to 0$ and $x \to 1$, $\kappa\sigma^2 \to 1$. When increasing the baryon chemical potential, there are simply not enough anti-nucleons in the system and as a result, the fluctuations follow the Poissonian (Binomial) baseline.

4.3.5   Result of the full SMASH hadron gas

Net baryon and net proton fluctuations

In this section, the full SMASH hadron gas is employed to extract the influence of global charge conservation on the fluctuations. For all presented results, in the final state of the simulation, the decay of resonances into stable particles is performed. Besides the exactly conserved net baryon number event-by-event, which has been shown to follow the analytical results of charge conservation, the net proton number is of interest here, since its fluctuations are used in the experiments as a proxy of the net baryon number.

In Fig. 4.9, the cumulants of the net baryon and net proton numbers are presented. Starting with the net baryon number, the results of all three ratios ω, $S\sigma$ and $\kappa\sigma^2$ follow the expected analytic curves. The net baryon scaled variance follows $(1 - x)$ and the skewness shows the dependency on the ratio of $N_{\text{net}}/N_{\text{tot}}$. $\kappa\sigma^2$ shows the transitions from the Poisson to the Binomial baseline when going from $\mu_B = 250\,\text{MeV}$ to $\mu_B = 0$. Similar to the previous section, this originates from a baryon-baryon annihilation process, increasing the fluctuation of the total charge number. At a finite value of baryon chemical potential, there are not as many anti-baryons in the system and the kurtosis goes to $\kappa\sigma^2(x = 1/2) = -1/2$. Similarly, when introducing a cut in momentum space, the fluctuations increase since the net baryon number is no longer conserved in the full volume. However, there still exist correlations from the charge conservation and as a result, the net proton cumulants are not independent of the size of the subvolume.

A similar phenomenon is seen for the ratios of the net proton number cumulants. As they are only a subset of the full set of baryons, the net proton number does not follow the analytic expectation as well. Similar to the net baryon cumulants, where a momentum cut is included, correlations from the net baryon number conservation are propagated to the net proton number and increase their fluctuations. Besides the skewness, the net proton scaled variance does not show a strong μ_B dependence. At
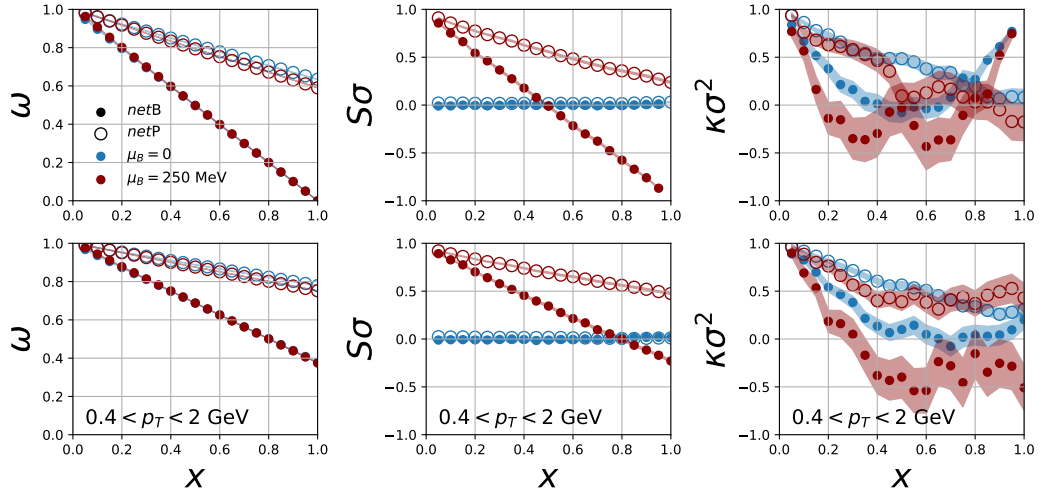
Figure 4.9: Scaled variance, skewness and kurtosis of the net baryon (full circles) and net proton (open circles) cumulants as a function of x. The results are presented for $\mu_B = 0$ (blue points) and $\mu_B = 250\,\text{MeV}$ (red points). The upper row shows the full whereas the lower row the restricted momentum space results.

large values of x the value of ω at zero baryon chemical potential is slightly larger due to a larger N_{ch} number. It is hard to make a clear statement for the net proton number kurtosis due to the large errors but the hierarchy $\kappa\sigma(\mu_B = 0) < \kappa\sigma(\mu_B = 250\,\text{MeV})$, which originates from the transition Binomial to Poisson baseline (similar to Fig. 4.6), is approximated present as well.

Comparison to ALICE data

To measure the grand canonical ensemble value of the fluctuations of the created QCD medium in a heavy-ion collision, only the fluctuations in a small window in rapidity are measured. However, the question of the extent to which this corresponds to the GCE value arises. In the limit $x \to 0$ all relevant correlations vanish and what is left is the Poisson baseline. In this section, the presented results are compared with an experimental measurement. It is worth noting that the systems are vastly different, so a comparison seems odd at first glance. The goal is to see how the correlations between the protons and anti-protons from this model match with the experimentally measured ones.

It is argued in [184], that especially at the highest beam energy, there exists a strong correlation between the subvolumes in coordinate space and in rapidity intervals measured in momentum space, due to the collective behavior in the longitudinal direction of the beam. This picture breaks down at low collisional energies where Bjorken picture is no longer valid. To relate the size of the subvolume $x = (V/V_0)$ to the rapidity interval Δy. Similar to Eq. 4.30 the relation $x \approx N_{ch}(\Delta y)/N_{ch}(\infty) \approx \text{erf}\left(\frac{\Delta y}{2\sqrt{2}\sigma_y}\right)$ is used [53]. The width of the rapidity distri-

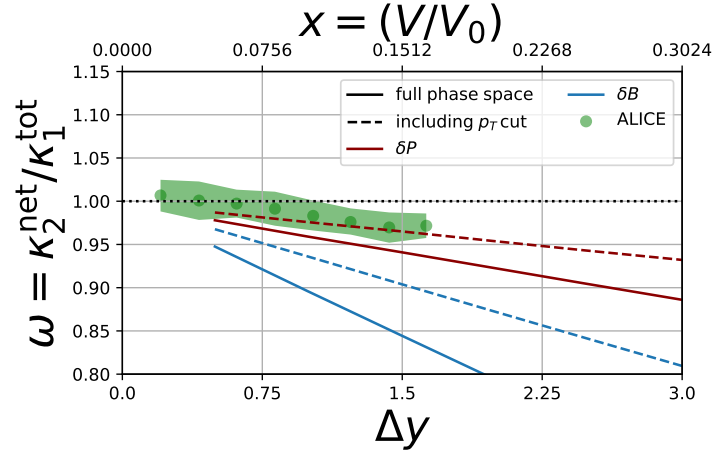bution has been measured as $\sigma_y = 3.86$ at $\sqrt{s_{NN}} = 2.76\,\text{TeV}$ [191].

Figure 4.10: Scaled variance as a function of the rapidity interval Δy. The results of the net proton (red) and net baryon (blue) cumulants are shown in full phase space (straight line) and includes a p_T cut (dashed line). The ALICE data points are taken from [192].

Fig. 4.10 shows the result of the scaled variance obtained from the SMASH box simulation at $\mu_B = 0$ and the ALICE measurement [192]. For comparison, the value of x is added on top of Fig. 4.10 for a better comparison. With the relation of x with Δy, it becomes clear that the fluctuations are measured within a small subvolume x in the experiment. To accommodate the experimental configuration, the cut in p_T has been adapted to $0.6 < p_T < 1.5\,\text{GeV}$. With decreasing rapidity interval Δy, the scaled variance goes to the Poisson limit of 1. With $x \to 0$, all relevant correlations vanish and one is only left with Poisson fluctuations. With increasing rapidity interval, ω decreases which is interpreted as a sign of charge conservation in full phase space. One can see that when going from the net baryon to the net proton fluctuations and when introducing a cut in momentum space, the strength of the correlation decreases. Since the net protons including a p_T cut denote the smallest subset of the presented baryons, the strength of the correlations is the smallest. The results of the equilibrium calculation match surprisingly well, which shows that the correlations due to global charge conservation are well described by SMASH.

Relation between net proton and net baryon cumulants

The goal of this section is to understand the relation between the net proton and net baryon cumulants. Since the net proton number represents a subset of the net baryon number, and in chemical equilibrium the averages are constant, it is interesting to see if there exists some relation between those two quantities.

In [193, 194] the idea to calculate the net baryon fluctuations from a binomial unfolding procedure was introduced and is based on the assumption that in the late

stages of a heavy-ion collision, above a certain beam energy ($\sqrt{s} \gtrsim 10\,\mathrm{GeV}$), isospin fluctuations randomize the isospin numbers and the net baryon fluctuations can be obtained from the net proton fluctuations. Starting from the following probability distribution

$$\mathcal{P}(N_p, N_{\bar{p}}; N_B, N_{\bar{B}}) = \mathcal{F}(N_B, N_{\bar{B}})\, B_r(N_p; N_B)\, B_{\bar{r}}(N_{\bar{p}}; N_{\bar{B}})\,. \qquad (4.51)$$

Here, $B_r(N_p; N_B)$ are Binomial distributions with probability $r = \langle N_p \rangle / \langle N_B \rangle$ and the same for the anti-protons $N_{\bar{p}}$. $\mathcal{F}$ is a function that contains information about the distribution of (anti-) baryons and their correlations.

The formulas for mapping the net proton number fluctuations onto the net baryons are derived without any assumption of $\mathcal{F}$ and they read

$$\langle N_B^{\mathrm{net}} \rangle = \langle \xi_1^{-1} N_p - \bar{\xi}_1^{-1} N_{\bar{p}} \rangle\,, \qquad (4.52)$$

$$\langle N_B^{\mathrm{tot}} \rangle = \langle \xi_1^{-1} N_p + \bar{\xi}_1^{-1} N_{\bar{p}} \rangle\,, \qquad (4.53)$$

$$\langle (\delta N_B^{\mathrm{net}})^2 = \langle (\xi_1^{-1} \delta N_p - \bar{\xi}_1^{-1} \delta N_{\bar{p}})^2 \rangle - \langle \xi_2 \xi_1^{-3} \delta N_p + \bar{\xi}_2 \bar{\xi}_1^{-3} \delta N_{\bar{p}} \rangle\,. \qquad (4.54)$$

The exact expression of the higher-order cumulants is not used in this work and therefore neglected and the polynomials ξ_n are the same as in Eq. 4.3.2. One problem that arises is, that the Binomial unfolding procedure effectively increases the error of the cumulants by a factor $r^{-n} \approx 2^n$ [195], for $r = \langle N_p \rangle / \langle N_B \rangle = 1/2$. This fact prohibits the present calculation from investigating cumulants of order $n > 2$, as the errors are simply too large. One of the premises to be able to use the unfolding procedure is that the isospin density is small enough, meaning that there exist enough thermal pions to mediate the randomization of the isospin fluctuations. It has been checked that this is indeed the case in the considered simulations.

The first step of the calculation is to determine the exact values of $r = \langle N_p \rangle / \langle N_B \rangle$ and $\bar{r}$ from the simulation. In order to have an estimated error of the calculation the probabilities are modified by $\pm 3\%$ which are presented as bands of the mapped cumulants.

Before showing the results from the Binomial unfolding procedure (Eq. 4.52-4.54) of the actual proton cumulants from SMASH mapped onto the baryon fluctuations, an additional calculation is presented to cross-check the presented methodology. A fictional proton number set is determined by a Binomial acceptance procedure with the given probability $r, \bar{r}$

$$\{N_p, N_{\bar{p}}\} = \{B_r(N_p; N_B), B_{\bar{r}}(N_{\bar{p}}; N_{\bar{B}})\}\,. \qquad (4.55)$$

From this set of protons, the same unfolding will be calculated to cross-check the implementation.

Fig. 4.11 shows the result of the Binomial mapping procedure. Starting with the mapped scaled variance of the artificial set of protons Eq. 4.55 onto the baryons, a perfect agreement is found. This results verifies the computation of Eq. 4.52-4.54. In addition, this means that the correlations from the global net baryon conservation survive the Binomial (re-)mapping procedure. However, when mapping the actual proton set from the dynamical simulation, a difference to the net baryon scaled
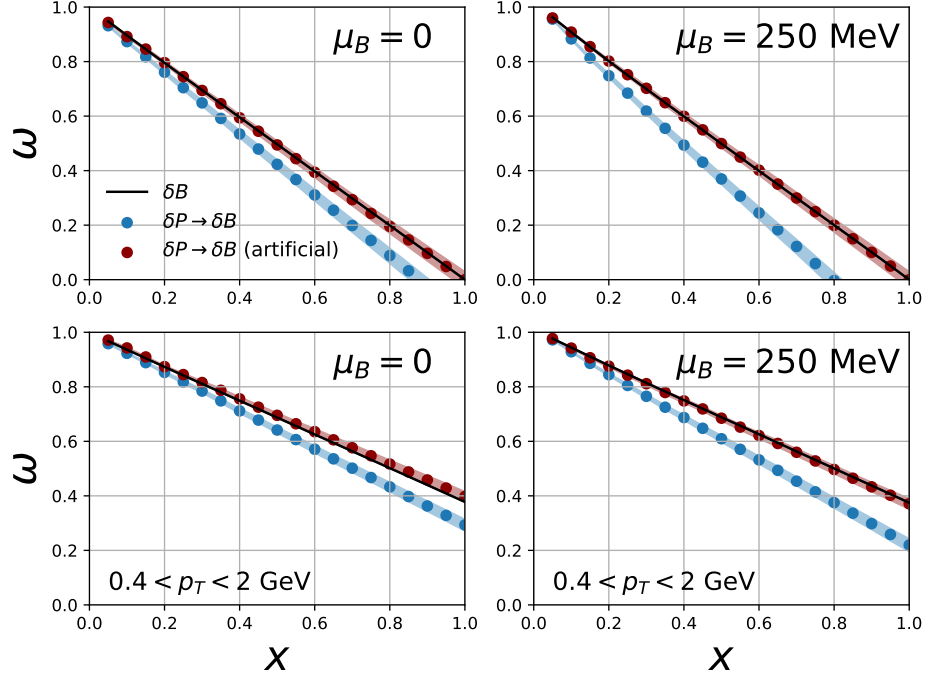
Figure 4.11: Scaled variance as a function of x of the net baryon number (black line), the mapped proton number fluctuations (blue) and artificial proton number fluctuations (red). Results on the left show the cumulants for $\mu_B = 0$ and on the right for $\mu_B = 250\,\mathrm{MeV}$. In the upper row, the results in full phase space are shown and in the lower the results with a p_T cut.

variance is found. For all four presented cases, the mapped fluctuations are smaller than the actual ones and therefore the baryon conservation line is not matched. Correlations that hinder the unfolding procedure are a result of the dynamical evolution of the medium and the interactions between the hadrons since they are not contained in the artificial proton number set. With increasing baryon chemical potential the unfolding procedure underestimates the net baryon scaled variance at large values of the subvolume even more.

The dependency of the success of the Binomial unfolding on the complexity of the hadronic medium is shown in Fig. 4.12, where the ratio of the baryon scaled variance to the mapped scaled variance of the proton fluctuations is presented. The results are shown for the full SMASH hadron gas and for the two simplified hadronic systems shown in Fig. 4.8. Interestingly, the mapping $\delta P \rightarrow \delta B$ in the system in which the nucleon-nucleon annihilation process is enabled via the h_1 meson (green symbols), is equally successful as in the system without the annihilation process (red symbols). This shows that such annihilation processes are not the origin of the correlations that hinder the unfolding.
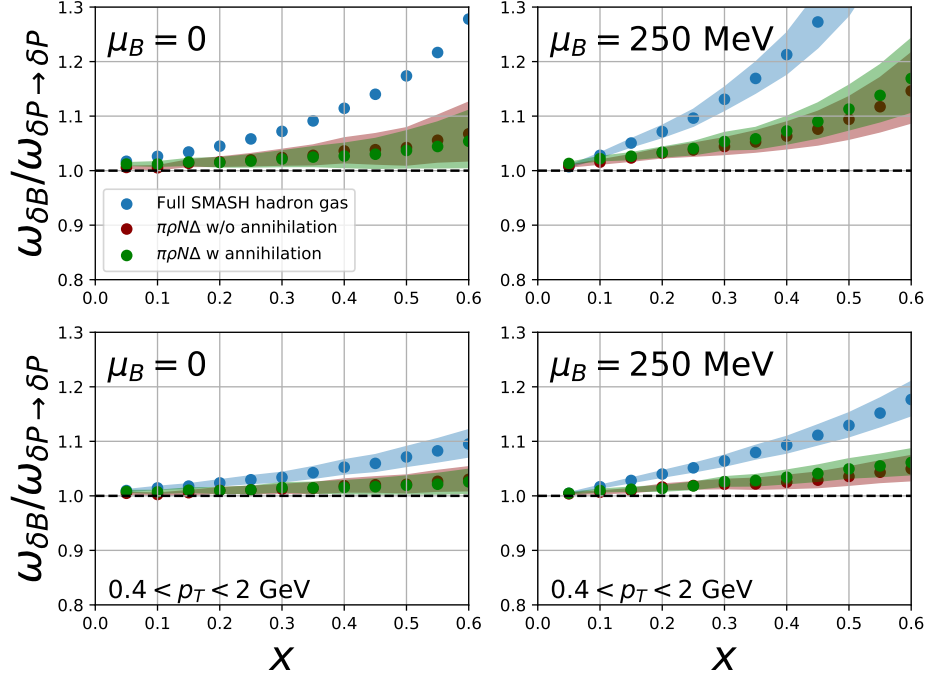
Figure 4.12: Ratio of the scaled variance of the actual net baryon fluctuations to the net proton mapped onto the net baryon scaled variance as a function of $x = (V/V_0)$. The ratio is shown for baryon chemical potential $\mu_B = 0$ (left column) and $\mu_B = 250\,\mathrm{MeV}$ (right column) for full phase space (upper row) and including a p_T cut (lower row). The results of three different systems with gradually increasing complexity are shown.

4.3.6 Influence of deuteron formation

In this section, the influence of deuteron cluster formation on conservation effects is calculated. For this, two different sets of particles and interactions are employed, where the only difference is the effective deuteron formation process (see Eq. 4.56). Deuteron cluster formation is an important process when studying fluctuations since they are produced in the late stages of a heavy-ion collision. An analysis of the influence of deuteron cluster formation on the net proton number fluctuations can be found e.g. in [196].

In this work, the goal is to determine how deuteron formation can modify the conservation effects of the proton and baryon number cumulants. By comparing systems with and without a deuteron cluster formation process the impact on the proton number cumulant can be studied as a function of the size of the subvolume. With a geometric collision criterion, the limitation is that only binary scatterings can be performed. The reaction in which a deuteron is created is a $3 \leftrightarrow 2$ reaction namely $\pi np \leftrightarrow d\pi$ and $Nnp \leftrightarrow Nd$. To be able to perform these interactions a fictional particle d' is introduced [197, 102]. Note that the deuteron in this microscopic

description is treated as a point particle. The individual reactions that model the $3 \leftrightarrow 2$ interaction $\pi np \leftrightarrow d\pi$ and $Nnp \leftrightarrow Nd$ are

$$pn \leftrightarrow d' \qquad\qquad \pi d' \leftrightarrow \pi d \qquad\qquad Nd' \leftrightarrow Nd\,. \quad (4.56)$$

The impact of deuteron clusters on conservation curves of the proton and baryon cumulants is now studied. To do this, the cumulants are calculated for a system with and without deuterons in a box of $V = (15\,\mathrm{fm})^3$. For the calculation of cumulants of deuterons, only the actual deuterons are counted and not the fictional d' resonance.
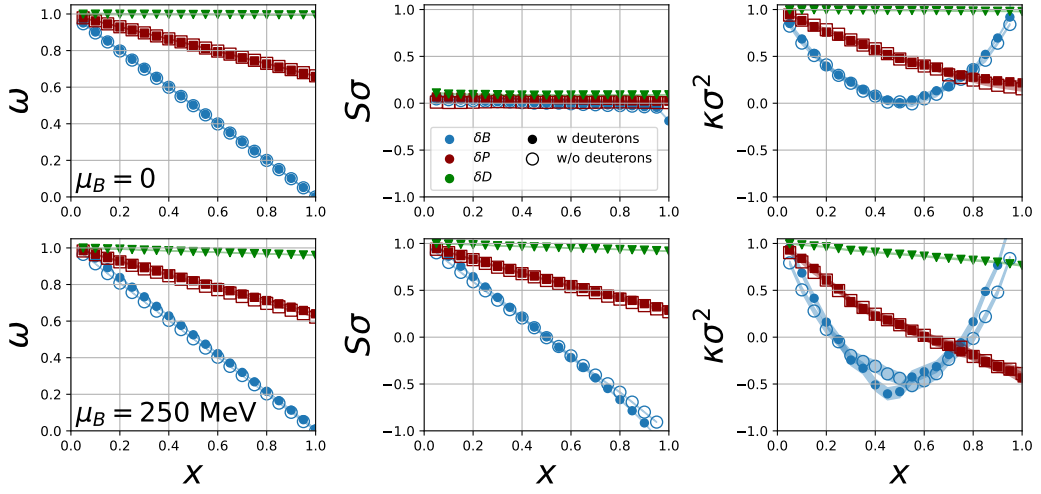

Figure 4.13: Scaled variance (left colum), skewness (center) and kurtosis (right colum) as a function of x of baryons (blue) protons (red) and deuterons (green). The results are presented for $\mu_B = 0$ (upper row) and finite $\mu_B = 250\,\mathrm{MeV}$ (lower row). Closed symbols show the result of a system that includes deuterons and open symbols one that has no deuterons.

Fig. 4.13 shows the cumulants as a function of the subvolume size. For both systems, with and without deuteron formation, the baryon number cumulants follow the expected analytic conservation curves, which were observed before. Interestingly, in the case where deuterons are produced, the cumulants show no large dependence on the size of the subvolume, meaning they are rarely affected by baryon number conservation and are produced thermally. In addition, the proton number cumulants of the two systems coincide with each other. This means that the proton cumulants are not affected by the deuteron cluster formation and deuterons are rarely affected by conservation effects, since their yields are small and therefore they follow the thermal expectation.

4.3.7 Summary

In this work, the effects of global conservation on fluctuations of conserved charges have been investigated and several hadronic systems have been evaluated in infinite

matter calculations, in order to study the influence of individual dynamic interactions. Resonance formations/decays have no large effect on the higher moments for electric charge cumulants, as long as the density of particles is small enough. The kinematic cuts have always the expected effects on the cumulants by reducing the correlations. For the net baryon number, which is of great interest in the context of identifying the critical endpoint in heavy-ion measurements, it has been shown that baryon annihilation plays a bigger role at zero chemical potential and mainly affects the kurtosis. Interestingly, the proposed binomial mapping from net protons to net baryons suggested from isospin randomization cannot fully reconstruct the proper net baryon number cumulants in large sizes of the subvolume and consistently underestimates their fluctuations. While for an artificial set of protons, the mapping works as expected, it does not for the actual SMASH protons containing correlations from the dynamical evolution. For $x < 0.2$ the mapping can be applied within an approximate error of 5%. Last, the influence of cluster formation has been studied and the proton cumulants are largely unaffected. The deuterons themselves follow a thermal expectation unaffected by conservation laws.

This is of relevance for the comparison of experimental results for fluctuation observables with theory calculations based on a grand canonical ensemble. In the next step, the goal is to study the evolution of critical equilibrium fluctuations in the same system.

4.4 Fate of critical fluctuations in an interacting hadronic medium

Motivation for the study of the influence of hadronic interactions on the evolution of critical fluctuations

The second project is about the evolution of critical equilibrium fluctuations in a hadronic medium and the results are based on [4].

There exist many problems when it comes to modeling on how to compare results from theoretical calculations to measurements. The theoretical description of fluctuations within the dynamical multi-stage evolution of the HIC is complicated and multiple questions must be addressed. First, the question arises of how the critical fluctuations form near the CP. This problem is typically tackled within a fluid dynamical framework in which the critical mode is treated as a field (see e.g. [198, 199, 200, 201, 202, 203]). The second question is then how such critical fluctuations survive the subsequent evolution in the dilute regime of the HIC towards the chemical and kinetic freeze-out. This work contributes to the second question. To this end, it is assumed that critical fluctuations have built up at the moment where microscopic transport validly describes the hadronic phase. This occurs typically in the late stage of the collision and is, for noncritical dynamics, described by the Cooper-Frye particlization. Equilibrium fluctuations of the critical mode according to the three-dimensional (3d) Ising model are assumed and coupled to a HRG background. Then, the distribution functions of particle species are generated using the principle of maximum entropy and evolved in a hadronic transport model.

Besides the question on the relation between the fluctuations of the net baryon and the net proton number which are measured in the experiment, one can then tackle the question of how formations and decays of resonances alter the proton number fluctuations.

Regarding the question of particlization, what is known is the cumulants that originate from the coupling of the HRG model to the critical mode however, the resulting distribution function of an affected particle species is not known. Instead, it is the cumulants up to some finite order of these distributions and reconstructing a probability distribution from a finite set of moments or cumulants is a classical ill-posed problem in mathematics. In the appendix of [204], a probability distribution was obtained by assuming the shape of the probability distribution of the sigma field $P(\sigma)$. However, the resulting distribution $P(N)$ only approximately generated the correct input cumulants. To circumvent this problem, an extension of the Cooper-Frye formula to include corrections of the critical field to a particle distribution function was performed up to second order in [205]. In [206], the same authors made the general argument that the principle of maximum entropy is suitable for freezing out critical fluctuations. In this work, the goal is to follow the idea of [206] and convert fluctuations from a thermodynamic model that includes critical equilibrium fluctuations to particle spectra using the principle of maximum entropy. By doing so, probability distribution functions of a specific particle species are obtained that can be put into a model for the dilute stage of a heavy-ion collision to evolve those particle spectra. Then, the second-mentioned problem can be addressed and the impact of the stochastic nature of the hadronic phase on the fluctuations can be investigated.

4.4.1   Mapping of the 3d-Ising model to QCD

Since the HRG model is a model without any criticality, the baseline model needs to be extended in order to incorporate critical behavior. By using the universality class argument [207], that in the vicinity of the critical point, the scaling behavior of the order parameter of QCD, the chiral condensate, is the same as the order parameter of the 3d Ising model, the magnetization. One can then relate the fluctuations of the order parameter of QCD with the one from the 3d Ising model.

The Ising model originates from condensed matter physics in order to explain ferromagnetism. The relevant degrees of freedom are the discrete spin states that take either $(+1, -1)$. The order parameter of the Ising model is the magnetization, defined as the sum of all spin states. When the phases of the spin states are studied depending on the temperature and an external magnetic field, one finds that the magnetization exhibits a phase transition. Fig. 4.14 shows a sketch of the behavior of the probability distribution of the order parameter of the Ising model along the temperature axes. At $T < T_c$, a coexistence region is located, meaning that the probability distribution has a double peak structure, whereas a cross-over type phase transition is located at $T > T_c$, where the distribution is single peaked. At the critical point, where the transition between the two phases occurs, the probability distribution shows a plateau which is also where the fluctuations of the order parameter increase. In
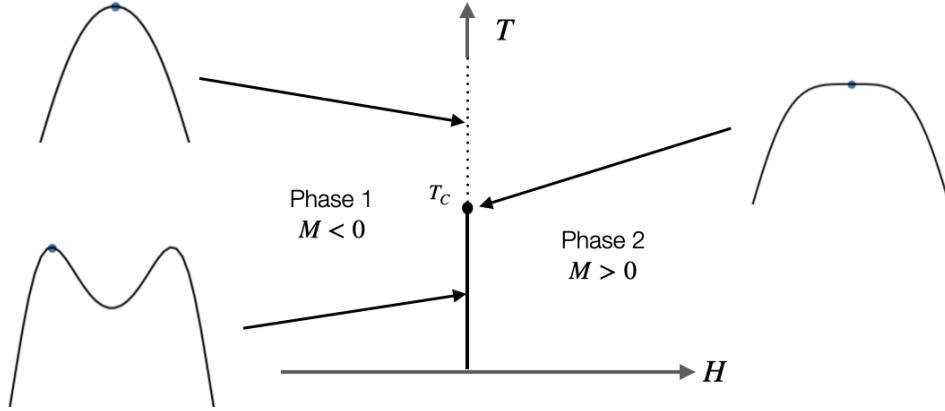
Figure 4.14: Sketch of the phase diagram of the Ising model.

an infinite medium the correlation length ξ diverges and the system becomes scale invariant. The model employed in this work to describe the critical fluctuations is the same that has been used in [208] and the description of the model is therefore taken from there.

In order to obtain fluctuations of the magnetization, the equation of state is needed. Before doing so, one first introduces the reduced temperature r and reduced external magnetic field h as

$$r = (T - T_c)/T_c \,, \tag{4.57}$$

$$h = H/H_0 \,. \tag{4.58}$$

The equation of state is obtained from a parametric equation of state [209], which preserves the invariance of the scaling of r, h and M [210]. It is additionally useful to introduce auxiliary quantities R and θ and write

$$M = M_0 R^\beta \theta \,, \tag{4.59}$$

$$r = R(1 - \theta^2) \,, \tag{4.60}$$

$$h = H/H_0 = R^{\beta\delta} \tilde{h}(\theta) \,. \tag{4.61}$$

With $\tilde{h}(\theta) = c\theta(1 + a\theta + b\theta^4)$. The universal scaling behavior is built into the EoS with the critical exponents $\beta = 0.3250$, $\delta = 4.8169$ and the coefficients in $\tilde{h}(\theta)$ are $a = -0.76145$, $b = 0.00773$ and $c = 1$.

The fluctuations of the magnetization can be calculated from the EoS by taking higher order derivatives of M with respect to the auxiliary field h

$$\langle (\delta\sigma)^n \rangle_c = \left(\frac{T}{VH_0} \right)^{n-1} \frac{\partial^{n-1} M}{\partial h^{n-1}} \bigg|_r \,. \tag{4.62}$$

The mapping between the 3d Ising model and QCD is then performed by relating the reduced Ising temperature and external magnetic field with the temperature and

the baryon chemical potential in the QCD phase diagram. An additional rotation of r by an angle α_1 is introduced and h is rotated by α_2. One can write the mapping in a general form as

$$\frac{T - T_c}{\Delta T_c} = r\rho \sin\alpha_1 + h\cos\alpha_2 \, , \qquad (4.63)$$

$$\frac{\mu_B - \mu_{B,c}}{\Delta\mu_{B,c}} = -r\rho\cos\alpha_1 - h\sin\alpha_2 \, . \qquad (4.64)$$

There are now multiple open parameters that have to be fixed. First, the angles of the h and r axes in the T and μ_B plane. And second, the size of the scaling region ΔT_c, $\Delta\mu_{B,c}$ and ρ. For the sake of simplicity and for a better comparison, the values of [208] have been adapted. The scaling size is chosen to be $\rho = 1$, $\Delta T_c = 0.02\,\text{GeV}$ and $\Delta\mu_{B,c} = 0.42\,\text{GeV}$. One can additionally eliminate two of the open parameters, assuming the critical point lies on the chiral phase transition line. The chiral phase transition defines the region where the cross-over is located in the T-μ_B-plane and it can be calculated at zero baryon chemical potential from lattice QCD. By Taylor expanding into the chemical potential, the chiral phase transition line can be evaluated using the value of the pseudocritical temperature $T_{c,0}$. The μ_B dependence of the pseudocritical temperature can be written in terms of the following expansion as [16, 211, 212]

$$T_c(\mu_B) = T_{c,0}\left[1 - \kappa_c\left(\frac{\mu_B}{T_c(\mu_B)}\right)^2 + ...\right] \, . \qquad (4.65)$$

Here, $\kappa_c = 0.007...0.059$ is the curvature of the chiral condensate [16]. By assuming the critical point is located on the cross-over line and assuming that the r-axis is tangential to the chiral phase transition line, one can eliminate the parameter T_c and α_1 by choosing $\mu_{B,c}$ appropriately. The value of the pseudocritical temperature is then computed by solving Eq. 4.65 up to leading order for a given critical temperature.

The h-axis is chosen to be parallel to the temperature axes. There exist studies investigating the effects of varying the open parameters of the angles and sizes of the critical region, see e.g. [213]. The location of the critical point is chosen to be $\mu_{B,c} = 390\,\text{MeV}$ which puts the critical temperature to $T_c \approx 149\,\text{MeV}$.

A sketch of the location and orientation of the axes after mapping the Ising EoS to the QCD phase diagram is shown in Fig. 4.15. Additionally, the rotation of the reduced temperature axis $\tilde{r}$ is included. In order to obtain the values of the auxiliary parameters R and θ that are used for the parametrization of the 3d Ising EoS, the equations 4.59-4.61 are solved for a given value of the temperature and baryon chemical potential. With these values, the cumulants $\langle(\delta\sigma)^n\rangle_c$ up to fourth order are obtained from the analytic expressions presented in App. A.5. It is known from effective calculations of QCD that the location of the critical point is located at rather $\mu_B/T \gtrsim 4$ (e.g. fRG calculations [19, 20, 21] or Dyson Schwinger computations [22, 23]). For the sake of a better comparison with [208] and since this work doesn't aim for a direct comparison to experimental measurements the described parameters are not modified.
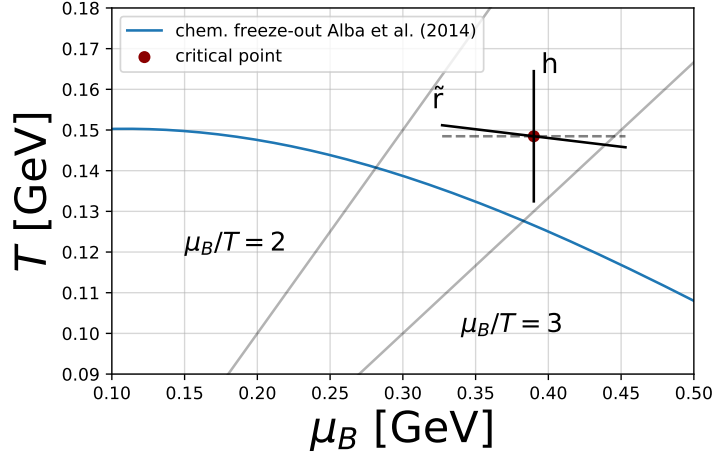
Figure 4.15: Sketch of the QCD-phase diagram and its critical point used in this work.

In order to couple the distribution function of the HRG model to the critical mode, the ansatz employed in [44, 45] is used, where the equilibrium distribution function is extended by an additional contribution $\delta f_i^{\text{critical}}$

$$f_{i,k} = f_{i,k}^0 + \delta f_i^{\text{critical}} . \tag{4.66}$$

The coupling to the critical mode of a particle species i originates from the dynamically generated masses via $\delta m_i = g_i \delta\sigma$. One can therefore write

$$\delta f_i^{\text{critical}} = -\delta\sigma \frac{g_i}{T} \frac{f_{i,k}^0}{\gamma_{i,k}} . \tag{4.67}$$

Here, $\gamma_{i,k} = E_{i,k}/m_i$ and g_i denotes the strength of the coupling and will be used as an open parameter.

From here, one can derive the cumulants of the individual particle and anti-particle numbers including the contribution from the critical fluctuations [208]. The mean of a given species is not affected by the coupling to the $\sigma-$field. Starting with the second order cumulants of the net particle number, which can be written as

$$\kappa_{2,i}^{\text{net}} = \langle(\delta N_i)^2\rangle + \langle(\delta N_{\bar{i}})^2\rangle - 2\langle\delta N_i \delta N_{\bar{i}}\rangle , \tag{4.68}$$

where $\bar{i}$ is representative for the anti-particle of i. The three terms on the right-hand side of the equation above are calculated as

$$\langle(\delta N_i)^2\rangle = \kappa_{2,i}^{\text{HRG}} + \langle(V\delta\sigma)^2\rangle I_i^2 , \tag{4.69}$$

$$\langle\delta N_i \delta N_j\rangle = \langle(V\delta\sigma)^2\rangle I_i I_j . \tag{4.70}$$

Here, I_i is defined as the momentum integration of Eq. 4.67 with

$$I_i = \frac{g_i d_i}{T} \int \frac{d^3k}{(2\pi)^3} \frac{f_{i,k}^0}{\gamma_{i,k}} . \tag{4.71}$$

84

As a result, the final expression of the second cumulant is

$$\kappa_{2,i}^{\text{net}} = \kappa_{2,i}^{\text{HRG}} + \kappa_{2,\bar{i}}^{\text{HRG}} + \langle (V\delta\sigma)^2 \rangle (I_i - I_{\bar{i}})^2 \, . \tag{4.72}$$

In Eq. 4.69, the cumulative property has been used and in Eq. 4.70, it is assumed that there exists no correlation between hadrons in the ideal HRG model. The third cumulant is modified in the following way

$$\kappa_{3,i}^{\text{net}} = \langle (\delta N_i)^3 \rangle - \langle (\delta N_{\bar{i}})^3 \rangle - 3\langle (\delta N_i)^2 \delta N_{\bar{i}} \rangle + 3\langle \delta N_i (\delta N_{\bar{i}})^2 \rangle \, , \tag{4.73}$$

which results in

$$\kappa_{3,i}^{\text{net}} = \kappa_{3,i}^{\text{HRG}} - \kappa_{3,\bar{i}}^{\text{HRG}} - \langle (V\delta\sigma)^3 \rangle (I_i - I_{\bar{i}})^3 \, . \tag{4.74}$$

Similarly, the fourth cumulant is

$$\kappa_{4,i}^{\text{net}} = \kappa_{4,i}^{\text{HRG}} + \kappa_{4,\bar{i}}^{\text{HRG}} + \langle (V\delta\sigma)^4 \rangle_c (I_i - I_{\bar{i}})^4 \, . \tag{4.75}$$

In order to generate discrete samples of particles and anti-particles of a specific kind, it is necessary to have not only the expression of the net but also of the total particle number cumulants. It is mathematically not possible to generate samples of protons and anti-protons where the net proton fluctuations follow those of the derived critical model and the total proton fluctuations the Poisson baseline. The reason is that if the sum of two independent Poisson distributed variables is of Poissonian nature, the two random variables are Poisson distributed as well (this is also known as Raikov's theorem [214]). Since the individual (anti-)proton numbers are affected via Eq. 4.68, the total proton number has to be affected by the critical field as well.

It is therefore necessary to also derive the expressions for the modification of the total particle number cumulants in response to the critical field which is in accordance with the derivation of the net particle cumulants. In compact form, the modification of the net and total particle number cumulant of a particle p and its anti-particle $\bar{p}$ for $n > 2$ can be written as

$$\kappa_{n,i}^{\text{net}} = \kappa_{n,i}^{\text{HRG}} + (-1)^n \kappa_{n,\bar{i}}^{\text{HRG}} + (-1)^n \langle (V\delta\sigma)^n \rangle_c (I_i - I_{\bar{i}})^n \tag{4.76}$$

$$\kappa_{n,i}^{\text{tot}} = \kappa_{n,i}^{\text{HRG}} + \kappa_{n,\bar{i}}^{\text{HRG}} + (-1)^n \langle (V\delta\sigma)^n \rangle_c (I_i + I_{\bar{i}})^n \, . \tag{4.77}$$

Fig. 4.16 shows the effect of the inclusion of the critical point on the net proton number cumulants. The upper and center rows are calculated from Eq. 4.76. The upper row shows only the HRG part, whereas the center row shows the term on the right-hand side of Eq. 4.76, the contribution of the critical field. The freeze-out curve shows the equilibrium values at different beam energies by Alba et al [215] (details will be explained later in this chapter). The lowest value in $\sqrt{s}$ probes the baryon dense regime of the QCD phase diagram whereas large $\sqrt{s}$ collisions probe ranges of low μ_B. One can see that in this case, where the critical point is located at $\mu_B = 390\,\text{MeV}$, the influence of the critical regions decreases when increasing the collision energy and between $\sqrt{s} \sim 11 - 25\,\text{GeV}$ the influence is the strongest.

After the cumulants including the critical mode have been described, in the step, the goal is to determine the probability distribution of the net and total particle numbers that generate these fluctuations.
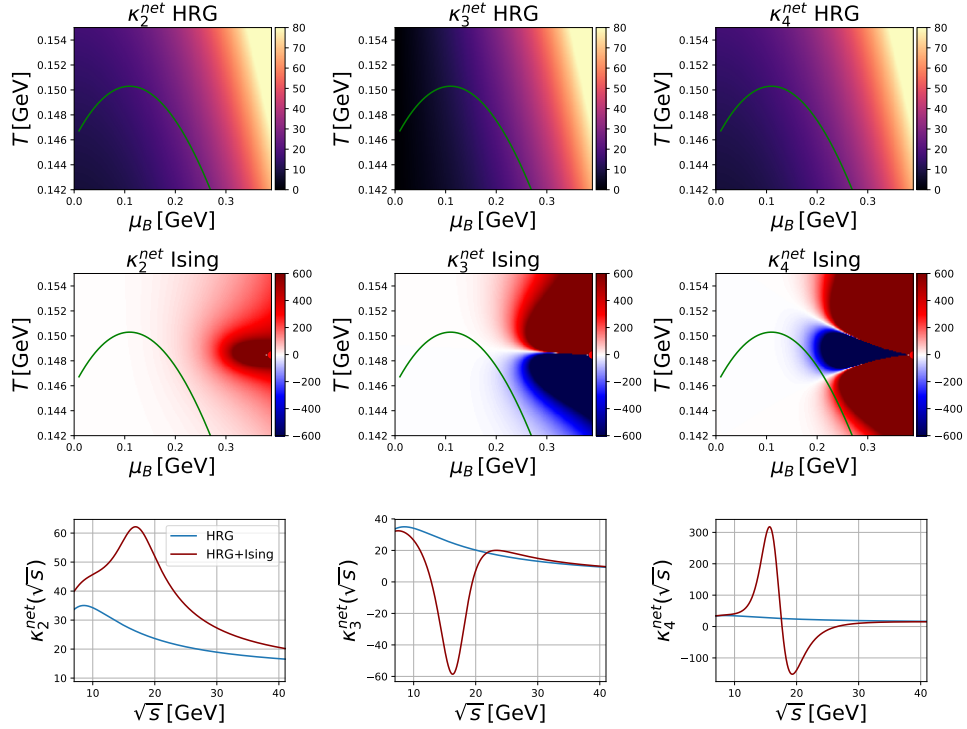
Figure 4.16: Second (left column), third (center column) and fourth (right column) net proton cumulants. The upper row depicts the HRG cumulants as a function of T and μ_B. The center row shows the critical contribution of the net proton cumulants $\delta f_p^{\mathrm{critical}}$ based on the mapping the 3D Ising model in the T-μ_B-plane of QCD. The coupling is chosen to be $g_c = 4$. In both the upper and center rows, the freeze-out curve by Alba et al. [215] is added as a green line. The bottom row shows the net proton cumulants along the freeze-out curve as a function of $\sqrt{s}$. The HRG cumulants plus the HRG cumulants are shown as a blue line and the HRG cumulants including the critical contribution are shown as red lines.

4.4.2 Maximum entropy method for freezing out critical fluctuations

The reconstruction of the probability distribution of a particle species coupled to the critical mode requires the full infinite set of cumulants (or moments). Since this set is not accessible, the reconstruction is a mathematically ill-posed problem. By imposing an additional criterion, however, the solution can be approximated. In this work, the criterion that the information entropy of the distribution function is maximized is employed. It is thought that distributions that are realized in nature do have a maximum information entropy [216]. It was also realized by Jaynes, that there exists a fundamental mathematical equivalence between the principle of maximum information entropy and statistical mechanics [217].

The Shannon information entropy (which is also equivalent to the entropy of the

canonical ensemble up to a factor of k_B) of a discrete probability distribution $P(x)$ is given by

$$S = -\sum_{x \in \Omega} P(x) \ln P(x) \,, \tag{4.78}$$

where Ω is the support of $P(x)$. By enforcing S to be maximized using Lagrange-multiplier λ, one can derive the expression of $P_\lambda(x)$ in the following way. Starting with the Lagrangian

$$H = -\sum_{x \in \Omega} P(x) \ln P(x) - \sum_k \lambda_k \left[\sum_{x \in \Omega} f_k(x) P(x) - F_k \right] - \mu \left(\sum_{x \in \Omega} P(x) - 1 \right) \,, \tag{4.79}$$

where $f_k(x)$ and F_k are functions representing the k number of constraints which are used to maximize S. To reconstruct the critical distributions for the number of (net/total) particles x, the quantities of interest are the moments of $P(x)$ so $f_k(x)$ and F_k can be identified as

$$f_k(x) = x^k \,, \qquad F_k = \mu_k \,. \tag{4.80}$$

The constraints to maximize Eq. 4.79 are

$$\frac{\delta H}{\delta P(x)} \stackrel{!}{=} 0 = -\sum_k \lambda_k x^k - 1 - \ln P(x) - \mu \,. \tag{4.81}$$

And one obtains

$$P(x) = \exp\left\{ -(1+\mu) - \sum_k \lambda_k x^k \right\} \,. \tag{4.82}$$

It is useful to define the partition function in the following way

$$Z_{\tilde{\lambda}} = \sum_{x \in \Omega} \exp\left\{ -\sum_k \lambda_k x^k \right\} \,. \tag{4.83}$$

Here, $\tilde{\lambda} = (\lambda_1, .., \lambda_k)$ and one can then rewrite

$$(1+\mu) = \ln Z_{\tilde{\lambda}} \,. \tag{4.84}$$

Together with $Z_{\tilde{\lambda}}$, the normalized maximum entropy (ME) probability distribution can be written as

$$P(x) = Z_{\tilde{\lambda}}^{-1} \exp\left\{ -\sum_k \lambda_k x^k \right\} \,. \tag{4.85}$$

To obtain the parameters λ, one would in an optimal case find an analytic relation between them and the coupled HRG + 3d Ising model. A similar work has been performed in [218], where distributions with viscous corrections were obtained from the ME principle. This however is not in the scope of this thesis and is left for future work.

The input conditions for the probability distribution function is the k-th moment

$$\mu_k = -\frac{\partial \log Z_{\tilde{\lambda}}}{\partial \lambda_k} = Z_{\tilde{\lambda}}^{-1} \tilde{\mu}_k \,. \tag{4.86}$$

With the input of in total n moments from the critical model (in this work, it is fixed to $n = 4$), one obtains n equations that have to be solved for $\tilde{\lambda}$. The conversion from cumulants to non-central moments can be done in the following, straightforward way

$$\mu_1 = \kappa_1 \,, \tag{4.87}$$

$$\mu_2 = \kappa_2 + \kappa_1^2 \,, \tag{4.88}$$

$$\mu_3 = \kappa_3 + 3\kappa_2\kappa_1 + \kappa_1^3 \,, \tag{4.89}$$

$$\mu_4 = \kappa_4 + 4\kappa_3\kappa_1 + 3\kappa_2^2 + 6\kappa_2\kappa_1^2 + \kappa_1^4 \,. \tag{4.90}$$

These four equations are solved using a Newton method together with the Jacobian which reads

$$J_{n,m} = \frac{\tilde{\mu}_m \tilde{\mu}_n}{Z(\tilde{\lambda})^2} - \frac{\tilde{\mu}_{m+n}}{Z(\tilde{\lambda})} \,. \tag{4.91}$$

The obtained distribution function is not necessarily the exact physical distribution of the particle number distribution. However, it is the one with the maximum amount of uncertainty given that only the first four cumulants from the 3d Ising model are currently available with the parametrizations in [208], the maximum entropy distribution is the "least biased" estimate of the critical particle number distribution that one can make with the given information.

It is also worth mentioning that the particle number distribution from the HRG model follows a Poisson distribution which itself is a distribution of maximum entropy. Therefore, in the limit $g_c \to 0$ of the coupling to the critical mode, the baseline distribution is restored. On the other hand, with the current technique, it is not possible to go to infinite values of the coupling strength with this approach. At some point, numerical difficulties arise to obtain reasonable values of the Lagrange multiplier in the sense that the probability distribution is well-behaved on the support Ω. In Fig. 4.17, this behavior can be seen where the ME distribution is shown, depending on the coupling strength to the critical mode g_c. Starting at $g_c = 6$ a minima appears in the tails of the total proton distribution around small values of N^{tot}. The reason is that with the fourth cumulant growing rapidly as the coupling strength increases, the root solver only finds negative values of the fourth Lagrange multiplier $\lambda_4 < 0$. As a result, $P(x)$ starts to grow again in $x \to \max(\Omega)$. It has been tested that increasing the upper value of the bound Ω does not solve this problem. An inclusion of the constraint $\lambda_4 > 0$ to the root solver has been tried, but did not work either. Another reason could be that the given information is not sufficient anymore to control the tails of the distribution. Adding more cumulants as input could resolve this issue, however, this is not in the scope of this thesis. In the other limit, $g_c \to 0$ one can see that the ME distribution converges towards the Poisson and Skellam distribution as it was already explained. This example confirms that the numerical implementation works as expected.
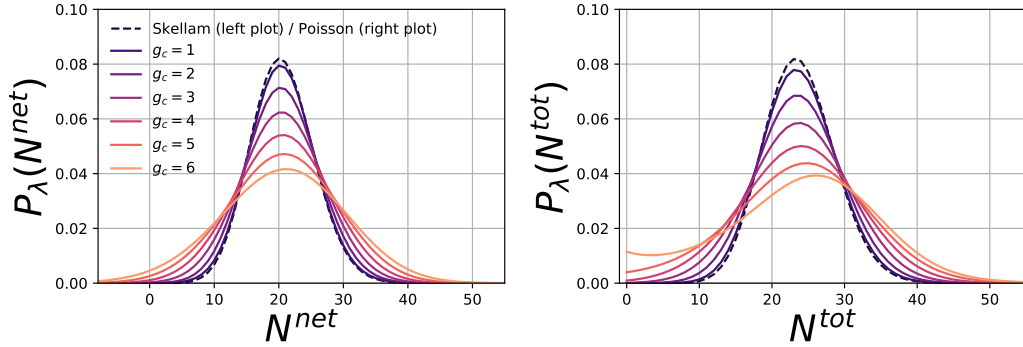
Figure 4.17: Net (left) and total (right) proton distribution as a function of the number of the net/total particle number. The ME distributions are presented for different values of coupling strength to the critical mode. The thermodynamic quantities are taken at the value of $\sqrt{s} = 19\,\text{GeV}$. The dashed line shows the respective HRG baseline distribution.

There also exist other possibilities to reconstruct probability distributions given a finite set of moments. They have failed for different reasons, but it is still worth mentioning those tries here, even though the physical motivation for using the maximum entropy principle is much more grounded. One alternative that has been tried is using the cumulant-generating function Eq. 4.2. One can see that the probability distribution serves as an input at the moment-generating function Eq. 4.1, since it is calculated from the expectation value of e^{xt}. By inverting the expression using an inverse Fourier transformation, one can express the probability distribution in terms of the cumulant-generating function K with

$$P(x) = \frac{1}{2\pi} \int_{-\pi}^{\pi} e^{-ixt} e^{-K(t)} dt \,. \tag{4.92}$$

Within this approach, however, the difficulty lies in evaluating the finite sum in the exponential $e^{-K(t)}$. As the higher-order cumulants close to the critical point grow very rapidly, the exponential of this series does even more. As a result, it gets numerically very demanding to evaluate the integral above. In addition, the convergence of the series is not known so the problem falls back to the issue that only the first four cumulants are known from the model. Other approaches that are worth mentioning are expanding $P(x)$ in terms of orthogonal polynomials or using fixed expressions of distribution e.g. the Pearson distribution family. Unfortunately, none of those were able to achieve accuracies such as the maximum entropy distributions.

4.4.3 Modeling the initial state of the medium

This section describes the modeling of the initial state of the simulation in both momentum and coordinate space. With the goal to initialize the transport model with critical equilibrium fluctuations to study their evolution, one needs the initial phase space information of the particles which, in this work, is called the initial state.

The temperature and chemical potentials of the initial state are obtained from the chemical freeze-out curve [215], that maps the beam energy $\sqrt{s_{NN}}$ of a heavy-ion collision to equilibrium values of temperature T and chemical potentials $\mu_{Q,B,S}$. This specific estimate is based on the analysis of net-electric charge and net-proton number fluctuations of experimental measurements. The parameterization used here originates from [208] and reads

$$\mu_X^{\mathrm{fo}}(\sqrt{s}) = \frac{d_X}{(e_X\sqrt{s} + f_X)^{g_X}} \, , \tag{4.93}$$

$$T^{\mathrm{fo}}(\sqrt{s}) = t_0 + t_1\mu_B^{\mathrm{fo}} + t_2(\mu_B^{\mathrm{fo}})^2 + t_4(\mu_B^{\mathrm{fo}})^4 + t_6(\mu_B^{\mathrm{fo}})^6 \, . \tag{4.94}$$

The individual parameters for the freeze-out values of the baryon, electric and strangeness chemical potential are displayed in Tab. 4.1. The parameters in Eq. 4.94

X	$d_X/\,\mathrm{GeV}$	$e_X/\,\mathrm{GeV}^{-1}$	f_X	g_X
B	1.161	0.392	-0.481	0.910
Q	-0.386	2.822	12.319	1.070
S	0.848	1.138	1.297	0.995

Table 4.1: Values of parameter in Eq. 4.93 for the chemical potential of conserved charges.

are $t_0 = 0.146\,\mathrm{GeV}$, $t_1 = 0.079\,\mathrm{GeV}$, $t_2 = -0.366\,\mathrm{GeV}$, $t_4 = 0.251\,\mathrm{GeV}$, $t_6 = -0.107\,\mathrm{GeV}$.

Furthermore, the hadrons are sampled uniformly within a sphere of radius R and the momentum space of the particles is obtained from the modified Boltzmann distribution

$$f_{i,k}^{(0)} = e^{(-u\cdot k_i)/T} \, . \tag{4.95}$$

Here, u is a velocity field that has been introduced to reproduce experimentally measured momentum distributions [219, 220].

$$\vec{u}(r) = \vec{e}_r u_0 r/R \, . \tag{4.96}$$

In the equation above, $\vec{e}_r$ is the radial unit vector on the sphere of radius R and u_0 is a parameter that is obtained from experimental measurements. Fig. 4.18 shows the mean expanding velocity, equivalent to u_0, defined in Eq. 4.96. The beam energy region of interest is between $\sqrt{s} = 7 - 50\,\mathrm{GeV}$. So for simplicity, the value of u_0 is taken as $u_0 = 0.5$ for all values of $\sqrt{s}$. The radius is fitted to the multiplicities with $R = 9\,\mathrm{fm}$.

Fig. 4.19 shows the p_T spectra of pions and protons measured by STAR at beam energies between $\sqrt{s} = 7.7 - 27\,\mathrm{GeV}$ in midrapidity [220]. The comparison to the results from SMASH shows that the single-particle distribution function Eq. 4.95 is well described by the chosen parameter set between $\sqrt{s} = 11 - 27\,\mathrm{GeV}$, whereas at $7.7\,\mathrm{GeV}$ the results don't exactly match. The anti-proton spectra are slightly underestimated. So far, only a spherical symmetric expansion is considered. In principle, the model could be improved towards a Blastwave description with a
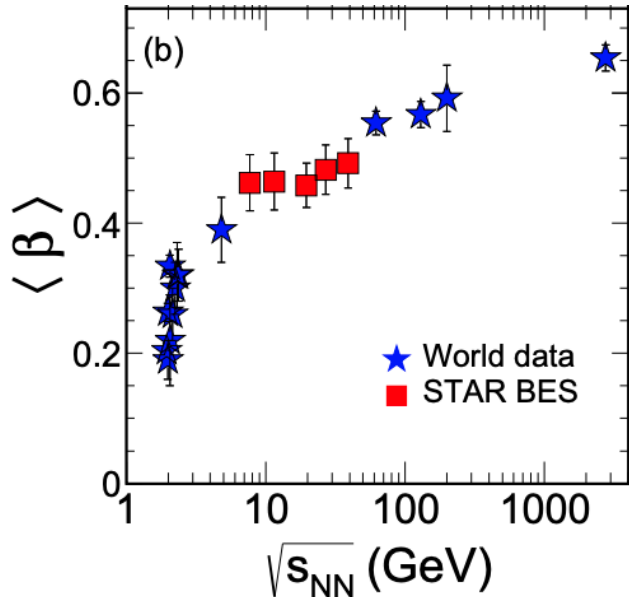
Figure 4.18: Expansion parameter β as a function of $\sqrt{s}$. Figure is taken from [220].

longitudinal expansion, see e.g. [219]. However, this is left for future work and the longitudinal dynamics are considered at this stage.

In the case of a coupling of the particle distribution to the critical mode, first, samples of $N^{\text{net/tot}}$ have to be generated from the ME distributions by sampling their cumulative distribution function. Since the transport model evolves the single-particle distribution function, one needs to generate samples of the particle and anti-particle numbers respectively. As not all pairs of net and total particle numbers are valid in the sense that they correspond to a positive integer-valued number of (anti)particles, one still has to find valid pairs in $\{N^{\text{net/tot}}\}$. This is achieved by simply searching for valid partners within $\{N^{\text{Net}}\}$ and $\{N^{\text{Tot}}\}$ and removing them from the samples.

Fig. 4.20 shows the net and total proton number cumulants up to the fourth order along the freeze-out line. The results of the ME samples were computed from the proton and anti-proton samples for a coupling of $g_p = 2$ and $g_p = 4$ to the critical mode. This result shows that the methodology successfully reproduces simultaneously the net and total proton cumulants up to the fourth order at a given value of $\sqrt{s}$.

It is worth mentioning that the generated critical distribution functions originate from an averaged sigma field over the whole volume $\langle\sigma(x)\rangle$, which is not necessarily correct since possible spatial dependencies are ignored. A more detailed description however is left for future work.

In the next step, these distributions in each point in $\sqrt{s}$ are evolved in the hadronic transport approach to see, how they get affected. To examine the influence of the evolution on the cumulants, different values of the coupling strength are used, where two cases are considered. The first case is where only protons and neutrons are coupled to the critical field. For the second case, more hadronic species are coupled and the following phenomenological approach to determine the coupling strength is
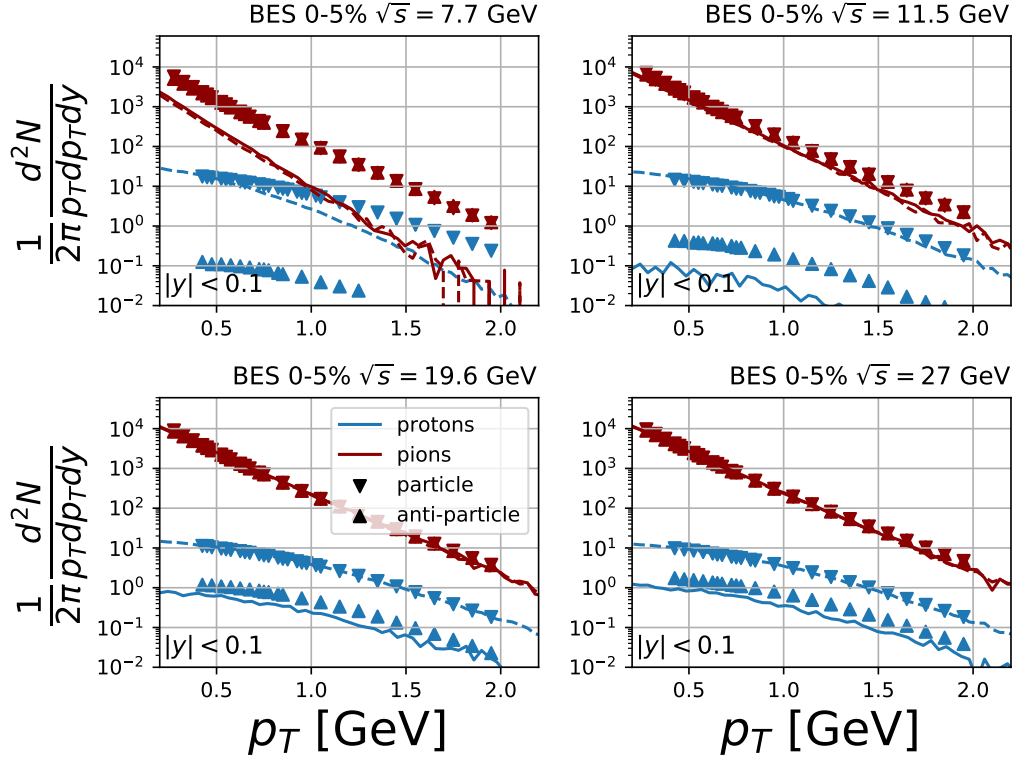
Figure 4.19: p_T spectra of protons (blue) and pions (red) at various different measurements of $\sqrt{s}$. The lines show the result from SMASH (the full line shows particles and the dashed line shows anti-particles) and the symbols the measurement by the BES collaboration. Experimental data points are taken from [220]

used [208]

$$g_R = \frac{g_c}{N_q} \frac{m}{m_R} (N_q - |S_R|). \tag{4.97}$$

Here, N_q is the number of valence quarks of the hadron, g_c and m the coupling and mass of the respective stable hadron and $|S_R|$ the absolute strangeness number. To summarize, three different coupling scenarios will be studied in the following sections:

- Couple only nucleons to the critical field using $g_c = 2$.

- Couple only nucleons to the critical field using $g_c = 4$.

- Couple particle species listed in App. A.6 with a baryonic and mesonic coupling of $g_c = 2$ (denoted as $g_c = 2+$).

With these three cases, the influence of the coupling strength can be studied. As the methodology of determining the critical probability distribution faces numerical issues when going to large values of the coupling strength g, this model is restricted to the relatively small value of the coupling in the $g_c = 2+$ case.
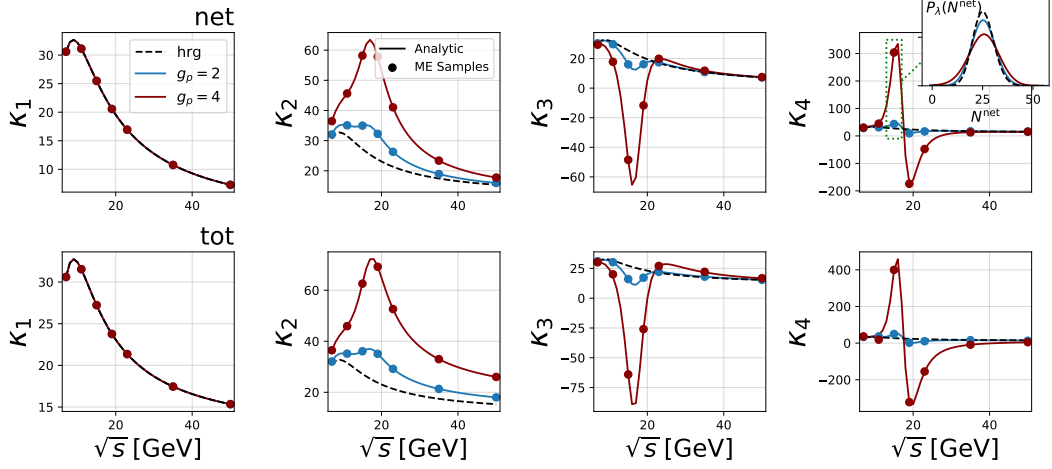
Figure 4.20: Net (upper row) and total (lower row) proton number cumulants as a function of $\sqrt{s}$ up to fourth order (from left to right). The analytic HRG baseline (grey dashed), as well as the calculation including the critical mode with a coupling of $g_p = 2, 4$ (full blue and red), are presented. In addition, the results from the generated particle samples are presented as red circles and the reconstructed net proton numbers from the ME distributions are shown for $\sqrt{s} = 15\,\text{GeV}$ plus the Skellam distribution in the inlet.

Finally, no modifications in momentum space are included even though it is expected that the critical mode affects them as well.

4.4.4 Thermodynamic evolution and collision chemistry of the medium

In the first step, the goal is to study the thermodynamic properties of the expanding sphere by determining the temperature and baryon chemical potential after the evolution of the medium. The thermodynamic evolution of the medium in terms of temperature and baryon chemical potential is shown in Fig. 4.21. For each point along the freeze-out curve a thermal model fit is performed on the final state of the evolution to obtain the equilibration values of the temperature, the chemical potentials as well as the volume. Here, the multiplicities of the following stable particles: $N, \pi, K, \Sigma, \Lambda$, plus their respective anti-particles are used. Together with Eq. 4.20 one then minimizes the following function to obtain the thermodynamic quantities plus the volume of the system

$$\chi(T, V, \mu_{B,Q,S}) = \frac{1}{N_{\text{species}}} \sum_{i}^{N_{\text{species}}} \left(N_i^{\text{SMASH}} - V n_i(T, \mu_{B,Q,S}) \right)^2 . \qquad (4.98)$$

One such a fit is shown in Fig. 4.22 for the $\sqrt{s} = 11\,\text{GeV}$. One can see that for the presented particles, the fit well reproduces the number of particles with the
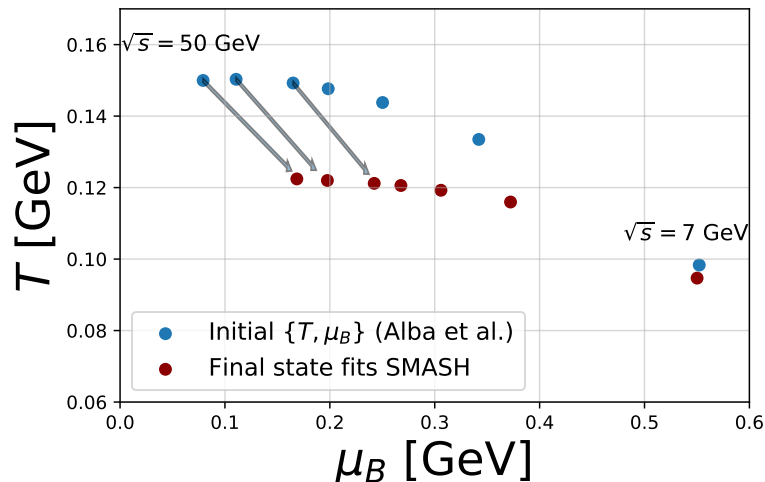
Figure 4.21: Evolution of the temperature and baryon chemical potential of the expanding medium. The initial state values are shown as blue and the final state values as red points.

exception of the anti-protons. It is not clear at this point where this difference comes from.

The final state is obtained by evolving the system until no interactions are occurring anymore and all resonances that are still present in the simulation are decayed into the ground states. It is found that the kinetic freeze-out is reached at approximately $t = 100\,\mathrm{fm}$, note that this is not a realistic average time for freeze-out in a realistic scenario, but the final time after the last interaction in our simplified spherical geometry occurs.

As the hadron gas including its resonances is initialized according to the temperature and chemical potentials from the freeze-out curve, the final thermodynamic values are expected to change as the chemical composition of hadron gas changes. The temperature of the system is found to be decreasing and the baryon chemical potential increases for the systems initialized at large $\sqrt{s}$ energies, due to the decay of heavy resonances.

In the next step, the collision chemistry of the expanding hadronic system is investigated. By doing so, one can directly observe which types of interaction are the most important ones during the evolution. Fig. 4.23 shows the number of specific collision channels as a function of time. In this example, an energy of $\sqrt{s} = 15\,\mathrm{GeV}$ has been chosen. It has been checked that similar results are obtained at other beam energies. From Fig. 4.23, one can see that during the whole evolution, the resonance decays, followed by resonance formations are the most dominant types of interaction. Inelastic $2 \rightarrow 2$ scatterings are on the order of $\sim 1\%$ and finally, the string formation processes play only a subdominant role during the expansion.

In [221], it has been derived how resonance decays affect particle number cumulants. The decay chain of unstable resonances into stable particles yields a source
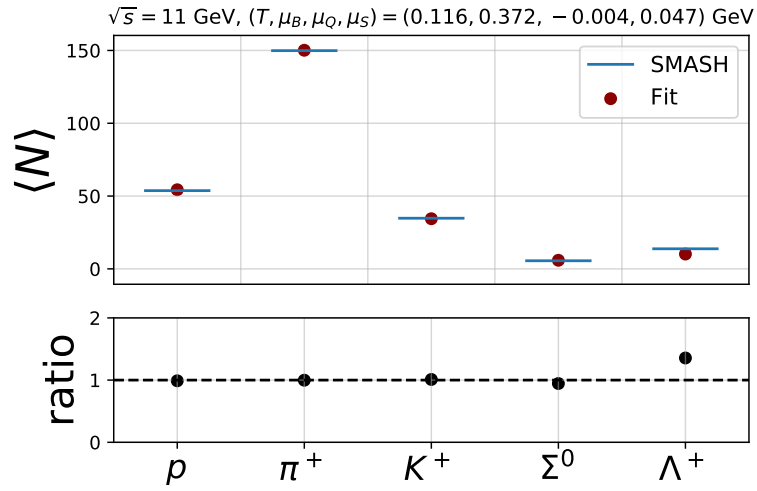
Figure 4.22: Yields from SMASH (blue line) and thermal model fit (red points) for $\sqrt{s} = 11\,\mathrm{GeV}$ of the most abundant stable particles.
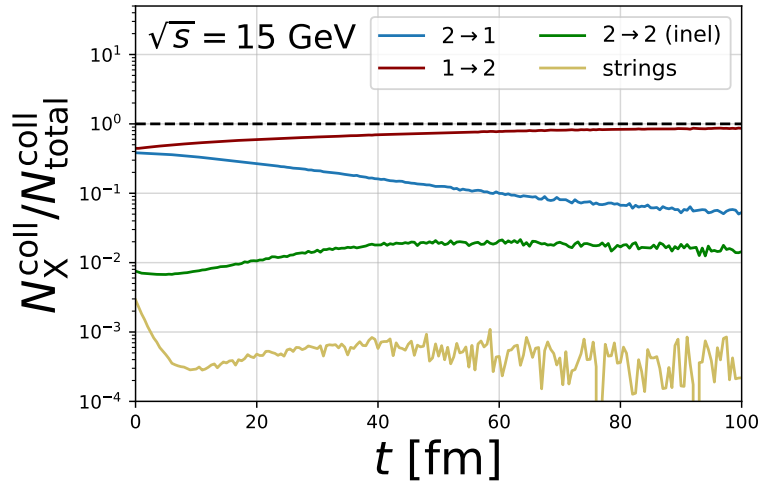

Figure 4.23: Number of resonance decays (red), resonance formations (blue), inelastic $2 \to 2$ (green) and string formation (yellow) normalized to the total amount of collisions as a function of time.

of fluctuations effectively increasing the cumulants. In the system studied here, an additional source of fluctuations exists as resonances can be newly formed resulting in a non-trivial interplay between formation and decay processes. In addition to the generation of resonances, they can also be created in inelastic $2 \to 2$ collisions such as $NN \to NN^\star$, even though these reactions are of sub-leading order, they do have an effect on the net proton number since they, first, reduce the net proton number at the time of the collision and second, randomize the isospin in the time of the decay

of the resonance, which additionally modifies the net proton cumulants.

4.4.5 Time evolution

In this section, the evolution of the individual cumulants as a function of time will be discussed. By doing so, one can distinguish the impact of different phases of the evolution on the fluctuations. Fig. 4.24 shows the evolution of the net proton and
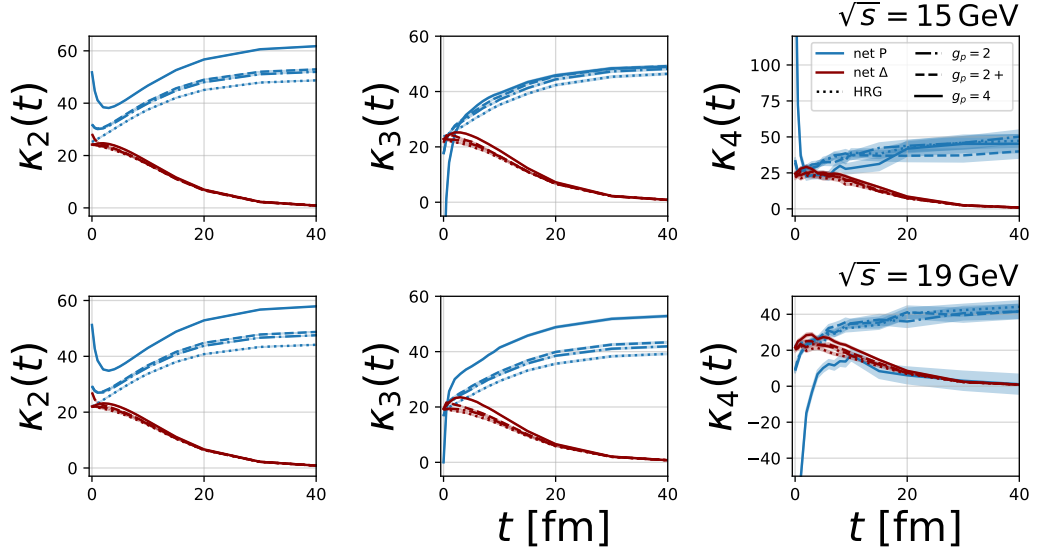

Figure 4.24: Time evolution of the net proton (blue) and net delta (red) cumulants as a function of time. The second (left column), third (center column) and fourth cumulant (right column) are shown for two energies $\sqrt{s} = 15\,\text{GeV}$ (upper row) and $\sqrt{s} = 19\,\text{GeV}$ (lower row). The results are presented for initializing the system with the cases $g_p = 2$ (dashed-dotted line), $g_p = 4$ (straight line) as well as the case where more hadron species are coupled to the critical field $g_p = 2+$ (dashed line) and finally the HRG model (dotted line). A momentum cut of $0.3 < p < 2.0\,\text{GeV}$ is included.

net delta cumulants as a function of time. Here, the two energies where the strength of the critical point is the strongest have been used. Note, that for $\sqrt{s} = 15\,\text{GeV}$, the system is initialized with $\kappa_4^{CP} \gg \kappa_4^{HRG}$, whereas for $\sqrt{s} = 19\,\text{GeV}$ $\kappa_4^{CP} \ll \kappa_4^{HRG}$. In addition, a cut on the absolute momentum of $0.3 < p < 2\,\text{GeV}$ is included in order to roughly mimic the experimental situation. Since the delta is the lightest baryonic resonance, its fluctuations and the interplay between the delta and proton cumulants are therefore shown as well.

First, the net proton fluctuations initialized with the HRG model show a strong increasing behavior over time for all presented cumulants. From a starting value of $\kappa_2(0) \approx 25$, the the variance nearly doubles to around $\kappa_2(40\,\text{fm}) \approx 50$. This is a result of an increasing (anti-)proton number, due to the decay of resonances during the evolution. The Δ-baryon cumulants of all presented orders show the opposite behavior and go to zero over time, as they decay into stable particles and

therefore the fluctuations vanish. A large difference between the cases where only nucleons are coupled to the critical mode ($g_p = 2$) or where a larger set of hadrons is coupled ($g_p = 2+$) is not observed. Even though increased net delta correlations exist in the initial state, they vanish within the first $\approx 5\,\text{fm}$. The difference between the net proton cumulants in the final state of the $g_p = 2$ and the $g_p = 2+$ case is approximately $\approx 2\%$. Going to the initialization with a stronger coupling to the critical mode $g_p = 4$, a strong modification of κ_n within the first 5 fm towards the HRG case is found within the first $\approx 5\,\text{fm}$. After the first couple of fm, the fluctuations start rising again and the correlations from the critical field are propagated to the final state in both $\sqrt{s} = 15\,\text{GeV}$ and $\sqrt{s} = 19\,\text{GeV}$. The evolution of the third cumulant $\kappa_3(t)$ is similar to $\kappa_2(t)$. From the initial value at $t = 0$, κ_3 strongly increases. In the case of negative initial value at $\sqrt{s} = 15\,\text{GeV}$, the signal from the critical point gets completely washed out and the sign of κ_3 changes. Contrary to $\sqrt{s} = 15\,\text{GeV}$, it is observed that at $\sqrt{s} = 19\,\text{GeV}$, correlations from the critical field survive the hadronic evolution. Similarly to $\sqrt{s} = 15\,\text{GeV}$ though, $\kappa_3(t)$ starts from $\kappa_3^{critical}(0) \ll \kappa_3^{\text{HRG}}(0)$ but ends with correlations $\kappa_3^{critical} \gg \kappa_3^{HRG}$. Similarly to the second and third cumulant, the fourth order cumulant is strongly affected within the first couple of fm. Here, the strong correlations in the initial state are reduced towards the HRG baseline. In the final state for $\sqrt{s} = 15\,\text{GeV}$, the value of κ_4 evolves towards the HRG evolution and in the final state, no difference within the errors can be observed. In the case $\sqrt{s} = 19\,\text{GeV}$ where $\kappa_4(0) \ll 0$, correlations from the critical point survive the hadronic evolution and are present in the final state. In addition, it is observed that e.g. $\kappa_3(t)$ at $\sqrt{s} = 19\,\text{GeV}$ in the case $g_p = 4$ the net delta correlations increases before going down to zero. In this case, the Δ-baryons are not coupled to the critical mode meaning that correlations from the net protons are passed between the different particle species in the transport model.

In the next step, the origin of the modifications of the net proton correlations at the beginning of the expansion is discussed. By switching specific interaction channels on and off, one can study the dependency of the evolution of the fluctuations on the collision kernel of the transport simulation. Fig. 4.25 shows the impact of specific interaction channels on the evolution of the net proton number cumulants. It is observed that the resonance formation and decays are not only the most occurring interactions during the evolution (see Fig. 4.23), but also the ones that have the largest effect on the evolution of net proton cumulants as a function of time.

When switching only to (in)elastic $2 \leftrightarrow 2$ interactions $\kappa_2(t)$ only slightly decrease when initialized with a coupling to the critical field. In contrast, when initialized using the HRG model the cumulants slightly increase. Now, in the case in which $2 \leftrightarrow 2$ interactions are switched off and only $2 \leftrightarrow 1$ interactions are considered, a much stronger effect on the cumulants in contrast to performing only $2 \leftrightarrow 2$ reactions can be seen. Here, a similar evolution as in the case of the full collision kernel is found. This shows that the resonance formation/decay processes have the strongest influence on the net proton correlations and the decays are responsible for the increase over time. In the case of $g_p = 4$, $\kappa_2(t)$ decreases until a minimum is reached around $t \approx 3\,\text{fm}$. Then, the variance grows again until it saturates. The reason for the non-monotonic behavior, when initialized with a coupling to the critical field is, that
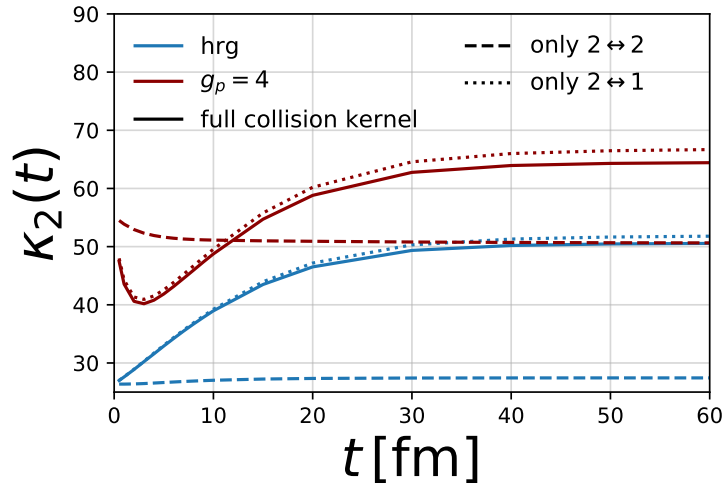
Figure 4.25: Time evolution of the second net proton cumulants as a function of time. The system is initialized using the HRG (blue lines) and with a coupling of $g_p = 4$ (red lines). The results of different simulations using the full collision kernel (straight line), employing only $2 \leftrightarrow 1$ interactions (dotted line) and (in)elastic scatterings (dashed line) are shown.

within the first stage of the expansion, resonances are created from interactions with a (anti-) proton in the initial state. As a result, the net proton fluctuations decrease in the first timesteps. After the initial resonance formations however the formed unstable particles decay and increase correlations between protons and anti-protons which is responsible for the increase of the variance. This effect is also observed for the HRG initialization. It has been checked that the discussed results for the second cumulants also hold for the κ_3 and κ_4.

4.4.6 Isospin fluctuations

In this section, the goal is to quantify the effect of the dynamical expansion of the hadronic medium on the final state cumulants. It has been shown that the largest sources of fluctuations are resonance formations and decays, which feed into the proton spectra. During the expansion of the medium and especially in the final state, there are of course no unstable particles left, but on top of the pure resonance decay processes, there are many scatterings and resonance regeneration processes that affect the cumulants in a different way. It is therefore useful for our purpose to define the following quantity

$$\tilde{\kappa}_n = \frac{\kappa_n^{\text{dynamical}}}{\kappa_n^{\text{decays}}} \ . \tag{4.99}$$

Here, $\kappa_n^{\text{dynamical}}$ are the final state cumulants after the dynamical expansion of the hadronic medium. On the other hand, one can also directly perform the decays

without evolving the medium dynamically and measure the cumulants which are denoted as κ_n^{decays}. The latter case is similar to calculations performed e.g. in [222, 223, 208]. Pure decays alter the cumulants of the net proton cumulant with feed-down processes. As an example, the mean net proton number is modified in the following way

$$\kappa_1 = \langle N_p \rangle - \langle N_{\bar{p}} \rangle + \sum_R \langle N_R \rangle (\langle n_p \rangle_R - \langle n_{\bar{p}} \rangle_R). \qquad (4.100)$$

Here, $\langle n_p \rangle_R = \sum_r b_r^R n_{i,r}^R$ is the average number of protons originating from all decay channels with branching ratios b_r^R. Within the transport code the above equation for the mean plus the ones for the higher order cumulants are performed on a Monte Carlo basis, where additional fluctuations arise due to the mass-dependent decay width $\Gamma(m)$ of each resonance and their sampled masses from the thermal spectral function $\mathcal{A}(m)$.
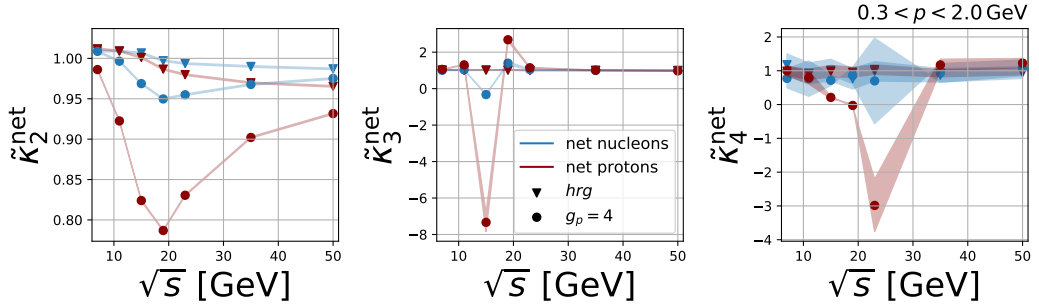

Figure 4.26: $\tilde{\kappa}_n$ as a function of $\sqrt{s}$ including a cut in momentum space for net proton (red) and net nucleon (blue) fluctuations. The results are shown for the hrg initialization (triangles) and with a coupling of $g_p = 4$ to the critical field (circles).

Fig. 4.26 shows the results of Eq. 4.99 as a function of the $\sqrt{s}$. In the case of initialization with the HRG model, a difference from unity in the second net proton cumulant $\tilde{\kappa}_2$, where a suppression of the dynamically evolved cumulant of $\approx 2\%$ is observed. A large portion of this suppression originates from isospin randomization processes since $\tilde{\kappa}$ of nucleons is not strongly affected. For example, the process $p\pi^0 \leftrightarrow \Delta^+ \leftrightarrow n\pi^+$ modifies the proton number, whereas the nucleon number is not affected. Within the errors, no difference from unity can be observed in the ratios $\tilde{\kappa}_3$ and $\tilde{\kappa}_4$.

If the system is initialized with a coupling of nucleons to the critical mode, larger modifications of $\tilde{\kappa}$ are observed. Similar to the HRG initialization, on the level of the second cumulants, a suppression of $\tilde{\kappa}_2$ of the final state cumulants after the dynamical evolution with respect to performing only the decays is seen. However, in this case, the suppression is on the order 20% at $\sqrt{s} = 19\,\text{GeV}$. As already described in the HRG case, the suppression originates from isospin randomization processes as the net nucleon fluctuations are less affected.

For the third and fourth cumulant, a strong modification in $\tilde{\kappa}_n$ is observed. The expansion of the medium at $\sqrt{s} = 15\,\text{GeV}$ evolves the third net proton cumulant

from a value $\kappa_3 \ll 0$ towards $\kappa_3 \gg 0$ (see e.g. Fig. 4.24), whereas the evolution using only decays preserve the negative skewness from the initial state. As a result, the ratio $\tilde{\kappa}_3$ changes its sign around the region where the signature of the critical point is the strongest.

It is found that the dynamical evolution modifies the net proton κ_4 in a similar way compared to the third cumulant. In the scaling region of the critical point, the strong correlations get washed out by the hadronic interactions whereas performing only decays preserve these correlations. Additionally, one can see that at $\sqrt{s} = 15\,\mathrm{GeV}$ and $\sqrt{s} = 19\,\mathrm{GeV}$, where the initial values are either $\kappa_4^{\mathrm{initial}} \gg 0$ or $\kappa_4^{\mathrm{initial}} \ll 0$, the cumulants in the final state are differently strong affected. The dynamical evolution washes out a strong positive initial κ_4 towards the HRG baseline, whereas performing the resonance decays preserves these initial correlations. The sign change in $\tilde{\kappa}_4$ originates from the fact that initial $\kappa_4^{\mathrm{initial}} \ll 0$ evolve towards positive κ_4 above $\sqrt{s} = 19\,\mathrm{GeV}$. Again, this change can be attributed to the isospin randomization processes as described above.

4.4.7 Final state observables

In this section, the goal is to present ratios of the final state cumulants after the full dynamical evolution of the hadronic medium. The results are presented with the same cuts in momentum space as before. Since this work is not in the stage of making any comparisons to experimental measurements, no experimental data points are included yet.

Fig. 4.27 shows the scaled variance, skewness and kurtosis of the final state after the dynamical evolution. Starting with the HRG initialization, one can see that both the net proton and net nucleon fluctuations are on top of the analytic initial state line. This means that the previously discussed effects of resonance regeneration processes and isospin randomization equally affect $\kappa_{2,3,4}$. As a result, the ratios are in line with the HRG expectation.

In the case of $g_p = 2$, the net proton cumulants of the final state are found to contain very little correlation from the critical point. σ/M shows a slight enhancement near the scaling region of the CP. Higher order cumulants however show no signs of the initial correlations. Due to fewer isospin fluctuations, the nucleon fluctuation contains more correlations in the final state in σ/M and $S\sigma$.

If the system is initialized with a stronger coupling of $g_p = 4$ it is observed that for all presented ratios of net proton cumulants, correlations from the critical point point survive the evolution of the hadronic medium, even though these correlations are much weaker than the ones from the initial state.

The ratio $\kappa\sigma^2$ shows a non-monotonic behavior similar to the initial state in comparison to the baseline curve. At $\sqrt{s} = 15\,\mathrm{GeV}$, where $\kappa\sigma^2_{\mathrm{initial}} \gg 1$, the final state value is ≈ 1, whereas at $\sqrt{s} = 19$ GeV where $\kappa\sigma^2_{\mathrm{initial}} \ll 1$ the final state value is ≈ 0. Similarly to $g_p = 2$, the net nucleon fluctuations show much larger correlations in the final state in comparison to the net proton cumulants. Even though the final state values are smaller in comparison to the initial state, the shape is very similar to what was put into. As a result and similar to the previous conclusions, isospin
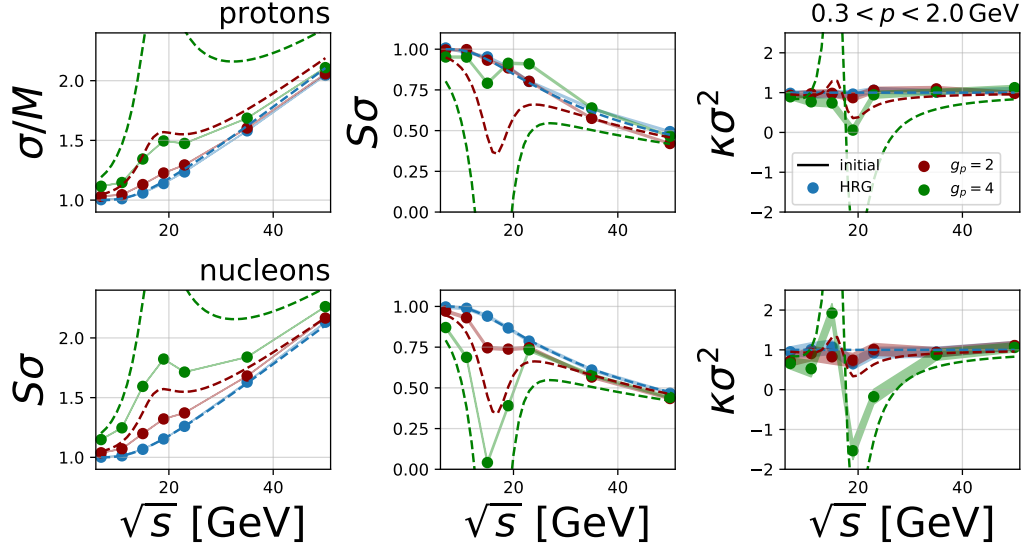
Figure 4.27: Ratios of final state proton (upper row) and nucleon (lower row) cumulants as a function of $\sqrt{s}$. The scaled variance (left column) and skewness (center) kurtosis (right column) are shown. The results from SMASH are shown as points for the HRG initialization (blue) and coupling nucleons to the critical field with $g_p = 2$ (red) and $g_p = 4$ (green) whereas the analytic results from the initial state are shown as dashed lines.

randomization processes are found to have a strong impact on the evolution of the cumulants.

4.4.8 Rapidity dependence

In this section, the dependency of the fluctuations as a function of the rapidity window $\Delta y = y_2 - y_1$ with $y = \frac{1}{2}\log((E + p_z)/(E - p_z))$ is investigated. This is important for comparison with experimental measurements where the cumulants are measured in momentum space and not the full phase space can be observed [219, 224]. It is worth noting that the dynamics of the system considered here are not the same as in heavy-ion collisions, since no distinct direction exists in the expanding sphere. However, for a comparison and in order to define the cuts in momentum space, the definition of rapidity and p_T is employed in this setup. The starting point is the integrated net proton density $n^{\mathrm{net}}(y, p_T)$ over a given rapidity and p_T interval. The total net proton numbers are obtained from the following integration

$$N^{\mathrm{net}}(\Delta y) = \int_{-\Delta y/2}^{\Delta y/2} dy \int_{0.3}^{2} dp_T \, n^{\mathrm{net}}(y, p_T) . \qquad (4.101)$$

From here, the cumulants $\langle (\delta N^{net}(\Delta y))^n \rangle$ are calculated in each rapidity interval and are shown as a function of Δy.
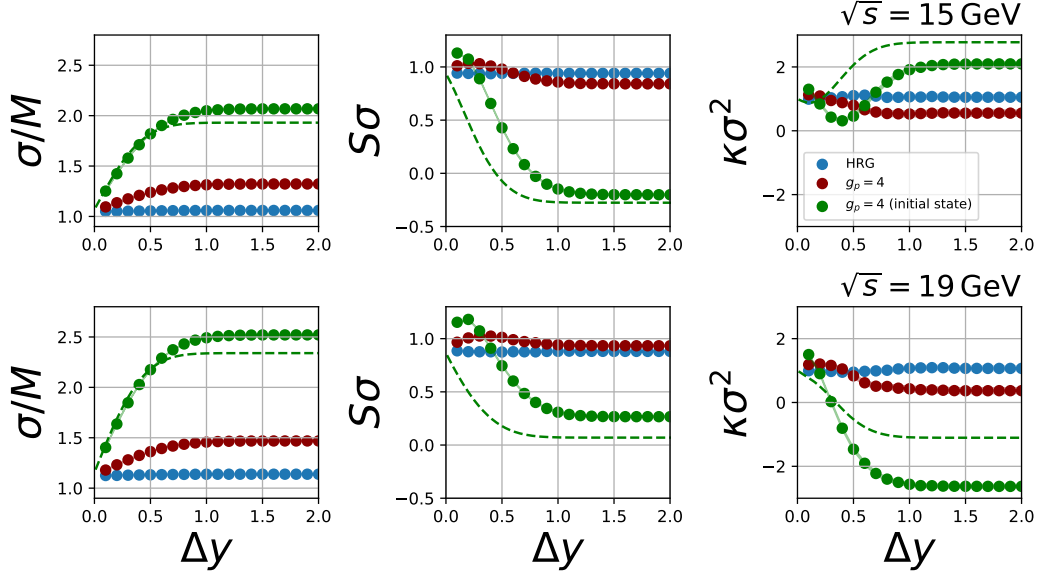
Figure 4.28: Net proton scaled variance (left), skewness (center) and kurtosis (right) as a function of the rapidity window Δy for $\sqrt{s} = 15\,\text{GeV}$ (upper row) and for $\sqrt{s} = 19\,\text{GeV}$ (lower row). The results of the initial (green) and final state (red) are shown for the case of $g_p = 4$ and the HRG (blue).

Fig. 4.28 shows the initial and final state ratios of cumulants as a function of the rapidity interval Δy. For the HRG results, no rapidity dependence is observed for both the initial and final state cumulants. This is expected as the system is initialized according to the grand canonical ensemble and therefore no correlations appear along the momentum directions. It is expected that the effects of global charge conservation have a strong influence on the rapidity dependence [183, 1]. When initialized with a coupling to the critical field, a difference between the initial and final state is observed. The scaled variance shows an increasing behavior with larger rapidity windows until it reaches a plateau. The difference between the initial and final state fluctuations is only in magnitude, whereas the shape is similar. The skewness starts at $S\sigma > 1$ with a positive slope at small rapidity windows, before decreasing. After the dynamical evolution, the strong correlations of the critical point vanish, however, the shape of the rapidity dependence is similar at the initial and final state. The maximum appears to grow towards a larger rapidity window. Similar to what has been shown in Fig. 4.27, the net proton skewness in the full rapidity window is above and below 1 for $\sqrt{s} = 15\,\text{GeV}$ and $\sqrt{s} = 19\,\text{GeV}$, even though $S\sigma \ll 1$ in the initial state. The kurtosis shows a similar behavior in the final state of the evolution as the skewness. The kurtosis is above unity for small rapidity windows $\Delta y < 0.5$ before decreasing to $\kappa\sigma^2 < 1$ at large rapidity windows. At $\sqrt{s} = 15\,\text{GeV}$ and compared to the initial state correlations the behavior of the final state kurtosis is opposite to the initial state. Similar to the skewness, the kurtosis, when initialized with $\kappa\sigma^2 \gg 1$, evolves towards $\kappa\sigma^2 < 1$. From Fig. 4.28 one can directly observe the importance of

the applied momentum cuts. Within this model, the strong correlations from the critical point appear at large acceptances whereas, when one only looks at small rapidity windows the fluctuations yield different results.

To understand the non-monotonic behavior of the rapidity dependence, one can also compare the results from the numerical simulation to semi-analytic ones. By splitting the momentum integral into transverse and longitudinal direction

$$\int d^3k \to \int k_T \sqrt{k_T^2 + m^2} \cosh y \, dk_T \, dy \, d\phi \,, \qquad (4.102)$$

where $k_T = \sqrt{k_x^2 + k_y^2}$ the transverse momentum and the rapidity $y = \frac{1}{2} \log \left(\frac{E + p_z}{E - p_z} \right)$. When splitting Eq. 4.19 and Eq. 4.71 in Eq. 4.76, the individual contributions can be investigated by solving the respective integrals numerically.
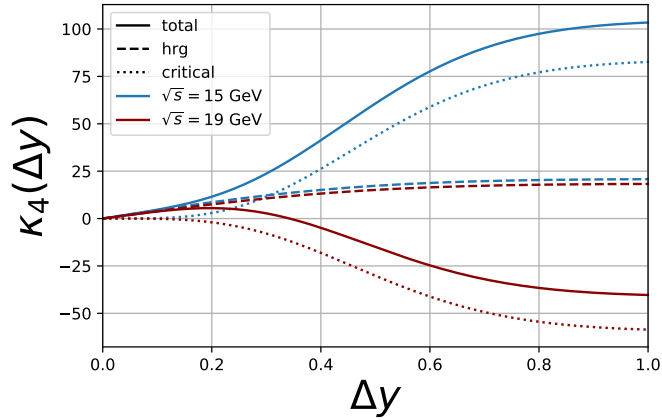

Figure 4.29: Net proton κ_4 as a function of the rapidity window Δy for two different energies $\sqrt{s} = 15\,\text{GeV}$ (blue) and $\sqrt{s} = 19\,\text{GeV}$ (red). The HRG (dashed) and the critical contribution (dotted) are shown as well as the total (full) result.

Fig. 4.29 shows the critical and baseline contribution to the rapidity dependence of the fourth cumulant. Starting with the HRG, $\kappa_4(\Delta y)$ increases with Δy starting at 0 until it saturates at some point. Contrary, the fourth cumulant of the critical contribution is zero until $\Delta y \approx 0.2$ when it starts growing towards its values in full phase space which is either strongly positive for $\sqrt{s} = 15\,\text{GeV}$ or negative for $\sqrt{s} = 19\,\text{GeV}$. As a result, the total fourth cumulant is dominated by the Poisson cumulants in small rapidity windows and the fourth cumulant at $19\,\text{GeV}$ is non-monotonic in Δy. For the sake of simplicity the equilibrium distribution function $f_{i,k}^0$ without radial or longitudinal modifications has been used for these results. However, it does show the difficulties when comes to measuring since detectors always have some cuts in rapidity which hinders measuring the full phase space cumulants. A more detailed investigation of this can be found in [224].

Summary

In this section, the influence of hadronic interactions on the evolution of critical fluctuations in a transport model has been studied. It has been shown in the first part, that the maximum entropy distribution successfully reproduces the first four cumulants from the HRG coupled to the 3d Ising model. In addition, the initial state in coordinate and momentum space was presented and the p_T-spectra compared to experimental results. Further, the expanding medium's thermodynamic evolution and collision types were investigated. In the next step, the time dependence of the cumulants was computed and it was found that resonance formation and decay processes have the strongest influence on the fluctuations. Then, the impact of isospin randomization processes and the final state net proton and net nucleon cumulants as a function of $\sqrt{s}$ were quantified. It has been shown that in the case of a coupling $g_p = 4$, correlations from the critical point survive the hadronic evolution and are present in the final state of the evolution and the rapidity dependence of the final state fluctuations are modified as well.

This study shows that, even without propagation of the critical field, the possibility exists that correlations associated with the critical field do survive the interacting hadronic medium in the case of a coupling of $g_p = 4$.

5

Modeling of heavy-ion collisions with global charge conservation

In this section, the goal is to study charge correlations within a hybrid approach of heavy-ion collisions. In the first part, a study of the effects of nuclear deformations on the initial state of hydrodynamical calculations is presented. In the second step, these initial states will be used for a hydrodynamic calculation and the effects of sampling the hypersurface using global charge conservation on final state event-by-event fluctuations will be investigated. The system of the colliding nuclei that will be used has been measured at the RHIC collider at BNL with the goal of studying the so-called chiral magnetic effect (CME), which will be explained in this section. Even though it is not the aim of this study to investigate the CME itself, it is still instructive to start with an introduction of what the goal of the experiment was.

In the year 2018, the RHIC experiment performed a measurement to detect the chiral magnetic effect [49]. The following will briefly discuss the underlying theory and the idea of the CME. The CME was proposed in [225, 226] and was already successfully measured in [227]. The observation of the CME from ultra-relativistic heavy-ion collisions is still pending. The goal of the CME is to measure unique vacuum properties of QCD, where domains of non-vanishing net axial charge are expected to be produced. The axial charge describes the difference between left and right-handed fields. It is a conserved quantity under the $U(N_f)_r \times U(N_f)_l$ transformation of a classical theory e.g. the Dirac Lagrangian. A quantization of such a theory however introduces an axial charge imbalance [228]. The resulting axial charge current j_5^μ is no longer a conserved quantity and the anomaly originates from multiple effects. First, the masses of fields introduce a breaking of the chiral symmetry and second, an anomaly occurs that originates from the Abelian field strength tensor. At high temperatures, where the quark masses can be neglected,

the anomaly can be approximated by

$$\partial_\mu j_5^\mu = -\frac{g^2}{16\pi^2} F_{\mu\nu}^a \tilde{F}^{a,\mu\nu}\,, \tag{5.1}$$

where $F_{\mu\nu}^a$ is the gluon field strength, $\tilde{F}^{a,\mu\nu}$ its dual and g the coupling strength. There are several contributing factors to the right-hand side of Eq. 5.1 that can appear at such high temperatures that are reached in heavy-ion collisions. The initial pre-equilibrium stage can be described by the Color Glass-Condensate, which employs the saturation scale and describes the initial dynamics of the collision purely with gluonic fields, governed by the classical Yang-Mills equation. This early gluon-dominated regime gives rise to a non-zero axial charge [229]. Another source producing imbalances are fluctuations of the chromo-electric and chromo-magnetic fields [230, 231]. Additionally, so-called sphaleron transitions which appear in the topological structures of the QCD vacuum induce axial charge imbalances [232, 233, 234] and these transitions have an increased rate at large temperatures.

The second mechanism that is important for measuring the axial charge imbalance is the strong magnetic field produced in a heavy-ion collision. In the case of peripheral collisions, where the number of spectators is large, very strong magnetic fields are thought to appear. The origin of these fields is the electric charges carried originally by the protons that have a velocity close to the speed of light. The resulting magnetic field strength is in the order of $eB \sim m_\pi^2 \sim 3 \cdot 10^{18}$ Gauss. In comparison, magnetars are assumed to produce magnetic fields of the order of $\sim 10^{14} - 10^{15}$ Gauss. In peripheral collisions, the spectators are separated from each other and have exactly opposite directions, therefore the resulting magnetic field has a distinct direction in the transverse plane. If an axial charge imbalance occurs during the time the magnetic fields are very strong, a separation of electric charge appears along the direction of $\vec{B}$, which is then called the CME. The origin of the effect of charge separation is the following: Consider a medium consisting of massless up and down quarks with equal amounts of left- and right-handed quark numbers as a starting point. In the massless limit, the chirality of a particle is proportional to the helicity which is defined as the projection of the momentum of the particle onto its spin. A left-handed particle has negative helicity with the spin and momenta pointing in opposite directions and a right-handed particle has the opposite property. In an external magnetic field, the spins will align along the field and if the total axial charge is zero, no charge separation appears because the amount of up and down quarks are equal. If however, an axial charge imbalance occurs during the lifetime of the medium this imbalance translates into an unequal amount of left and right-handed particles propagating along and in opposite directions to the magnetic field effectively separating the electric charge. The effective axial charge current $\mathbf{j}_5$ can be written as

$$\mathbf{j}_5 = \frac{N_c e}{2\pi^2} \mu_5 \mathbf{B}\,. \tag{5.2}$$

Here, μ_5 is the axial charge chemical potential associated with the axial charge Q_5.

To measure the CME in heavy-ion collisions the problematic issue is that one cannot directly control the external magnetic field in order to vary the charge

separation process, since the energy of the colliding nuclei is fixed. In addition, other processes might exist that generate a similar charge current that could be misinterpreted as the CME. The idea was then to conduct two experiments with nuclei with the same number of nucleons, in order to fix the background signal but with an unequal amount of protons to increase the magnetic field in one of the systems. Nuclei that have these properties are isobars and the ones that have been chosen are $^{96}_{40}$Zr and $^{96}_{44}$Ru and the energy of the collider is $\sqrt{s_{NN}} = 200\,\mathrm{GeV}$. Since the number of protons in Ru is larger it is expected that the signal of any observable O, that is thought to be sensitive to the CME should yield $O(\mathrm{Ru})/O(\mathrm{Zr}) > 1$. This however was not the case in the first measurement by STAR [49], where the ratio of all measurements lie below unity, see Fig. 26 in [49]. This result raises the question of whether one of the premises is correct for the two isobars. As it turned out, even though the two isobars have the same amount of nucleons, their nuclear shape is different which might lead to differences in the background of the CME observation. One of the experimental measurements, besides the CME signals for the charge separation, that can be used to estimate whether the background of the two isobaric collisions is the same, are flow observables that describe the distribution of the particle spectra in the transverse plane with the azimuthal angle ϕ. In the Fourier expansion, one can write

$$\frac{dN}{d\phi} = \frac{1}{2\pi}\left[1 + \sum_{n=1}^{\infty} 2v_n\cos(n(\phi - \psi_{RP}))\right] , \qquad (5.3)$$

where v_n are the flow coefficients and ψ_{RP} is the reaction plane of the collision. The ratio of v_2 as a function of the centrality of Ru/Zr measured by STAR already shows a non-trivial shape (see Fig. 4 in [49]) and the understanding of this result motivates the first section of this work.

This observable provides a good starting point to determine the influence of the nuclear shape on the background signal in the measurements of the isobaric system. However, the full modeling of a HIC at these energies is very demanding in terms of computational costs. It is also known that at the considered energy a large portion of the final state flow originates from the initial spatial geometry of the created QCD medium [235]. This might not be a precise determination of the final state flow, however, since only ratios of observables will be presented and the goal is to determine the influence of the nuclear structure, only the initial geometry will be studied in the first step. Besides the study of the initial geometry of the collision, the second part of this chapter aims to investigate the effects of global charge conservation on final state fluctuations of particle numbers. As has been already introduced, within the standard description of HIC, the QGP stage can be modeled using hydrodynamical tools whereas the dilute stage is described using transport models. Switching between the two descriptions of the hydrodynamical fields and the single-particle distribution function is performed using the Cooper-Frye formula [84]. The goal of this study is to extend the hybrid model introduced in [5], such that the hydrodynamical hypersurface can be sampled with exact charge conservation within the particle spectra via the description of the canonical ensemble.

5.1 Initial state to hydrodynamical simulations

In this section, the influences of the nuclear structure on the initial state of HIC are studied. The initial state is calculated within the framework of [5], in which the first collisions of the nuclei are described by SMASH. This model will be shortly introduced. In the next step, the observables that determine the geometry of the collision are presented and finally, the results are shown.

5.1.1 Extension of the collision term towards high-energy collisions

In a recent work [5], an infrastructure for a hybrid approach was built to fully describe the HIC in the energy range from $\sqrt{s_{NN}} = 4.3$ GeV to $\sqrt{s_{NN}} = 200$ GeV. In the first part of this work, only the first stage of the hybrid approach is used with the goal of analyzing the initial condition for hydrodynamical modeling.

So far, the described collision term of SMASH is able to model the interactions with resonance formations/decays and (in)elastic processes. In the energy regime of $\sqrt{s_{NN}} = 200$ GeV however, these interactions are not relevant and the interactions within SMASH have to be extended.

In the energy regime of collisions between hadrons at $\sqrt{s} \gtrsim 5$ GeV the Lund model is employed [236]. The idea of this model is that the hadrons at the time of collision break up into their constituents and the interaction between the partons are then the ones that dominate the evolution in accordance to asymptotic freedom of QCD. When two quarks interact, a color flux is formed between them, and when the two are separated, the energy of the color flux increases. At large distances, one can approximately write the potential between two quarks as $U(r) \sim \kappa r$ with κ being a constant and r the distance between the two quarks. At some point in the evolution, when the two quarks have separated far enough, the energy deposited in the color flux (or string) is large enough, such that it breaks and two new partons are created forming new color singlet states. The color flux between the original quarks and the newly created ones still exists and the string breaking continues with new hadrons being formed until the energy of the color flux is not sufficiently large enough. In SMASH, there exists a distinction between the so-called "soft" and "hard" string interaction. The soft string routine is explained in detail in [99]. For hard string processes SMASH employs PYTHIA8 [237, 238] to perform the hard scatterings. The difference between the two regions of string interactions originates from the applicability of perturbative QCD (pQCD) cross-sections. The transition region in the cross-sections between two hadrons a and b between the region of resonance formation and where the dynamics of the Lund string model becomes important starts at energies of $m_a + m_b + 0.9$ GeV. At the energy considered in this study, only hard QCD processes appear which are performed by PYTHIA.

5.1.2 The shape of the nucleus

So far, SMASH has been only employed in the box modus simulating infinite matter and in an expanding sphere mode. The initialization for heavy-ion collisions collision differs so far, as the shape of the colliding nuclei has to be modeled first. The most

common way to describe the density distribution of a large nucleus is by using the Woods-Saxon distribution

$$\rho(r, \theta, \phi) = \frac{\rho_0}{\exp\left\{\frac{r - r(r_0, \theta, \phi)}{d}\right\} + 1} \ . \tag{5.4}$$

Here, ρ_0 is the ground state density, d the diffusiveness and $r(r_0, \theta, \phi)$ a function that describes the surface of the nucleus. A common ansatz is to expand the surface in terms of spherical harmonics

$$r(r_0, \theta, \phi) = r_0 \left\{ 1 + \beta_2 \left[\cos(\gamma) Y_2^0(\theta, \phi) + \sqrt{2}\sin(\gamma)\text{Re}(Y_2^2(\theta, \phi)) \right] + \beta_3 Y_3^0(\theta, \phi) \right\}, \tag{5.5}$$

where r_0, $\beta_{2,3}$, as well as γ, are parameters taken from experiments or theoretical calculations to describe the size and the shape of the nucleus. $Y_m^n(\phi, \theta)$ are the spherical harmonics.

On an event-by-event basis, the positions of the nucleons are sampled from Eq. 5.4 and both nuclei are rotated randomly around all axes. The nuclei are then placed according to the impact parameter b along the x direction such that the outer shell of the spheres including the Lorentz contraction $(R + d)/\gamma$ touch each other at $t = 0$. The beam direction is set as the z axis. In order to systematically study the influence of the nuclear shape of the colliding nuclei on the initial state of hydrodynamic calculations, different Woods-Saxon parameters from Tab. 5.1 are used. The values

name	r_0 [fm]	d [fm]	β_2	β_3	γ [°]
Case 1 ^{96}Ru (full)	5.09	0.46	0.16	0	30
Case 2	5.09	0.46	0.16	0	0
Case 3	5.09	0.46	0.16	0.20	0
Case 4	5.09	0.46	0.06	0.20	0
Case 5	5.09	0.52	0.06	0.20	0
Case 6 ^{96}Zr (full)	5.02	0.52	0.06	0.20	0

Table 5.1: Woods-Saxon parameter used in this work.

of Tab. 5.1 are built such that the influence of the individual deformation parameters can be observed when comparing the different cases with each other. E.g. when comparing the results of case 1 to the results of case 2, the only difference is the value of the triaxiality γ. Therefore, differences that γ induce are directly observable. The "full" configurations that are thought to represent the nuclear shapes of Ru and Zr respectively are case 1 and case 6. The influence of the individual deformation parameter can be seen in Fig. 5.1. Here, the surface $r(r_0, \theta, \phi)$ Eq. 5.5 is shown for $r_0 = 1$ fm for extrem cases of β_n. The inclusion of a β_2 forms the nucleus in an ellipsoid shape, β_3 creates a pear-like shape whereas a non-zero β_4 creates an ellipsoid shape with an additional disc around its center. The triaxiality γ is the only deformation parameter that breaks the symmetry with respect to rotations around the angle ϕ. The resulting nucleus has a so-called prolate shape. The interesting aspect of the presented deformation parameter will be to study their effects on the initial geometry of the collision.
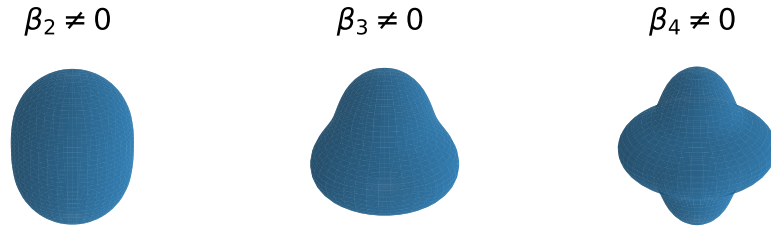
$$\beta_2 \neq 0 \qquad \beta_3 \neq 0 \qquad \beta_4 \neq 0$$

Figure 5.1: Influence of non-zero β_n deformation parameter on the surface of the nuclei. For the three cases values of $\beta_n = 0.4$ have been used.

In addition to the six different cases from Tab. 5.1, the influence on the initial state when modeling the nuclei in a more physical way is investigated. It is known from experimental measurements that there exist nucleon-nucleon (NN) short-range correlations (SRC) in momentum space, see e.g. [239] which also translate into short-range correlations in coordinate space [240]. These correlations are not captured by purely sampling Eq. 5.4 as by chance, a NN pair is sampled very close in coordinate space. As a result, the radial two-body density $\rho^{(2)}(r_{12})$, which describes the density of states between two nucleons 1 and 2 has a non-zero value at small distances r_{12}. To properly capture the NN SRC effects in this work, the configurations generated by Alvioli et al. [241] are used. They are based on modeling the wavefunction of the nucleus using realistic correlations between the nucleons

$$\psi(\vec{x}_1, \vec{x}_2, ..., \vec{x}_N) = \prod_{i<j}^{A} \hat{f}_{i,j} \phi(\vec{x}_1, \vec{x}_2, ..., \vec{x}_n) \,. \tag{5.6}$$

Here, ψ is the wave function of the nucleus and $\hat{f}_{i,j}$ is a correlation operator acting on the uncorrelated wave function ϕ. In this work, the correlations originating from spin- and isospin dependencies are incorporated [242]. The computation is performed using a method proposed by Alvioli et al. [241], to generate nuclear configurations that properly describe the wavefunction of the nucleus Eq. 5.6 including the non-trivial effects correlations. Fig. 5.2 shows the one and two body densities of $\approx 10^4$ configurations of Ruthenium nuclei with the Woods-Saxon parameter case 1 (see Tab. 5.1). Whereas the one-body density yields the same results as the two descriptions, one can see a clear difference between them on the level of $\rho^{(2)}(r_{12})$. At small distances between the nucleon pairs, the configurations including NN SRC yield a better description in contrast to purely sampling Eq. 5.4. The calculations with short-range correlations rely on externally provided configurations for the nucleons, otherwise, the propagations and collisions are described in the same way in SMASH.

In most theoretical studies for heavy-ion collisions, it is assumed, that protons and neutrons are distributed equally within the nucleus. However, in 1978 it was found in the case of ^{208}Pb that the average radius of the neutron distribution is larger compared to the one of protons [243]. The difference in the average radii of the
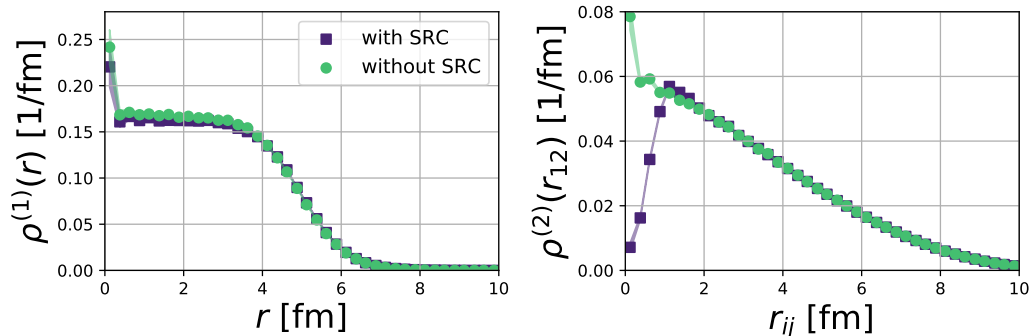
Figure 5.2: One (left) and two (right) body density of nuclear configurations of Ruthenium (case 1). The blue squares correspond to the results obtained from configurations by Alvioli et al and the green circles to configurations obtained from sampling Eq. (5.4).

nucleons is called the neutron skin effect and it is defined as the difference between the root mean square radius of neutrons to protons

$$\Delta r_{np} = \sqrt{\langle r_n^2 \rangle} - \sqrt{\langle r_p^2 \rangle}. \tag{5.7}$$

Measurements of the average radii of neutrons are difficult, however, a summary of charge radii of many different nuclei of two different measurement techniques has been published in [73, 244]. The determination of the neutron radii is still dominated by errors since the probing mechanism is based on the strong interaction and not the electromagnetic. However, recent studies exist to determine the value of the neutron skin from measurements of heavy-ion collisions [72].

The neutron skin effect is an effect of nuclear matter in which the neutrons are populated at larger radii in neutron-rich heavy-nuclei [245]. It originates from the symmetry energy in the nuclear equation of state (EoS) which describes the effect of differences of proton and neutron numbers on the EoS and its precise value is not known. Due to the imbalance, the effective pressure on the neutrons is larger in comparison to the protons and as a result, the neutrons are pushed towards the outer shell of the nucleus. The determination of the value of the symmetry energy is subject to many other fields e.g. astrophysical observations of neutron stars [246].

In the context of heavy-ion collisions, a short review of the existing literature will be given in the following. In [247], the influence of the neutron skin on the direct-photon and charged hadron production was investigated. [248] studied, how the neutron skin affects centrality classifications in heavy-ion collisions. In [249], an improved Glauber Monte Carlo study was presented including a more precise description of the nuclei through distinct density distributions for protons and neutrons. In [156] the influence of the neutron skin effect was studied within the context of the isobar collision system. Specifically, it was found that the generated magnetic field is larger in peripheral Zr Zr collisions in comparison to Ru. Finally, in [72], a Bayesian analysis study was performed in order to extract Δr_{np} of Pb.

In this work the Zr nucleus is modified with the same argument as in [156]. The measured neutron skin thickness of Zr is [245, 250]

$$\Delta r_{np}|_{\text{Zr}} = 0.12 \pm 0.03 \, \text{fm} . \qquad (5.8)$$

To study the maximum effect a value of $\Delta r_{np}^{\text{Zr}} = 0.15 \, \text{fm}$ is used. The method to compute the different Woods-Saxon parameters is presented in App. A.7. The final radius and the diffusiveness of the protons and neutrons of Zr are shown in Tab. 5.2. There exist two different types of neutron skin when it comes to modeling. First, the thickness-like neutron skin in which $R_n > R_p$, $d_n \sim d_p$ and the second the halo-like neutron skin with $R_n \sim R_p$ and $d_n > d_p$. In this work, the latter type has been chosen, in accordance with [156]. The resulting changes of the neutron skin in

Nucleon	r_0 [fm]	d [fm]
proton	5.075	0.428
neutron	5.075	0.526

Table 5.2: Proton and neutron Woods-Saxon parameters of Zirconium to include the neutron skin effect.
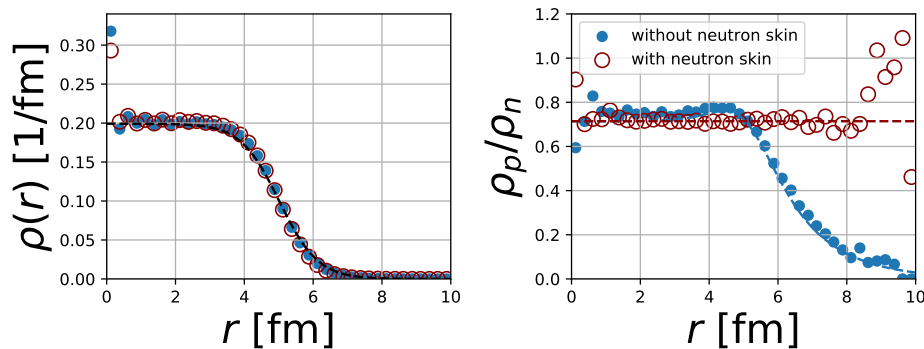
Figure 5.3: One body density ratio of protons to neutrons as a function of the radius. The results are presented for Zr with (red) and without (blue) the neutron skin. Results from the sampled distribution are shown as circles and analytic expectation as dashed line.

Zirconium are shown in Fig. 5.3. On the level of the one-body density, the two systems have the same distribution, whereas the ratio of proton to neutron density shows a significant difference. In the case of no neutron skin, the ratio is constant as expected. With neutron skin, the ratio drops at large radii where the neutron density is larger. One can see that the analytic expectation coincides with the sampled nuclei.

The neutron skin effect has no influence on the geometric shape of the initial condition which is studied in the first part of this chapter. Its effect will be investigated in the second part when the full heavy-ion collisions are modeled.

5.1.3 Modeling of the initial conditions to hydrodynamical calculations

After the nuclei are initialized, they are then propagated and the collisions are performed until the hadrons cross a hypersurface of constant iso-τ. Since most hydrodynamical codes run in Milne coordinates, there must be a transition between the Cartesian and the Milne one. The definition of τ is

$$\tau = \sqrt{t^2 - z^2}\,. \tag{5.9}$$

Here, t and z are the time and z components respectively. The value of the iso-τ_0 hypersurface is determined from

$$\tau_0 = \max\left(0.5\,\mathrm{fm}, \frac{R_P + R_T}{\sqrt{\left(\frac{\sqrt{s_{NN}}}{2m_N}\right)^2 - 1}}\right), \tag{5.10}$$

where $R_{P,T}$ are the values of the radii of the projectile and target nuclei respectively and $m_N = 938\,\mathrm{MeV}$ the mass of a nucleon. Eq. 5.10 describes the time at which the two nuclei completely overlap with each other and it is at this time when the energy density is thought to be the largest. At the considered energy of $\sqrt{s_{NN}} = 200\,\mathrm{GeV}$, the minimal time of τ_0 is already reached. Fig. 5.4 shows the participants of one
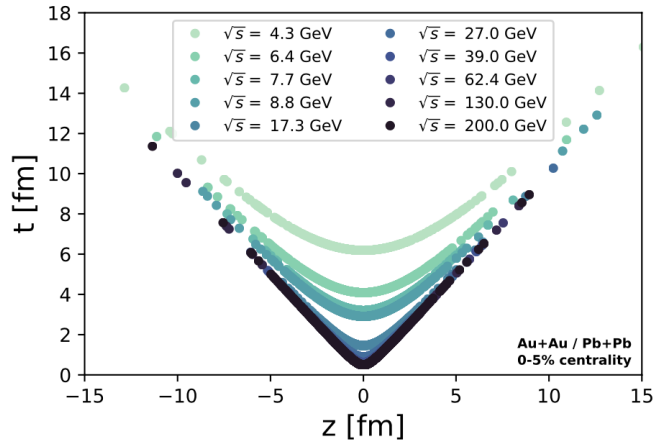

Figure 5.4: Iso-τ initial conditions hypersurface for various different collisional energies. The figure is taken from [181].

event for different beam energies. With increasing $\sqrt{s}$, the time that the nuclei take to overlap gets shorter, until it converges towards $t = 0.5\,\mathrm{fm}$ at $z = 0$.

After the methodology to determine the initial conditions for hydrodynamic calculations has been established, the goal is now to run simulations using the Woods-Saxon parameter from Tab. 5.1, plus the nuclear configurations which incorporate the NN SRC and study the properties of the created medium. In the next section, the details of how the geometric properties are obtained are presented.

5.1.4 Observables

The starting point of the calculations is the energy density profile of the collision in the transverse plane. The energy density profile is calculated by summing over all participants on the iso-τ hypersurface with their coordinates $\mathbf{x_i}$ and energy p_i^0 respectively

$$e(\mathbf{x}, \tau) = \sum_{i=0}^{N_{\text{part}}} p_i^0 K(\mathbf{x} - \mathbf{x}_i, \mathbf{p}_i) . \tag{5.11}$$

A participant is, by definition a particle that has collided at least once or is not part of the original set of nucleons. This definition however is not strict and a different one can easily be defined as well. $K(\mathbf{x} - \mathbf{x}_i, \mathbf{p}_i)$ is the Lorentz invariant smearing kernel [251]

$$K(\Delta\mathbf{x}_i = \mathbf{x} - \mathbf{x}_i, \mathbf{p}_i) = \frac{\gamma_i}{(2\pi\sigma^2)^{3/2}} \exp\left\{ -\frac{\Delta\mathbf{x}_i + \gamma_i^2(\Delta\mathbf{x}_i \cdot \beta_i)^2}{2\sigma^2} \right\} . \tag{5.12}$$

Where γ_i is the gamma-factor of each particle and $\beta_\mathbf{i} = \mathbf{v}_i/c$ the velocity. In this work, the width of the Gaussian is set to $\sigma = 1\,\text{fm}$ and it is the only free parameter of the model. This also yields a benefit in comparison to the previously defined smearing kernel used in [5], in which the energy density was smeared in the longitudinal direction R_η and transverse direction $R_\perp$ separately. Since only observables in midrapidity are of interest, a rapidity cut of $|y| < 0.5$ is incorporated.

The initial state is quantified based on the energy density profile in the transverse plane $e(\mathbf{x}, \tau)$. Starting from the total energy of the collision, which can be calculated by integrating $e(\mathbf{x}, \tau)$

$$E = \tau_0 \int d^2\mathbf{x}\, e(\mathbf{x}, \tau_0) . \tag{5.13}$$

The entropy density $s(\mathbf{x}, \tau)$ is obtained by using the ideal gas equation of state $s(\mathbf{x}, \tau) \sim e(\mathbf{x}, \tau)^{3/4}$ and the total entropy is calculated similarly to the energy density as

$$S = \tau_0 \int d^2\mathbf{x}\, s(\mathbf{x}, \tau_0) . \tag{5.14}$$

In addition to the energy and entropy density, the geometric properties of the created medium are of interest. For example the final state flow v_n can be related to the eccentricity ε_n [235] which defines variations from a perfect sphere

$$v_2 \sim \alpha_2\, \varepsilon_2 + \mathcal{O}(W^2) \tag{5.15}$$

$$v_3 \sim \alpha_3\, \varepsilon_3 + \mathcal{O}(W^2) . \tag{5.16}$$

Here, W is the generating function for the eccentricity harmonics and $\alpha_{2,3}$ are constants. The geometric properties of the medium are calculated in the following way. First, the average radius and its moments are calculated via

$$\langle r^n \rangle = \frac{1}{S} \int d^2\mathbf{x}|\mathbf{x}|^n s(\mathbf{x}, \tau_0) . \tag{5.17}$$

For the eccentricity harmonics that are used to estimate the final state flow, one first needs to calculate the following vector

$$\mathcal{E}_n = \frac{1}{S\langle r^n \rangle} \int d^2\mathbf{x} |\mathbf{x}|^n e^{in\phi} s(\mathbf{x}, \tau_0) \,, \tag{5.18}$$

with $\phi = \text{atan2}(y, x)$. Finally the eccentricity ε_n and orientation ψ_n are calculated as

$$\varepsilon_n = |\mathcal{E}_n| \,, \tag{5.19}$$

$$\psi_n = \frac{1}{n} \text{atan2} \left[\text{Im}(\mathcal{E}_n), \text{Im}(\mathcal{E}_n) \right] + \frac{\pi}{n} \,. \tag{5.20}$$

Together with the defined observables, the collisions can be performed and the results of the defined observables computed. For each case, $\mathcal{O}(10^6)$ events have been simulated and the above quantities computed on an event-by-event basis.

5.1.5 Results

Quantification of the medium

The first part of the results section is dedicated to describing the created system that is analyzed. The initial collisions of the participating nucleons at $\sqrt{s_{NN}} = 200\,\text{GeV}$ are performed by PYTHIA which, after performing the hard processes, creates particles from the string fragmentation mechanism described above. The newly created particles are propagated in SMASH. Since these new hadrons are formed on a constant proper time themselves, at the time of the iso-τ hypersurface of the simulation, some of them are technically not formed yet but will of course add to the total energy density of the system. Technically, this is done by creating the new hadrons directly after the initial collision, but assigning no cross-section to them such that they cannot collide with other particles [99] until their formation time is reached.

Fig. 5.5 shows the energy density profile of one exemplary event of a RuRu collision. The individual narrow lines can be attributed to hadrons with a large p_T. As a result of the Lorentz contraction of the smearing kernel K (Eq. 5.12), the energy density of such a high p_T particle then appears as a straight line in the computational frame, which coincides with the center of mass frame of the medium.

Ratios of eccentricity

In this section, the results of Eq. 5.13-5.20 are going to be discussed. In addition to the 7 different Woods-Saxon cases, simulations were the nuclear configurations that incorporate NN SRC of the two full nuclei descriptions of Ru and Zr (case $1 + 6$), are performed as well. Since the total entropy of the system is directly related to the number of produced (charged) particles $S \sim N_{ch}$, the quantities are presented as a function of S to mimic experimental measurements as a function of N_{ch} [49]. The total entropy is calculated by integrating the entropy density profile in the transverse plane. Its exact value is not important and could be rescaled to match with N_{ch}. The interesting quantity that is also measured in the experiment are differences between
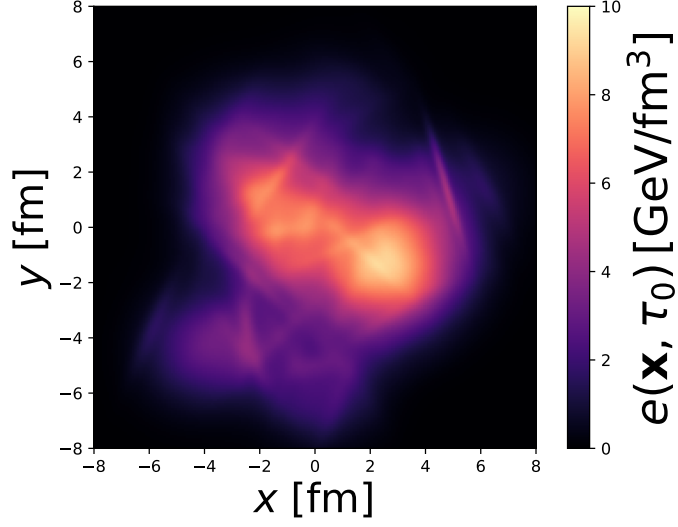
Figure 5.5: Energy density profile in the transverse plane of one event of a RuRu collision at $\sqrt{s} = 200$ GeV with an impact parameter of $b = 4.4$ fm.

observables in RuRu and ZrZr collisions. Therefore, only ratios of Ru (case 1-5) / Zr (case 6) are shown and the impact of the Woods-Saxon parameter can then be seen from differences in the Ru nucleus.
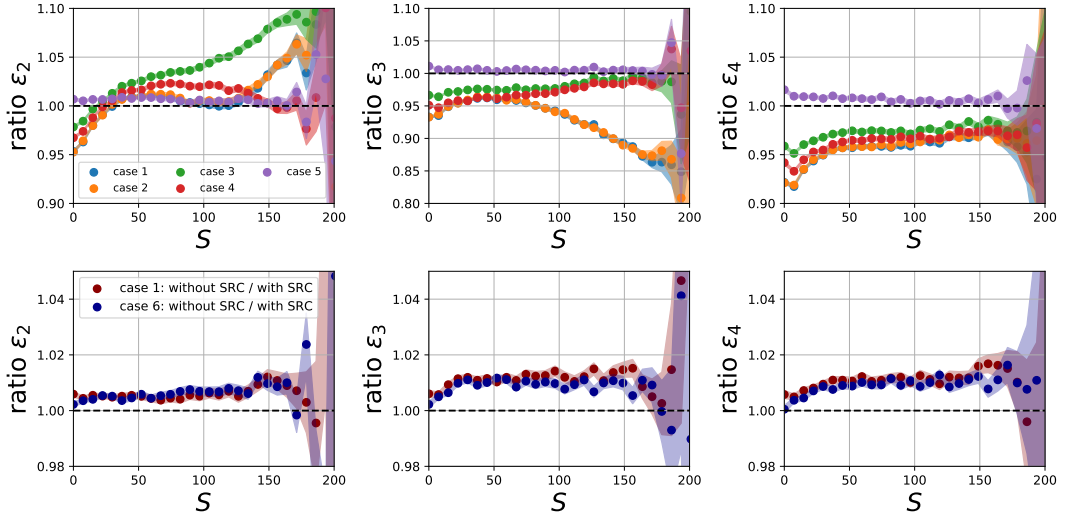

Figure 5.6: Ratio of ε_2 (left), ε_3 (center) and ε_4 (right) as a function of the total entropy S. In the upper row, the ratio is taken of the results of cases 1-5 with respect to case 6 (see Tab. 5.1). In the lower row, the ratio is taken between the nuclear configurations without and with NN SRC of case 1 (red) and case 6 (blue).

Fig. 5.6 shows the five described ratios of the eccentricities ε_n as a function of S.

The ratio case 1 to case 6 is the baseline calculation since the actual Woods-Saxon parameters are used. Comparing the ratio case 1 to case 2, the difference of a non-zero triaxiality γ can be seen, however, it is found that γ has no influence on the eccentricities $\varepsilon_{2,3,4}$. Going to the ratio of case 3, which in comparison to case 2 has a different β_3 parameter, it is found that at more central collisions, ε_2 and ε_3 are strongly affected. Including β_3, increases the eccentricity ε_2 and ε_3 of the initial state of the Ruthenium collisions. The influence of a varying β_2 parameter is contained in the comparison between ratios 4 and 3. Here, mainly the second eccentricity is modified. If one goes to larger entropy bins, a larger β_2 parameter increases ε_2, meaning that the collision area appears to be less spherical. Both ε_3 and ε_4 are only slightly affected. Finally, the diffusiveness has a strong influence on the eccentricities of all orders that are presented here. With the matching of the diffusiveness of Ru to the one of Zr, it is found that the main driver of the non-monotonic behavior of the ratios of ε_n is originating from the difference in d since the ratios are close to 1. Differences from unity of case 5 / case 6 is an effect, originating only from a different radius.

The impact of NN SRC can be seen in the lower row of Fig. 5.6. Throughout the shown eccentricities of order $n = 2, 3, 4$, the inclusion of NN SRC reduces the eccentricity by about $\approx 1\%$. As a result of the improved description of the nuclei on the level of $\rho^{(2)}(r_{12})$, the initial state of the hydrodynamical description appears to be more spherical in comparison to simply sampling the Woods-Saxon distribution. However, as the ratios of case 1 and case 6 are on the same order of magnitude, the ratio, where NN SRC are included in both Ru and Zr, the results in the upper row are unaffected.

A different observable where the NN SRC could possibly play a role is higher-order fluctuations of the eccentricity harmonics. In [252], the influence of NN SRC was studied in a Glauber model. Within the approach that is used here fluctuations of ε_n can also be obtained. Due to the modeling of the hard scatterings by PYTHIA however, it describes a more dynamic medium in comparison to the classical Glauber model used in [252]. In order to have a better comparison to [252], the fluctuations are calculated as a function of N_{ch}, which is a proxy of N_{part} that can be obtained from a Glauber model. N_{ch} describes the number of charged particles at the proper time τ_0 in midrapidity. The quantity of interest which is the standard deviation is computed by taking the square root of the variance

$$\sqrt{\varepsilon_n\{2\}} = \sqrt{\langle (\delta\varepsilon_n)^2 \rangle}. \tag{5.21}$$

Fig. 5.7 shows the fluctuations of the eccentricity harmonics Eq. 5.21. The main result is that the NN SRC does not have an effect on the normalized standard deviation. In comparison, the results of [252] found that one specific type of NN SRC changes the fluctuations of the ε_n, called central correlations. However, when the full correlations are included, the fluctuations return to the no correlation case. In the present calculation, the NN SRC incorporates the full correlation operator which is why again no differences are observed. Here, the dynamical evolution has no difference as well.
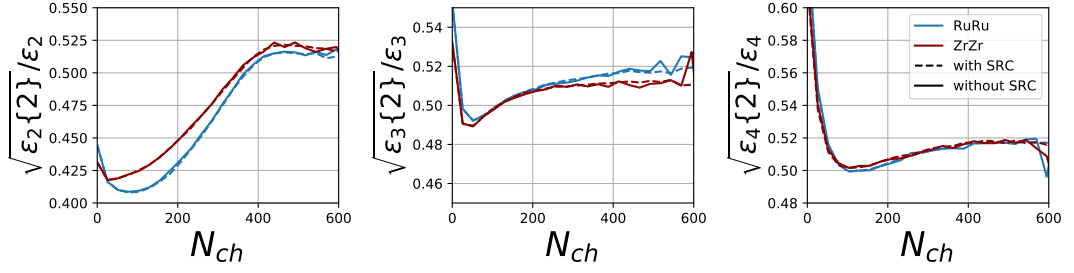
Figure 5.7: Normalized fluctuation of the second, third and fourth eccentricity harmonics as a function of N_{ch}. The results are shown for Ru case 1 (blue) and Zr case 6 (red) collisions. Results with NN SRC are shown as dashed lines and without NN SRC in full lines.
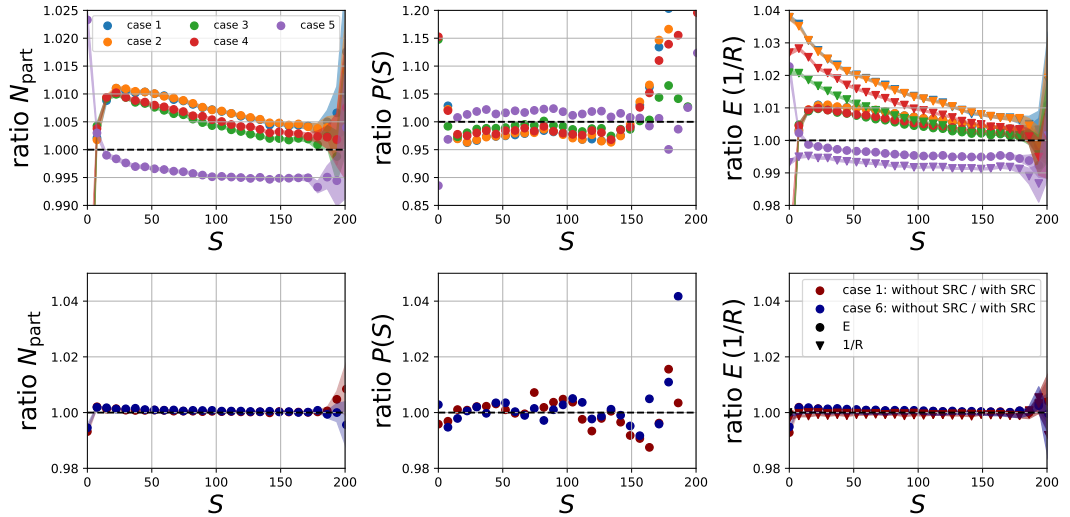
Ratios of N_{part}, $P(S)$ and R

Figure 5.8: Ratio of number of paricipants N_{part} (left), probability distribution $P(S)$ (center), total energy E and inverse radius $1/R$ (right). In the upper row ratios of case 1-5 with respect to case 6 are presented, whereas the lower row shows ratios of results obtained without to the ones obtained with NN SRC of case 1 (red) and case 6 (blue).

In this section the observables are switched to the number of participants N_{part}, probability density of S, the total energy of the system E and the inverse mean squared radius $1/R$ shown in Fig. 5.8. First, it is observed that the NN SRC has no impact on any of the quantities shown. A possible explanation is that the observables presented in Fig. 5.8 are only sensitive to modifications of the one-body rather than the two-body density. In contrast to ε_n which probes the spatial structure of the collision, the quantities N_{part}, $P(S)$ and E or $1/R$ are bulk quantities that wash

difference on the level of $\rho^{(2)}$ out. For all four observables, the main driver for differences is the diffusiveness of the nuclei. The deformation parameters $\beta_{2,3}$ and γ play only in the strength of the ratio, not its shape.

5.2 Effects of exact global charge conservation on observables

In this section, the previously obtained initial condition will be taken and fed into a hydrodynamical simulation and consequentially into the transport approach to study fluctuations of the final state particle spectra. Before the final results are presented, the model is described in detail.

5.2.1 Hydrodynamical modeling

The goal is now to take the previously investigated initial conditions and run hydrodynamical simulations with these initial conditions. After the hydrodynamical description of the QCD medium breaks down, the transition to the dilute stage has to be modeled. This will be described in the next section.

The initial condition of the hydrodynamic simulation of the hot and dense stage of the heavy-ion collision is obtained by averaging multiple SMASH events. In this work, $N = 10^3$ events have been used. Within each event, the impact parameter was sampled according to a specific centrality class. The classes were obtained from a MC Glauber calculation. The information about the nuclear structure gets lost during the process of averaging the events for the bulk observables of interest. It is, however, not the incentive to study the effects of nuclear deformation on final state event-by-event fluctuations yet, but to first quantify the influence of the canonical sampler. The study of the effects of the nuclear structure is left for future studies.

In this work, the framework of vHLLE [83] is used. The following derivations originate from their work. The hydrodynamic equations in covariant form are

$$\partial_\nu T^{\mu\nu} = 0\,, \tag{5.22}$$

$$\partial_\mu J^\mu_{B,Q,S} = \partial_\mu(n_{B,Q,S}u^\mu + V^\mu_{B,Q,S}) = 0\,. \tag{5.23}$$

Where n_q is the density of conserved charge q and V^μ_q the charge diffusion currents which are defined similar to Eq. 1.9 as

$$V^\mu_q = \kappa_{qq'}\nabla^\mu\left(\frac{\mu'_q}{T}\right)\,. \tag{5.24}$$

It would be in principle desirable to include the diffusive dynamics that originate from the diffusion coefficient matrix $\kappa_{qq'}$, in accordance with the results of Chapter 3. However, at this stage, the diffusion coefficients are set to zero and the conserved charge currents $q \in \{B, Q, S\}$, Eq. 5.23 are propagated throughout the simulation.

The energy momentum tensor $T^{\mu\nu}$ can be decomposed into an ideal and viscous part

$$T^{\mu\nu} = \varepsilon u^\mu u^\nu - (p + \Pi)\Delta^{\mu\nu} + \pi^{\mu\nu}\,. \tag{5.25}$$

Here, ε is the energy density and p is the equilibrium pressure in the local rest frame. $\Delta^{\mu\nu} = g^{\mu\nu} - u^\mu u^\nu$. $\pi^{\mu\nu}$ represents the shear stress tensor and Π the bulk pressure. These equations are then solved on a discrete grid in Milne coordinates. vHLLE solves the relativistic hydrodynamical equations in the second-order Israel-Stewart framework in the 14-moment approximation. The resulting equations for the relaxation of the viscous corrections are [253, 5]

$$D\Pi = \frac{-\zeta\theta - \Pi}{\tau_\Pi} - \frac{\delta_{\Pi\Pi}}{\tau_\Pi}\Pi\theta + \frac{\lambda_{\Pi\pi}}{\tau_\Pi}\pi^{\mu\nu}\sigma_{\mu\nu} \,, \tag{5.26}$$

$$D\pi^{\langle\mu\nu\rangle} = \frac{2\eta\sigma^{\mu\nu} - \pi^{\mu\nu}}{\tau_\pi} - \frac{\delta_{\pi\pi}}{\tau_\pi}\pi^{\mu\nu}\theta + \frac{\phi_7}{\tau_\pi}\pi_\alpha^{\langle\mu}\pi^{\nu\rangle\alpha} - \frac{\tau_{\pi\pi}}{\tau_\pi}\pi_\alpha^{\langle\mu}\sigma^{\nu\rangle\alpha} + \frac{\lambda_{\pi\Pi}}{\tau_\pi}\Pi\sigma^{\mu\nu} \,. \tag{5.27}$$

In the equations above, θ is an expansion scalar, τ_π and τ_Π are relaxation times for the shear and bulk corrections respectively and $\sigma^{\mu\nu}$ the shear stress tensor. $\lambda_{\Pi\pi}$, $\lambda_{\pi\Pi}$, $\delta_{\pi\pi}$, $\tau_{\pi\pi}$ and ϕ_7 are higher order couplings which expressions can be found in [253]. For further details, the interested reader is referred to [83].

The systems of equations Eq. 5.22 and Eq. 5.23 have to be closed using the EoS, which relates the energy density and pressure with thermodynamic quantities such as temperature, chemical potential and charge densities. This yields a strong benefit of hydrodynamical calculations as the microscopic interactions do not have to be modeled but are exchanged with the bulk properties of the medium. For the hot and dense stage of the heavy-ion collision, the EoS of a chiral model is used [78]. In this effective QCD EoS model, hadrons and quarks are included. At zero baryon chemical potential, the cross-over phase transition is reproduced which is expected from first principle lattice QCD calculations [15]. For low temperatures, the chiral EoS is fitted to the HRG EoS. At some point of the evolution, when the energy density per hydrodynamic cell is below a certain value $\varepsilon_{\mathrm{crit}}$, the hypersurface is constructed using the CORNELIUS routine [254]. This hypersurface is often called freezeout hypersurface even though it is not equivalent to the chemical or kinetic freezeout in a heavy-ion collision. After this particular freezeout hypersurface associated with a constant energy density is found, the thermodynamic quantities are recalculated using the hadronic EoS of the transport model that is used for the dilute stage of the heavy-ion collision. For this case, the HRG EoS of the SMASH particle list is used. For further details, see Section 4.2.

5.2.2 Switching between hydrodynamical and kinetic description

The transition between the hydrodynamical and the kinetic regime of the heavy-ion collision is performed using the Cooper-Frye formula [84]

$$\frac{dN_i}{d^3k} = \frac{g_i}{(2\pi)^3}\int k^\mu d\Sigma_\mu f_{i,k}^0(1 + \delta f_{i,k}) \,. \tag{5.28}$$

Here, $d\Sigma^\mu$ is the normal vector of the freezeout hypersurface element which includes the thermodynamic quantities such as temperatures and chemical potentials. The non-equilibrium correction originating from the shear stress tensor is modeled via

$$\delta f_i = (1 \mp f_{i,k}^0)\frac{p^\mu p^\nu \pi_{\mu\nu}}{2T^2(\epsilon + P)} \,. \tag{5.29}$$

The goal of this section is to perform the sampling of the hydrodynamical hypersurface using the canonical ensemble (CE), in which the charges are exactly conserved on the total hypersurface. This is done within the fist-sampler [195] (see Appendix B in [195]). To do so, the fist-sampler has been modified to use the numerical output of VHLLE. The sampling procedure will now be briefly explained.

When sampling an element on the hypersurface $d\Sigma^\mu$, one has to take into account that the total number of conserved charges within the hydrodynamical simulation is fixed and therefore the hypersurface cannot be sampled according to the grand-canonical ensemble, where the particles freely exchange energy with the heat bath. Since the total charge is fixed the joint multiplicity has to follow the probability distribution [255]

$$P^{CE}\left(\{\ N_j\}_{j=1}^s\right) = \prod_{j=1}^s P^{HRG}(N_j; T_j, V_j, \mu_j)$$

$$\times \delta(Q_X^{tot} - \sum_{j=1}^s Q_{X,j}). \tag{5.30}$$

Here, the Dirac delta ensures that the total baryonic electric and strangeness of the hypersurface is conserved. The first step is to calculate the yields of the HRG model of the full hypersurface, then the yields of each individual hydro cell, plus their respective momenta can be generated which is in accordance to [256]. The algorithm to generate the sets of multiplicities that satisfy Eq. 5.30 goes as follows

- Calculate the GCE expectation value of the multiplicities of each hadron by integrating over the full hypersurface $N_i = \int d\Sigma_\mu(x)u^\mu n_i(x)$. This also determines the total B, Q, S that is conserved.

- Sampling the particle numbers for one event according to the Poisson statistics (GCE) and using a rejection sampling procedure by [256], to enforce global charge conservation in each event.

- After the multiplicities per event are fixed by the previous step, each hypersurface element is sampled from a multinomial distribution with weights according to the particle number per cell $N_i(x)$ and the density $n_i(x)$. Finally, the momenta of the hadron are sampled according to the Cooper-frye formula Eq. 5.28

After the set of particles is obtained from the hypersurface using the fist-sampler, they are fed into SMASH to simulate the dilute stage of the heavy-ion collision. Here again, two distinct types of calculations are investigated. The first is to directly perform only the decays of all unstable particles including free-streaming and second, run the full dynamics of SMASH. The goal is to compare sampling the hypersurface according to the GCE and according to the CE ensemble. In addition to the effects of global charge conservation on the hydrodynamical hypersurfaces, results with the presented modified charge distribution within the Zr according to the neutron skin will be shown.

5.2.3 Results

The previous section determined the event geometry by analyzing the eccentricities and other initial state observables. It is also instructive to analyze not only the energy density profiles of the initial condition but also the distribution of the conserved charges. Fig. 5.9 shows the averaged initial conditions for the hydrodynamical
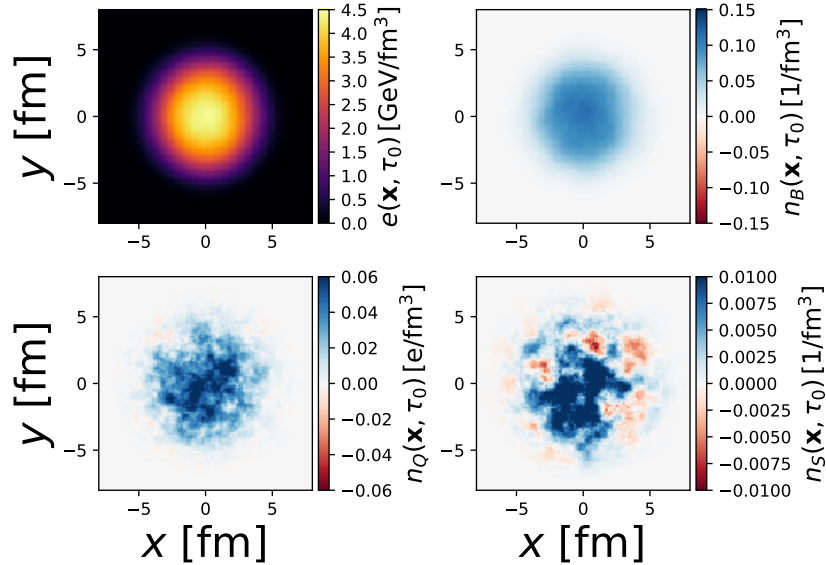

Figure 5.9: Initial energy density (upper left) baryon number (upper right) electric charge (lower left) and strangeness density (lower right) in the transverse plane at $z = 0$. The system is ZrZr at $\sqrt{s} = 200\,\mathrm{GeV}$.

simulations obtained from SMASH for 10^3 events in the $0 - 10\%$ most central events. For the baryonic, electric and strange charge, the fluctuations are of small order, however, the net baryon density shows a non-zero distribution in the transverse plane. This is known to be wrong since at these energies, the deposition of baryonic charge in midrapidity should be much closer to zero [108]. The reason for the non-zero value originates from the initial hard scatterings performed by PYTHIA and a possible solution could be to change the angular distribution of these initial hard processes.

The calculations used for the following results depend on external parameters which are listed in Tab. 5.3. Since it is not the purpose of this work to precisely

Parameter	Value
Smearing σ	$1\,\mathrm{fm}$
η/s	0.08
ζ/s	0
e_{switch}	$0.5\,\mathrm{GeV/fm^3}$

Table 5.3: Parameters used for the hydrodynamical calculations.

match e.g. the multiplicities of this model to experimental measurements, but rather to determine the effects of the neutron skin plus global charge conservation on the hydrodynamical hypersurfaces, the values of Tab. 5.3 were not tuned to fit any experimental data.
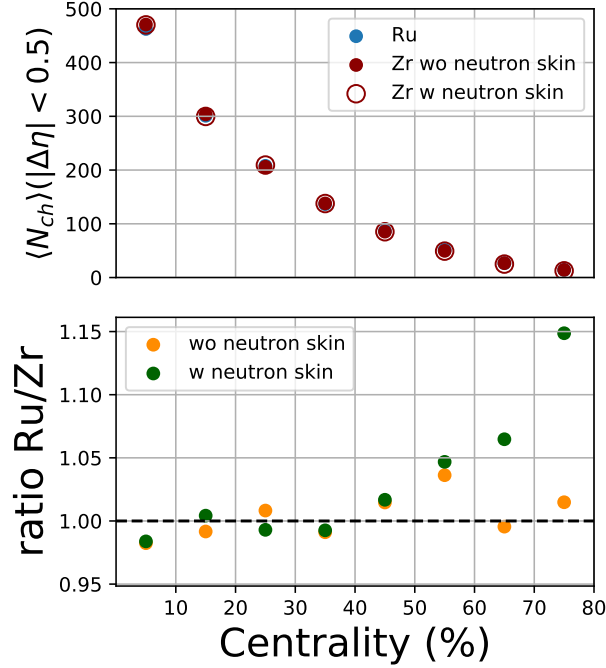

Figure 5.10: Top: Mean number of produced charge particles in midrapidity as a function of the centrality class. An additional cut of $p_T > 0.2\,\text{GeV}$ has been applied. The results are presented for Ruthenium (blue) Zirconium without neutron skin (closed red circle) and Zirconium with neutron skin (open red circle). Bottom: Ratio of Ruthenium over Zirconium with (green) and without (orange) neutron skin.

The mean number of produced charged particles as a function of the centrality class is shown in Fig. 5.10. With increasing centrality the mean number of produced charged particles decreases which is expected as the created medium gets smaller in its size. When comparing the results of Ru to the Zr with and without neutron skin, a difference between the two systems is visible in the largest centrality classes. When the neutron skin is included and in the largest centrality classes, the neutron-rich regions of the nuclei collide and the produced medium has a lower net electric charge number. As a result, the mean number of charged particles in the final state decreases and the ratio Ru/Zr increases. One can see the effect of the neutron skin already on the level of bulk observables. The next step is to investigate fluctuations of conserved charges and the effects of the canonical ensemble at the sampling stage and the neutron skin.

Fig. 5.11 shows the scaled variance of the net proton number obtained from the centrality class 0-10% of RuRu collisions. The differences between sampling the
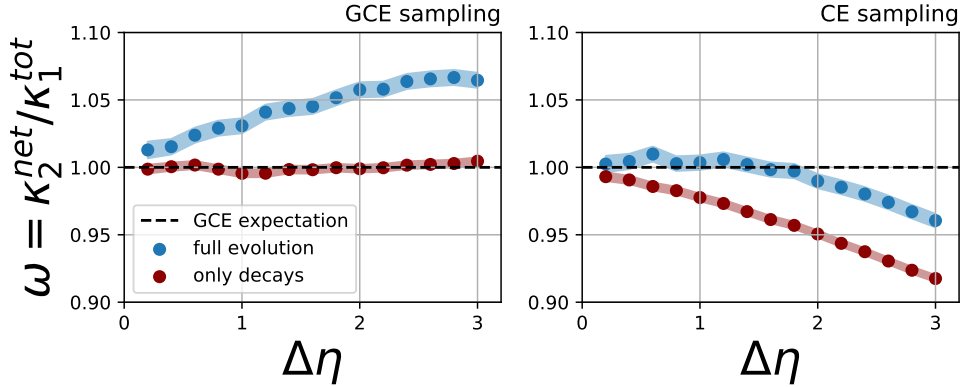
Figure 5.11: Net proton scaled variance as a function of the rapidity window $\Delta\eta$. The results are shown for the full evolution (blue line) or only performing decays (red line). The hadrons were sampled using the GCE (left) and the CE (right).

CE and the GCE can be seen between the left and the right plot and in addition, the effects of the hadronic rescattering stage are shown. The latter has a strong effect on the net proton scaled variance. In the case when the decays of resonances into stable hadrons are performed, ω is in alignment with the expectation from the grand-canonical ensemble which is unity. However, when the SMASH transport model's full dynamics are applied, the fluctuations increase. This effect has already been studied in [257], where the influence of baryon annihilation processes was studied on the scaled variance at LHC energies. It was found that previously thought global baryon conservation cannot explain the experimental measurements if the effects of baryon annihilation processes are taken into account. It is rather a mixture of global plus local conservation effects that are important. Here, a similar effect is found but since this observable is not measured yet, there is no data to compare to. The dynamical evolution and the (nucleon) annihilation process via the h_1 meson pushes the variance up. When the hypersurfaces are sampled with the CE, generally the fluctuations decrease with increasing rapidity window. This is the same effect that has been studied in Sec. 4.3. However, when the dynamical evolution is switched on, the baryon annihilation processes increase ω. In the next step, the same observable is studied in the ZrZr collisions and the effects of the neutron skin are studied.

Fig. 5.12 again shows the scaled variance as a function of the rapidity window of the lightest hadrons that contain the three conserved charges. The hypersurface was sampled only using the CE. For the hadronic rescattering phase, the full dynamical evolution of SMASH was employed. Contrary to the previous result however, where only the result of RuRu collisions was shown, here, the result of RuRu, ZrZr without and ZrZr collisions including the neutron skin are presented. This analysis aims to determine, whether the different charge distributions in the three nuclear configurations including the CE have an observable effect on the final state event-by-event fluctuations. For all three species, the fluctuations are suppressed when the rapidity window is increased, which has already been discussed. Unfortunately, no
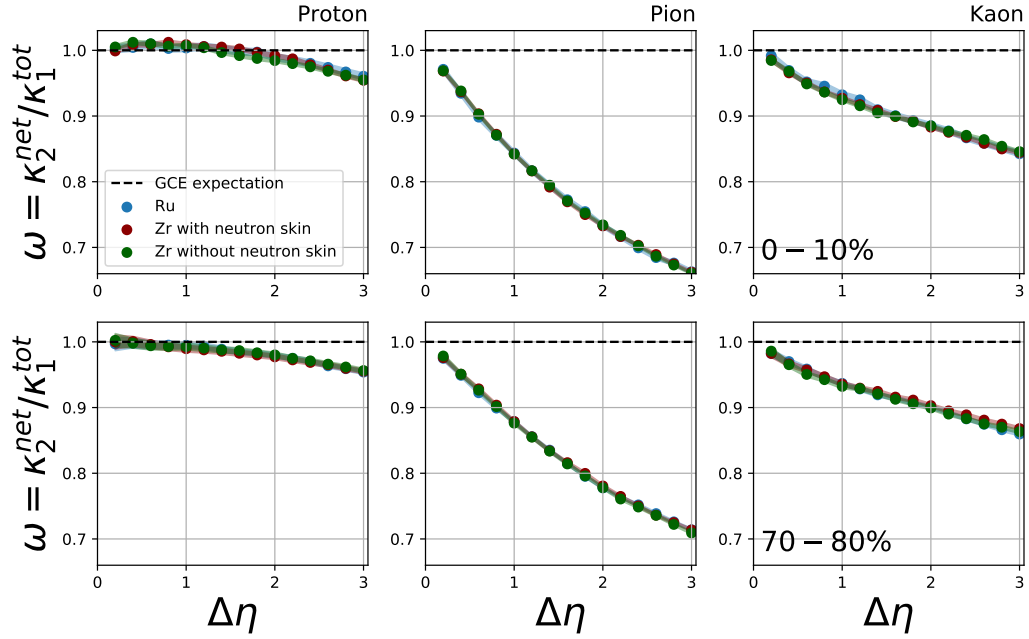
Figure 5.12: Scaled variance as a function of the rapidity window $\Delta\eta$ of the net proton (left column) net Pion (middle column) and net Kaon number (right column). The results are shown for Ru (blue) Zr with (green) and Zr without (red) neutron skin. The upper row shows the results for the most central collisions and the lower row the results for the most peripheral centrality class.

differences with respect to the different charge configurations are observed. When it comes to the differences between the two centrality classes, slight enhancement due to an increased baryon annihilation process rate pushes the fluctuations at small rapidity windows up. The total magnitude however is relatively unaffected. The pion fluctuations show a much stronger dependency on the rapidity window in comparison to the net proton. There are several factors that decrease the scaled variance. Similar to the baryonic charge, the electric charge is affected by annihilation processes. However, many more resonance decays exist such as $\rho^0 \to \pi^+\pi^-$ that further decrease ω. Electric charge annihilation processes like the reverse reaction, simply don't end up being preserved until the kinetic freeze-out. But similarly, as in the case of the proton fluctuations, the different electric charge distributions in the initial state do not have any effect on the final state fluctuations. For the kaon scaled variance, the same picture as for the pion fluctuations is visible. However, the dominant reaction is the decay $\phi \to K^+K^-$, and no difference between the configurations is observed.

5.2.4 Summary

In this chapter, the influence of modeling heavy-ion collisions with the exact global conservation of conserved charges was studied. The modeling of the heavy-ion

collision at the considered $\sqrt{s_{NN}} = 200\,\text{GeV}$ starts with the initial stage and is described using SMASH. A detailed calculation has been conducted to investigate the influence of the nuclear structure of Ru and Zr on the geometric shape of the created medium after the very first collisions. It has been found that the eccentricities $\varepsilon_{2,3,4}$ are mainly driven by the deformation parameters β and that the triaxiality γ has no influence. In addition, the diffusiveness has a strong influence as well. Incorporating realistic NN SRC into the nuclei have no influence on the level of the mean and the variance of the eccentricities. In the second step of this study, the initial conditions were fed into hydrodynamical simulations to evolve the QGP stage of the collision. The switching to the dilute stage of the HIC was performed using the Cooper-Frye formula and the conserved charges $\{B, Q, S\}$ are forced to be exactly conserved on the hypersurfaces of the hydrodynamic evolution. In addition, a calculation to study the influence of the neutron skin in Zr in the initial state of the HIC has been performed. The neutron skin modifies the mean number of charged particles produced at large centrality classes of ZrZr collisions. Fluctuations of the net proton, net pion and net kaon number are affected by sampling using the CE. Modifications due to the neutron skin are not observed. The hadronic rescattering phase strongly affects the scaled variance as a function of the rapidity window.

6

Conclusion and Outlook

In this work, the overall goal was to study fluctuations of conserved charges in order to better understand the created QCD medium in heavy-ion collisions. For this purpose, the hadronic transport approach SMASH has been used to describe the hadronic interactions. The results obtained in this work are manifold and tackle different topics. In Chapter 3, the diffusion coefficient matrix $\kappa_{qq'}$ and the shear viscosity η are studied. Transport coefficients are important quantities that determine the evolution of the medium in a heavy-ion collision. It is shown, how a precise description of the collision kernel affects these quantities. In Chapter 4 and Chapter 5, cumulants of particle numbers were studied. These observables are important when it comes to the study of the QCD phase diagram using heavy-ion collisions. In Chapter 3, the interacting hadronic medium of the transport model SMASH has been established simultaneously with studying the influence on the shear viscosity and the diffusion coefficient matrix of conserved charges. The transport coefficients are obtained from numerical integration of the corresponding correlation function of the charge currents $\mathbf{J}_q$ and the energy-momentum tensor T^{ij}. It has been presented, that this method is consistent with the results obtained in the CE approximation in a simple, elastically interacting hadron gas.

In the following calculations, it has been shown qualitatively that multi-particle reactions decrease the shear viscosity at $T \gtrsim 130\,\mathrm{MeV}$. In contrast, the electric charge diffusion coefficient κ_{QQ}/T^2 is not affected by the treatment. This result nicely shows that the shear viscosity predicted by the transport model from previous works overestimates the value of η around the cross-over temperature of $T \approx 130\,\mathrm{MeV}$ since multi-particle reactions become important in these temperature regimes. In the next step, the influence of angular-dependent cross-sections and additional elastic cross-sections via the description of the AQM model was studied. Both, η and $\kappa_{qq'}$, strongly depend on the AQM cross-sections. Whereas the shear viscosity is affected by the anisotropic cross-sections between baryonic and mesonic interactions, the

diffusion coefficients are unaffected. On the other hand, the dependency of the number of degrees of freedom on $\kappa_{qq'}$ is stronger in comparison to the shear viscosity. For the newly computed baryonic and strange diffusion coefficients $\kappa_{BB,BS,SS}$, the previously observed scaling behavior, as in the electrically charged sector, with the degrees of freedom is not found. Comparisons between CE calculations and the results from SMASH in finite baryon chemical potential are quantitatively consistent with each other. Finally, the comparison between the results of this work with other calculations can be summarized as follows. The newly implemented interactions in SMASH result in a more consistent comparison of η/s. Around the cross-over temperature, SMASH overpredicts η/s. Here, a reason could be the missing multi-particle reactions, which have been shown to reduce the value of η. In the case of the diffusion coefficient matrix $\kappa_{qq'}$, the important aspects are the charge densities and the total cross-sections between the constituents of the hadron gas. For the electric charge diffusion coefficient (which is equal to the electric conductivity) the specific values are consistent with the values from lattice QCD calculations in the temperature region of the cross-over phase transition. At low temperatures, however, the results from partonic models diverge from the hadronic ones. These results nicely show that the hadronic interactions and the number of degrees of freedom in SMASH are consistent with other (effective) models of QCD and SMASH can be used to study fluctuations in the hadronic phase of QCD.

In Chapter 4, properties of the hadronic medium are accessed via cumulants of conserved charges. This quantity is important for the ongoing search for the critical point of QCD. In the first part of this chapter, the influence of hadronic interactions on cumulants of conserved charges κ_n^q is studied in a system, in which the total charge is fixed. The system is a box with periodic boundary conditions and the cumulants are computed within subvolumes in coordinate space. In accordance with other findings, it is shown that in a simplified hadron gas, consisting only of electric charges, the fluctuation of the total charge number is important for the fourth cumulant. With this knowledge, previous results could be reproduced. In the next step, the influence of baryon annihilation processes on the cumulants was studied. Similar to the more simplified, electrically charged case, a baryon annihilation process induces fluctuations of the total charge number that modifies the kurtosis. In the case of the full SMASH hadron gas, the net proton fluctuations, contrary to the net baryon fluctuations, are not exactly conserved and their correlations due to global charge conservations are reduced. Further, the binomial unfolding procedure to determine the net baryon fluctuations from the net proton ones underestimates the correlations. In addition, a comparison between measurements from ALICE and this calculation shows that the net proton fluctuations are comparable, even though the systems are very different. Finally, it has been shown that the formation of deuterons has no effect on the net proton cumulants since they are rare and their fluctuations are consistent with the Poissonian baseline. This study can be seen as a background study of the effects of the hadronic stage on the measurements of cumulants in a heavy-ion collision, in which the total number of charges is conserved as well.

In the second part of Chapter 4, the influence of the hadronic stage on critical equilibrium cumulants is computed. The hadronic system is initialized with critical

equilibrium fluctuations originating from a coupling of the 3d Ising model to the HRG. The critical particle number distributions are obtained from the principle of maximum entropy and it has been shown that the generated numbers of particles and antiparticles return the correct cumulants up to the fourth order. The evolution of these distributions is studied in a simplified geometry in SMASH. The non-equilibrium expansion is initialized with a momentum space and volume fitted to measured p_T spectra at various different beam energies. During the hadronic evolution, the critical fluctuations are strongly affected by resonance formation and decay processes and the effects of the stochastic resonance regeneration processes are presented. In addition, it has been shown that a large part of the initial critical net proton fluctuations vanish, due to isospin randomization processes. At the kinetic freeze-out of this simplified expanding geometry, strong correlations from the critical point survive the evolution and are present in the final state of the expansion, in the case of a coupling of $g_p = 4$ whereas, at $g_p = 2$, all critical correlations vanish. In the final step, the rapidity dependence of the final state cumulants was studied and a non-monotonic behavior was found. This is important for experimental measurements since only a limited phase space can be covered.

In Chapter 5, isobar collisions at a beam energy of $\sqrt{s_{NN}} = 200\,\mathrm{GeV}$ are studied. The dynamical description of the HIC at these considered energies consists of various stages, in which different models have to be used in order to describe the full collision. The initial stage, in which the very first collisions of the nuclei are described, models the highly non-equilibrium system to the time at which a hydrodynamic description can be applied. This stage of the HIC can be modeled using SMASH and by studying the geometric properties, one can estimate final state flow observables. In the first part of the chapter, the dependency of eccentricity harmonics ε_n on the nuclear structure of the ZrZr and RuRu collisions is calculated. It is found that the eccentricity is strongly influenced by the β_n parameters whereas the triaxiality γ has no impact. Employing a more detailed description using NN SRC does not modify any of the considered observations. In the next step, these previously analyzed states were fed into a hydrodynamic model, to evolve the hot and dense stage of the HIC. When switching between the hydrodynamical and the kinetic description for the dilute stage of the HIC, an improved algorithm has been used in order to sample the hypersurface using the CE. To obtain the final state of the HIC at kinetic freeze-out, the hadronic medium was evolved by SMASH. The sampling of the CE instead of the GCE provides a more realistic picture and influences fluctuations of particle numbers, due to the exact conservation of the conserved charges. It is found that the scaled variance of the net proton, net pion, and net kaon fluctuations are suppressed. Additionally, hadronic interactions such as e.g. baryon annihilation processes modify the fluctuations. The neutron skin has no influence on the cumulants of conserved charges, but a modification of the number of charged particles is found.

Outlook

In this work, aspects of fluctuations of conserved charges and their application with respect to heavy-ion collisions have been discussed. Now that the full hadronic diffusion coefficient matrix of conserved charges of SMASH has been calculated, the

inclusion of these transport coefficients into the hybrid model developed in [5] could give rise to interesting observations. A similar calculation has been performed in [111], where it was found that regions of non-zero strangeness density develop, due to the coupling of the charge currents $\mathbf{J}_q$. A study of this effect, using realistic initial conditions from SMASH, could give new insights, and more realistic simulations can be established. Especially in the baryon-dense regime, the proper description of the diffusive effects is desirable.

In addition, it is known that in these baryon-dense regimes, the influence of nuclear potentials becomes important (see e.g. [258]). It would be therefore interesting to study the dependencies of the various aspects investigated in this work on the nuclear EoS. Starting with the transport coefficients, an inclusion of nuclear potentials at large values of μ_B could give large insights into the dynamics of HIC at, e.g. HADES beam energies. A calculation of both η and $\kappa_{qq'}$ with mean-field nuclear potentials at large μ_B is important for the understanding of HIC.

Regarding the study of fluctuations of conserved charges using cumulants of particle numbers on an event-by-event basis, there are multiple aspects of the presented calculations that can be improved. The reconstruction of the particle number distribution coupled to the critical mode is based on the principle of maximum entropy. However, it was shown that at large values of the coupling g_c, the distribution becomes non-physical. For further studies, it would be important to better control this issue, and incorporating cumulants of order larger than 4 could be necessary. In addition, it would be interesting to study more realistic heavy-ion collision scenarios and incorporate the described procedure in a Cooper-Frye sampler for hydrodynamic calculations. It is also worth noting, that the transport model used to evolve the hadronic medium does not propagate the n-particle correlations but only the single-particle distribution function. It would therefore be important to incorporate the effects of a critical point on the level of mean-field potentials in the transport model similar to [259]. On the other hand, a first-order phase transition can also be incorporated in a hydrodynamic description of a heavy-ion collision via the EoS and the effects can be studied. Using such a model, one can study the effects of a first-order phase transition on various different observables.

In the final chapter, there are various different aspects that can be further investigated. Most importantly, the influence of sampling the CE on the hydrodynamical hypersurfaces has, so far, only been investigated on cumulants of particle numbers. An extension for observables related to the CME, e.g. balance functions would be desirable in order to be able to estimate the background signal in a better way. In addition, by using an event-by-event basis for the simulations, one could calculate the exact influence of the nuclear structure.

Bibliography

[1] J. Hammelmann, H. Elfner, Impact of hadronic interactions and conservation laws on cumulants of conserved charges in a dynamical model, Phys. Rev. C 107 (4) (2023) 044910. `arXiv:2202.11417, doi:10.1103/PhysRevC.107.044910`.

[2] J. Hammelmann, H. Elfner, Impact of hadronic interactions and conservation laws on cumulants of conserved charges in a dynamical model, PoS FAIRness2022 (2023) 019. `doi:10.22323/1.419.0019`.

[3] J. Hammelmann, J. Staudenmaier, H. Elfner, Collision term dependence of the hadronic shear viscosity and diffusion coefficients`arXiv:2307.15606`.

[4] J. Hammelmann, M. Bluhm, M. Nahrang, H. Elfner, Fate of critical fluctuations in an interacting hadronic medium using maximum entropy distributions`arXiv:2310.06636`.

[5] A. Schäfer, I. Karpenko, X.-Y. Wu, J. Hammelmann, H. Elfner, Particle production in a hybrid approach for a beam energy scan of Au+Au/Pb+Pb collisions between $\sqrt{s_{NN}} = 4.3$ GeV and $\sqrt{s_{NN}} = 200.0$ GeV, Eur. Phys. J. A 58 (11) (2022) 230. `arXiv:2112.08724, doi:10.1140/epja/s10050-022-00872-x`.

[6] R. Kumar, et al., Theoretical and Experimental Constraints for the Equation of State of Dense and Hot Matter`arXiv:2303.17021`.

[7] J. S. San Martin, R. Hirayama, J. Hammelmann, J. M. Karthein, P. Parotto, J. Noronha-Hostler, C. Ratti, H. Elfner, Thermodynamics of an updated hadronic resonance list and influence on hadronic transport`arXiv:2309.01737`.

[8] M. E. Peskin, D. V. Schroeder, An Introduction to Quantum Field Theory, Westview Press, 1995, reading, USA: Addison-Wesley (1995) 842 p.

[9] R. E. Taylor, Deep inelastic scattering: The Early years, Rev. Mod. Phys. 63 (1991) 573–595. `doi:10.1103/RevModPhys.63.573`.

[10] D. J. Gross, F. Wilczek, Ultraviolet Behavior of Nonabelian Gauge Theories, Phys. Rev. Lett. 30 (1973) 1343–1346. `doi:10.1103/PhysRevLett.30.1343`.

[11] H. D. Politzer, Reliable Perturbative Results for Strong Interactions?, Phys. Rev. Lett. 30 (1973) 1346–1349. `doi:10.1103/PhysRevLett.30.1346`.

[12] K. G. Wilson, Confinement of Quarks, Phys. Rev. D 10 (1974) 2445–2459. doi:10.1103/PhysRevD.10.2445.

[13] V. A. Goy, V. Bornyakov, D. Boyda, A. Molochkov, A. Nakamura, A. Nikolaev, V. Zakharov, Sign problem in finite density lattice QCD, PTEP 2017 (3) (2017) 031D01. arXiv:1611.08093, doi:10.1093/ptep/ptx018.

[14] S. Borsanyi, Z. Fodor, J. N. Guenther, R. Kara, S. D. Katz, P. Parotto, A. Pasztor, C. Ratti, K. K. Szabo, QCD Crossover at Finite Chemical Potential from Lattice Simulations, Phys. Rev. Lett. 125 (5) (2020) 052001. arXiv:2002.02821, doi:10.1103/PhysRevLett.125.052001.

[15] Y. Aoki, G. Endrodi, Z. Fodor, S. D. Katz, K. K. Szabo, The Order of the quantum chromodynamics transition predicted by the standard model of particle physics, Nature 443 (2006) 675–678. arXiv:hep-lat/0611014, doi:10.1038/nature05120.

[16] S. Borsanyi, Z. Fodor, C. Hoelbling, S. D. Katz, S. Krieg, C. Ratti, K. K. Szabo, Is there still any T_c mystery in lattice QCD? Results with physical masses in the continuum limit III, JHEP 09 (2010) 073. arXiv:1005.3508, doi:10.1007/JHEP09(2010)073.

[17] V. Vovchenko, D. V. Anchishkin, M. I. Gorenstein, R. V. Poberezhnyuk, Scaled variance, skewness, and kurtosis near the critical point of nuclear matter, Phys. Rev. C 92 (5) (2015) 054901. arXiv:1506.05763, doi:10.1103/PhysRevC.92.054901.

[18] K. Fukushima, T. Hatsuda, The phase diagram of dense QCD, Rept. Prog. Phys. 74 (2011) 014001. arXiv:1005.4814, doi:10.1088/0034-4885/74/1/014001.

[19] W.-j. Fu, J. M. Pawlowski, F. Rennecke, QCD phase structure at finite temperature and density, Phys. Rev. D 101 (5) (2020) 054032. arXiv:1909.02991, doi:10.1103/PhysRevD.101.054032.

[20] F. Gao, J. M. Pawlowski, QCD phase structure from functional methods, Phys. Rev. D 102 (3) (2020) 034027. arXiv:2002.07500, doi:10.1103/PhysRevD.102.034027.

[21] W.-j. Fu, X. Luo, J. M. Pawlowski, F. Rennecke, R. Wen, S. Yin, Hyper-order baryon number fluctuations at finite temperature and density, Phys. Rev. D 104 (9) (2021) 094047. arXiv:2101.06035, doi:10.1103/PhysRevD.104.094047.

[22] C. S. Fischer, QCD at finite temperature and chemical potential from Dyson–Schwinger equations, Prog. Part. Nucl. Phys. 105 (2019) 1–60. arXiv:1810.12938, doi:10.1016/j.ppnp.2019.01.002.

[23] P. Isserstedt, M. Buballa, C. S. Fischer, P. J. Gunkel, Baryon number fluctuations in the QCD phase diagram from Dyson-Schwinger equations, Phys.

Rev. D 100 (7) (2019) 074011. `arXiv:1906.11644`, `doi:10.1103/PhysRevD.100.074011`.

[24] J. M. Maldacena, The Large N limit of superconformal field theories and supergravity, Adv. Theor. Math. Phys. 2 (1998) 231–252. `arXiv:hep-th/9711200`, `doi:10.4310/ATMP.1998.v2.n2.a1`.

[25] A. V. Manohar, Effective field theories, in: H. Latal, W. Schweiger (Eds.), Perturbative and Nonperturbative Aspects of Quantum Field Theory, Springer Berlin Heidelberg, Berlin, Heidelberg, 1997, pp. 311–362.

[26] M. G. Alford, A. Schmitt, K. Rajagopal, T. Schäfer, Color superconductivity in dense quark matter, Rev. Mod. Phys. 80 (2008) 1455–1515. `arXiv:0709.4635`, `doi:10.1103/RevModPhys.80.1455`.

[27] `https://www.guinnessworldrecords.com/world-records/highest-man-made-temperature`, accessed: 2023-07-08.

[28] B. P. Abbott, et al., Multi-messenger Observations of a Binary Neutron Star Merger, Astrophys. J. Lett. 848 (2) (2017) L12. `arXiv:1710.05833`, `doi:10.3847/2041-8213/aa91c9`.

[29] B. P. Abbott, et al., GW190425: Observation of a Compact Binary Coalescence with Total Mass $\sim 3.4 M_\odot$, Astrophys. J. Lett. 892 (1) (2020) L3. `arXiv:2001.01761`, `doi:10.3847/2041-8213/ab75f5`.

[30] J. Antoniadis, et al., A Massive Pulsar in a Compact Relativistic Binary, Science 340 (2013) 6131. `arXiv:1304.6875`, `doi:10.1126/science.1233232`.

[31] B. P. Abbott, et al., GW170817: Observation of Gravitational Waves from a Binary Neutron Star Inspiral, Phys. Rev. Lett. 119 (16) (2017) 161101. `arXiv:1710.05832`, `doi:10.1103/PhysRevLett.119.161101`.

[32] E. Shuryak, Physics of Strongly coupled Quark-Gluon Plasma, Prog. Part. Nucl. Phys. 62 (2009) 48–101. `arXiv:0807.3033`, `doi:10.1016/j.ppnp.2008.09.001`.

[33] C. Adler, et al., Disappearance of back-to-back high p_T hadron correlations in central Au+Au collisions at $\sqrt{s_{NN}} = 200$-GeV, Phys. Rev. Lett. 90 (2003) 082302. `arXiv:nucl-ex/0210033`, `doi:10.1103/PhysRevLett.90.082302`.

[34] I. Arsene, et al., Quark gluon plasma and color glass condensate at RHIC? The Perspective from the BRAHMS experiment, Nucl. Phys. A 757 (2005) 1–27. `arXiv:nucl-ex/0410020`, `doi:10.1016/j.nuclphysa.2005.02.130`.

[35] J. Adams, et al., Experimental and theoretical challenges in the search for the quark gluon plasma: The STAR Collaboration's critical assessment of the evidence from RHIC collisions, Nucl. Phys. A 757 (2005) 102–183. `arXiv:nucl-ex/0501009`, `doi:10.1016/j.nuclphysa.2005.03.085`.

[36] N. Armesto, E. Scomparin, Heavy-ion collisions at the Large Hadron Collider: a review of the results from Run 1, Eur. Phys. J. Plus 131 (3) (2016) 52. `arXiv:1511.02151, doi:10.1140/epjp/i2016-16052-4`.

[37] L. Adamczyk, et al., Energy Dependence of Moments of Net-proton Multiplicity Distributions at RHIC, Phys. Rev. Lett. 112 (2014) 032302. `arXiv:1309.5681, doi:10.1103/PhysRevLett.112.032302`.

[38] P. Spiller, G. Franchetti, The fair accelerator project at gsi, Nuclear Instruments and Methods in Physics Research Section A: Accelerators, Spectrometers, Detectors and Associated Equipment 561 (2) (2006) 305–309.

[39] V. Kekelidze, R. Lednicky, V. Matveev, I. Meshkov, A. Sorin, G. Trubnikov, NICA project at JINR, Phys. Part. Nucl. Lett. 9 (2012) 313–316. `doi:10.1134/S1547477112040164`.

[40] H. Sako, et al., Towards the heavy-ion program at J-PARC, Nucl. Phys. A 931 (2014) 1158–1162. `doi:10.1016/j.nuclphysa.2014.08.065`.

[41] H. Elfner, B. Müller, The exploration of hot and dense nuclear matter: introduction to relativistic heavy-ion physics, J. Phys. G 50 (10) (2023) 103001. `arXiv:2210.12056, doi:10.1088/1361-6471/ace824`.

[42] Y. Hatta, M. A. Stephanov, Proton number fluctuation as a signal of the QCD critical endpoint, Phys. Rev. Lett. 91 (2003) 102003, [Erratum: Phys.Rev.Lett. 91, 129901 (2003)]. `arXiv:hep-ph/0302002, doi:10.1103/PhysRevLett.91.102003`.

[43] A. M. Halasz, A. D. Jackson, R. E. Shrock, M. A. Stephanov, J. J. M. Verbaarschot, On the phase diagram of QCD, Phys. Rev. D 58 (1998) 096007. `arXiv:hep-ph/9804290, doi:10.1103/PhysRevD.58.096007`.

[44] M. A. Stephanov, K. Rajagopal, E. V. Shuryak, Event-by-event fluctuations in heavy ion collisions and the QCD critical point, Phys. Rev. D 60 (1999) 114028. `arXiv:hep-ph/9903292, doi:10.1103/PhysRevD.60.114028`.

[45] M. A. Stephanov, On the sign of kurtosis near the QCD critical point, Phys. Rev. Lett. 107 (2011) 052301. `arXiv:1104.1627, doi:10.1103/PhysRevLett.107.052301`.

[46] Z. Sweger, Recent Results and Future Prospects from the STAR Beam Energy Scan Program, in: 57th Rencontres de Moriond on QCD and High Energy Interactions, 2023. `arXiv:2305.07139`.

[47] M. S. Abdallah, et al., Measurements of Proton High Order Cumulants in $\sqrt{s_{\mathrm{NN}}} = 3$ GeV Au+Au Collisions and Implications for the QCD Critical Point, Phys. Rev. Lett. 128 (20) (2022) 202303. `arXiv:2112.00240, doi:10.1103/PhysRevLett.128.202303`.

[48] J. Adamczewski-Musch, et al., Proton-number fluctuations in $\sqrt{s_{NN}}$ =2.4 GeV Au + Au collisions studied with the High-Acceptance DiElectron Spectrometer (HADES), Phys. Rev. C 102 (2) (2020) 024914. `arXiv:2002.08701, doi: 10.1103/PhysRevC.102.024914.`

[49] M. Abdallah, et al., Search for the chiral magnetic effect with isobar collisions at $\sqrt{s_{NN}}$=200 GeV by the STAR Collaboration at the BNL Relativistic Heavy Ion Collider, Phys. Rev. C 105 (1) (2022) 014901. `arXiv:2109.00131, doi: 10.1103/PhysRevC.105.014901.`

[50] Z. Li, Overview of intermittency analysis in heavy-ion collisions, Mod. Phys. Lett. A 37 (13) (2022) 2230009. `arXiv:2203.01490, doi:10.1142/ S0217732322300099.`

[51] N. G. Antoniou, F. K. Diakonos, A. S. Kapoyannis, K. S. Kousouris, Critical opalescence in baryonic QCD matter, Phys. Rev. Lett. 97 (2006) 032002. `arXiv:hep-ph/0602051, doi:10.1103/PhysRevLett.97.032002.`

[52] T. Czopowicz, Search for critical point via intermittency analysis in NA61/SHINE, PoS CPOD2021 (2022) 039. `doi:10.22323/1.400.0039.`

[53] V. Vovchenko, Phenomenological developments for event-by-event fluctuations of conserved charges, PoS CPOD2021 (2022) 013. `arXiv:2110.02446, doi: 10.22323/1.400.0013.`

[54] J. Steinheimer, V. Vovchenko, J. Aichelin, M. Bleicher, H. Stöcker, Conserved charge fluctuations are not conserved during the hadronic phase, Phys. Lett. B 776 (2018) 32–37. `arXiv:1608.03737, doi:10.1016/j.physletb.2017.11. 012.`

[55] M. Luzum, P. Romatschke, Conformal Relativistic Viscous Hydrodynamics: Applications to RHIC results at s(NN)**(1/2) = 200-GeV, Phys. Rev. C 78 (2008) 034915, [Erratum: Phys.Rev.C 79, 039903 (2009)]. `arXiv:0804.4015, doi:10.1103/PhysRevC.78.034915.`

[56] F. Gelis, E. Iancu, J. Jalilian-Marian, R. Venugopalan, The Color Glass Condensate, Ann. Rev. Nucl. Part. Sci. 60 (2010) 463–489. `arXiv:1002.0333, doi:10.1146/annurev.nucl.010909.083629.`

[57] B. Schenke, P. Tribedy, R. Venugopalan, Event-by-event gluon multiplicity, energy density, and eccentricities in ultrarelativistic heavy-ion collisions, Phys. Rev. C 86 (2012) 034908. `arXiv:1206.6805, doi:10.1103/PhysRevC.86. 034908.`

[58] D. Kharzeev, E. Levin, Manifestations of high density QCD in the first RHIC data, Phys. Lett. B 523 (2001) 79–87. `arXiv:nucl-th/0108006, doi:10.1016/ S0370-2693(01)01309-0.`

[59] H. J. Drescher, Y. Nara, Effects of fluctuations on the initial eccentricity from the Color Glass Condensate in heavy ion collisions, Phys. Rev. C 75 (2007) 034905. `arXiv:nucl-th/0611017, doi:10.1103/PhysRevC.75.034905`.

[60] A. Kurkela, A. Mazeliauskas, J.-F. Paquet, S. Schlichting, D. Teaney, Effective kinetic description of event-by-event pre-equilibrium dynamics in high-energy heavy-ion collisions, Phys. Rev. C 99 (3) (2019) 034910. `arXiv:1805.00961, doi:10.1103/PhysRevC.99.034910`.

[61] A. Kurkela, A. Mazeliauskas, J.-F. Paquet, S. Schlichting, D. Teaney, Matching the Nonequilibrium Initial Stage of Heavy Ion Collisions to Hydrodynamics with QCD Kinetic Theory, Phys. Rev. Lett. 122 (12) (2019) 122302. `arXiv:1805.01604, doi:10.1103/PhysRevLett.122.122302`.

[62] Z. Xu, C. Greiner, Thermalization of gluons in ultrarelativistic heavy ion collisions by including three-body interactions in a parton cascade, Phys. Rev. C 71 (2005) 064901. `arXiv:hep-ph/0406278, doi:10.1103/PhysRevC.71.064901`.

[63] M. L. Miller, K. Reygers, S. J. Sanders, P. Steinberg, Glauber modeling in high energy nuclear collisions, Ann. Rev. Nucl. Part. Sci. 57 (2007) 205–243. `arXiv:nucl-ex/0701025, doi:10.1146/annurev.nucl.57.090506.123020`.

[64] H. Petersen, G.-Y. Qin, S. A. Bass, B. Muller, Triangular flow in event-by-event ideal hydrodynamics in Au+Au collisions at $\sqrt{s_{NN}} = 200A$ GeV, Phys. Rev. C 82 (2010) 041901. `arXiv:1008.0625, doi:10.1103/PhysRevC.82.041901`.

[65] K. Werner, I. Karpenko, M. Bleicher, T. Pierog, S. Porteboeuf-Houssais, Jets, Bulk Matter, and their Interaction in Heavy Ion Collisions at Several TeV, Phys. Rev. C 85 (2012) 064907. `arXiv:1203.5704, doi:10.1103/PhysRevC.85.064907`.

[66] L. Pang, Q. Wang, X.-N. Wang, Effects of initial flow velocity fluctuation in event-by-event (3+1)D hydrodynamics, Phys. Rev. C 86 (2012) 024911. `arXiv:1205.5019, doi:10.1103/PhysRevC.86.024911`.

[67] Y. Akamatsu, M. Asakawa, T. Hirano, M. Kitazawa, K. Morita, K. Murase, Y. Nara, C. Nonaka, A. Ohnishi, Dynamically integrated transport approach for heavy-ion collisions at high baryon density, Phys. Rev. C 98 (2) (2018) 024909. `arXiv:1805.09024, doi:10.1103/PhysRevC.98.024909`.

[68] C. Bierlich, et al., A comprehensive guide to the physics and usage of PYTHIA 8.3`arXiv:2203.11601, doi:10.21468/SciPostPhysCodeb.8`.

[69] C. Bierlich, S. Chakraborty, N. Desai, L. Gellersen, I. Helenius, P. Ilten, L. Lönnblad, S. Mrenna, S. Prestel, C. T. Preuss, T. Sjöstrand, P. Skands, M. Utheim, R. Verheyen, Codebase release 8.3 for PYTHIA, SciPost Phys. Codebases (2022) 8–r8.3`doi:10.21468/SciPostPhysCodeb.8-r8.3`.
URL `https://scipost.org/10.21468/SciPostPhysCodeb.8-r8.3`

[70] B. Bally, G. Giacalone, M. Bender, The shape of gold, Eur. Phys. J. A 59 (3) (2023) 58. `arXiv:2301.02420, doi:10.1140/epja/s10050-023-00955-3`.

[71] W. Ryssens, G. Giacalone, B. Schenke, C. Shen, Evidence of Hexadecapole Deformation in Uranium-238 at the Relativistic Heavy Ion Collider, Phys. Rev. Lett. 130 (21) (2023) 212302. `arXiv:2302.13617, doi:10.1103/PhysRevLett.130.212302`.

[72] G. Giacalone, G. Nijs, W. van der Schee, Determination of the neutron skin of ^{208}Pb from ultrarelativistic nuclear collisions`arXiv:2305.00015`.

[73] I. Angeli, K. P. Marinova, Table of experimental nuclear ground state charge radii: An update, Atom. Data Nucl. Data Tabl. 99 (1) (2013) 69–95. `doi:10.1016/j.adt.2011.12.006`.

[74] C. Shen, L. Yan, Recent development of hydrodynamic modeling in heavy-ion collisions, Nucl. Sci. Tech. 31 (12) (2020) 122. `arXiv:2010.12377, doi:10.1007/s41365-020-00829-z`.

[75] V. Khachatryan, et al., Evidence for collectivity in pp collisions at the LHC, Phys. Lett. B 765 (2017) 193–220. `arXiv:1606.06198, doi:10.1016/j.physletb.2016.12.009`.

[76] G. Aad, et al., Observation of Long-Range Elliptic Azimuthal Anisotropies in $\sqrt{s}$ =13 and 2.76 TeV pp Collisions with the ATLAS Detector, Phys. Rev. Lett. 116 (17) (2016) 172301. `arXiv:1509.04776, doi:10.1103/PhysRevLett.116.172301`.

[77] P. Huovinen, P. Petreczky, QCD Equation of State and Hadron Resonance Gas, Nucl. Phys. A 837 (2010) 26–53. `arXiv:0912.2541, doi:10.1016/j.nuclphysa.2010.02.015`.

[78] J. Steinheimer, S. Schramm, H. Stocker, An Effective chiral Hadron-Quark Equation of State, J. Phys. G 38 (2011) 035001. `arXiv:1009.5239, doi:10.1088/0954-3899/38/3/035001`.

[79] P. F. Kolb, U. W. Heinz, Hydrodynamic description of ultrarelativistic heavy ion collisions (2003) 634–714`arXiv:nucl-th/0305084`.

[80] X. An, G. Başar, M. Stephanov, H.-U. Yee, Fluctuation dynamics in a relativistic fluid with a critical point, Phys. Rev. C 102 (3) (2020) 034901. `arXiv:1912.13456, doi:10.1103/PhysRevC.102.034901`.

[81] B. Schenke, S. Jeon, C. Gale, (3+1)D hydrodynamic simulation of relativistic heavy-ion collisions, Phys. Rev. C 82 (2010) 014903. `arXiv:1004.1408, doi:10.1103/PhysRevC.82.014903`.

[82] L.-G. Pang, H. Petersen, X.-N. Wang, Pseudorapidity distribution and decorrelation of anisotropic flow within CLVisc hydrodynamics`arXiv:1802.04449`.

[83] I. Karpenko, P. Huovinen, M. Bleicher, A 3+1 dimensional viscous hydro-dynamic code for relativistic heavy ion collisions, Comput. Phys. Commun. 185 (2014) 3016–3027. `arXiv:1312.4160`, `doi:10.1016/j.cpc.2014.07.010`.

[84] F. Cooper, G. Frye, Comment on the Single Particle Distribution in the Hydro-dynamic and Statistical Thermodynamic Models of Multiparticle Production, Phys. Rev. D 10 (1974) 186. `doi:10.1103/PhysRevD.10.186`.

[85] J. Weil, et al., Particle production and equilibrium properties within a new hadron transport approach for heavy-ion collisions, Phys. Rev. C 94 (5) (2016) 054905. `arXiv:1606.06642`, `doi:10.1103/PhysRevC.94.054905`.

[86] O. Buss, T. Gaitanos, K. Gallmeister, H. van Hees, M. Kaskulov, O. Lalakulich, A. B. Larionov, T. Leitner, J. Weil, U. Mosel, Transport-theoretical Description of Nuclear Reactions, Phys. Rept. 512 (2012) 1–124. `arXiv:1106.1344`, `doi:10.1016/j.physrep.2011.12.001`.

[87] S. A. Bass, et al., Microscopic models for ultrarelativistic heavy ion collisions, Prog. Part. Nucl. Phys. 41 (1998) 255–369. `arXiv:nucl-th/9803035`, `doi:10.1016/S0146-6410(98)00058-1`.

[88] W. Cassing, E. L. Bratkovskaya, Hadronic and electromagnetic probes of hot and dense nuclear matter, Phys. Rept. 308 (1999) 65–233. `doi:10.1016/S0370-1573(98)00028-3`.

[89] W. Cassing, E. L. Bratkovskaya, Parton transport and hadronization from the dynamical quasiparticle point of view, Phys. Rev. C 78 (2008) 034919. `arXiv:0808.0022`, `doi:10.1103/PhysRevC.78.034919`.

[90] Y. Nara, N. Otuka, A. Ohnishi, K. Niita, S. Chiba, Study of relativistic nuclear collisions at AGS energies from p + Be to Au + Au with hadronic cascade model, Phys. Rev. C 61 (2000) 024901. `arXiv:nucl-th/9904059`, `doi:10.1103/PhysRevC.61.024901`.

[91] Z.-W. Lin, C. M. Ko, B.-A. Li, B. Zhang, S. Pal, A Multi-phase transport model for relativistic heavy ion collisions, Phys. Rev. C 72 (2005) 064901. `arXiv:nucl-th/0411110`, `doi:10.1103/PhysRevC.72.064901`.

[92] J. Xu, Transport approaches for the description of intermediate-energy heavy-ion collisions, Prog. Part. Nucl. Phys. 106 (2019) 312–359. `arXiv:1904.00131`, `doi:10.1016/j.ppnp.2019.02.009`.

[93] `https://smash-transport.github.io`, accessed: 2023-21-06.

[94] D. Oliinychenko, V. Steinberg, J. Weil, J. Staudenmaier, M. Kretz, A. Schäfer, H. E. (Petersen), S. Ryu, J. Rothermel, J. Mohs, F. Li, A. Sorensen, D. Mitrovic, L. Pang, J. Hammelmann, A. Goldschmidt, M. Mayer, O. Garcia-Montero, N. Kübler, Nikita, smash-transport/smash: Smash-2.0 (Dec. 2020). `doi:10.5281/zenodo.4336358`.
URL `https://doi.org/10.5281/zenodo.4336358`

[95] J. Staudenmaier, J. Weil, V. Steinberg, S. Endres, H. Petersen, Dilepton production and resonance properties within a new hadronic transport approach in the context of the GSI-HADES experimental data, Phys. Rev. C 98 (5) (2018) 054908. `arXiv:1711.10297, doi:10.1103/PhysRevC.98.054908`.

[96] A. Schäfer, O. Garcia-Montero, J.-F. Paquet, H. Elfner, C. Gale, Out-of-equilibrium photon production in the late stages of relativistic heavy-ion collisions, Phys. Rev. C 105 (4) (2022) 044910. `arXiv:2111.13603, doi:10.1103/PhysRevC.105.044910`.

[97] V. Steinberg, J. Staudenmaier, D. Oliinychenko, F. Li, O. Erkiner, H. Elfner, Strangeness production via resonances in heavy-ion collisions at energies available at the GSI Schwerionensynchrotron, Phys. Rev. C 99 (6) (2019) 064908. `arXiv:1809.03828, doi:10.1103/PhysRevC.99.064908`.

[98] V. Steinberg, J. Steinheimer, H. Elfner, M. Bleicher, Constraining resonance properties through kaon production in pion–nucleus collisions at low energies, J. Phys. G 48 (2) (2021) 025109. `arXiv:1912.09895, doi:10.1088/1361-6471/abd232`.

[99] J. Mohs, S. Ryu, H. Elfner, Particle Production via Strings and Baryon Stopping within a Hadronic Transport Approach, J. Phys. G 47 (6) (2020) 065101. `arXiv:1909.05586, doi:10.1088/1361-6471/ab7bd1`.

[100] J. Staudenmaier, N. Kübler, H. Elfner, Particle production in AgAg collisions at $E_{\text{Kin}} = 1.58A$ GeV within a hadronic transport approach, Phys. Rev. C 103 (4) (2021) 044904. `arXiv:2008.05813, doi:10.1103/PhysRevC.103.044904`.

[101] O. Garcia-Montero, J. Staudenmaier, A. Schäfer, J. M. Torres-Rincon, H. Elfner, Role of proton-antiproton regeneration in the late stages of heavy-ion collisions, Phys. Rev. C 105 (6) (2022) 064906. `arXiv:2107.08812, doi:10.1103/PhysRevC.105.064906`.

[102] D. Oliinychenko, C. Shen, V. Koch, Deuteron production in AuAu collisions at $\sqrt{s_{NN}}$ =7–200 GeV via pion catalysis, Phys. Rev. C 103 (3) (2021) 034913. `arXiv:2009.01915, doi:10.1103/PhysRevC.103.034913`.

[103] J. B. Rose, J. M. Torres-Rincon, A. Schäfer, D. R. Oliinychenko, H. Petersen, Shear viscosity of a hadron gas and influence of resonance lifetimes on relaxation time, Phys. Rev. C 97 (5) (2018) 055204. `arXiv:1709.03826, doi:10.1103/PhysRevC.97.055204`.

[104] P. Dorau, J.-B. Rose, D. Pablos, H. Elfner, Jet Quenching in the Hadron Gas: An Exploratory Study, Phys. Rev. C 101 (3) (2020) 035208. `arXiv:1910.07027, doi:10.1103/PhysRevC.101.035208`.

[105] J. Hammelmann, J. M. Torres-Rincon, J.-B. Rose, M. Greif, H. Elfner, Electrical conductivity and relaxation via colored noise in a hadronic gas, Phys.

Rev. D 99 (7) (2019) 076015. `arXiv:1810.12527`, `doi:10.1103/PhysRevD.99.076015`.

[106] J. B. Rose, J. M. Torres-Rincon, H. Elfner, Inclusive and effective bulk viscosities in the hadron gas, J. Phys. G 48 (1) (2020) 015005. `arXiv:2005.03647`, `doi:10.1088/1361-6471/abbc5c`.

[107] J.-B. Rose, M. Greif, J. Hammelmann, J. A. Fotakis, G. S. Denicol, H. Elfner, C. Greiner, Cross-conductivity: novel transport coefficients to constrain the hadronic degrees of freedom of nuclear matter, Phys. Rev. D 101 (11) (2020) 114028. `arXiv:2001.10606`, `doi:10.1103/PhysRevD.101.114028`.

[108] G. S. Denicol, C. Gale, S. Jeon, A. Monnai, B. Schenke, C. Shen, Net baryon diffusion in fluid dynamic simulations of relativistic heavy-ion collisions, Phys. Rev. C 98 (3) (2018) 034916. `arXiv:1804.10557`, `doi:10.1103/PhysRevC.98.034916`.

[109] A. Monnai, Dissipative Hydrodynamic Effects on Baryon Stopping, Phys. Rev. C 86 (2012) 014908. `arXiv:1204.4713`, `doi:10.1103/PhysRevC.86.014908`.

[110] M. Greif, J. A. Fotakis, G. S. Denicol, C. Greiner, Diffusion of conserved charges in relativistic heavy ion collisions, Phys. Rev. Lett. 120 (24) (2018) 242301. `arXiv:1711.08680`, `doi:10.1103/PhysRevLett.120.242301`.

[111] J. A. Fotakis, M. Greif, C. Greiner, G. S. Denicol, H. Niemi, Diffusion processes involving multiple conserved charges: A study from kinetic theory and implications to the fluid-dynamical modeling of heavy ion collisions, Phys. Rev. D 101 (7) (2020) 076007. `arXiv:1912.09103`, `doi:10.1103/PhysRevD.101.076007`.

[112] J. A. Fotakis, O. Soloveva, C. Greiner, O. Kaczmarek, E. Bratkovskaya, Diffusion coefficient matrix of the strongly interacting quark-gluon plasma, Phys. Rev. D 104 (3) (2021) 034014. `arXiv:2102.08140`, `doi:10.1103/PhysRevD.104.034014`.

[113] K. Tuchin, Particle production in strong electromagnetic fields in relativistic heavy-ion collisions, Adv. High Energy Phys. 2013 (2013) 490495. `arXiv:1301.0099`, `doi:10.1155/2013/490495`.

[114] G. Inghirami, L. Del Zanna, A. Beraudo, M. H. Moghaddam, F. Becattini, M. Bleicher, Numerical magneto-hydrodynamics for relativistic nuclear collisions, Eur. Phys. J. C 76 (12) (2016) 659. `arXiv:1609.03042`, `doi:10.1140/epjc/s10052-016-4516-8`.

[115] V. Roy, S. Pu, L. Rezzolla, D. H. Rischke, Effect of intense magnetic fields on reduced-MHD evolution in $\sqrt{s_{\mathrm{NN}}} = 200$ GeV Au+Au collisions, Phys. Rev. C 96 (5) (2017) 054909. `arXiv:1706.05326`, `doi:10.1103/PhysRevC.96.054909`.

[116] H.-T. Ding, O. Kaczmarek, F. Meyer, Thermal dilepton rates and electrical conductivity of the QGP from the lattice, Phys. Rev. D 94 (3) (2016) 034504. `arXiv:1604.06712`, `doi:10.1103/PhysRevD.94.034504`.

[117] J. Ghiglieri, O. Kaczmarek, M. Laine, F. Meyer, Lattice constraints on the thermal photon rate, Phys. Rev. D 94 (1) (2016) 016005. `arXiv:1604.07544`, `doi:10.1103/PhysRevD.94.016005`.

[118] D. Fernandez-Fraile, A. Gomez Nicola, The Electrical conductivity of a pion gas, Phys. Rev. D 73 (2006) 045025. `arXiv:hep-ph/0512283`, `doi:10.1103/PhysRevD.73.045025`.

[119] M. Greif, C. Greiner, G. S. Denicol, Electric conductivity of a hot hadron gas from a kinetic approach, Phys. Rev. D 93 (9) (2016) 096012, [Erratum: Phys.Rev.D 96, 059902 (2017)]. `arXiv:1602.05085`, `doi:10.1103/PhysRevD.93.096012`.

[120] C. Gale, S. Jeon, B. Schenke, Hydrodynamic Modeling of Heavy-Ion Collisions, Int. J. Mod. Phys. A 28 (2013) 1340011. `arXiv:1301.5893`, `doi:10.1142/S0217751X13400113`.

[121] P. Romatschke, U. Romatschke, Viscosity Information from Relativistic Nuclear Collisions: How Perfect is the Fluid Observed at RHIC?, Phys. Rev. Lett. 99 (2007) 172301. `arXiv:0706.1522`, `doi:10.1103/PhysRevLett.99.172301`.

[122] K. Dusling, D. Teaney, Simulating elliptic flow with viscous hydrodynamics, Phys. Rev. C 77 (2008) 034905. `arXiv:0710.5932`, `doi:10.1103/PhysRevC.77.034905`.

[123] R. D. Weller, P. Romatschke, One fluid to rule them all: viscous hydrodynamic description of event-by-event central p+p, p+Pb and Pb+Pb collisions at $\sqrt{s} = 5.02$ TeV, Phys. Lett. B 774 (2017) 351–356. `arXiv:1701.07145`, `doi:10.1016/j.physletb.2017.09.077`.

[124] A. Adams, L. D. Carr, T. Schaefer, P. Steinberg, J. E. Thomas, Focus on strongly correlated quantum fluids: From ultracold quantum gases to QCD plasmas, New J. Phys. 15 (2013) 045022. `doi:10.1088/1367-2630/15/045022`.

[125] P. Kovtun, D. T. Son, A. O. Starinets, Viscosity in strongly interacting quantum field theories from black hole physics, Phys. Rev. Lett. 94 (2005) 111601. `arXiv:hep-th/0405231`, `doi:10.1103/PhysRevLett.94.111601`.

[126] A. Muronga, Shear viscosity coefficient from microscopic models, Phys. Rev. C 69 (2004) 044901. `arXiv:nucl-th/0309056`, `doi:10.1103/PhysRevC.69.044901`.

[127] N. Demir, S. A. Bass, Shear-Viscosity to Entropy-Density Ratio of a Relativistic Hadron Gas, Phys. Rev. Lett. 102 (2009) 172302. `arXiv:0812.2422`, `doi:10.1103/PhysRevLett.102.172302`.

[128] C. Wesp, A. El, F. Reining, Z. Xu, I. Bouras, C. Greiner, Calculation of shear viscosity using Green-Kubo relations within a parton cascade, Phys. Rev. C 84 (2011) 054911. `arXiv:1106.4306`, `doi:10.1103/PhysRevC.84.054911`.

[129] S. Plumari, A. Puglisi, F. Scardina, V. Greco, Shear Viscosity of a strongly interacting system: Green-Kubo vs. Chapman-Enskog and Relaxation Time Approximation, Phys. Rev. C 86 (2012) 054902. `arXiv:1208.0481`, `doi:10.1103/PhysRevC.86.054902`.

[130] V. Ozvenchuk, O. Linnyk, M. I. Gorenstein, E. L. Bratkovskaya, W. Cassing, Shear and bulk viscosities of strongly interacting "infinite" parton-hadron matter within the parton-hadron-string dynamics transport approach, Phys. Rev. C 87 (6) (2013) 064903. `arXiv:1212.5393`, `doi:10.1103/PhysRevC.87.064903`.

[131] S. Pratt, A. Baez, J. Kim, Determining Transport Coefficients for a Microscopic Simulation of a Hadron Gas, Phys. Rev. C 95 (2) (2017) 024901. `arXiv:1610.07239`, `doi:10.1103/PhysRevC.95.024901`.

[132] J. M. Torres-Rincon, Hadronic transport coefficients from effective field theories, Ph.D. thesis, UCM, Madrid, Dept. Phys., UCM, Somosaguas (2012). `arXiv:1205.0782`, `doi:10.1007/978-3-319-00425-9`.

[133] E. McLaughlin, J. Rose, T. Dore, P. Parotto, C. Ratti, J. Noronha-Hostler, Building a testable shear viscosity across the QCD phase diagram, Phys. Rev. C 105 (2) (2022) 024903. `arXiv:2103.02090`, `doi:10.1103/PhysRevC.105.024903`.

[134] J. E. Bernhard, J. S. Moreland, S. A. Bass, J. Liu, U. Heinz, Applying Bayesian parameter estimation to relativistic heavy-ion collisions: simultaneous characterization of the initial state and quark-gluon plasma medium, Phys. Rev. C 94 (2) (2016) 024907. `arXiv:1605.03954`, `doi:10.1103/PhysRevC.94.024907`.

[135] D. Everett, et al., Multisystem Bayesian constraints on the transport coefficients of QCD matter, Phys. Rev. C 103 (5) (2021) 054904. `arXiv:2011.01430`, `doi:10.1103/PhysRevC.103.054904`.

[136] D. Everett, et al., Phenomenological constraints on the transport properties of QCD matter with data-driven model averaging, Phys. Rev. Lett. 126 (24) (2021) 242301. `arXiv:2010.03928`, `doi:10.1103/PhysRevLett.126.242301`.

[137] G. Nijs, W. van der Schee, U. Gürsoy, R. Snellings, Bayesian analysis of heavy ion collisions with the heavy ion computational framework Trajectum, Phys. Rev. C 103 (5) (2021) 054909. `arXiv:2010.15134`, `doi:10.1103/PhysRevC.103.054909`.

[138] J. E. Parkkila, A. Onnerstad, D. J. Kim, Bayesian estimation of the specific shear and bulk viscosity of the quark-gluon plasma with additional flow harmonic observables, Phys. Rev. C 104 (5) (2021) 054904. `arXiv:2106.05019`, `doi:10.1103/PhysRevC.104.054904`.

[139] J. E. Parkkila, A. Onnerstad, S. F. Taghavi, C. Mordasini, A. Bilandzic, M. Virta, D. J. Kim, New constraints for QCD matter from improved Bayesian parameter estimation in heavy-ion collisions at LHC, Phys. Lett. B 835 (2022) 137485. `arXiv:2111.08145, doi:10.1016/j.physletb.2022.137485`.

[140] T. Reichert, G. Inghirami, M. Bleicher, A first estimate of η/s in Au+Au reactions at $E_{lab} = 1.23$ A GeV, Phys. Lett. B 817 (2021) 136285. `arXiv:2011.04546, doi:10.1016/j.physletb.2021.136285`.

[141] Z. Yang, R. J. Fries, Shear stress tensor and specific shear viscosity of hot hadron gas in nuclear collisions, Phys. Rev. C 105 (1) (2022) 014910. `doi:10.1103/PhysRevC.105.014910`.

[142] J. Staudenmaier, D. Oliinychenko, J. M. Torres-Rincon, H. Elfner, Deuteron production in relativistic heavy ion collisions via stochastic multiparticle reactions, Phys. Rev. C 104 (3) (2021) 034908. `arXiv:2106.14287, doi:10.1103/PhysRevC.104.034908`.

[143] G. Aarts, C. Allton, A. Amato, P. Giudice, S. Hands, J.-I. Skullerud, Electrical conductivity and charge diffusion in thermal QCD from the lattice, JHEP 02 (2015) 186. `arXiv:1412.6411, doi:10.1007/JHEP02(2015)186`.

[144] M. Tanabashi, et al., Review of Particle Physics, Phys. Rev. D 98 (3) (2018) 030001. `doi:10.1103/PhysRevD.98.030001`.

[145] `http://theory.gsi.de/~smash/analysis_suite/SMASH-2.2/cross_sections/`, accessed: 2023-12-08.

[146] `http://theory.gsi.de/~smash/analysis_suite/SMASH-2.2/index.html`, accessed: 2023-12-08.

[147] `http://theory.gsi.de/~smash/analysis_suite/SMASH-2.2/detailed_balance/`, accessed: 2023-25-09.

[148] J. Tindall, J. M. Torres-Rincon, J. B. Rose, H. Petersen, Equilibration and freeze-out of an expanding gas in a transport approach in a Friedmann–Robertson–Walker metric, Phys. Lett. B 770 (2017) 532–538. `arXiv:1612.06436, doi:10.1016/j.physletb.2017.04.080`.

[149] R. Kubo, The fluctuation-dissipation theorem, Reports on Progress in Physics 29 (1) (1966) 255. `doi:10.1088/0034-4885/29/1/306`.
URL `https://dx.doi.org/10.1088/0034-4885/29/1/306`

[150] J.-B. Rose, Transport coefficients in the hadronic medium, Ph.D. thesis, Goethe U., Frankfurt (main), Goethe U., Frankfurt (main) (2020).

[151] J. I. Kapusta, B. Muller, M. Stephanov, Relativistic Theory of Hydrodynamic Fluctuations with Applications to Heavy Ion Collisions, Phys. Rev. C 85 (2012) 054906. `arXiv:1112.6405`, `doi:10.1103/PhysRevC.85.054906`.

[152] K. Murase, T. Hirano, Relativistic fluctuating hydrodynamics with memory functions and colored noises`arXiv:1304.3243`.

[153] J. I. Kapusta, C. Plumberg, Causal Electric Charge Diffusion and Balance Functions in Relativistic Heavy Ion Collisions, Phys. Rev. C 97 (1) (2018) 014906, [Erratum: Phys.Rev.C 102, 019901 (2020)]. `arXiv:1710.03329`, `doi:10.1103/PhysRevC.97.014906`.

[154] G. Pihan, M. Bluhm, M. Nahrgang, Coupled baryon, electric charge and strangeness fluctuations in heavy-ion collisions, EPJ Web Conf. 259 (2022) 10003. `arXiv:2111.13977`, `doi:10.1051/epjconf/202225910003`.

[155] T. Hirano, Y. Nara, Dynamical modeling of high energy heavy ion collisions, PTEP 2012 (2012) 01A203. `arXiv:1203.4418`, `doi:10.1093/ptep/pts007`.

[156] J. Hammelmann, A. Soto-Ontoso, M. Alvioli, H. Elfner, M. Strikman, Influence of the neutron-skin effect on nuclear isobar collisions at energies available at the BNL Relativistic Heavy Ion Collider, Phys. Rev. C 101 (6) (2020) 061901. `arXiv:1908.10231`, `doi:10.1103/PhysRevC.101.061901`.

[157] D. M. Manley, E. M. Saleski, Multichannel resonance parametrization of pi N scattering amplitudes, Phys. Rev. D 45 (1992) 4002–4033. `doi:10.1103/PhysRevD.45.4002`.

[158] J. M. Blatt, V. F. Weisskopf, Theoretical nuclear physics, Springer, New York, 1952. `doi:10.1007/978-1-4612-9959-2`.

[159] R. Hirayama, J. Staudenmaier, H. Elfner, Effective spectral function of vector mesons via lifetime analysis, Phys. Rev. C 107 (2) (2023) 025208. `arXiv:2206.15166`, `doi:10.1103/PhysRevC.107.025208`.

[160] W. Cassing, Anti-baryon production in hot and dense nuclear matter, Nucl. Phys. A 700 (2002) 618–646. `arXiv:nucl-th/0105069`, `doi:10.1016/S0375-9474(01)01322-7`.

[161] E. Seifert, W. Cassing, Baryon-antibaryon annihilation and reproduction in relativistic heavy-ion collisions, Phys. Rev. C 97 (2) (2018) 024913. `arXiv:1710.00665`, `doi:10.1103/PhysRevC.97.024913`.

[162] `http://geb.uni-giessen.de/geb/volltexte/2013/10253/`, accessed: 2023-09-08.

[163] L. L. Frankfurt, M. I. Strikman, Hard Nuclear Processes and Microscopic Nuclear Structure, Phys. Rept. 160 (1988) 235–427. `doi:10.1016/0370-1573(88)90179-2`.

[164] J. Cugnon, J. Vandermeulen, D. L'Hote, Simple parametrization of cross-sections for nuclear transport studies up to the GeV range, Nucl. Instrum. Meth. B 111 (1996) 215–220. `doi:10.1016/0168-583X(95)01384-9`.

[165] `http://theory.gsi.de/~smash/analysis_suite/SMASH-2.2/angular_distributions/`, accessed: 2023-28-07.

[166] T. C. Bacon, F. M. Bomse, T. B. Cochran, W. J. Fickinger, E. R. Goza, H. W. K. Hopkins, E. O. Salant, Comparison of Isobar Production in pp and $\bar{p}n$ Interactions at 2.8 GeV/c, Phys. Rev. 162 (1967) 1320–1322. `doi:10.1103/PhysRev.162.1320`.

[167] N. Christiansen, M. Haas, J. M. Pawlowski, N. Strodthoff, Transport Coefficients in Yang–Mills Theory and QCD, Phys. Rev. Lett. 115 (11) (2015) 112002. `arXiv:1411.7986, doi:10.1103/PhysRevLett.115.112002`.

[168] P. Romatschke, S. Pratt, Extracting the shear viscosity of a high temperature hadron gas `arXiv:1409.0010`.

[169] J. Ghiglieri, G. D. Moore, D. Teaney, QCD Shear Viscosity at (almost) NLO, JHEP 03 (2018) 179. `arXiv:1802.09535, doi:10.1007/JHEP03(2018)179`.

[170] O. N. Moroz, Analytical formulas, general properties and calculation of transport coefficients in the hadron gas: shear and bulk viscosities `arXiv:1301.6670`.

[171] M. Greif, I. Bouras, C. Greiner, Z. Xu, Electric conductivity of the quark-gluon plasma investigated using a perturbative QCD based parton cascade, Phys. Rev. D 90 (9) (2014) 094014. `arXiv:1408.7049, doi:10.1103/PhysRevD.90.094014`.

[172] B. B. Brandt, A. Francis, B. Jäger, H. B. Meyer, Charge transport and vector meson dissociation across the thermal phase transition in lattice QCD with two light quark flavors, Phys. Rev. D 93 (5) (2016) 054510. `arXiv:1512.07249, doi:10.1103/PhysRevD.93.054510`.

[173] A. Amato, G. Aarts, C. Allton, P. Giudice, S. Hands, J.-I. Skullerud, Electrical conductivity of the quark-gluon plasma across the deconfinement transition, Phys. Rev. Lett. 111 (17) (2013) 172001. `arXiv:1307.6763, doi:10.1103/PhysRevLett.111.172001`.

[174] B. B. Brandt, A. Francis, H. B. Meyer, H. Wittig, Thermal Correlators in the \rho\ channel of two-flavor QCD, JHEP 03 (2013) 100. `arXiv:1212.4200, doi:10.1007/JHEP03(2013)100`.

[175] R. Rougemont, J. Noronha, J. Noronha-Hostler, Suppression of baryon diffusion and transport in a baryon rich strongly coupled quark-gluon plasma, Phys. Rev. Lett. 115 (20) (2015) 202301. `arXiv:1507.06972, doi:10.1103/PhysRevLett.115.202301`.

[176] S. I. Finazzo, J. Noronha, Holographic calculation of the electric conductivity of the strongly coupled quark-gluon plasma near the deconfinement transition, Phys. Rev. D 89 (10) (2014) 106008. `arXiv:1311.6675`, `doi:10.1103/PhysRevD.89.106008`.

[177] X. Luo, N. Xu, Search for the QCD Critical Point with Fluctuations of Conserved Quantities in Relativistic Heavy-Ion Collisions at RHIC : An Overview, Nucl. Sci. Tech. 28 (8) (2017) 112. `arXiv:1701.02105`, `doi:10.1007/s41365-017-0257-0`.

[178] M. Asakawa, M. Kitazawa, Fluctuations of conserved charges in relativistic heavy ion collisions: An introduction, Prog. Part. Nucl. Phys. 90 (2016) 299–342. `arXiv:1512.05038`, `doi:10.1016/j.ppnp.2016.04.002`.

[179] H.-T. Ding, F. Karsch, S. Mukherjee, Thermodynamics of strong-interaction matter from Lattice QCD, Int. J. Mod. Phys. E 24 (10) (2015) 1530007. `arXiv:1504.05274`, `doi:10.1142/S0218301315300076`.

[180] A. Bazavov, et al., Equation of state in (2+1)-flavor QCD, Phys. Rev. D 90 (2014) 094503. `arXiv:1407.6387`, `doi:10.1103/PhysRevD.90.094503`.

[181] A. K. Schäfer, Dynamical production of hadrons and photons in hydrodynamics + transport approaches for relativistic heavy-ion collisions, Ph.D. thesis, Goethe U., Frankfurt (main), Frankfurt U. (2022). `doi:10.21248/gups.68090`.

[182] V. Koch, Hadronic Fluctuations and Correlations, 2010, pp. 626–652. `arXiv:0810.2520`, `doi:10.1007/978-3-642-01539-7_20`.

[183] A. Bzdak, V. Koch, V. Skokov, Baryon number conservation and the cumulants of the net proton distribution, Phys. Rev. C 87 (1) (2013) 014901. `arXiv:1203.4529`, `doi:10.1103/PhysRevC.87.014901`.

[184] V. Vovchenko, O. Savchuk, R. V. Poberezhnyuk, M. I. Gorenstein, V. Koch, Connecting fluctuation measurements in heavy-ion collisions with the grand-canonical susceptibilities, Phys. Lett. B 811 (2020) 135868. `arXiv:2003.13905`, `doi:10.1016/j.physletb.2020.135868`.

[185] M. Nahrgang, T. Schuster, M. Mitrovski, R. Stock, M. Bleicher, Net-baryon-, net-proton-, and net-charge kurtosis in heavy-ion collisions within a relativistic transport approach, Eur. Phys. J. C 72 (2012) 2143. `arXiv:0903.2911`, `doi:10.1140/epjc/s10052-012-2143-6`.

[186] V. A. Kuznietsov, O. Savchuk, M. I. Gorenstein, V. Koch, V. Vovchenko, Critical point particle number fluctuations from molecular dynamics, Phys. Rev. C 105 (4) (2022) 044903. `arXiv:2201.08486`, `doi:10.1103/PhysRevC.105.044903`.

[187] H. Petersen, D. Oliinychenko, J. Steinheimer, M. Bleicher, Influence of kinematic cuts on the net charge distribution, Nucl. Phys. A 956 (2016) 336–339. `arXiv:1512.05603`, `doi:10.1016/j.nuclphysa.2016.01.059`.

[188] O. Savchuk, R. V. Poberezhnyuk, V. Vovchenko, M. I. Gorenstein, Binomial acceptance corrections for particle number distributions in high-energy reactions, Phys. Rev. C 101 (2) (2020) 024917. `arXiv:1911.03426`, `doi:10.1103/PhysRevC.101.024917`.

[189] R. V. Poberezhnyuk, O. Savchuk, M. I. Gorenstein, V. Vovchenko, K. Taradiy, V. V. Begun, L. Satarov, J. Steinheimer, H. Stoecker, Critical point fluctuations: Finite size and global charge conservation effects, Phys. Rev. C 102 (2) (2020) 024908. `arXiv:2004.14358`, `doi:10.1103/PhysRevC.102.024908`.

[190] N. S. Demir, Extraction of Hot QCD Matter Transport Coefficients utilizing Microscopic Transport Theory, Ph.D. thesis, Duke U. (main) (2010).

[191] E. Abbas, et al., Centrality dependence of the pseudorapidity density distribution for charged particles in Pb-Pb collisions at $\sqrt{s_{NN}} = 2.76$ TeV, Phys. Lett. B 726 (2013) 610–622. `arXiv:1304.0347`, `doi:10.1016/j.physletb.2013.09.022`.

[192] S. Acharya, et al., Global baryon number conservation encoded in net-proton fluctuations measured in Pb-Pb collisions at $\sqrt{s_{NN}} = 2.76$ TeV, Phys. Lett. B 807 (2020) 135564. `arXiv:1910.14396`, `doi:10.1016/j.physletb.2020.135564`.

[193] M. Kitazawa, M. Asakawa, Revealing baryon number fluctuations from proton number fluctuations in relativistic heavy ion collisions, Phys. Rev. C 85 (2012) 021901. `arXiv:1107.2755`, `doi:10.1103/PhysRevC.85.021901`.

[194] M. Kitazawa, M. Asakawa, Relation between baryon number fluctuations and experimentally observed proton number fluctuations in relativistic heavy ion collisions, Phys. Rev. C 86 (2012) 024904, [Erratum: Phys.Rev.C 86, 069902 (2012)]. `arXiv:1205.3292`, `doi:10.1103/PhysRevC.86.024904`.

[195] V. Vovchenko, V. Koch, C. Shen, Proton number cumulants and correlation functions in Au-Au collisions at sNN=7.7–200 GeV from hydrodynamics, Phys. Rev. C 105 (1) (2022) 014904. `arXiv:2107.00163`, `doi:10.1103/PhysRevC.105.014904`.

[196] Z. Fecková, J. Steinheimer, B. Tomášik, M. Bleicher, Formation of deuterons by coalescence: Consequences for deuteron number fluctuations, Phys. Rev. C 93 (5) (2016) 054906. `arXiv:1603.05854`, `doi:10.1103/PhysRevC.93.054906`.

[197] D. Oliinychenko, L.-G. Pang, H. Elfner, V. Koch, Microscopic study of deuteron production in PbPb collisions at $\sqrt{s} = 2.76 TeV$ via hydrodynamics and a hadronic afterburner, Phys. Rev. C 99 (4) (2019) 044907. `arXiv:1809.03071`, `doi:10.1103/PhysRevC.99.044907`.

[198] M. Nahrgang, S. Leupold, C. Herold, M. Bleicher, Nonequilibrium chiral fluid dynamics including dissipation and noise, Phys. Rev. C 84 (2011) 024912. `arXiv:1105.0622`, `doi:10.1103/PhysRevC.84.024912`.

[199] M. Nahrgang, S. Leupold, M. Bleicher, Equilibration and relaxation times at the chiral phase transition including reheating, Phys. Lett. B 711 (2012) 109–116. `arXiv:1105.1396`, `doi:10.1016/j.physletb.2012.03.059`.

[200] G. Pihan, M. Bluhm, M. Kitazawa, T. Sami, M. Nahrgang, Critical net-baryon fluctuations in an expanding system, Phys. Rev. C 107 (1) (2023) 014908. `arXiv:2205.12834`, `doi:10.1103/PhysRevC.107.014908`.

[201] K. Rajagopal, G. Ridgway, R. Weller, Y. Yin, Understanding the out-of-equilibrium dynamics near a critical point in the QCD phase diagram, Phys. Rev. D 102 (9) (2020) 094025. `arXiv:1908.08539`, `doi:10.1103/PhysRevD.102.094025`.

[202] M. Nahrgang, M. Bluhm, Modeling the diffusive dynamics of critical fluctuations near the QCD critical point, Phys. Rev. D 102 (9) (2020) 094017. `arXiv:2007.10371`, `doi:10.1103/PhysRevD.102.094017`.

[203] L. Du, U. Heinz, K. Rajagopal, Y. Yin, Fluctuation dynamics near the QCD critical point, Phys. Rev. C 102 (5) (2020) 054911. `arXiv:2004.02719`, `doi:10.1103/PhysRevC.102.054911`.

[204] C. Athanasiou, K. Rajagopal, M. Stephanov, Using Higher Moments of Fluctuations and their Ratios in the Search for the QCD Critical Point, Phys. Rev. D 82 (2010) 074008. `arXiv:1006.4636`, `doi:10.1103/PhysRevD.82.074008`.

[205] M. Pradeep, K. Rajagopal, M. Stephanov, Y. Yin, Freezing out fluctuations in Hydro+ near the QCD critical point, Phys. Rev. D 106 (3) (2022) 036017. `arXiv:2204.00639`, `doi:10.1103/PhysRevD.106.036017`.

[206] M. S. Pradeep, M. Stephanov, Maximum Entropy Freeze-Out of Hydrodynamic Fluctuations, Phys. Rev. Lett. 130 (16) (2023) 162301. `arXiv:2211.09142`, `doi:10.1103/PhysRevLett.130.162301`.

[207] P. C. Hohenberg, B. I. Halperin, Theory of Dynamic Critical Phenomena, Rev. Mod. Phys. 49 (1977) 435–479. `doi:10.1103/RevModPhys.49.435`.

[208] M. Bluhm, M. Nahrgang, S. A. Bass, T. Schaefer, Impact of resonance decays on critical point signals in net-proton fluctuations, Eur. Phys. J. C 77 (4) (2017) 210. `arXiv:1612.03889`, `doi:10.1140/epjc/s10052-017-4771-3`.

[209] R. Guida, J. Zinn-Justin, 3-D Ising model: The Scaling equation of state, Nucl. Phys. B 489 (1997) 626–652. `arXiv:hep-th/9610223`, `doi:10.1016/S0550-3213(96)00704-3`.

[210] A. Bzdak, S. Esumi, V. Koch, J. Liao, M. Stephanov, N. Xu, Mapping the Phases of Quantum Chromodynamics with Beam Energy Scan, Phys. Rept. 853 (2020) 1–87. `arXiv:1906.00936`, `doi:10.1016/j.physrep.2020.01.005`.

[211] P. Cea, L. Cosmai, A. Papa, Critical line of 2+1 flavor QCD: Toward the continuum limit, Phys. Rev. D 93 (1) (2016) 014507. `arXiv:1508.07599`, `doi:10.1103/PhysRevD.93.014507`.

[212] G. Endrodi, Z. Fodor, S. D. Katz, K. K. Szabo, The QCD phase diagram at nonzero quark density, JHEP 04 (2011) 001. `arXiv:1102.1356`, `doi:10.1007/JHEP04(2011)001`.

[213] T. Dore, J. M. Karthein, I. Long, D. Mroczek, J. Noronha-Hostler, P. Parotto, C. Ratti, Y. Yamauchi, Critical lensing and kurtosis near a critical point in the QCD phase diagram in and out of equilibrium, Phys. Rev. D 106 (9) (2022) 094024. `arXiv:2207.04086`, `doi:10.1103/PhysRevD.106.094024`.

[214] D. Raikov, On the decomposition of Gauss and Poisson laws, Izv. Akad. Nauk SSSR Ser. Mat. 2:1 (1938) (1938) 91–124.

[215] P. Alba, W. Alberico, R. Bellwied, M. Bluhm, V. Mantovani Sarti, M. Nahrgang, C. Ratti, Freeze-out conditions from net-proton and net-charge fluctuations at RHIC, Phys. Lett. B 738 (2014) 305–310. `arXiv:1403.4903`, `doi:10.1016/j.physletb.2014.09.052`.

[216] L. R. Mead, N. Papanicolaou, Maximum entropy in the problem of moments, Journal of Mathematical Physics 25 (8) (1984) 2404–2417. `arXiv:https://pubs.aip.org/aip/jmp/article-pdf/25/8/2404/8805488/2404\_1\_online.pdf`, `doi:10.1063/1.526446`.
URL `https://doi.org/10.1063/1.526446`

[217] E. T. Jaynes, Information Theory and Statistical Mechanics, Phys. Rev. 106 (1957) 620–630. `doi:10.1103/PhysRev.106.620`.

[218] D. Everett, C. Chattopadhyay, U. Heinz, Maximum entropy kinetic matching conditions for heavy-ion collisions, Phys. Rev. C 103 (6) (2021) 064902. `arXiv:2101.01130`, `doi:10.1103/PhysRevC.103.064902`.

[219] B. Ling, M. A. Stephanov, Acceptance dependence of fluctuation measures near the QCD critical point, Phys. Rev. C 93 (3) (2016) 034915. `arXiv:1512.09125`, `doi:10.1103/PhysRevC.93.034915`.

[220] L. Adamczyk, et al., Bulk Properties of the Medium Produced in Relativistic Heavy-Ion Collisions from the Beam Energy Scan Program, Phys. Rev. C 96 (4) (2017) 044904. `arXiv:1701.07065`, `doi:10.1103/PhysRevC.96.044904`.

[221] J. Fu, Higher moments of net-proton multiplicity distributions in heavy ion collisions at chemical freeze-out, Phys. Lett. B 722 (2013) 144–150. `doi:10.1016/j.physletb.2013.04.018`.

[222] P. Garg, D. K. Mishra, P. K. Netrakanti, B. Mohanty, A. K. Mohanty, B. K. Singh, N. Xu, Conserved number fluctuations in a hadron resonance gas model, Phys. Lett. B 726 (2013) 691–696. `arXiv:1304.7133`, `doi:10.1016/j.physletb.2013.09.019`.

[223] M. Nahrgang, M. Bluhm, P. Alba, R. Bellwied, C. Ratti, Impact of resonance regeneration and decay on the net-proton fluctuations in a hadron resonance gas, Eur. Phys. J. C 75 (12) (2015) 573. `arXiv:1402.1238, doi:10.1140/epjc/s10052-015-3775-0`.

[224] J. Brewer, S. Mukherjee, K. Rajagopal, Y. Yin, Searching for the QCD critical point via the rapidity dependence of cumulants, Phys. Rev. C 98 (6) (2018) 061901. `arXiv:1804.10215, doi:10.1103/PhysRevC.98.061901`.

[225] K. Fukushima, D. E. Kharzeev, H. J. Warringa, The Chiral Magnetic Effect, Phys. Rev. D 78 (2008) 074033. `arXiv:0808.3382, doi:10.1103/PhysRevD.78.074033`.

[226] A. Bzdak, V. Koch, J. Liao, Charge-Dependent Correlations in Relativistic Heavy Ion Collisions and the Chiral Magnetic Effect, Lect. Notes Phys. 871 (2013) 503–536. `arXiv:1207.7327, doi:10.1007/978-3-642-37305-3_19`.

[227] Q. Li, D. E. Kharzeev, C. Zhang, Y. Huang, I. Pletikosic, A. V. Fedorov, R. D. Zhong, J. A. Schneeloch, G. D. Gu, T. Valla, Observation of the chiral magnetic effect in ZrTe5, Nature Phys. 12 (2016) 550–554. `arXiv:1412.6543, doi:10.1038/nphys3648`.

[228] B. R. Holstein, Anomalies for pedestrians, American Journal of Physics 61. `doi:dx.doi.org/10.1119/1.17328`.

[229] T. Lappi, L. McLerran, Some features of the glasma, Nucl. Phys. A 772 (2006) 200–212. `arXiv:hep-ph/0602189, doi:10.1016/j.nuclphysa.2006.04.001`.

[230] T. Lappi, S. Schlichting, Linearly polarized gluons and axial charge fluctuations in the Glasma, Phys. Rev. D 97 (3) (2018) 034034. `arXiv:1708.08625, doi:10.1103/PhysRevD.97.034034`.

[231] P. Guerrero-Rodríguez, Topological charge fluctuations in the Glasma, JHEP 08 (2019) 026. `arXiv:1903.11602, doi:10.1007/JHEP08(2019)026`.

[232] F. R. Klinkhamer, N. S. Manton, A Saddle Point Solution in the Weinberg-Salam Theory, Phys. Rev. D 30 (1984) 2212. `doi:10.1103/PhysRevD.30.2212`.

[233] M. Mace, S. Schlichting, R. Venugopalan, Off-equilibrium sphaleron transitions in the Glasma, Phys. Rev. D 93 (7) (2016) 074036. `arXiv:1601.07342, doi:10.1103/PhysRevD.93.074036`.

[234] M. Mace, N. Mueller, S. Schlichting, S. Sharma, Non-equilibrium study of the Chiral Magnetic Effect from real-time simulations with dynamical fermions, Phys. Rev. D 95 (3) (2017) 036023. `arXiv:1612.02477, doi:10.1103/PhysRevD.95.036023`.

[235] N. Borghini, S. Feld, N. Kersting, Scaling behavior of anisotropic flow harmonics in the far from equilibrium regime, Eur. Phys. J. C 78 (10) (2018) 832. `arXiv:1804.05729, doi:10.1140/epjc/s10052-018-6313-z`.

[236] B. Andersson, G. Gustafson, G. Ingelman, T. Sjostrand, Parton Fragmentation and String Dynamics, Phys. Rept. 97 (1983) 31–145. `doi:10.1016/0370-1573(83)90080-7`.

[237] T. Sjostrand, S. Mrenna, P. Z. Skands, PYTHIA 6.4 Physics and Manual, JHEP 05 (2006) 026. `arXiv:hep-ph/0603175`, `doi:10.1088/1126-6708/2006/05/026`.

[238] T. Sjostrand, S. Mrenna, P. Z. Skands, A Brief Introduction to PYTHIA 8.1, Comput. Phys. Commun. 178 (2008) 852–867. `arXiv:0710.3820`, `doi:10.1016/j.cpc.2008.01.036`.

[239] M. Duer, et al., Direct Observation of Proton-Neutron Short-Range Correlation Dominance in Heavy Nuclei, Phys. Rev. Lett. 122 (17) (2019) 172502. `arXiv:1810.05343`, `doi:10.1103/PhysRevLett.122.172502`.

[240] M. Alvioli, C. Ciofi Degli Atti, L. P. Kaptari, C. B. Mezzetti, H. Morita, Universality of nucleon-nucleon short-range correlations and nucleon momentum distributions, Int. J. Mod. Phys. E 22 (2013) 1330021. `arXiv:1306.6235`, `doi:10.1142/S021830131330021X`.

[241] M. Alvioli, H. J. Drescher, M. Strikman, A Monte Carlo generator of nucleon configurations in complex nuclei including Nucleon-Nucleon correlations, Phys. Lett. B 680 (2009) 225–230. `arXiv:0905.2670`, `doi:10.1016/j.physletb.2009.08.067`.

[242] M. Alvioli, M. Strikman, Spin-isospin correlated configurations in complex nuclei and neutron skin effect in $W^{\pm}$ production in high-energy proton-lead collisions, Phys. Rev. C 100 (2) (2019) 024912. `arXiv:1811.10078`, `doi:10.1103/PhysRevC.100.024912`.

[243] A. Chaumeaux, V. Layly, R. Schaeffer, Proton Scattering at 1-GeV, Annals Phys. 116 (1978) 247–357. `doi:10.1016/0003-4916(78)90236-1`.

[244] D. Adhikari, et al., Accurate Determination of the Neutron Skin Thickness of ^{208}Pb through Parity-Violation in Electron Scattering, Phys. Rev. Lett. 126 (17) (2021) 172502. `arXiv:2102.10767`, `doi:10.1103/PhysRevLett.126.172502`.

[245] A. Trzcinska, J. Jastrzebski, P. Lubinski, F. J. Hartmann, R. Schmidt, T. von Egidy, B. Klos, Neutron density distributions deduced from anti-protonic atoms, Phys. Rev. Lett. 87 (2001) 082501. `doi:10.1103/PhysRevLett.87.082501`.

[246] C. J. Horowitz, J. Piekarewicz, Neutron star structure and the neutron radius of Pb-208, Phys. Rev. Lett. 86 (2001) 5647. `arXiv:astro-ph/0010227`, `doi:10.1103/PhysRevLett.86.5647`.

[247] I. Helenius, H. Paukkunen, K. J. Eskola, Neutron-skin effect in direct-photon and charged hadron-production in Pb+Pb collisions at the LHC, Eur. Phys. J. C 77 (3) (2017) 148. `arXiv:1606.06910`, `doi:10.1140/epjc/s10052-017-4709-9`.

[248] H. Paukkunen, Neutron skin and centrality classification in high-energy heavy-ion collisions at the LHC, Phys. Lett. B 745 (2015) 73–78. `arXiv:1503.02448`, `doi:10.1016/j.physletb.2015.04.037`.

[249] C. Loizides, J. Kamin, D. d'Enterria, Improved Monte Carlo Glauber predictions at present and future nuclear colliders, Phys. Rev. C 97 (5) (2018) 054910, [Erratum: Phys.Rev.C 99, 019901 (2019)]. `arXiv:1710.07098`, `doi:10.1103/PhysRevC.97.054910`.

[250] A. Trzcinska, J. Jastrzebski, P. Lubinski, F. J. Hartmann, R. Schmidt, T. von Egidy, B. Klos, Information on the nuclear periphery deduced from the properties of heavy antiprotonic atoms, Nucl. Instrum. Meth. B 214 (2004) 157–159. `doi:10.1016/j.nimb.2003.08.017`.

[251] D. Oliinychenko, H. Petersen, Deviations of the Energy-Momentum Tensor from Equilibrium in the Initial State for Hydrodynamics from Transport Approaches, Phys. Rev. C 93 (3) (2016) 034905. `arXiv:1508.04378`, `doi:10.1103/PhysRevC.93.034905`.

[252] M. Alvioli, H. Holopainen, K. J. Eskola, M. Strikman, Initial state anisotropies and their uncertainties in ultrarelativistic heavy-ion collisions from the Monte Carlo Glauber model, Phys. Rev. C 85 (2012) 034902. `arXiv:1112.5306`, `doi:10.1103/PhysRevC.85.034902`.

[253] G. S. Denicol, S. Jeon, C. Gale, Transport Coefficients of Bulk Viscous Pressure in the 14-moment approximation, Phys. Rev. C 90 (2) (2014) 024912. `arXiv:1403.0962`, `doi:10.1103/PhysRevC.90.024912`.

[254] P. Huovinen, H. Petersen, Particlization in hybrid models, Eur. Phys. J. A 48 (2012) 171. `arXiv:1206.3371`, `doi:10.1140/epja/i2012-12171-9`.

[255] V. Vovchenko, V. Koch, Particlization of an interacting hadron resonance gas with global conservation laws for event-by-event fluctuations in heavy-ion collisions, Phys. Rev. C 103 (4) (2021) 044903. `arXiv:2012.09954`, `doi:10.1103/PhysRevC.103.044903`.

[256] F. Becattini, L. Ferroni, Statistical hadronization and hadronic microcanonical ensemble. 2., Eur. Phys. J. C 38 (2004) 225–246, [Erratum: Eur.Phys.J. 66, 341 (2010)]. `arXiv:hep-ph/0407117`, `doi:10.1140/epjc/s10052-010-1243-4`.

[257] O. Savchuk, V. Vovchenko, V. Koch, J. Steinheimer, H. Stoecker, Constraining baryon annihilation in the hadronic phase of heavy-ion collisions via event-by-event fluctuations, Phys. Lett. B 827 (2022) 136983. `arXiv:2106.08239`, `doi:10.1016/j.physletb.2022.136983`.

[258] A. Sorensen, et al., Dense Nuclear Matter Equation of State from Heavy-Ion Collisions`arXiv:2301.13253`.

[259] A. Sorensen, V. Koch, Phase transitions and critical behavior in hadronic transport with a relativistic density functional equation of state, Phys. Rev. C 104 (3) (2021) 034904. `arXiv:2011.06635, doi:10.1103/PhysRevC.104.034904.`

[260] M. Kitazawa, M. Asakawa, H. Ono, Non-equilibrium time evolution of higher order cumulants of conserved charges and event-by-event analysis, Phys. Lett. B 728 (2014) 386–392. `arXiv:1307.2978, doi:10.1016/j.physletb.2013.12.008.`

<div align="right">

A

</div>

Appendix

A.1 Units

In this work, the system of natural units is used, in which the following constants are set to 1

$$\hbar = c = \epsilon_0 = k_B = 1 \,. \tag{A.1}$$

As a result, the energy given in units of eV and the length scale are in the following relation to each other

$$1\mathrm{fm} \cdot 1\mathrm{GeV} \approx \frac{1}{0.197} \tag{A.2}$$

The Minkowski metric is chosen to be with the mostly minus convention

$$g^{\mu\nu} = \mathrm{diag}(1, -1, -1, -1) \,. \tag{A.3}$$

A.2 Degrees of freedom for transport coefficient computation

Here the detailed properties of the particles used are presented. Starting with system 1, it contains only the most abundant stable particles and their interactions with each other are purely of isotropic and elastic nature with a cross section of $\sigma_{el} = 30\,\mathrm{mb}$. Within the legends, it is denoted as $\pi K N \Lambda \Sigma$ (const.). System 2 consists of the stable hadrons of system 1 as well as the first lightest mesonic and baryonic resonances and it is denoted as $\pi K N \Lambda \Sigma$ (+Res.). Finally system 3 is the full SMASH hadron gas with all implemented hadrons.

Particle	Mass [GeV/c²]	Degenercy	Width [GeV]	In system
π	0.138	3	0	1,2,3
K	0.494	4	0	1,2,3
η	0.548	2	0.548	2,3
ρ	0.776	6	0.149	2,3
σ	0.800	1	0.400	2,3
$K^\star(892)$	0.892	8	0.050	2,3
N	0.938	8	0	1,2,3
Λ	1.116	2	0	1,2,3
Σ	1.189	12	0	1,2,3
Δ	1.232	32	0.117	2,3
$\Sigma(1385)$	1.385	24	0.036	2,3
$N(1440)$	1.440	8	0.350	2,3
$N(1520)$	1.520	8	0.110	2,3
$N(1535)$	1.535	8	0.150	2,3
$N(1650)$	1.650	8	0.125	2,3
See [94]				3

Table A.1: Hadronic degrees of freedom used for the calculation of the transport coefficients. The degeneracy is the product of spin, charged and anti-particle states.

A.3 From the susceptibilities to the cumulants

This section aims to derive the expression Eq. 4.15 that relates the cumulants κ_n^q with derivatives of the grand-canonical partition function $\mathcal{Z}$ with respect to the chemical potential. As a starting point, it is useful to recall the definition of the susceptibilities defined as the derivative of the adimensional pressure P/T^4 (Eq. 4.15) with respect to the chemical potential of charge q over the temperature $\hat{\mu}_q \equiv \mu_q/T$

$$\chi_n^q = \frac{1}{VT^3} \frac{\partial^n \ln \mathcal{Z}}{\partial \hat{\mu}_q^n} \, . \tag{A.4}$$

In order to determine the cumulants of conserved charge q, the probability ω_N^q of the appearance of exactly N particles of charge q is needed to construct the cumulant generating functional. It is therefore instructive to express the grand-canonical partition function in terms of the sum over all canonical partition function Z_N

$$\mathcal{Z}(T, V, \hat{\mu}_q) = \sum_N e^{\hat{\mu}_q N} Z_N(T, V, \hat{\mu}_q) \, . \tag{A.5}$$

The canonical partition function contains the information about the system having exactly N particles. The probability of the grand canonical system of having exactly N particles is therefore simply

$$\omega_N^q \equiv \frac{e^{\hat{\mu}_q N} Z_N(T, V, \hat{\mu})}{\mathcal{Z}(T, V, \hat{\mu})} \, . \tag{A.6}$$

From these probabilities, one can construct the cumulant generating function $K(t)$ as the natural logarithm of the expectation value with weight e^{tN} (see Eq. 4.1-4.3)

$$K_q(t) = \ln \sum_N \omega_N^q e^{tN} \,, \tag{A.7}$$

$$= \ln \sum_N e^{(\hat{\mu}_q + t)N} \frac{Z_N(T, V)}{\mathcal{Z}(T, V, \hat{\mu}_q)} \,, \tag{A.8}$$

$$= \ln \mathcal{Z}(T, V, \hat{\mu}_q + t) - \ln \mathcal{Z}(T, V, \hat{\mu}_q) \,. \tag{A.9}$$

The cumulants are then computed by taking derivatives with respect to t at $t = 0$

$$\kappa_n^q = \left. \frac{\partial^n K_q(t)}{\partial t^n} \right|_{t=0} \,, \tag{A.10}$$

$$= \left. \frac{\partial^n \ln \mathcal{Z}(T, V, \hat{\mu}_q + t)}{\partial t^n} \right|_{t=0} \,, \tag{A.11}$$

$$= \frac{\partial^n \ln \mathcal{Z}(T, V, \hat{\mu}_q)}{\partial \hat{\mu}_q^n} \,, \tag{A.12}$$

$$= V T^3 \chi_n^q \,. \tag{A.13}$$

This result shows the direct relation between the cumulants of conserved charge κ_n^q and the corresponding thermal susceptibility χ_n^q.

A.4 Toy model for the impact of charge annihilation on conserved charge fluctuations

In order to explain the influence of the fluctuation of the total charge number, a simplistic monte carlo toy model is introduced. The idea is based on the diffusion master equation and describes the medium on a discrete 1d grid and a sketch of it is shown in Fig. A.1. A similar model has been studied in [260] with the goal to study the diffusion of non-Gaussian fluctuations along the rapidity line. Here the rapidity is exchanged by simply an x coordinate and in addition a periodic boundary condition is introduced. There exist three types of particle species with charges $\{0, +, -\}$ in the system. On a discrete timestep basis each particle can move either into a neighboring cell or stay with an equal probability of $\gamma = 1/3$. If a particle moves beyond the grid it is instantly placed on the other side. In addition, a reaction that annihilates two opposite charges and creates a neutral charged state is introduced. Within each timestep and in each cell such a reaction takes place between one of such a pair with a probability ψ_1. It then moves freely within the grid and it decays with a probability $P_{\text{decay}} = \exp(-t \cdot \psi_2)$. For all calculations 10 bins with a bin width of 0.1 are used.

The fluctuations of the system is studied within the following setup. In the initial state 25 positive and negative charged particles are distributed homogeneously in the grid. Then the medium is evolved in time with the the following three sets of probabilities ψ_1 and ψ_2 (see Tab. A.2) that dictate the produced amount of charge 0 zero states.
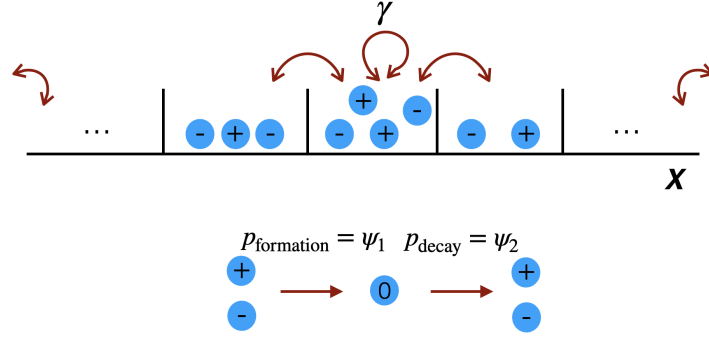
Figure A.1: System described by the monte carlo toy model.

	ψ_1	ψ_2
Set 1	0.5	0.9
Set 2	0.1	0.95
Set 3	0.01	0.95

Table A.2: Sets of parameters ψ_1 and ψ_2 used.

To study the cumulants of the system, it has to be in an equilibrium state and detailed balance has to be present.
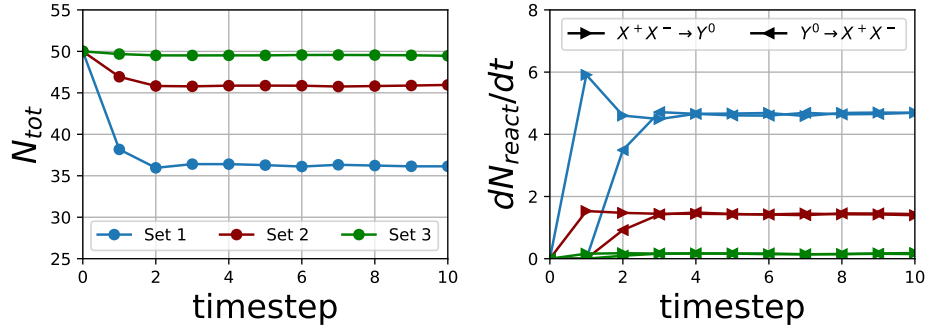

Figure A.2: Time evolution of the total charge number (left) and the number of forward and back reactions (right).

Fig. A.2 shows the evolution of the total amount of charges and the number of reactions as a function of the timestep and for the three different sets of probabilities. One can see that for each set of $\{\psi_1, \psi_2\}$ different equilibration values of N_{tot} are reached meaning that a certain amount of charges are annihilated. For the results of set 3 only a very small fraction of the particles are in the charge 0 state whereas for set 1 a larger portion of particles have interacted and their charges annihilated. On the right hand side of Fig. A.2 one can see that the system is in detailed balance since for all three sets of probabilities the number of forward and backward reactions are the same after the equilibration process. In the first 2 timesteps the creation

process $X^+X^- \to Y^0$ dominates since there are only stable particles in the initial state. Then the decay processes start to grow and detailed balance is restored.

From the charge density $n(x)$ the net charge as a function of x is calculated as

$$Q = \int_0^x n(x)dx\,. \tag{A.14}$$

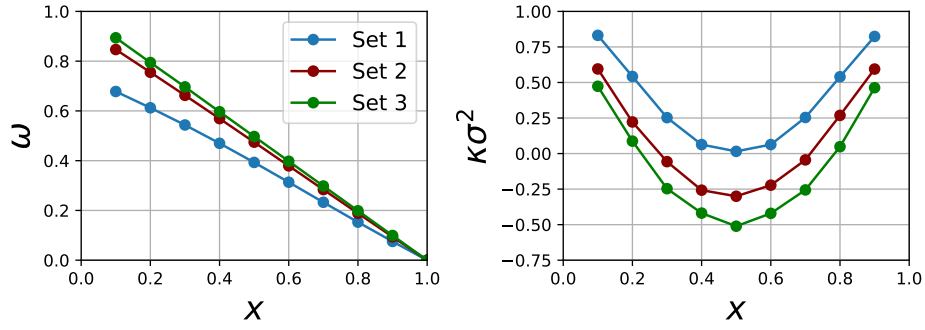Similar to the previous studies, the cumulants $\langle(\delta Q)^n\rangle$ are then calculate from Q.

Figure A.3: Scaled variance (left) and kurtosis (right) as a function of x. The results of three different sets of probabilities are shown.

Since the net charge number of the system is a conserved quantity it is expected that the cumulants follow a similar trend as the results presented in Section 4.3. Fig. A.3 shows the scaled variance and the kurtosis of the toy model presented above. Starting with the results of Set 3, both ω and $\kappa\sigma^2$ follow the Binomial baseline. This means that the implementation of the model itself is correct and can be used for further studies. Going on from to the results of set 2 and set 3 where a larger fraction of the total charge is annihilated and the total charge fluctuation increases, the cumulants start to deviate from the Binomial baseline. For the scaled variance and at small values of x the fluctuations decrease and for the kurtosis the transition from the Binomial to the Poisson baseline is observed. So a dependency on the interaction between the constituents is found.

On top, a deviation from the cumulants including charge fluctuations is found on the level of the scaled variance.

A.5 Parametrization of the Ising model cumulants

The following parametrization of the higher order cumulants were derived in [208]. They read

$$\langle(\delta\sigma)^2\rangle = \frac{T}{V}\frac{M_0}{cH_0}R^{\beta-\beta\delta}$$

$$\times \frac{(1+(2\beta-1)\theta^2)}{(1+(3a+2\beta\delta-1)\theta^2+(a(2\beta\delta-3)+5b)\theta^4+b(2\beta\delta-5)\theta^6)} \quad (A.15)$$

$$\langle(\delta\sigma)^3\rangle = -2\frac{T^2}{V^2}\frac{M_0}{(cH_0)^2}R^{\beta-2\beta\delta}$$

$$\times \frac{\theta(A_0+A_1\theta^2+A_2\theta^4+A_3\theta^6+A_4\theta^8)}{(1+(3a+2\beta\delta-1)\theta^2+(a(2\beta\delta-3)+6b)\theta^4+b(2\beta\delta-5)\theta^6)^3} \quad (A.16)$$

$$\langle(\delta\sigma)^4\rangle_c = 2\frac{T^3}{V^3}\frac{M_0}{(cH_0)^3}R^{\beta-3\beta\delta}$$

$$\times \frac{(B_0+B_1\theta^2+B_2\theta^4+B_3\theta^6+B_4\theta^8+B_5\theta^{10}+B_6\theta^{12}+B_7\theta^{14}+B_8\theta^{16})}{(1+(3a+2\beta\delta-1)\theta^2+(a(2\beta\delta-3)+6b)\theta^4+b(2\beta\delta-5)\theta^6)^5}$$

$$(A.17)$$

$$(A.18)$$

The parameter A_n in $\langle(\delta\sigma)^3\rangle$ are functions on scaling parameter of the critical region and they read

$$A_0 = 3a+3\beta(\delta-1) \quad (A.19)$$
$$A_1 = a(\beta(7\delta-3)-9)+2\beta(\delta-1)(\beta\delta+\beta-2)+10b \quad (A.20)$$
$$A_2 = a(2\beta(\beta(\delta(\delta+4)-3)-6\delta)+9)+\beta(2\beta-1)(\delta-1)(2\beta\delta-1)$$
$$+b(11\beta\delta+5\beta-30) \quad (A.21)$$
$$A_3 = a((2\beta-1)(\beta(\delta-1)-1)(2\beta\delta-3))+2b(\beta^2(\delta(\delta+8)-5)$$
$$-10\beta(\delta+1)+15) \quad (A.22)$$
$$A_4 = b((2\beta-1)(\beta(\delta-1)-2)(2\beta\delta-5)) \quad (A.23)$$
$$(A.24)$$

The functions B_n in $\langle(\delta\sigma)^4\rangle_4$ are defined as

$$B_0 = -1(3a + 3\beta(\delta - 1)) \tag{A.25}$$

$$B_1 = 45a^2 + 3a(2\beta(11\delta - 7) + 5) + 12\beta^2(\delta - 1)(3\delta - 1) - 30b \tag{A.26}$$

$$B_2 = 15a^2(11\beta\delta - 3(\beta + 5)) + 6a(2\beta(17\beta\delta^2 - 3(6\beta + 7)\delta + 3\beta + 17) - 5)$$
$$+ 255ab + 2\beta(\delta - 1)(2\beta(\beta(\delta(11\delta - 4) - 1) - 18\delta + 6) + 5)$$
$$+ 30b(7\beta(\delta - 1) + 5) \tag{A.27}$$

$$B_3 = 30a^2(2\beta\delta - 3)(\beta(4\delta - 2) - 5) + a(4\beta(82\delta + \beta(38\beta\delta^3 - 3\delta^2(6\beta + 41)$$
$$+ 6\delta(19 - 3\beta) + 6\beta - 9) - 78) + 30) + 15ab(54\beta\delta - 14\beta - 85)$$
$$+ 4\beta(\delta - 1)(2\beta\delta - 1)(\beta(2\beta(\delta(\delta + 2) - 1) - 7\delta + 3) + 2)$$
$$+ 12b(2\beta(\delta(2\beta(8\delta - 7) - 29) + 35) - 25) + 450b2 \tag{A.28}$$

$$B_4 = 6a^2(\beta(161\delta + 2\beta(\delta(6 - 53\delta) + \beta(\delta(\delta(9\delta + 11) - 15) + 3) + 9) - 33) - 75)$$
$$+ a(4\beta(\beta(4\delta\beta^2(\delta(2\delta(\delta + 5) - 15) + 4) - 4\beta(16\delta^3 - 15\delta + 3)$$
$$+ \delta(97\delta - 74) - 9) - 41\delta + 45) - 15) + 6ab(2\beta(\beta(\delta(67\delta + 2) - 15)$$
$$- 263\delta + 55) + 425) + \beta(2\beta - 1)(\delta - 1)(1 - 2\beta\delta)2(\beta(4\delta - 2) - 1)$$
$$+ 4b(2\beta3(3\delta(9\delta^2 + 3\delta - 11) + 5) + 6\beta^2(\delta(34 - 41\delta) + 5) + 5\beta(39\delta - 59) + 75)$$
$$+ 15b^2(\beta(59\delta + 5) - 150) \tag{A.29}$$

$$B_5 = a^2(2\beta\delta - 3)(2\beta(4\beta^2(\delta(\delta(\delta + 9) - 12) + 3) - 6\beta(\delta(7\delta + 6) - 6) + 77\delta - 6) - 75)$$
$$+ a((2\beta - 1)(2\beta\delta - 3)(2\beta\delta - 1)(2\beta(\beta(4\delta^2 - 6\delta + 2) - 5\delta + 4) - 1))$$
$$+ 2ab(2\beta(2\beta^2(\delta(\delta(35\delta + 87) - 93) + 15) - 9\beta(\delta(61\delta + 26) - 25) + 8(142\delta - 15)) - 1275)$$
$$+ 2b(4\beta(85 + 2\beta(2\beta^2\delta^4 + 6\beta\delta^3(3\beta - 4) + \delta^2(52 - 3\beta(8\beta + 7)) + 6\delta(\beta(\beta + 7) - 7)$$
$$- 5(\beta + 3)) - 39\delta) - 75) + 12b2(\beta(53\beta\delta^2 + 10\delta(4\beta - 29) - 25(\beta + 2)) + 375)$$
$$\tag{A.30}$$

$$B_6 = a^2((2\beta - 1)(\beta(\delta - 1) - 1)(\beta(4\delta - 2) - 5)(3 - 2\beta\delta)2) + ab(4\beta(\beta(4\delta\beta2(\delta(2\delta(\delta + 13) - 33) + 8)$$
$$- 4\beta(\delta(2\delta(16\delta + 51) - 105) + 15) + \delta(499\delta + 434) - 315) - 5(143\delta + 9)) + 1275)$$
$$+ 2b((2\beta - 1)(2\beta\delta - 5)(2\beta\delta - 1)(\beta(\beta(4\delta^2 - 6\delta + 2) - 9\delta + 7) - 3))$$
$$+ 2b^2(\beta(\beta^2(2\delta(\delta(43\delta + 177) - 165) + 50) - 24\beta(\delta(37\delta + 45) - 25) + 2545\delta + 775) - 2250)$$
$$\tag{A.31}$$

$$B_7 = ab(2\beta\delta - 5)((2\beta - 1)(2\beta\delta - 3)(2\beta(\beta(4\delta^2 - 6\delta + 2) - 13\delta + 10) + 17))$$
$$+ b^2(2\beta\delta - 5)(4\beta(2\beta^2(\delta(\delta(\delta + 17) - 21) + 5) - 5\beta(\delta(7\delta + 22) - 15) + 119\delta + 80) - 450)$$
$$\tag{A.32}$$

$$B_8 = b^2((2\beta - 1)(\beta(\delta - 1) - 2)(5 - 2\beta\delta)2(\beta(4\delta - 2) - 9)) \tag{A.33}$$

A.6   Particles coupled to the critical mode

The list of particles that are coupled to the critical field is shown in Tab. A.3.

Particle	Mass [GeV/c^2]	Degeneracy
π	0.138	3
ρ	0.776	6
K	0.494	4
$K^\star(892)$	0.892	8
N	0.938	8
Δ	1.232	32
Λ	1.116	2
Σ	1.189	12

Table A.3: Hadronic degrees of freedom used in the presented calculations. The degeneracy is the product of spin, charged and anti-particle states.

A.7 Obtaining the diffusiveness and radii for the neutron skin effect

The starting point for obtaining the different Woods-Saxon parameters for protons and neutrons, such that the difference between the proton and neutron mean-square radii Δr_{np} has some specific value, is the expression of the mean square charge distribution which is the one that is measured by experiments

$$\langle r_{\text{ch}}^2 \rangle = \frac{3R_0^2}{5} \left(1 + \frac{7\pi^2 d^2}{3R_0^2} \right) . \tag{A.34}$$

The mean radius of the proton distribution then is obtained by the following unfolding procedure

$$\langle r_{\text{ch}}^2 \rangle = \langle r_p^2 \rangle + R_p^2 . \tag{A.35}$$

With $R_p = 0.875 \, \text{fm}$ the radius of the proton. After $\langle r_p^2 \rangle$ has been calculated, the value of the Woods-Saxon proton radius and diffusiveness can be determined via

$$R_p = R_0 + \frac{5R_0 \langle r_p^2 \rangle}{7\pi^2 d^2 + 15R_0^2} , \tag{A.36}$$

$$d_p^2 = d^2 - \frac{5\langle r_p^2 \rangle (d^2 + 3R_0^2/\pi^2)}{7\pi^2 d^2 + 15R_0^2} . \tag{A.37}$$

The resulting neutron Woods-Saxon parameter can be computed by simply exchanging $\langle r_p^2 \rangle$ with $(\Delta r_{np} + \langle r_p^2 \rangle)^2$ in Eq. A.37. Here, the assumption is, as already explained, that the type of neutron skin is a neutron-halo-like type ($R_p \sim R_n$).